Development of Design Methodologies on the Trailing Edge Architecture and Application of Variable Camber to a Segmented Flap System

Entwicklung von Entwurfsmethodologien für die Flügelhinterkantenarchitektur und Anwendung von variabler Wölbung auf ein segmentiertes Klappensystem

Von der Fakultät für Maschinenwesen der Rheinisch-Westfälischen Technischen Hochschule Aachen zur Erlangung des akademischen Grades eines Doktors der Ingenieurwissenschaften genehmigte Dissertation

vorgelegt von

Ralph Stephan

Berichter: Universitätsprofessor Dr.-Ing. Eike Stumpf
Assoc. Prof. Imon Chakraborty, Ph.D.

Tag der mündlichen Prüfung: 17. April 2025

Abstract

Enhancing the efficiency of commercial aircraft is crucial in the context of the global climate change in order to reduce the share of the environmental impact of aviation. The optimization of aerodynamic characteristics offers great potential for saving fuel and reducing emissions. In addition, technologies that can respond to climate-optimized flight altitude variation by adapting the wing geometry during flight become more important in the future.

The aim of this thesis is to investigate variable camber principles applied to a segmented trailing edge flap on the overall aircraft level. Furthermore, methods need to be developed that allow the trailing edge flaps, which are essential for variable camber, to be precisely modeled in the preliminary aircraft design stage. Moreover, the thesis introduces a new methodology to ensure valid longitudinal trimming in the iterative design process.

To achieve this, a set of methodologies will first be developed for the design of control surfaces, which will later incorporate variable camber. This development includes the optimization of high-lift configurations, the modeling of flap loads in different flight regimes, and the design of actuators. Depending on the application, techniques such as neural networks, fluid simulations, or regression models from existing data are employed. Subsequently, variable camber is applied as a retrofit design to segmented trailing-edge flaps within the preliminary aircraft design environment MICADO of the Institute of Aerospace Systems of the RWTH Aachen University. In order to classify the potential for fuel savings calculated for a variable camber application, the given reference aircraft is compared with an optimization of the twist distribution and finally with a combined application.

High predictive accuracies have been demonstrated for all developed models and methodologies, considering the limited data availability at the preliminary design level and the available computing time. At the overall aircraft level, the potential of a variable camber application varies by aircraft type, with a 3.5 % reduction in fuel consumption when applied to an aircraft with a previous wing twist optimization. The segmentation of trailing edge flaps shows a slight but noticeable fuel savings potential, depending on the reference aircraft under investigation.

The increase in fuel savings potential is particularly relevant when aircraft operate outside their design optimum. This aspect might become increasingly important for minimizing the climate impact of existing aircraft by altering flight routes to alternative altitudes, such as to avoid the formation of long-lasting contrail-induced cirrus clouds.

Zusammenfassung

Die Effizienzsteigerung von Verkehrsflugzeugen spielt eine zentrale Rolle bei der Reduzierung der Klimawirkung der Luftfahrt vor dem Hintergrund des globalen Klimawandels. Die Optimierung aerodynamischer Eigenschaften bietet dabei ein großes Potenzial zur Treibstoffeinsparung und Emissionsreduktion. Zudem gewinnen Technologien zunehmend an Bedeutung, die auf klimaoptimierte Flughöhenvariationen mit einer Anpassung der Flügelgeometrie während des Fluges reagieren können.

Das Ziel dieser Arbeit ist es, das Prinzip einer variablen Wölbung durch segmentierte Hinterkantenklappen auf der Ebene des Gesamtflugzeugs zu untersuchen. Ferner wurden Methoden entwickelt, die es ermöglichen, die für die variable Wölbung essentiellen Hinterkantenklappen im Flugzeugvorentwurf präzise zu modellieren. Darüber hinaus wurde für valide Aussagen die longitudinale Trimmung mit einer neuen Methodik sichergestellt.

Dazu wird zunächst ein Satz an Methodiken entwickelt, welche zur Auslegung der Steuerflächen dienen, die anschließend mit variabler Wölbung eingesetzt werden. Dies umfasst die Optimierung von Hochauftriebskonfigurationen, die Modellierung der Klappenlasten in verschiedenen Flugbereichen und die Auslegung von Aktuatoren. Je nach Anwendungen kommen dabei neuronale Netze, Strömungssimulationen oder Regressionen aus bestehenden Daten zur Anwendung. Anschließend erfolgt auf Gesamtflugzeugebene innerhalb der Flugzeugvorentwurfsumgebung MICADO des Instituts für Luft- und Raumfahrtsysteme der RWTH Aachen University die Anwendung von variabler Wölbung als Retrofitdesign auf segmentierten Hinterkantenklappen. Zur Einordnung des berechneten Potenzials zur Kerosineinsparung wird das vorgegebene Referenzflugzeug sowohl mit einer hinsichtlich der Verwindungsverteilung optimierten Referenz, als auch einer kombinierten Anwendung aus optimierter Verwindungsverteilung und variabler Wölbung verglichen.

Für alle entwickelten Modelle und Methodiken konnten unter Berücksichtigung der reduzierten Datenverfügbarkeit auf Vorentwurfsebene hohe Vorhersagegenauigkeiten gezeigt werden. Dabei wird auch die zur Verfügung stehende Rechenzeit berücksichtigt. Auf der Ebene des Gesamtflugzeugs variieren die Potenziale je nach angewendetem Flugzeugtyp, wobei eine Kerosinverbrauchsreduktion von bis zu 3,5 % erzielt wird, wenn variable Wölbung auf ein vorher hinsichtlich der Verwindung optimiertes Flugzeug angewendet wird. Die Segmentierung von Hinterkantenklappen zeigt ein Steigerungspotenzial gegenüber der Referenzkonfiguration.

Die Potenzialsteigerung ist insbesondere von Relevanz, wenn Flugzeuge nicht im Designoptimum betrieben werden. Dies wird zunehmend wichtig, um die Klimaauswirkungen bestehender Flugzeuge zu minimieren, etwa durch Flugrouten in alternativen Höhen, um die Bildung langlebiger, durch Kondensstreifen verursachter Zirruswolken zu vermeiden.

Acknowledgments

I would like to start by thanking Prof. Dr. Stumpf, head of the Institute of Aerospace Systems at RWTH Aachen University, in his role as my Ph.D. supervisor. His support, rigorous feedback, and the autonomy he granted me to work independently and tackle challenges on my own were cornerstones of my work at the institute. My gratitude also goes to Prof. Chakraborty, the second examiner, whose expertise and guidance improved the clarity and development of this work, and to Prof. Dr. Broeckmann, chair of the examination committee, for creating a fair and positive atmosphere during my defense.

Just as the academic guidance I received laid the foundation for this research, the personal support carried me through to its completion. I am incredibly thankful for the unwavering support I received from my family—above all, my dearest Meike. From turning Aachen into a true home, to those late-night cups of coffee that kept me going through endless writing sessions, you were always there without condition and gave me the strength I needed. Another great source of support, for which I am endlessly grateful, comes from my parents and my brother, Thomas. Back in my school days, my mother helped me through math and physics problems, while my father gave me the enthusiasm for engineering. Their support, which I received both before and during my studies as well as during my time at the institute, has been a major factor in the completion of my degree.

An essential factor in making my time at the institute both rewarding and enjoyable has been my colleagues. While intense technical discussions at the whiteboard fueled the work, it was the coffee-break conversations, kiosk runs, soccer matches, and shared conferences that kept motivation high. I want to thank Dr. Tim Effing (in particular for his thorough proofreading), Laura Babetto, Paul Mauerer, Maurice Zimmnau, Ansgar Kirste, Kim Goldschmidt, Lutz Wortmann, and Sebastian Hille—their solidarity and (occasionally questionable) humor made even the busiest weeks something to look forward to. I would like to highlight my deepest thanks to Martin Bremm, a longtime friend and an unfailingly positive office companion throughout this whole time—it was truly a pleasure working with you. My appreciation extends to senior colleagues Florian Schültke and Dr. Benedikt Aigner, whose guidance and support helped me to find my way at the institute, and to Fabian Peter, Dr. Tobias Röben, and Kuno Jandaurek, whose collaboration and expertise provided valuable input for this research. Furthermore, my sincere thanks go to my thesis students Henri Schottmüller, Gerrit Weber, Nicolas Schneiders, Cedric Heyen, and Lutz Wortmann. Your commitment and enthusiasm made supervising your theses a pleasure, advanced my own research, and set a positive standard for teamwork.

Parts of this thesis were conducted within the LuFo project Bimod, and I would like to thank Dr. Johannes Ruhland and, once again, Martin Bremm for their collaboration. To everyone mentioned here—and to those I may have inadvertently omitted—thank you all.

Table of Contents

List of Figures

List of Tables

List of Symbols

General Symbols

A	Area	[m^2]
a	Speed of sound	[$\frac{\mathrm{m}}{\mathrm{s}}$]
b	Wing span	[m]
$\mathbf{C}$	Curve	[$-$]
C	Coefficient	[$-$]
c	Chord length	[m]
D	Drag	[N]
e	Oswald factor	[$-$]
$\mathbf{F}(x)$	Target function for landing configuration	[$-$]
F	Force per unit volume	[$\frac{\mathrm{N}}{\mathrm{m}^3}$]
f	Body force per unit mass	[$\frac{\mathrm{N}}{\mathrm{kg}}$]
G	Gap, in relation to the chord	[$-$]
g	Gravitational acceleration	[$\frac{\mathrm{m}}{\mathrm{s}^2}$]
$\mathbf{H}(x)$	Target function for takeoff configuration	[$-$]
h	Elevation	[m]
J	Ball screw pitch	[$\frac{\mathrm{m}}{\mathrm{rev}}$]
L	Lift	[N]
L'	Lift (sectional)	[$\frac{\mathrm{N}}{\mathrm{m}}$]
M	Moment	[$\mathrm{N\,m}$]
m	Mass	[kg]
Ma	Mach number	[$-$]

Symbol	Description	Unit
N	Quantity	[$-$]
n	Load factor	[$-$]
O	Overlap, in relation to the chord	[$-$]
P	Power	[W]
p	Pressure	[$\frac{\mathrm{N}}{\mathrm{m}^2}$]
Q	Volume flow	[$\frac{\mathrm{m}^3}{\mathrm{s}}$]
Re	Reynolds number	[$-$]
S	Wing area	[m^2]
s	Length	[m]
T	Torque	[N m]
t	Time	[s]
u,v,w	Velocities in the Cartesian coordinate system	[$\frac{\mathrm{m}}{\mathrm{s}}$]
U	(Scalar value of) velocity	[$\frac{\mathrm{m}}{\mathrm{s}}$]
$\mathbf{V}$	(Vector field of the) velocity in the Cartesian coordinate system	[$\frac{\mathrm{m}}{\mathrm{s}}$]
V	Volume	[m^3]
W	Weight	[N]
X	Input value in artificial neural networks	[$-$]
x,y,z	Cartesian coordinate system	[m]
Y	Target value in artificial neural networks	[$-$]
α	Angle of attack	[deg]
β	Bias in artificial neural networks	[$-$]
Γ	Circulation	[$\frac{\mathrm{m}^2}{\mathrm{s}}$]
Δ	Step width	[$-$]
δ	Boundary layer thickness	[m]
ϵ	Motor load peak factor	[$-$]
ζ	Motor-type factor	[$-$]
η	Deflection angle	[deg]

ϑ	Temperature	[K]
Λ	Wing aspect ratio	[–]
μ	Dynamic viscosity	[$\frac{\mathrm{N\,s}}{\mathrm{m}^2}$]
ξ	Relative deviation	[–]
ρ	Density	[$\frac{\mathrm{kg}}{\mathrm{m}^3}$]
τ	Ratio between permanent and peak power	[–]
ω	Weight in artificial neural networks	[–]
χ	Neuron input (activation function)	[–]
ψ	Neuron output (activation function)	[–]

Subscripts

∞	Free flow conditions
a	Absolute
BBG	Ball-bearing gears
BS	Ball screw
C	Cruise
d, D	(sectional) Drag
F	Flap
GB	Gearbox
GBP	Gearbox planets
GBS	Gearbox stages
Hou	Housing
l, L	(sectional) Lift
m, M	(sectional) Moment
mech	Mechanical
P	Power
p	Pressure

PP	Pole pairs
ref	Reference
S1g	1-g stall
S	Slat
Sp	Spoiler
stat	Static
tang	Tangential
tot	Total
w	Wall

Abbreviations

AI	Artificial Intelligence
AC	Alternating Current
CoA	Center of Aerodynamics
CoG	Center of Gravity
CS	Certification Specifications
DC	Direct Current
DFS	Differential Flap Setting
EAS	Equivalent Airspeed
EASA	European Union Aviation Safety Agency
ECU	Electric Control Unit
EDC	Extension and Damping Control
EHA	Electrohydrostatic Actuator
ELU	Exponential Linear Unit
FE	Flap Extended
GD	Green Dot speed (optimum lift-to-drag)
HTP	Horizontal Tail Plane

IAS	Indicated Airspeed
ICA	Initial Cruise Altitude
ILR	Institute of Aerospace Systems
ISA	International Standard Atmosphere
LE	Leading Edge
LEMA	Linear Electromechanical Actuator
LoF	Line-of-Flight
LST	Local Sweep Transformation
LVDT	Linear Variable Differential Transformer
MICADO	Multidisciplinary Integrated Conceptual Aircraft Design and Optimization
MO	Maximum Operating
MTOM	Maximum Takeoff Mass
NM	Nautical Mile
OME	Operating Mass Empty
PAX	Number of passengers
PCU	Power Control Unit
RANS	Reynolds Averaged Navier-Stokes equations
ReLU	Rectified Linear Unit
REMA	Rotary Electromechanical Actuator
SAF	Sustainable Aviation Fuel
SSE	Sum of Squared Errors
TAS	True Airspeed
TE	Trailing Edge
UNICADO	UNIversity Conceptual Aircraft Design and Optimization
VC	Variable Camber
WB	Wing Body

1 Motivation

Aviation is one of the most important cultural and economic achievements since the beginning of the 20th century. From an economic perspective, its connectivity, reliability, and speed are of great value, particularly for time-critical, high-value goods. Although air transport costs are higher—4 to 5 times more than road transport and 12 to 16 times more than sea transport—it accounted for 35 % of global trade by value in 2019 [49]. In addition to the infrastructure required by the industry, the aviation sector directly creates millions of jobs within manufacturers, airlines, and airports, as well as indirectly within the broader aviation industry [1]. Another economically relevant factor is tourism, with more than half of all international tourist trips in 2017 being traveled by air [49]. Besides its ecological value, tourism promotes cultural exchange and mutual understanding by enabling people from different backgrounds to meet and learn from each other. Apart from tourism, the fast and affordable way of traveling by air allows people to experience first-hand different ways of life, customs, traditions, exchange ideas, and build bonds through international cooperation.

However, the climate change is a very present challenge that affects all sectors, including aviation. The share of global CO_2 emissions attributed to aviation has increased significantly, from approximately 0.6 % in 1950 to about 1.9 % in 1990. From 1990 to 2019, the share fluctuated around an average of 2 % [1] or slightly higher [96], excluding the exceptional situation during the COVID-19 pandemic. In absolute numbers, the yearly CO_2 emissions from aviation nearly doubled from 1990 to 2019 to a value of 1 Gt [10], equivalent to 10^{12} kg. This value needs to be put into context with additional data from the same time period, including the increase in demand and the increase in efficiency. The demand for air travel, combining passenger and freight, quadrupled from about 0.25 trillion ton-kilometers equivalent ($\mathrm{tkm_e}$) to 1 trillion $\mathrm{tkm_e}$ [10]. This increase was accompanied by nearly a doubling of efficiency in terms of Joules per ton-kilometer [10]. The importance of continuous efficiency improvements in aviation is highlighted by this development. For reasons of data availability and explanatory value, the discussions above focus on the pre-COVID period. While air traffic collapsed considerably during the times of restrictions [96], most regions of the world have shown a rapid recovery [1]. By May 2023, internationally averaged domestic air traffic had already exceeded 2019 levels [1]. While the above-mentioned share of global CO_2 emissions from aviation is currently around 2 %, the relative impact on global warming is estimated at 4 % [96]. A characteristic that distinguishes aviation from other sectors is that the emissions are produced at high altitudes, which needs to be taken into account for the climate impact [36]. Apart from the CO_2 effects, which are well understood and documented [36], the determination of the global warming impact needs to take more complex considerations into account. The combustion of jet fuel, primarily Jet A-1, releases not only CO_2, but also several other emissions including nitrogen oxides, soot, and water vapor [36], summarized under the term non-CO_2 impact. Due to differences in lifetime, temperature, and humidity, these pollutants vary regarding the climate impact [36]. For instance, water vapor is very short-lived compared to CO_2 emissions, however, under suitable atmospheric conditions, it can lead to the formation of contrails, which may evolve into extensive cirrus clouds and exert a notable greenhouse effect [42].

Various strategies to address the challenge have been implemented. In 2012, the European Union (EU) introduced the Flightpath 2050 [31], aiming to reduce CO_2 emissions from new aircraft by 75 % compared to the year 2000. This initiative was later strengthened by the European Green Deal [121], which sets the broader goal of making Europe the first climate-neutral continent by 2050, further emphasizing the need for significant reductions in aviation emissions [118]. The economic pressure on airlines, particularly in terms of fuel costs, is another important factor pushing the development of more efficient aircraft [39]. A link between ecological and economical objectives is established with the EU's Emissions Trading Scheme (EU ETS) [48] and the ICAO's Carbon Offset and Reduction Scheme for International Aviation (CORSIA) [47], which aims to limit aviation emissions to 2019 levels. Both approaches aim at greener air traffic via market-based measures.

Three primary strategies are available to mitigate the environmental impact of aviation: optimized operations, alternative fuels, and increased aircraft efficiency. Operational optimizations include route planning that prioritizes climate impact over cost. For example, scenarios for transatlantic flights have shown that a 1 % increase in operational costs can reduce climate impact by 10 % [40]. The contradictory trade-off between costs and climate impact could be compensated by considering non-CO_2 effects in market-based approaches [40] similar to those presented above. Sustainable Aviation Fuel (SAF), which summarizes synthetic and bio-based fuels, offers a long-term option for net-zero CO_2 emissions [22]. However, these fuels cannot be mixed with conventional jet fuel in high ratios, are currently only available in very limited quantities, and cannot easily be produced in the required amount [22]. Hydrogen, particularly liquid hydrogen, is another widely discussed alternative fuel that could theoretically enable CO_2-free aviation, assuming a CO_2-neutral hydrogen production. However, this requires a conversion of the infrastructure, proof of safe handling during operation, and fundamental changes to the aircraft themselves [9]. Both SAF and hydrogen as alternative fuels also have to consider non-CO_2 effects. Finally, increased aircraft efficiency provides an important contribution to reducing emissions [63], even though more efficient systems alone cannot achieve zero emissions. The major gains in aircraft efficiency are primarily due to advancements in engine technology and aerodynamics [63], with additional contributions from improvements in aircraft structure.

The motivation for this thesis is derived from maintaining the achievements of air travel and its role in connecting individuals and industries, alongside the challenges posed by climate change.

This thesis focuses on the last strategy mentioned: improving aircraft efficiency. In order to draw conclusions at the overall aircraft level, the methodologies, the evaluations, and the analyses in this thesis are carried out at the preliminary aircraft[*] design level. In particular, this work focuses on the design of and applications for control surfaces, providing new and extended methodologies which form a cohesive tool set. These methodologies include the optimization of high-lift configurations, taking into account the available computational time of the method applicant. Additionally, the thesis presents a modeling approach using artificial neural networks to predict aerodynamic loads on flaps under various flight conditions and deflection angles. It also introduces models for power-by-wire actuators, designed component-wise. The modular approach is intended to enable the adaptation of single modules in future applications. The aim of all the developed methodologies is to achieve the optimum results with minimum input data, reflecting the common constraint of limited data availability in the preliminary design phase. The development of methodologies at component level provides the foundation for the investigations at overall aircraft level. These investigations focus on the increase in efficiency in terms of fuel consumption using a variable camber application. This variable camber application utilizes the control surfaces, for which the methodologies at component level have been introduced, allowing them to act as multifunctional control surfaces. In particular, the effect of multiple segmented trailing edge flaps for the variable camber application with differential flap settings is investigated. In order to make valid statements about the results obtained, a new methodology for longitudinal trim is introduced within the preliminary aircraft design.

---

[*] The term "aircraft" in the context of this thesis refers to large aircraft according to the EASA CS-25 [30] certification specifications.

2 Fundamentals and state of the art

This thesis presents a comprehensive approach to design essential components of high-lift control surfaces and the subsequent application of variable camber (VC) with differential flap setting (DFS) on segmented trailing edge devices in the preliminary aircraft design. The approach is divided into the component design, enabling the VC application, and the overall aircraft design methodology itself. The fundamentals are given in this chapter, in order to provide the understanding for the methodologies and analyses, introduced in Chapter 3, as well as the application introduced in Chapter 4.

On the component side, key aspects are the high-lift design, the flap load calculation, and the required actuation mechanisms. Section 2.1 presents the theory of high-lift on aircraft wings. This foundation is essential as it establishes the geometry of the trailing edge devices that are required by subsequent design stages. Section 2.2 addresses the principles of modeling with neural networks, specifically applied to predicting flap loads. This modeling is an essential input for the accurate sizing of the actuation system, with actuator architectures as described in Section 2.3.

In terms of the investigation at the overall aircraft design level, the theory of longitudinal stability of aircraft is first discussed in Section 2.4, particularly with regard to the influence of the horizontal tail plane (HTP). This thesis introduces a novel methodology in Section 3.4.4, emphasizing the importance of accurate trim for conducting meaningful investigations at the overall aircraft level. Section 2.5 addresses the concept of variable camber, with a particular emphasis on its modes of action and the resulting impacts on mission performance. This section also covers the technical realizations of variable camber systems.

2.1 High-lift aerodynamics and technology

There is a large number of publications on the subject of high-lift, two of which are particularly noteworthy for the fundamentals of this thesis. One is the habilitation thesis by WILD [132], which deals extensively with aspects of high-lift, including the theory, technical implementation of various systems and design, as well as the history of development. Secondly, there is the publication by SMITH [111], which is considered to be the first adequate theoretical approach to understanding slotted high-lift devices, even though such devices had already been in use for several decades. Two further sources are worth noting that focus on fluid mechanics and lift generation. On the one hand, the book by ANDERSON [5] providing a broad overview of basic fluid mechanics principles with special regard to aircraft, and the book by MCLEAN [72] offering a very good approach to understanding the physics behind lift generation.

High-lift systems with retractable elements on the leading and trailing edge of the wing are an important and integral part of today's wing architectures. Their required utilization in critical flight phases close to the ground, typically the takeoff, climb, and landing segment [132], is due to the different requirements in these phases of low flight speeds compared to the cruise flight with speeds of today's commercial aircraft up to the transonic range [34]. The aerodynamic optimization of the wing for the cruise flight is the result of meeting the economic and also ecological demand for reduced fuel consumption [14]. The challenge to be solved by high-lift systems in low-speed flight becomes apparent when the following equation is considered, assuming unaccelerated steady flight and a low angle of attack [132]:

$$L = C_L \cdot U_\infty^2 \cdot S_{\text{ref}} \cdot 0.5 \cdot \rho_\infty. \tag{2.1}$$

The lift depends quadratically on speed and the speed must be significantly reduced, not only due to runway requirements, but also due to, e.g., limitations of the tires [132]. To give an order of magnitude, the airspeed is reduced by a factor of 3.57 for an assumed true airspeed (TAS) of 250 m/s at flight level (FL) 350 and a landing speed of 70 m/s at sea level. According to Eq. (2.1), several variables are now available to keep the lift L constant. However, changes of the wing area S_{ref} in this order of magnitude and manipulations of the fluid's density ρ_∞ are not technically feasible [132].

VAN DAM [127] has given some thought about the effect that would occur if, as an alternative approach, an aircraft were to be fitted with a wing that has the necessary surface area permanently installed. The results show a significantly increased wing area, which would require active flow control to even approach the cruise efficiency of a conventional aircraft.

Therefore, the main control variable is the lift coefficient C_L, which, taking into account the different atmospheric densities [77] between sea level and FL350, has to increase by the factor 3.63 for the above-mentioned indicative example, disregarding the minor wing area changes that occur during flap deflection. Taking into account safety factors and certain approach corridors, WILD [132] estimates that the required lift coefficient is two to three times higher than the actually achievable lift coefficient of a clean swept wing*. As if these insights were not enough motivation, BUTTER [21] indicates other positive influences an improvement of the high-lift system would have. For example an increase of the maximum lift coefficient during landing by 5 % is estimated with a possible increase of the payload by 25 %. However, it should be mentioned that, for example, RECKZEH [92] makes such assessments dependent on the aircraft configuration.

---

*The clean wing refers to a wing with all control surfaces retracted.

The use of these systems was actually advantageous even for early aircraft types that did not require high-lift systems due to their lower wing loading and a smaller difference between cruising and landing speed. These systems made it easier to maintain control in the glideslope and gave pilots a better view of the runway [101].

With these considerations in mind, Section 2.1.1 outlines the basic flow and lift mechanisms, followed by discussions on the mechanisms and implementations of high-lift systems in Sections 2.1.2 and 2.1.3, respectively.

2.1.1 General lift generation principles

Before discussing the mechanisms and correlations in high-lift, a brief summary of fluid physics in general and applied to the lift on an airfoil in particular is given. The aim of this subsection is to provide an explanation of the crucial physical principles involved. The understanding thus created will later be of importance in the special case of high-lift.

Navier-Stokes equations - general fluid mechanics

The Navier-Stokes equations are a set of nonlinear partial differential equations that describe the motion of fluids. These equations fundamentally express the principles of conservation of mass, momentum, and energy in fluid dynamics; a detailed derivation and explanation are provided by ANDERSON [5].

Despite the initial complexity in comprehending the phenomena occurring on an airfoil by means these equations, they capture all necessary time-dependent fluid mechanical relationships between the scalar quantities pressure p and density ρ, as well as the vector field of the velocity $\mathbf{V}$, enabling the derivation of numerous conclusions. Equation (2.2) states the continuity equation, Eqs. (2.3a)-(2.3c) state the momentum equations in Cartesian coordinates [5]. The energy equation is not relevant in this thesis, refer to the literature [5] for details.

Continuity:
$$\frac{\partial \rho}{\partial t} + \nabla \cdot (\rho \mathbf{V}) = 0, \text{ with } \mathbf{V} = \begin{bmatrix} u \\ v \\ w \end{bmatrix} \tag{2.2}$$

x momentum:
$$\frac{\partial (\rho u)}{\partial t} + \nabla \cdot (\rho u \mathbf{V}) = -\frac{\partial p}{\partial x} + \rho f_x + (F_x)_{\text{visc}} \tag{2.3a}$$

y momentum:
$$\frac{\partial (\rho v)}{\partial t} + \nabla \cdot (\rho v \mathbf{V}) = -\frac{\partial p}{\partial y} + \rho f_y + (F_y)_{\text{visc}} \tag{2.3b}$$

z momentum: $$\frac{\partial(\rho w)}{\partial t} + \nabla \cdot (\rho w \mathbf{V}) = -\frac{\partial p}{\partial z} + \rho f_z + (F_z)_{\text{visc}} \tag{2.3c}$$

According to the current state of research, these equations cannot be solved analytically in this form [72]. A direct numerical simulation (DNS) of the equations is very computationally intensive [5]. However, these equations in their time-averaged form, the so-called Reynolds averaged Navier-Stokes equations, in short RANS [72], provide the basis for the high fidelity computational fluid dynamics (CFD) applications carried out later in this thesis. In addition to the time averaging approach, simplifications can be made under certain conditions that allow for a considerably less computationally intensive calculation. For example, neglecting the viscosity, e.g. for an external flow, results in the Euler equations [94]. Another popular example is obtained by assuming a frictionless, incompressible flow, considering a fluid along a streamline. After integrating the terms, the so-called Bernoulli's equation (2.4) is found [5]. This equation includes the terms for the unsteady acceleration, the static pressure, the dynamic pressure, and the gravitational potential energy, taking into account the gravitational acceleration g and the elevation h.

$$\rho \cdot \int \frac{\partial \mathbf{V}}{\partial t}\, ds + p_{\text{stat}} + \frac{\rho}{2} U^2 + \rho g h = \text{const} \tag{2.4}$$

The equations discussed in this paragraph provide the essential physical principles. The transfer of understanding lift on an airfoil is dealt with in the following paragraph. In addition to the physical principles, mathematical approaches such as the circulation are also discussed. Although these do not replace the physical basics, they are a practical tool that is also helpful for understanding high-lift.

A physics-based approach to understanding lift generation on airfoils

This paragraph is intended to provide a physical understanding after the comprehensive equations of the previous paragraph. An extensive treatment is offered by McLean [72], who quotes *"It's easy to explain how a rocket works, but explaining how a wing works takes a rocket scientist."* (P. Spalart) to emphasize the complexity of this topic.

The issue is not made any easier by the fact that there are numerous false or incomplete explanations that appear to be reasonable at first glance but are erroneous on closer inspection [72]. These include, for instance, false statements such as an "equal transit time", assuming that two fluid particles, which are separated at the leading edge and rejoin at the trailing edge, transit the different path lengths on the upper and lower surfaces in the same time, which is supposed to result in differences in velocity and pressure. Other physical effects are incorrectly used to explain the lift, such as the "Coanda effect", which usually refers to a jet with a higher total pressure than the surrounding fluid and the tendency to follow a curved surface [72]. Yet other approaches describe observations and present them as explanations, for example the momentum of the deflected flow [72]. There are also attempts to explain lift using mathematical models like circulation; however, these models do not account for the origin of lift [72]. This statement is by no means intended to negate the purpose of modeling lift as circulation, it just does not serve as a physical explanation. Finally, the approaches based on Bernoulli's equation, see Eq. (2.4), should be mentioned. Pressure and velocity are indeed an essential part of the lift, but an explanatory attempt with a one-way causation is not correct [72].

Following the dismissal of erroneous lift theories, an explanation by McLean [72] is addressed. Initially, it is important to clarify that a continuum flow is studied in which molecules move randomly, collide frequently, and travel only very short distances between collisions [72]. Without this random movement and collision, molecules would only touch the forward-facing parts of an airfoil, but never the aft-facing parts [72], see Fig. A.1(a) for clarification. Therefore, due to the random movements and collisions, the flow deforms and changes its direction around an airfoil, touching all of its surface, like a continuous material [72].

Lift is determined by the pressure distribution on the surface of the airfoil. In the exemplary illustration in Fig. 2.1, two possibilities for the graphical representation of the pressure coefficient C_p are provided, with [5]:

$$C_p = \frac{p - p_\infty}{\frac{1}{2}\,\rho_\infty U_\infty^2} \tag{2.5}$$

The upper diagram shows the progression over the upper and lower surface, while the bottom diagram shows a segmented vector representation with information about the surface normal.

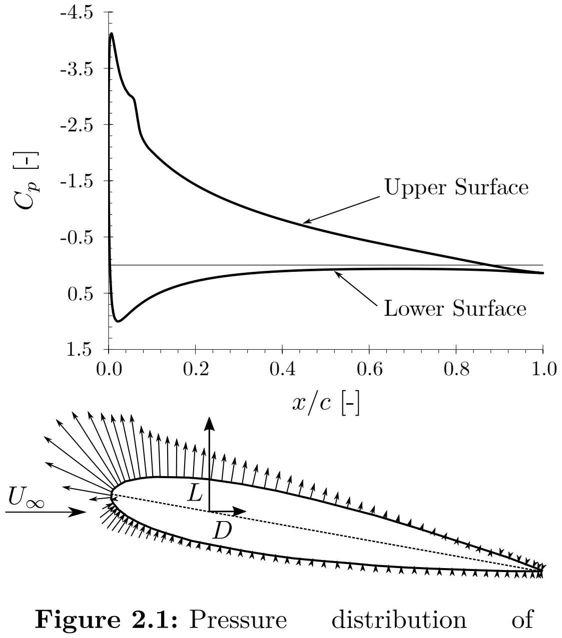

Figure 2.1: Pressure distribution of a symmetrical airfoil at $\alpha = 10°$, modified from [73].

In both cases, it should be noted that the pressure is not divided into negative or positive but represented as a deviation from atmospheric pressure, as calculated in Eq. (2.5). When a pressure difference, integrated and perpendicular to the airflow, is present, it is regarded as lift.

In the context of a frictionless and incompressible flow, Bernoulli's equation (2.4) is applicable, though not in the one-way between pressure and velocity causation mentioned above [72]. According to Newton's second law, a change in velocity (acceleration), multiplied with the fluid's mass, equates to a force, which is equal to pressure times area [72]. The reciprocal effects between velocity and pressure changes can be summarized as follows: The fluid changes its speed or direction in response to a pressure difference, and its resistance to do so is due to its mass inertia. This resistance is the reason that a the pressure difference is sustained [72]. This pressure difference, which ultimately causes the force on the airfoil as described above, can only be maintained if there is a counter pressure, in this case due to the mass inertia [72].

Although the direct effect in terms of lift is limited to the airfoil wall, the entire flow field is important for these interactions. It is therefore not meaningful to separate the importance of the upper and lower sides [72]. In order for these interactions to occur, the airfoil requires a downward chord, whether due to an angle of attack α or a camber. This downward slope causes the changes in speed and pressure as described above [72].

One way to control the flow is by means of a sharp trailing edge. Due to viscous effects, the flow tends to detach cleanly at a sharp trailing edge, until the onset of stalling [72]. This physical effect should not be mixed with the Kutta condition, a theoretical criterion for smooth flow at the trailing edge employed in mathematical models. It is important to note that in real-world conditions, the flow at the outflow might not be perfectly streamlined.

Boundary layer and flow separation

The importance of taking viscosity into account has been briefly addressed in the previous paragraph. This importance becomes even more apparent, in particular to the topic of flow separation, which is of great relevance for high-lift.

As described by Anderson [5], the concept of dividing the flow into a frictionless outer part and a friction-dominated boundary layer was first introduced by Prandtl [87]. For a two-dimensional flow, McLean [72] simplifies the Navier-Stokes equations, resulting in the following equations for the continuity and conservation of momentum:

Continuity (boundary layer):
$$\frac{\partial u}{\partial x} + \frac{\partial v}{\partial y} = 0 \tag{2.6}$$

x momentum (boundary layer):
$$u\frac{\partial u}{\partial x} + v\frac{\partial u}{\partial y} = -\frac{1}{\rho}\frac{\partial p}{\partial x} + \frac{\mu}{\rho}\left(\frac{\partial^2 u}{\partial y^2}\right) \tag{2.7a}$$

y momentum (boundary layer):
$$0 = \frac{\partial p}{\partial y} \tag{2.7b}$$

Following this simplification, one conclusion is, as stated in Eq. (2.7b), that the pressure perpendicular to the main flow direction is constant. Another important conclusion is obtained by applying the no-slip condition to the wall, thus setting the velocities u and v at the wall equal to zero [5].

Equation (2.7a) is thus simplified[†] to $\frac{dp}{dx} = \mu \left(\frac{\partial^2 u}{\partial y^2}\right)$, reflecting a direct dependence of the pressure profile on the change in velocity in x direction on the wall. In the provided example of an airfoil, illustrated in Fig. 2.1, the pressure distribution on the upper surface indicates a notable suction peak followed by a region characterized by a positive pressure gradient, commonly referred to as an adverse pressure gradient, along the wall. This adverse pressure gradient $\frac{dp}{dx} > 0$ thus causes an equally positive second derivative $\left.\frac{\partial^2 u}{\partial y^2}\right|_\mathrm{w} > 0$ [106], when applying the no-slip condition to Eq. (2.7a). The second derivative of u is to be interpreted as the curvature of the boundary layer velocity profile.

Figure 2.2 shows this change in the boundary layer profile depending on $\frac{dp}{dx}$, respectively $\left.\frac{\partial^2 u}{\partial y^2}\right|_\mathrm{w}$, caused by a curvature of the surface [106]. On the left-hand side, an accelerated flow results in a monotonic boundary layer profile, whereas on the right-hand side, with a decelerated flow due to the adverse pressure gradient, there is a inflection point in the boundary layer profile. The sign of the second derivative allows a statement about the curvature of the boundary layer profile, in this case at the wall. However, no statement can be made in this way regarding the direction of the flow or the magnitude of the velocity.

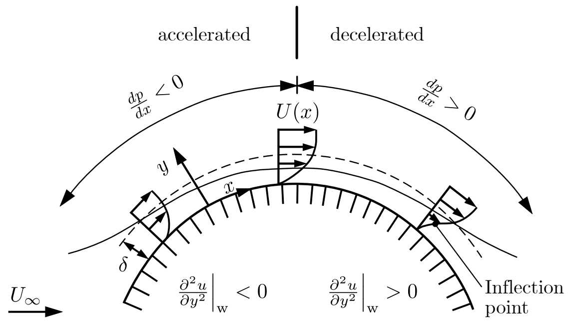

Figure 2.2: Boundary layer velocity profile for different pressure gradients, adapted from [106].

The direction of flow is relevant, since as soon as a backwards flow occurs at the wall, it is referred to as a separation of the boundary layer [5]. A graphic explanation: The further the flow experiences a positive pressure gradient, the more energy is required to build up this pressure. This energy comes from the kinetic energy of the flow, which means that the flow decelerates [5]. Figure 2.3 illustrates this process for a positive pressure gradient and the effect on the flow direction at the wall. As soon as $\frac{\partial u}{\partial y} < 0$, a reverse flow occurs with the aforementioned separation of the flow. This flow separation has a considerable influence on the pressure distribution around the airfoil [5] and is usually to be prevented.

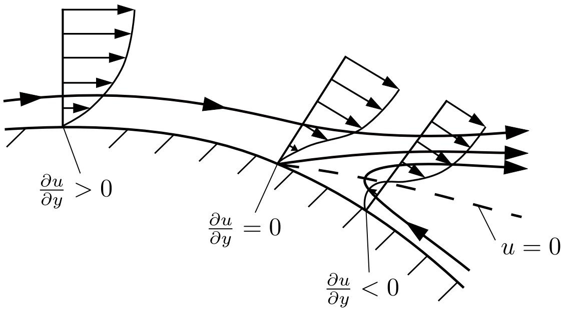

Figure 2.3: Reversed flow due to adverse pressure gradient, adapted from [106].

[†] Note: For a steady-state, two dimensional flow, together with Eq. (2.7b), all other partial differentials of p are equal to zero, thus the partial differential of $\frac{\partial p}{\partial x} = \frac{dp}{dx}$

The discussed relationships are relevant in the following sections on high-lift, further information on the boundary layer, especially occurring instabilities, are originally stated in [103] and discussed for example in [5] and [93].

Concept of circulation

At this point, the Navier-Stokes equations provide the possibility to calculate fluid properties and, for example, the resulting lift. Furthermore, a comprehension of the physical dynamics involved in lift generation and flow separation is established. The next step requires a mathematical model that allows for an understanding of the interactions between multiple airfoils, as discussed in the subsequent Section 2.1.2. To achieve this, the concept of circulation will be introduced in the following segment. The circulation Γ is defined as a closed line integral around a flow field [5], as depicted in Fig. 2.4 and introduced in Eq. (2.8):

$$\Gamma \equiv - \oint_{\mathbf{C}} \mathbf{V} \cdot d\mathbf{s}. \tag{2.8}$$

According to Anderson [5], the minus sign is chosen in order to define a positive circulation for a clockwise circulation, in accordance with the mathematical convention of a positive-counterclockwise direction of the line integral. From the aerodynamic point of view, this definition is favorable, as described below. Note that the term might be misleading, circulation does not necessarily mean that something, such as fluid particles, rotate in a circle [5].

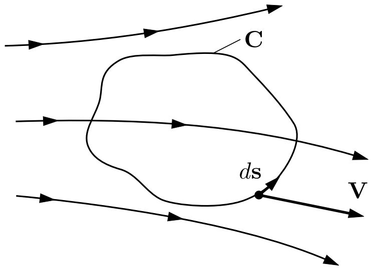

Figure 2.4: Definition of the circulation as a line integral, adapted from [5].

In order to clarify the relationship between the mere definition of circulation and its application to lift, the reason for the occurring circulation, namely the airfoil, is added to the flow field in Fig. 2.5. The Kutta-Joukowski theorem defines a quantitative correlation linking the airfoil's lift L', the circulation, and the free-stream conditions [5]:

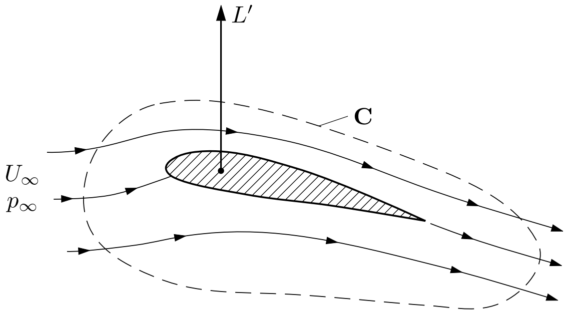

Figure 2.5: Circulation on an airfoil, adapted from [5].

$$L' = \rho_\infty U_\infty \Gamma. \tag{2.9}$$

The circulation provides a mathematical model for the lift, which allows for a better understanding of the interactions in the following sections. The basic aerodynamic principles discussed in this section provide the foundation for the following sections with special application to high-lift.

2.1.2 Fundamental effects in high-lift aerodynamics

This subsection discusses the aerodynamic interactions of high-lift systems on the basis of the previous sections. Regarding the scope for this thesis, the term *high-lift system* is specified as a passive system with a multi-element design. For other designs, such as active high-lift systems, refer to [132].

The primary components of a multi-element high-lift system, including a leading edge device, the main wing, and a trailing edge device, are depicted in Fig. 2.6. In the following, a slat on the leading edge and a flap on the trailing edge are considered. Both open a single gap to the main wing. Further details regarding the technological implementation are given in Section 2.1.3.

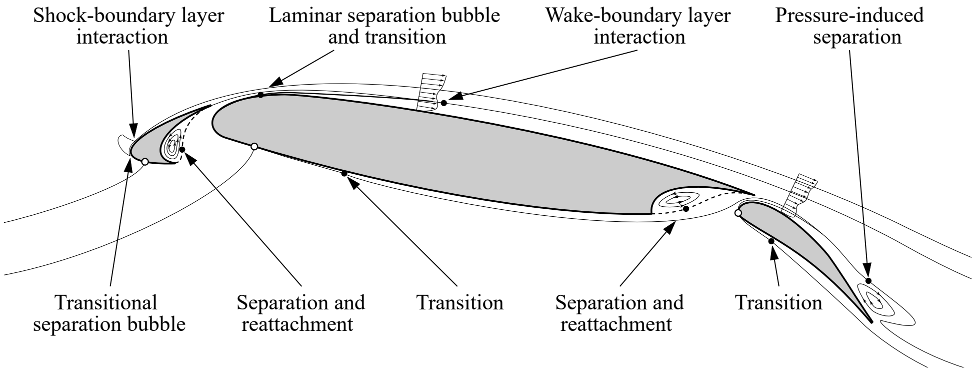

Figure 2.6: Flow phenomena on high-lift configurations, adapted from [14].

Figure 2.6 schematically presents a range of aerodynamic phenomena in high-lift configurations. The subsequent discussion focuses specifically on the five effects as described by Smith [111], along with an in-depth examination of viscous effects.

The five effects of multi-element high-lift systems according to Smith

This paragraph focuses on the five effects on multi-element high-lift systems. Smith [111] was the first to compile and demonstrate these effects [132]. Comprehensive and detailed discussions of the effects are given in [14, 132]. In particular, it should be emphasized that, as described by the first three effects, the high-lift elements exert a positive influence via the pressure distributions on each other, and not exclusively via fresh boundary layers as often assumed. Thus, for the first three effects, elements such as slats or flaps are replaced by a potential vortex with a specific circulation.

I. Slat effect This effect describes the significant increase of the stalling angle of attack for an airfoil by reducing the suction peak and consequently the pressure gradient on the upper surface [14]. In multi-element systems, the slat effect influences the downstream components [132].

Figure 2.7 shows how a slat, represented theoretically by a potential vortex at the leading edge, influences the flow velocities at the main airfoil, reducing the lift of the main airfoil. By using simplifying assumptions, LIEBECK AND SMYTH [64] show that this reduction in lift on the main airfoil corresponds approximately to the lift caused by the circulation of the potential vortex at the location of the slat [132]. Thus, the total lift of the system remains approximately the same.

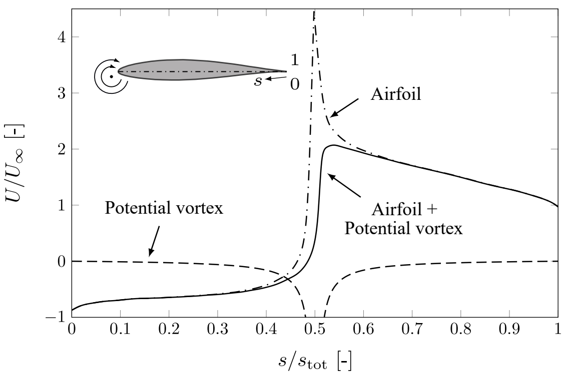

Figure 2.7: Velocity distribution over an airfoil with and without preceding potential vortex (slat effect), [111] adapted by [105].

Formulated more graphically, the high suction peak on a clean airfoil is caused by the centrifugal forces caused by the flow deflection at the airfoil nose. As an upstream element, a slat or potential vortex acts as a flow deflection aid [132].

II. Circulation effect This effect refers to a higher lift due to an accelerated flow on the main airfoil at the same angle of attack compared to a clean airfoil [14]. In multi-element systems, the circulation effect influences the upstream components [132].

The substitution of the flap by a potential vortex, as shown in Fig. 2.8, induces a vertical velocity on the main airfoil's trailing edge [132]. For a smooth flow at this trailing edge, the circulation, respectively the flow velocity, on the entire main airfoil increases. This increase in circulation results in an additional lift on the main airfoil, besides the lift of the flap, but also leads to a higher risk of stall due to the increased suction peak [132]. In contrast, the slat effect only shows a local effect on the nose of the downstream element [132]. The slat effect and the circulation effect do not act separately but have a mutual influence that must be taken into account in the high-lift design [132].

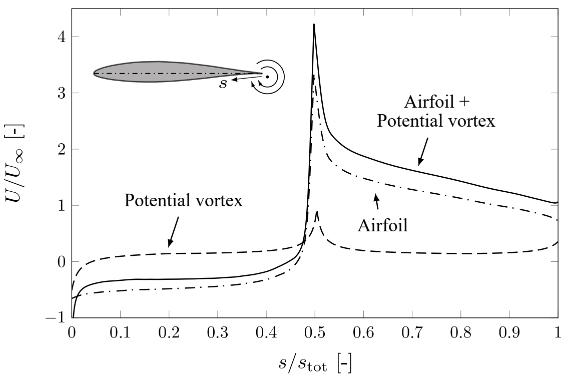

Figure 2.8: Velocity distribution over an airfoil with and without trailing potential vortex (circulation effect), [111] adapted by [105].

III. Dumping effect This effect, while occurring together with the circulation effect, involves different physical mechanisms [132].

The circulation effect refers to the increase in overall circulation around the airfoil system due to the presence of downstream elements, which can be modeled using potential flow theory. In contrast, the dumping effect refers exclusively to the stabilization of the boundary layer at the trailing edge of the upstream airfoil [132]. Due to the influence of the downstream element, the pressure at the trailing edge of the upstream airfoil is reduced, decreasing the adverse pressure gradient and accelerating the flow. This flow acceleration relieves the boundary layer at the trailing edge, making it less prone to separation [14]. Figure 2.9 shows a distinction between the circulation effect, the slat effect, and the dumping effect. Although these effects are interconnected through the interaction of upstream and downstream elements, the dumping effect requires consideration of viscous boundary layer behavior and cannot be fully explained by potential vortices alone.

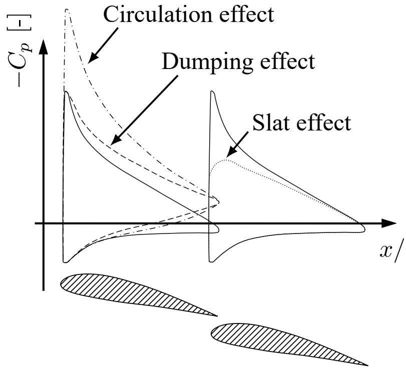

Figure 2.9: Distinction between slat, circulation, and dumping effect, [132], adapted from [11].

IV. Off-the-surface pressure recovery This two-part effect indicates that part of the pressure recovery takes place in the wake rather than directly on the main airfoil surface, due to the described dumping effect with downstream elements. Firstly, the risk of pressure gradient-based separation is reduced on the main airfoil [14]. Secondly, the pressure recovery behind the main airfoil leads to a decelerated flow field above the flap, effectively thickening the local flow region and acts as a relieving displacement body.

In high-lift systems, particularly when slotted flaps are deployed extensively, a distinct wake forms downstream of the main airfoil [132]. This wake originates from the boundary layer of the main airfoil, which experiences a pressure rise as it moves downstream [132]. The pressure rise can lead to a flow stagnation above the flap, leading to a recirculation area. This recirculation area acts as a displacement body over the flap, effectively altering the flow path and pressure distribution. The flap experiences reduced suction, making flow detachment less likely. As a result, configurations of high angles of attack particularly benefit from this effect, as the relieving effect is more pronounced and helps maintain attached flow over the flap. However, if the displacement effect is not sufficiently large, separation of the flap at low angles of attack may occur. This effect underlines that the flow around the flap can be strongly dependent on the set angle of attack. As the flow at the airfoil and flap surface is still attached, the lift is unchanged by the recirculation area. However, drag is greatly increased with a flow recirculation area, meaning such an effect is only acceptable during landing [132].

V. Fresh boundary layers According to this effect, by separating the surface into separate elements, a new boundary layer is formed each time [111]. This configuration means that the boundary layer attachment is only required over shorter distances and not over the entire chord length and can therefore withstand higher pressure gradients. However, WILD [132] points out that this effect is more of an addition to the effects mentioned above and not the main contribution.

Boundary layer - wake interaction

The flow around multi-element airfoils is significantly influenced by viscous effects. BLUME [14] provides a comprehensive overview, which is summarized in the following. Each element forms its own boundary layer, impacting the subsequent element's flow due to the interaction of boundary layers and wake. The flap, in particular, is influenced by the interactions of these layers from both the main airfoil and the slat, an overview is shown in Fig. 2.10.

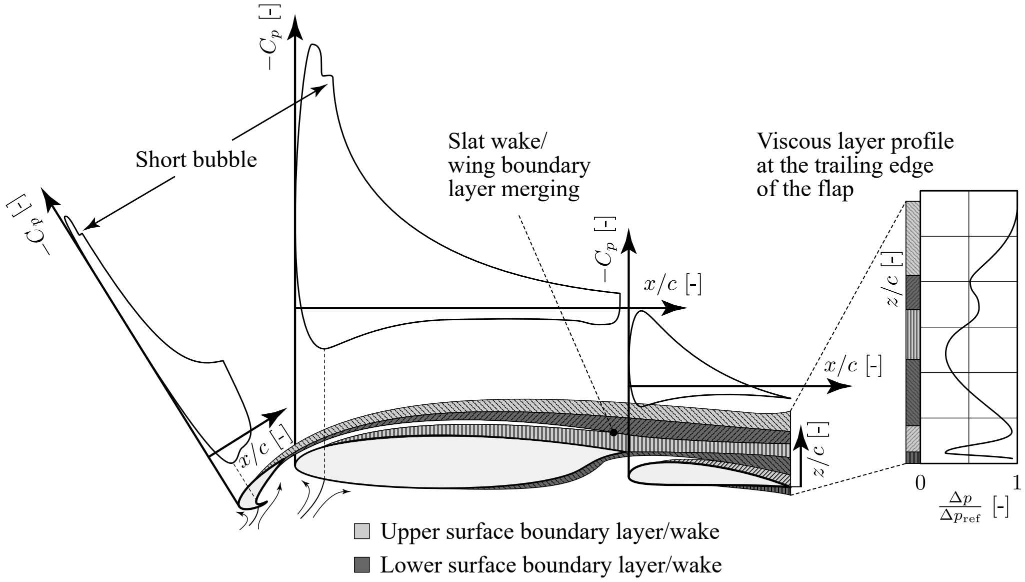

Figure 2.10: Boundary layers and wakes on a three-element high-lift configuration, [14] adapted from [135].

The nature of this interaction varies; it can either lead to the merging of wakes and boundary layers or just provide a dampening effect. YING ET AL. [136] describe three stages of interaction [14], as depicted in Fig. 2.11. Initially, the wake and boundary layer remain distinct, separated by a potential flow region unaffected by viscous effects. In the second stage, this region vanishes, and the boundary layer begins to merge with the wake. In the final stage, this merging is complete, resulting in a noticeably thicker boundary layer [14].

LJUNGSTRÖM [66] highlights the impact of the slat gap on the flap's pressure profile. A smaller gap induces a merging of the boundary layer and wake on the main airfoil, enhancing the flap's dampening effect despite increasing separation risk at moderate angles of attack. This thicker

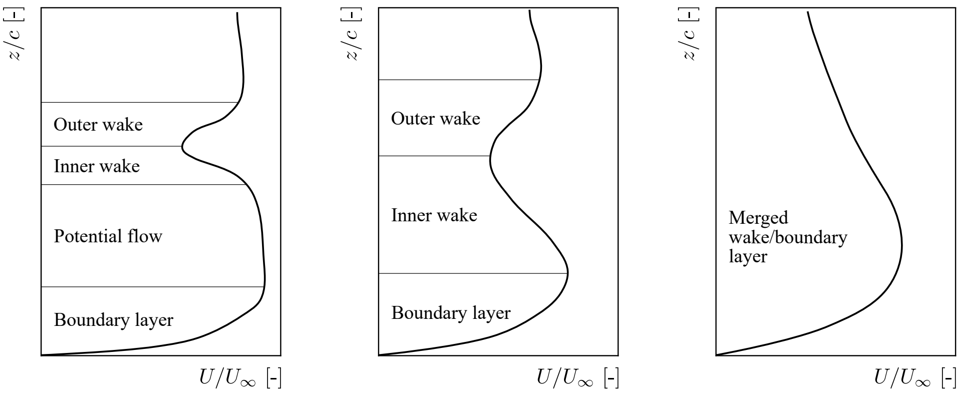

(a) Unmerged **(b)** Merging **(c)** Merged

Figure 2.11: Different stages of the merging of wake and boundary layer, adapted from [14, 136].

boundary layer also causes a broader wake, which further decreases the flap's risk of separation and reduces the suction peak but at the cost of reduced flap lift.

With larger gaps, the interaction between the boundary layer and wake diminishes, leading to decreased dampening and increased risk of flap separation. However, this also results in a reduced separation risk on the main airfoil due to a thinner boundary layer [14].

The dependence of the merging process from different gap sizes is illustrated in an exemplary case, shown in Fig. 2.12. Small gaps (0.5 %) lead to boundary layer merging, causing thickening on the flap and eventual rear separation. For a 4 % gap, trailing edge separation occurs due to insufficient dampening. The ideal gap size for this case is between 2.0 % and 2.5 %, where a stable potential flow region between the boundary layer and wake prevents mixing but still positively affects the flap's boundary layer [14]. It is important to highlight that these values are strongly case-dependent.

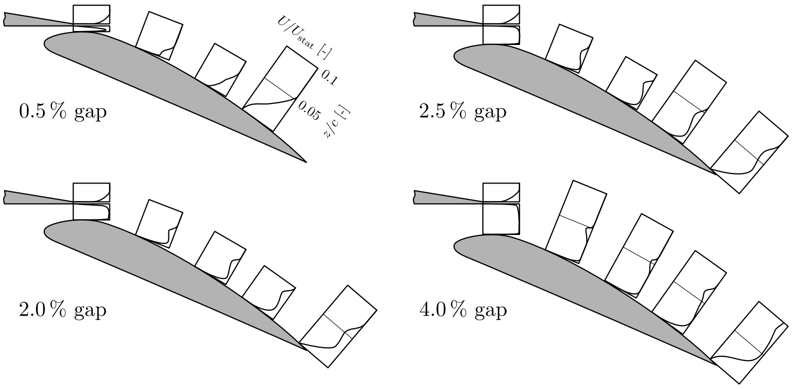

Figure 2.12: Influence of the gap between airfoil and flap on the velocity profile of the upper flap surface, adapted from [32].

Influence of the Reynolds number

The Reynolds number Re defines the ratio of inertial forces to viscous forces in a fluid [5] and is calculated using the reference length s_{ref}:

$$Re = \frac{\rho_\infty \, U_\infty \, s_{\mathrm{ref}}}{\mu_\infty}. \tag{2.10}$$

A summary of the extensive description from [14] is given below. The Reynolds number influences the boundary layer thickness significantly, as stated by Eq. (2.11) for a turbulent boundary layer on a flat plate [5]:

$$\delta = \frac{0.37 \cdot s_{\mathrm{ref}}}{Re_{s_{\mathrm{ref}}}^{1/5}}. \tag{2.11}$$

As described in the paragraph above, the thickness of the boundary layer significantly affects the high-lift performance. According to the Eq. (2.11), a high Reynolds number results in a thinner boundary layer, which can withstand higher adverse pressure gradients [14, 81]. However, due to the interactions of various high-lift elements, opposing effects can occur depending on the angle of attack α [14].

These effects for an identical airfoil at different Reynolds numbers are illustrated in Fig. 2.13. A lower Reynolds number, marked as dashed line, causes a thicker boundary layer and wake over the downstream elements. The resulting damping effect on the suction peak of the flap leads to a longer attachment of the flow and thus a higher lift compared to high Reynolds numbers, marked as solid line [14]. However, above a certain angle of attack, this effect is reversed. Due to the high angle of attack, the thickened boundary layer and wakes have a sufficient damping effect on the flap even at high Reynolds numbers [14]. In contrast, at high angles of attack and low Reynolds numbers, the disadvantages of a thickened boundary layer and wake, as discussed in the above paragraph, predominate. Thus, separation occurs earlier than at high Reynolds numbers [14].

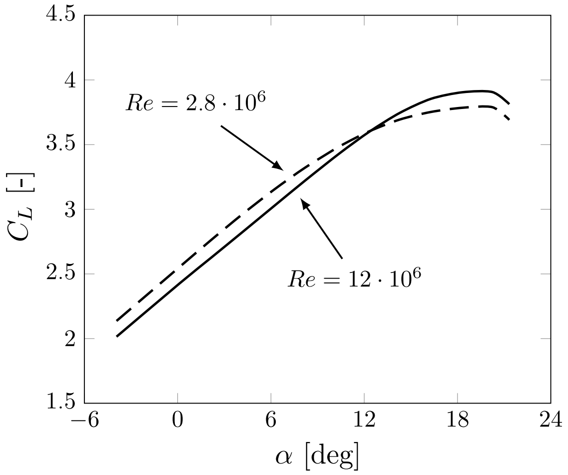

Figure 2.13: Influence of the Reynolds number on the lift coefficient of a high-lift configuration, adapted from [75].

The aerodynamic effects of multi-element high-lift systems discussed in this section provide the necessary tools for the methodological preliminary aircraft design in Section 3.1. The phenomena addressed above apply to two-dimensional high-lift airfoils. In the context of wing configurations, particularly those involving sweep, additional complexities arise. For a detailed discussion of these aspects, the works of Blume [14], Wild [132], and Woodward et al. [135] are recommended references.

2.1.3 Overview of high-lift technology implementation

With the theoretical foundations for the aerodynamic effects of multi-element high-lift systems established in the previous chapters, technical realizations are discussed below. This discussion includes common geometric definitions, the design of the flaps themselves, and their kinematics. A comprehensive and widely cited source is given by Rudolph [101], who shows and discusses existing systems in detail, as well as presenting historical developments, and providing predictions of future developments.

Common geometric definitions

Besides the deflection angles η of the control surfaces of the high-lift system, which are in this thesis the flap, the slat, and if applicable the spoiler, there are further geometric parameters that are relevant for the performance of the system.

The gap G and the overlap O refer to the relative positioning of two elements to each other as shown in Fig. 2.14. These parameters, typically expressed as a percentage of the chord length in a clean configuration, play a significant role in the interaction of the boundary layer and wake, as discussed in Section 2.1.2.

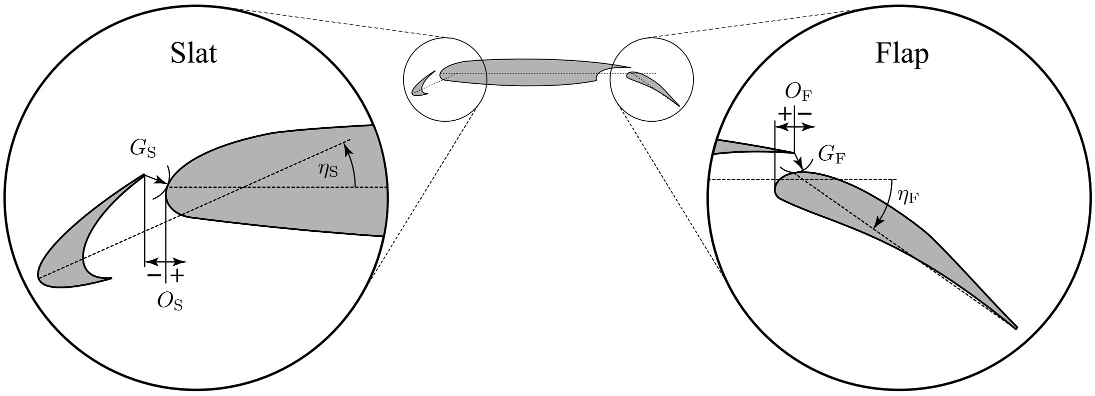

Figure 2.14: Definition of the airfoil parameters gap G, overlap O and deflection angle η, adapted from [14].

The gap is defined as the minimum distance from the airfoil to the flap, or the slat, respectively [14]. The overlap represents the conjoint distance between two elements along the chord line, considering the trailing edge of the upstream element and the leading edge of the downstream element [82].

For an elaboration of the mutual effects, refer to Section 2.1.2 or [14]. Very briefly, it can be summarized that an excessively narrow gap can lead to the immediate merging of the boundary layer and wake, potentially thickening the boundary layer to the point of separation risk. However, an overly wide gap could reduce the beneficial effects these elements are intended to provide [81].

Device implementation

While the analysis of aerodynamic effects always have to consider the interaction of all elements, trailing edge devices are primarily mentioned in the following due to the focus of this thesis on modifications to the trailing edge.

Trailing edge devices These devices range from simple gapless flaps to complex multi-slot configurations and aim for optimal lift enhancement. Trends are shifting towards less complex [101], lighter, and more maintenance-friendly designs, as in modern aircraft like the Airbus A350XWB [91, 117]. The most common systems are shown in Fig. 2.15. The design of high-lift systems is carried out under the aerodynamic aspects mentioned in Section 2.1.2, but other constraints, imposed by the overall aircraft design, apply as well. For example, spatial limitations, such as landing gear integration, may arise, as well as maintenance requirements of the kinematics [14].

During flap deployment, the area of the wing is increased, but the reference area S_{ref}, as for example required in Eq. (2.1), has to remain constant and is defined on the clean case [33]. A changing reference area would undermine the purpose of a reference area.

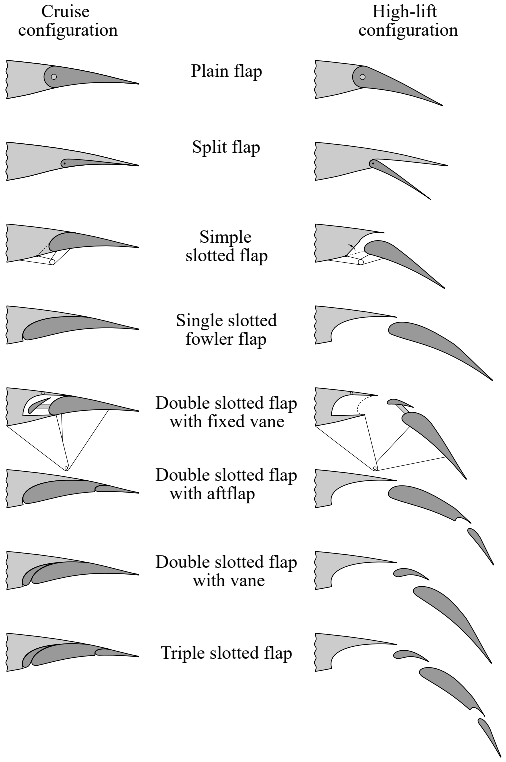

Figure 2.15: Various trailing edge devices in retracted and deployed settings, adapted from [14].

The deployment of the high-lift system especially needs to cover the takeoff, climb, and landing phases, each with distinct requirements [132]. A good overview is given by RECKZEH [92] and WILD ET AL. [133]. Briefly summarized, a high maximum lift coefficient $C_{L,\max}$ and attached flow are important for landing, with enough drag to maintain the glide path [92]. In the takeoff segment, a maximized lift-to-drag ratio (L/D) is important. However, other constraints, such as costs [92] or noise certification [133], are also important.

A frequently used type of flap is the Fowler type [33], often combined with a so-called Fowler movement. Wild [132] points out that there are two Fowler types, the first of which only aims to increase the surface area. The second, which is usually referred to, increases the surface area, deflects the flap, and opens a gap. The freedom in the kinematics design allows the movement path of the flap to be optimized for the respective takeoff and landing requirements.

The development of the high-lift system known as the Adaptive Dropped Hinge Flap (ADHF) [91, 117] is of particular relevance to this thesis. The ADHF serves as the foundation for the upcoming high-lift configuration optimization in Section 3.1, and the variable camber system discussed in Sections 3.4.3 and 4.2 is based on it. In this system, a spoiler or a droop panel is actuated for high-lift gap control [117]. In addition, the ADHF kinematics are a crucial factor, as the rotation around the hinge point determines the entire motion path of the flap [117]. In order to keep the fairings as small as possible for minimum drag, the flap hinge points need to be close to the wing. This positioning has the disadvantage of reducing the Fowler motion path, i.e., increasing the wing area when the flaps are deployed [117].

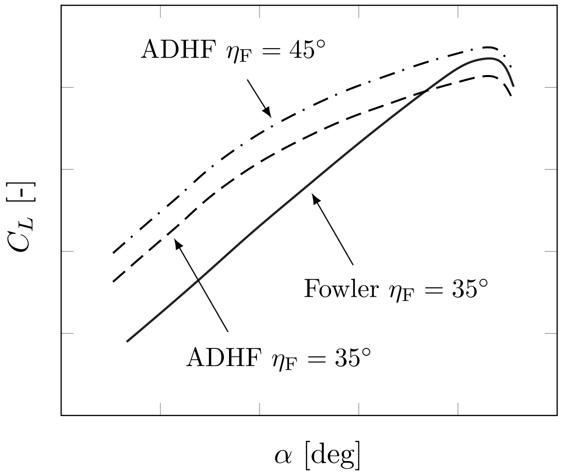

Figure 2.16: Comparison of the polars of a conventional Fowler flap to ADHF, adapted from [91].

Strüber [117] discusses the aerodynamic differences between ADHF and Fowler devices in more detail. As shown in Fig. 2.16, for an identical flap deflection angle, the non-linear section starts at lower α for the ADHF, which results in a lower $C_{L,\max}$. However, with the gap control provided by the spoiler, higher flap angles can be achieved before a flow separation occurs.

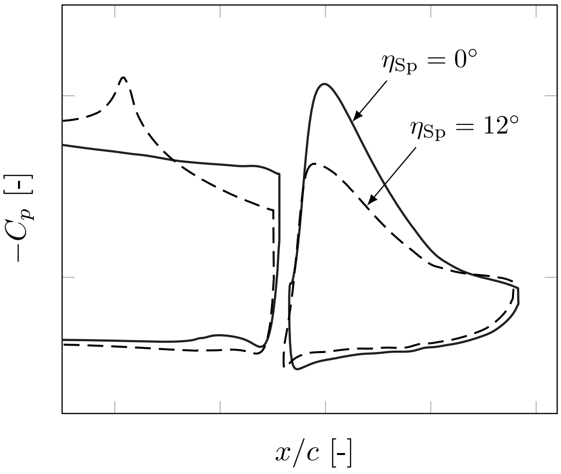

Figure 2.17: Pressure distribution over a flap with and without spoiler deployment at constant C_L, adapted from [117].

In addition, the pressure distribution, shown in Fig. 2.17, demonstrates how the spoiler movement significantly influences the aerodynamic characteristics. The retracted spoiler is indicated by a solid line, and the extended spoiler is represented by a dashed line. A suction peak is developed at the leading edge of the extended spoiler due to the sharp change in curvature. The pressure at the trailing edge of the spoiler thus increases, which leads to a reduction in the spoiler torque [117]. As a result, the applied lift force shifts closer to the leading edge of the wing. The extended spoiler leads to an increase in the camber at the trailing edge of the main airfoil and thus to an increase in circulation [117], see also Section 2.1.2. The resulting increased slat effect on the flap leads to a reduction in the suction peak on the flap, which can therefore be extended further. At the same time, the increased circulation of the main airfoil also causes increased circulation of the slat through the circulation effect, increasing the lift of the slat.

Several reasons contributed to the introduction of the ADHF system on the Airbus A350XWB, such as a demand for high efficiency, low kinematics complexity, and weight [117]. In addition, the requirement for multifunctional control surfaces is addressed [117], allowing the flaps to be used not only for the usual monofunctional task in high-lift, but also to adjust, e.g., the wing geometry in cruise flight, see also the variable camber application in Section 2.5.

Leading edge devices These elements on aircraft wings, such as slats and droop noses, are designed to prevent early flow separation at high angles of attack, thus delaying stall during critical phases like takeoff and landing. As described in Section 2.1.2, the design of the systems is inseparably linked to the overall high-lift system design. Numerous design options are available, a corresponding overview is provided in the appendix in Fig. A.3. The slat and droop nose systems will be briefly discussed here. An aircraft can be fitted with multiple different leading edge devices. One example is the Airbus A350XWB, which uses droop nose devices inboard and slats outboard [117].

Droop nose devices do not open a gap when deployed, see Fig. A.3. One of the reasons for the decision to install a droop nose device inboard is that, due to the large chord lengths inboard, only a relatively low lift coefficient is required for a defined lift, which can be achieved well with droop nose devices [117]. These have the properties of lower drag and noise levels compared to slats installed outboard [117].

Slats, on the other hand, typically open a gap and are more effective for separation control. In the case of the Airbus A350XWB, the implementation allows the slat to be extended during takeoff in a way that no gap is opened [117]. This implementation offers the advantage of a higher lift-to-drag ratio [117].

High-lift kinematics

Although the separation of device implementation and kinematics in the previous paragraph may seem somewhat artificial, as they are closely linked in systems such as the ADHF, this paragraph briefly addresses the kinematics, especially since the kinematic design ultimately directs the loads to be counteracted.

The basic idea of ADHF kinematics is shown as an exemplary in Fig. 2.18. Since the ADHF configuration serves as the underlying system in the following chapters, it is discussed here in more detail. By applying a torque to the actuator lever, it rotates, causing the drive strut to move outward and the flap to rotate around the hinge point. The spoiler is adjusted accordingly to control the gap.

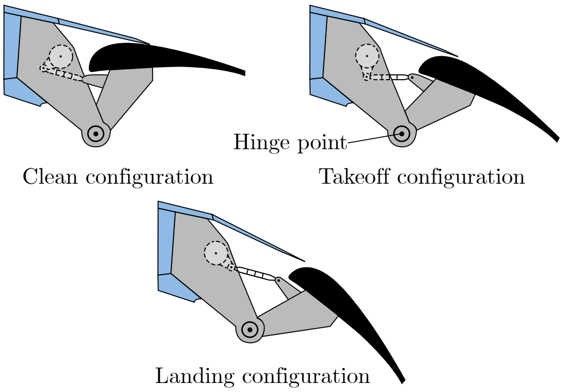

Figure 2.18: Schematic diagram of the airfoil kinematics with ADHF, adapted from [91].

Generally, the kinematics have to meet various requirements, on the one hand from the specifications of aerodynamic optimization, but on the other hand regarding safety, maintenance, and costs [101]. One particular challenge is addressing the hinge kinematics for swept wings, where the flap may not extend in streamwise direction [101]. This misalignment can create gaps between the flaps, resulting in increased drag and noise [91].

As the focus in this thesis is less on the kinematic design, for details refer to the comprehensive overview of existing kinematics on aircraft by Rudolph [101] and the design methodology for trailing edge mechanisms by Zaccai et al. [137].

High-lift speed limitations

Speed limits with regard to high-lift are important for the design. First, the equivalent airspeed (EAS) is defined, as it will be used in the following explanation. The EAS is a crucial parameter in structural aircraft design [88, 132]. The true airspeed (TAS), as used in aerodynamic calculations such as Eq. (2.1), is the actual speed of an aircraft relative to the surrounding air. In contrast, the EAS, represents the speed at sea level in the International Standard Atmosphere (ISA) [77] at which the dynamic pressure is the same as experienced by the aircraft at its actual altitude and TAS [88]. The relationship using the actual density ρ and the density after ISA at sea level ρ_0 is defined in Eq. (2.12) [132]. Due to the reduction in air density, the EAS is less than the TAS at altitude.

$$v_{\text{EAS}} = v_{\text{TAS}} \cdot \sqrt{\frac{\rho}{\rho_0}} \tag{2.12}$$

The limits that define the design and certification of the aircraft, and that subsequently constrain flight operations, can be represented in two different envelopes. In the following, the regulations of the European Union Aviation Safety Agency (EASA) [30] are referred to.

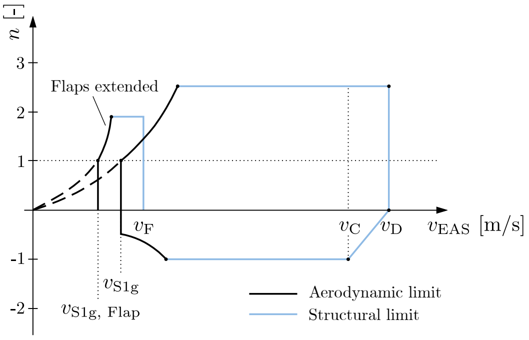

Figure 2.19: Maneuvering load v-n diagram, including characteristics with flaps extended, adapted from [30, 132].

The load factor $n = L/W$, defining the ratio of lift and the weight W, is plotted over the EAS in the v-n[‡] maneuvering load envelope in Fig. 2.19, as defined in CS 25.333 [30]. The aerodynamic limits determined by $C_{L,\max}$ are shown by the black line, limited on the left side by the stall speed v_S at $n = 1$, denoted as v_S1g, meaning an unaccelerated level flight [132]. The blue line shows the limitations due to the structure [132], with the speed definitions for cruise v_C and design dive v_D according to CS 25.355 [30]. It should be emphasized that safety factors according to CS 25.303 and CS 25.305 [30] must be taken into account when determining the v_C. This consideration also affects the ensuing component sizing. Furthermore, gust loads in accordance with CS 25.341 [30] also have to be taken into account.

Especially relevant for high-lift is the curve shown at lower speeds with the high-lift devices extended. Due to the higher $C_{L,\max}$ achieved with high-lift devices, this curve exhibits a steeper increase while the maximum load factor is limited to 2.0. Note that this diagram shows only one flap setting. In this case, the maximum speed limit is the design flap speed v_F according to CS 25.335(e) [30], which, among other things, has to maintain a minimum distance to the stall speed. The flap extended speed v_FE has to be selected in such a way that v_F is not exceeded, as stated in CS 25.1511 [30], also considering conditions from CS 25.345 [30].

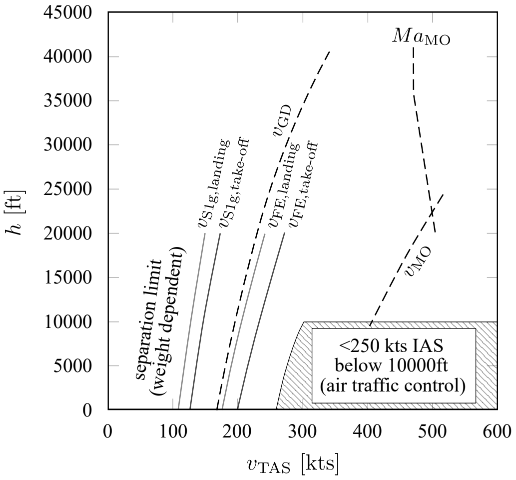

Figure 2.20: v-h diagram with high-lift devices; only the operational range of the clean wing configuration is shown, adapted from [132].

Besides the v-n diagram, which is not constant for an aircraft, for example at higher altitudes [132], the v-h diagram, as shown in Fig. 2.20, indicates the permitted range of airspeed at different altitudes. In this case, the speed is given in TAS in order to take into account the effects due to changes in air density [132]. At lower altitudes, specifically below FL100 (10 000 ft), a limitation of 250 knots Indicated Airspeed (IAS) is enforced by air traffic control to maintain separation and ensure safe operations among multiple aircraft [132]. The so-called green dot speed (GD) indicates the speed for optimal lift-to-drag ratio [132]. This speed is critical for climb performance and best glide efficiency,

---

[‡] Note that in the v-n and v-h diagram, v is used to represent the velocity, as it is a fixed term; otherwise, U is used as the scalar value for velocity.

especially in clean configurations without high-lift devices. At higher altitudes, the maximum operating speed (MO) is constrained by the Mach limit rather than the TAS [132]. This constraint is due to the compressibility effects that occur at transonic speeds [132]. The diagram shows the crossover point where the speed limit transitions from the maximum operating speed v_{MO} to the maximum operating Mach number Ma_{MO} as altitude increases. Regarding high-lift limitations, the v-h diagram illustrates the constraints on both the lower and higher speeds of the operational envelope, especially in the context of take-off and landing. On the one hand, at low speeds, in order to maintain sufficient distance from the stall area, the v_{S1g} speeds represent the minimum allowable speeds [132]. On the other hand, at high speeds, the flap extended speeds v_{FE} represent the maximum allowable speeds with deflected high-lift devices [132].

Although the certification guidelines mentioned above may seem complex and interrelated, it is crucial to understand that the speeds chosen for different flap settings by designers are not arbitrary. These speeds are defined within the framework of certification requirements, leading to specific structural demands that must be met. This, in turn, defines and restricts the allowable flight envelope.

Summary The above discussion on high-lift systems provides the foundation for the methodological steps presented in Section 3.1. This foundation is crucial within the scope of this thesis since it renders the high-lift systems, taking a particularly central role in the flap load modeling, the actuation requirement, and the variable camber application in the subsequent chapters.

2.2 Flap load modeling fundamentals using artificial neural networks

This section provides the link in between the specifications for the high-lift system discussed in Section 2.1 and the required actuators that will be discussed in Section 2.3. The flap positions in the various settings experience aerodynamic loads, which, together with the mechanical loads, are transferred to the actuators via the kinematics. This thesis focuses on trailing edge systems, but the following principles for modeling can be applied analogously to other wing elements.

The flow at the trailing edge is complex for high-lift applications, since, e.g., the wake of the upstream elements and 3D effects of the wing need to be taken into account. In Section 2.1, the correlations are described, demonstrating non-linear effects. In addition to the subsonic high-lift case, the transonic cruise flight case for a VC application is intended for this thesis. These two cases are fundamentally different, as the high-lift application involves a high range for both flap deflections and angles of attack, while the VC application has to consider a differential flap setting and transonic effects such as shocks on the wing, as detailed in Section 2.5.

Since the investigations are carried out in the preliminary aircraft design stage, a discrepancy arises from the conflicting requirements [113]: On the one hand, the process of modeling has to be carried out in minimal computing time. On the other hand, high accuracy is required to capture the above mentioned aerodynamic effects. Calculations using 3D CFD RANS simulations promise high accuracy, but are computationally intensive and not suitable for an iterative preliminary design such as the MICADO design environment [113]. For details regarding MICADO, refer to Section 3.4.

Different approaches are discussed in the literature, for example physics-based models[§], coupling the vortex lattice method (VLM) with section airfoils for a 2.5D cross-flow correction [83]. An empirical approach uses data-driven models[¶] for capturing the flap normal forces [137]. Another data-driven modeling approach is presented in [51], based on an extensive collection of data points with various parameters. Generally, the data-driven modeling includes rather simple regressions as well as machine learning approaches, including a neural network.

In preliminary studies, other tools, e.g., based on a panel code, did not achieve the desired accuracy [113]. In particular, simplifying methods can lead to the problem of neglecting compressibility or make assumptions in order to capture compressibility effects [113]. The application case applied in this thesis includes not only the subsonic high-lift applications presented in the literature, but also the transonic VC application as described above. In order to take this into account, a dedicated model will be established in Section 3.2. A neural network approach is chosen in this thesis considering the given regression problem with a large amount of data [113], allowing only those parameters as input data, that are available in the preliminary design stage. All relevant configurations are simulated prior to the iterative design loop using 3D CFD in order to establish the modeling and validation foundation; the detailed model generation is described in Section 3.2. The discussions in Sections 2.2.1 and 2.2.2 cover the fundamental aspects of an artificial neural network, focusing on its architecture, as this is the key element optimized during the setup of the model.

2.2.1 Artificial neural networks and architecture

In order to introduce the basics of artificial neural networks required in this thesis, a classification of neural networks within the terminology of artificial intelligence is given first. A simplified example is then used to discuss the key elements of a neural network, its operating function and the learning process. Finally, data pre-processing and evaluation are addressed.

[§] Physics-based models utilize governing equations to describe known physical phenomena in systems, offering good generalizability [13].

[¶] Data-driven models utilize data sets to derive correlations. They are usually computationally inexpensive, but the generalizability is limited by the data set and a bias may be present [13].

Artificial intelligence (AI) is the broad concept of machines performing tasks that typically require human intelligence [112]. A subset of AI, machine learning, includes algorithms that enable machines to learn and improve from input data [112]. Deep learning is a specialized area of machine learning that uses multi-layer artificial neural networks, for example, to process large amounts of data [112].

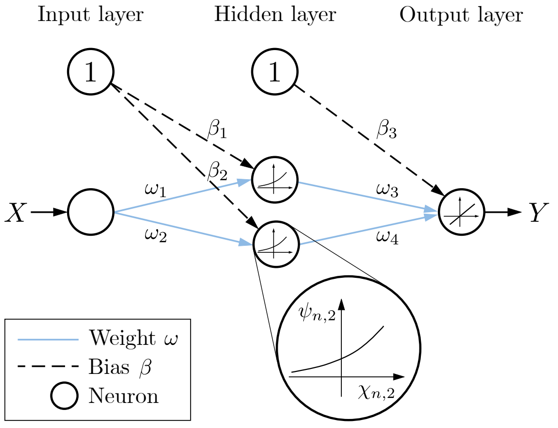

Figure 2.21: Basic terms and structure of an artificial neural network.

Figure 2.21 shows a simplified example of a feed forward neural network with one input neuron, one hidden layer with two neurons, and one output neuron. Numerical values in the direction of the arrows are multiplied by the weights W or the bias B, respectively, and all input values in a neuron are summed up [41]. In each neuron, an activation function converts the summarized neuron input χ_n to a neuron output ψ_n, allowing the representation of nonlinear correlations [110]. In the following, a selection of the large variety of possible activation functions will be mentioned according to [110, 113], the corresponding equations and curves are plotted in Fig. 2.22.

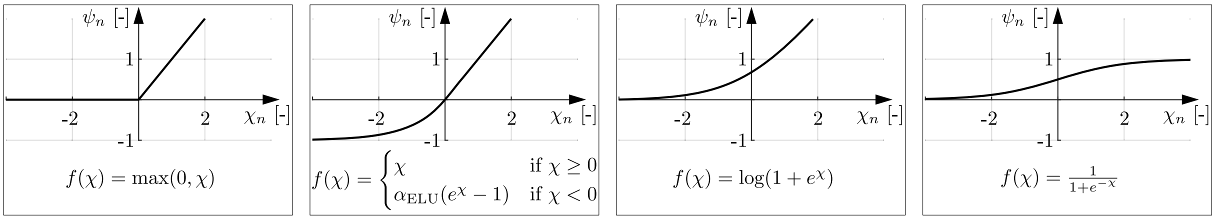

(a) Rectified linear unit

(b) Exponential linear unit

(c) Softplus function

(d) Sigmoid function

Figure 2.22: Diagram of the outputs of the neuron activation functions (ψ_n) depending on the input value of the neuron (χ_n) [113].

The *rectified linear unit* (ReLU) returns the input value if it is positive, otherwise, it returns zero. One advantage of the ReLU function is its computational efficiency. However, a potential drawback is that neurons could become permanently inactive during the learning process when their input is negative, as the output in these cases is zero. [113]

The *exponential linear unit* (ELU) returns nonzero output even for negative input values, in contrast to the ReLU. This characteristic helps avoid the issue of neuron inactivation. However, it leads to greater computational complexity. Additionally, the ELU allows adjustment of its response to negative inputs by modifying the parameter α_{ELU}. The function is continuously differentiable. [113]

The *softplus function* returns a continuously differentiable curve and converges to zero for negative input values. This characteristic helps mitigating the issue of neuron inactivation, especially for inputs near zero. [113]

The *sigmoid function* maps input values to a range between 0 and 1, which makes it particularly useful for binary classification problems. A disadvantage of this function is that very large or very small input values lead to minimal change in the output. This issue, known as the vanishing gradient problem, effectively prevents the weight from changing its value during the learning process. [113]

In the output neuron, a linear function is typically employed [41]. The discussion to this point focused on the functioning of neural networks. Below, terms associated with the primary learning process of these networks will be defined and explained.

2.2.2 Data pre-conditioning, learning process parameters, and evaluation

Before the data are used to generate the neural network, they need to be pre-conditioned [2]. First, all data are normalized in order not to handle individual parameters with a bias during the learning process [2]. There are several methods for normalization from which, in this thesis, the min-max normalization is chosen, which maps all available parameters to values between 0 and 1 [2]. The output must then be back-calculated using the same normalization values for each parameter. The selection of the relevant input parameters can be based, e.g., on correlation analyses [51].

The overall data set has to be divided into a training data set, which is used to create the neural network, and at least one more data set for independent evaluation of the results [50]. In the following, one independent data set is used [54] and called test data set. Guidelines for the splitting proportions of the data set into training and test data sets range from 50 - 50 % to 80 - 20 % [54], whereas for this thesis a split of 75 - 25 % is used as in [113].

Regarding the learning process, with a focus on the backpropagation method, the values for all weights and biases are determined. A previously defined error function is minimized using methods such as gradient descent. In this case, the error function is the sum of squared errors (SSE) as shown in Eq. (2.13). This formulation is according to [41] assumes one output node, where n represents the number of observations in the dataset. In this iterative learning process, various parameters are taken into account, such as the learning rate, the threshold and the repetitions.

$$\mathrm{SSE} = \sum_{i=1}^{n} (Y_{\mathrm{observed},i} - Y_{\mathrm{predicted},i})^2 \tag{2.13}$$

The *learning rate* determines the increments between the iterations; a value that is too small significantly increases the computing time, while a value that is too large can lead to instability.

The *threshold* is a termination criterion of the iterative backpropagation learning process [41]. It refers to the partial derivatives of the error functions [41], see Eq. (2.13), and as soon as the set value is reached, the neural network is assumed to be adequately trained [113]. Setting a very low threshold value can initially improve the approximation of the model to the training data set. However, there are also detrimental effects: a threshold set too low may result in the network failing to converge or in overfitting. Overfitting is a scenario in statistical modeling where the model becomes overly aligned with the training data [120], as illustrated in Fig. 2.23(a). Thereby it loses the ability to make generalized predictions on new, independent test data sets. The model also adapts to random deviations and anomalies in the training data that are not necessarily representative of the physical mechanisms [50, 120]. This adaption makes the model highly specialized and unable to detect patterns beyond the training data. Overfitting can be checked for by examining the model with the test data set. Furthermore, if applicable, limiting the complexity of the model may help the model to make generalized predictions [120]. Underfitting occurs when a model fails to capture the essential patterns in the training data, resulting in poor predictions and high error rates on both training and test data [113]. A good fit occurs when the model accurately captures the essential patterns in the training data while maintaining the ability to generalize well to new, independent test datasets.

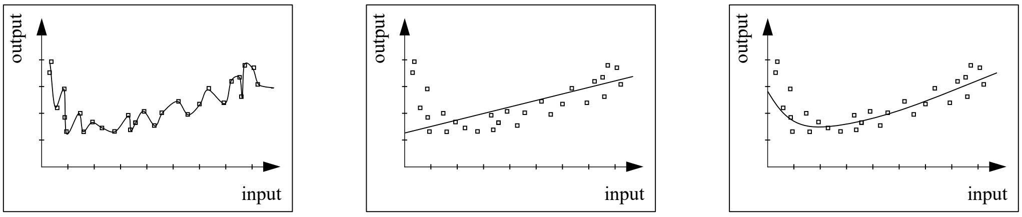

(a) Overfitting **(b)** Underfitting **(c)** Good fit

Figure 2.23: Schematic representation of overfitting and underfitting [113].

The number of *repetitions* is important, since in the initialization of the learning process, random values are assigned to the weights while zeros are assigned to the biases [41]. In the following iterations of the backpropagation process, the weights and biases converge until the threshold is reached. However, the final result is dependent from the initialization [76]. To reduce this dependency, the network can be created multiple times, with the number of repetitions specified. This thesis uses a method by the author [113] that determines the root mean square error of the pre-defined test set for all repetitions. Based on this root mean square error, the model repetition with the lowest deviation in predicting the test data set, which is unseen during the training, is selected.

Boxplots, as shown in Fig. 2.24, are used in Section 3.2 for a graphical evaluation of the results. In the side-by-side comparison, the results are shown as a deviation in percent of both the training data set and the test data set. For instance, small deviations in the training data set but high deviations in the test data set would indicate the aforementioned overfitting. Furthermore, this visualization has the advantage of showing the median, upper whisker, and lower whisker together.

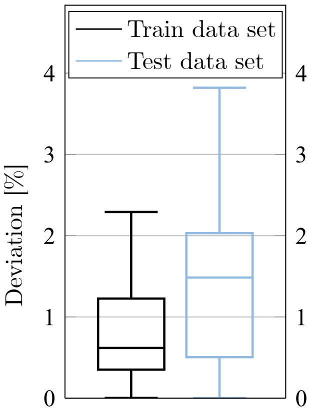

Figure 2.24: Example boxplot showing prediction deviations for training and test data sets.

Summary With the fundamentals of flap load modeling covered in this section, the methodology is established in Section 3.2. In the context of the thesis, this section is important as it provides the input for actuator loading and design based on the trailing edge flaps created for high-lift and VC applications.

2.3 Flight control actuation technology

This section covers the necessary basics of actuator technology, focusing on flaps. First, a summary of present systems and current developments is given. This summary is followed by an overview of existing approaches for the preliminary design of actuators.

2.3.1 General information and development in flight control actuation

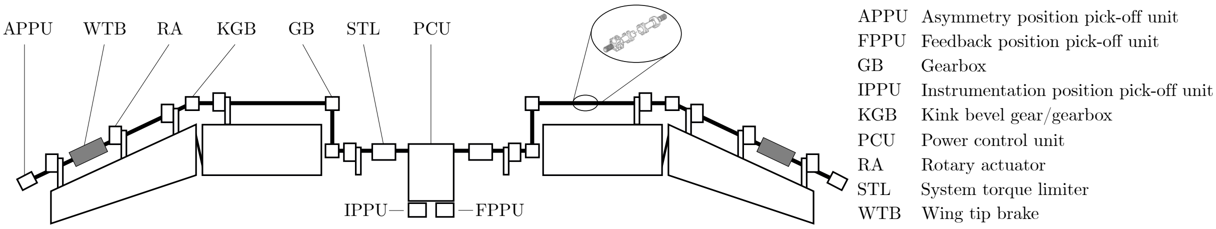

Figure 2.25: Conventional actuator architecture of the trailing edge devices, adapted from [90].

The actuator technology for trailing edge devices with reference to the high-lift system is discussed below. A distinction is made between primary control systems, such as ailerons that control the aircraft's fundamental movements, and secondary control systems, such as flaps that enhance performance during specific flight phases [97]. Currently, control surfaces are being developed beyond their monofunctional tasks towards multifunctional movables [91].

In general, the actuators interact with the kinematics to move the control surface as required and overcome the loads acting on the control surface. In the particular case of high-lift systems, a shaft system as shown in Fig. 2.25 serves as an established solution [90]. The shaft is driven by two independent hydraulic motors in the power control unit (PCU) and monitored by various sensors [12, 90]. The mechanical power is taken from the rotating shaft at the respective actuator stations, with the gears transforming the rotary movement to the kinematics [90, 137]. This system architecture ensures synchronous extension, but severely restricts the freedom for other functions [90]. For the sake of completeness, it is noted that besides the shaft system, in a few aircraft types such as the MD87, synchronous extension was designed using a hydraulic system with corresponding valve circuits for the high-lift system [90].

The pressure for the hydraulic system is generated centrally via pumps driven by the engine shaft and distributed to the corresponding sinks in the aircraft [97]. The system is typically operated at a pressure of 206 bar (3 000 psi). Newer aircraft, such as the Boeing 787 and Airbus A380, use 345 bar (5 000 psi) to allow for lower fluid flows and reduced pipe diameters [97].

Hydraulics are convenient due to the ability to apply high forces and the well-established operational principles. However, hydraulics are also associated with high maintenance costs, potential risks of toxic fluid leaks, and significant system weight—particularly in larger aircraft due to extensive hydraulic piping [25, 97]. As a result, there is a trend towards replacing hydraulic or pneumatic systems with electrically operated actuation components [97]. These electrically operated actuation components are intended to have the advantages of being more lightweight, more precise, and easier to integrate [97], but the introduction is moderated by safety and reliability concerns due to limited experience [97].

For the actuators of the high-lift system in particular, a conversion from centralized power supply to distributed electrical actuation, or power-by-wire actuation, is of interest. In addition to the above-mentioned advantages of the electrical components, differential flap settings—meaning that each flap angle may be adjusted independently—can, for example, optimize the L/D [90], accelerate vortex decay [90], reduce energy consumption [60], and reduce maintenance costs [60]. However, implementing differential flap settings with a centralized power supply requires additional components such as Active Differential Gearboxes (ADGB) [67, 129]. Therefore, power-by-wire actuation facilitate the application of differential flap settings. Within the context this thesis, the concept of DFS is further explored in the frame of variable camber in Section 2.5. Two types of power-by-wire are used for implementation: the electrohydrostatic actuator (EHA) and the electromechanical actuator (EMA) [97]. Both are operated via power and signal cables [97].

Linear electromechanical actuator

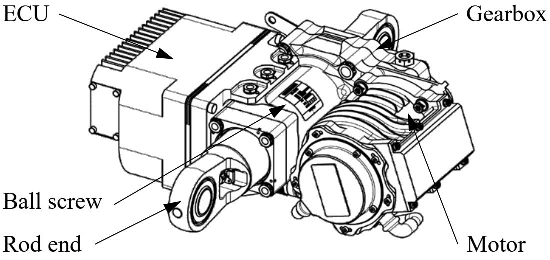

Figure 2.26: Linear electromechanical actuator (LEMA) [116].

This realization of an EMA is designed for linear motion, short LEMA, as shown in Fig. 2.26. The electric control unit (ECU) houses all connections for power supply and bus interface. Within the ECU, the power and signal electronics manage the input voltage. For alternating current (AC) input, the voltage is rectified, smoothed, and stabilized. In another scenario, the rectification from AC to direct current (DC) is handled by a central unit outside the actuator, and the ECU modulates this rectified voltage to AC for the motor. The ECU comprises a power board, a control board, and a monitor board. The power board manages the motor's power supply, the control board regulates aspects like motor speed through a closed-loop system, and the monitor board provides status updates. A spur gear connected to the motor adjusts the output from high speed and low torque to low speed and high torque. This motion is then transferred to a ball screw, which transforms the rotary motion into linear output. The ball screw consists of a spindle and a surrounding nut. Depending on the requirement, an extension and damping control (EDC) may be included in the gearbox to prevent unintended movements in case of failure. The EMA is equipped with rod ends and ball joints on both sides, allowing for attachment to the airframe and the control surface. [116]

Rotary electromechanical actuator

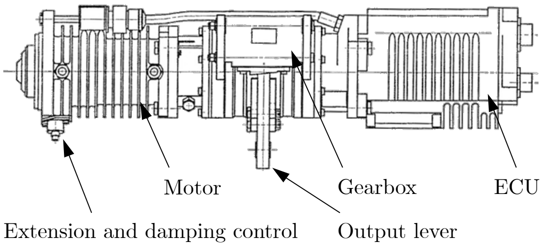

Figure 2.27: Rotary electromechanical actuator (REMA) [116].

The second realization of an EMA is designed for rotary motion, short REMA, as shown in Fig. 2.27. The process of power input handling in REMA is similar to that of the LEMA: The ECU receives either AC or DC voltage from the aircraft's power system and converts it into the AC voltage needed for the motor. Attached to the motor is a multistage planetary gear, which is characterized by a high reduction ratio, potentially up to 900. This gear system is crucial for converting the motor's output to the required level of force and speed for the actuator's operation. Similar to the LEMA, an extension and damping control device is integrated into the REMA to prevent unwanted movements in case of system failures. Finally, the output lever, which is responsible for rotating the control surface, is connected directly to the final stage of the gearbox. [116]

Electrohydrostatic actuator

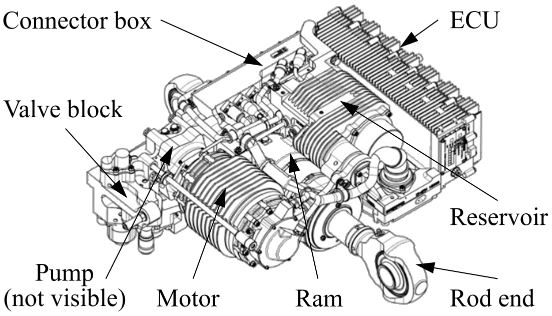

Figure 2.28: Electrohydrostatic actuator (EHA) [116].

The EHA incorporates a self contained fluid system for linear motion, as depicted in Fig. 2.28. This actuator gathers its power from the aircraft's system through a connector box, which allocates electricity to all components needing power. Its power electronics, resembling those in the EMA, adapt AC input by rectification, smoothing, and modulation to suit the motor's needs. For DC input, the system omits rectification and proceeds directly to modulation. Linked to the motor is an axial piston pump with a fixed displacement, responsible for generating the hydraulic circuit's pressure. This circuit is equipped with a valve block, containing sensors, control valves, and a hydraulic fluid reservoir. The pressurized fluid drives a ram that translates this hydraulic force into linear motion. Connection to the aircraft's airframe and control surface is achieved through rod ends featuring ball joints, enabling the required movement. [116]

While the general advantages and disadvantages of power-by-wire actuators are discussed above, distinctions have to be made between EMA and EHA. Fully electromechanical actuators offer the advantages of precision, less weight and the absence of hydraulic fluid [97]. However, three key advantages of EHAs over EMAs are highlighted. First of all, EMAs may suffer from jamming within their mechanical components [97, 128, 137]. Furthermore, the wear predictions for EMAs with the mechanical transmissions are less well known [128]. Finally, an EHA is easier to integrate into existing architectures as it can be switched to a damping mode identical to the prevailing systems [97, 128].

2.3.2 Approaches for preliminary actuator design

Designing actuators for aerospace applications involves balancing numerous factors, including installation requirements, customer demands, and qualification standards [116]. Components are engineered in specialized departments to meet the standards of durability and maintainability [116]. The various actuator designs, such as electromechanical and electrohydrostatic actuators, have an impact on the overall aircraft level [116]. Early knowledge of mass and power requirement of the actuators is important due to the mass growth factor [45] in the integrated design process [93], resulting in design optimizations [122] or limitations for new aircraft configurations [37]. The design of actuators shifts towards a multifunctional movable application, with functions, such as variable camber, active flutter control, and gust load alleviation [91]. However, to efficiently integrate an actuator design into preliminary aircraft design, a short computational time is demanded. This requirement is in contrast to the above mentioned detailed and individual design of actuators [116].

Given the range of approaches to designing power-by-wire actuators found in the literature, this thesis emphasizes using a coherent and validated actuator design concept applicable at the preliminary aircraft design stage. For instance, a force-to-mass ratio with factors for different technology states is introduced in [24], allowing estimates to be made with little time consumption, but neglecting important variables such as the positioning speed. Other sources provide information about a component-wise design approach [18, 25, 123], but do not provide a self-contained, validated overall concept for all actuator components, or do not specify all parameter values, preventing further use. Furthermore, numerous sources go into great detail on all aspects of actuators [69–71], but are therefore outside the preliminary aircraft design stage. Calculations at this level of detail are not appropriate in this thesis, as many of the parameters are not known in the preliminary aircraft design stage, and the computational conflicts with the low computational cost requirement. This gap between self-contained implementability, sufficiently high accuracy, and the sub-second calculation time requirements of the preliminary aircraft design is addressed by the author [116] regarding power-by-wire actuators.

Regarding a conventional high-lift actuation system design in the preliminary aircraft design, the approach in [59] uses fitting functions for the respective components, such as the torque shaft, the PCU, or the gearboxes. This approach is implemented in MICADO and takes load estimations for an actuation dimensioning regarding power and mass into account.

Summary This section provides the rationale for a more in-depth investigation of power-by-wire actuators, the methodological gap to be addressed is dealt with accordingly in Section 3.3. Ensuring an appropriately dimensioned actuator is fundamental for high-lift applications, as well as variable camber applications (as in Section 4.2).

2.4 Principles of longitudinal trim in flight mechanics

In the following, the basics for trimming the flight condition are discussed in order to provide the fundamentals for the methodologies developed in Section 3.4.4. First, the aerodynamic moment and basic terms are discussed regarding an airfoil in Section 2.4.1. Subsequently, the longitudinal stability of an airfoil is discussed. Finally, the application of a horizontal tail plane (HTP) is introduced. In this context, two literature sources are recommended in particular [3, 99], which discuss the relationships in detail and more extensively.

2.4.1 Aerodynamic moment of an airfoil

To understand the aerodynamic moment on an airfoil, a pressure distribution as in Fig. 2.1 is used. Note that the moment around the center of gravity, M_{CoG}, is decisive for the rotation of the airfoil. The overall integration of the pressure distribution on the airfoil surface may be abstracted to a single force vector, which acts in the so-called center of pressure. The aerodynamic moment is influenced by the distance of this center of pressure to the center of gravity. However, it is difficult to incorporate the center of pressure as it changes its position depending on the flow condition. For the purpose of visualization, the airfoil is separated into an upper and lower surface, and the respective pressure on the surfaces is integrated and drawn as force vectors [3], as shown in Fig. 2.29.

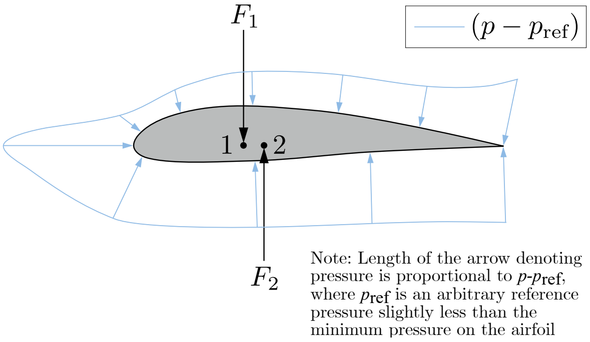

Note: Length of the arrow denoting pressure is proportional to p-p_{ref}, where p_{ref} is an arbitrary reference pressure slightly less than the minimum pressure on the airfoil

Figure 2.29: Abstraction of the pressure distribution into two individual forces for visualization of the aerodynamic moment, adapted from [3].

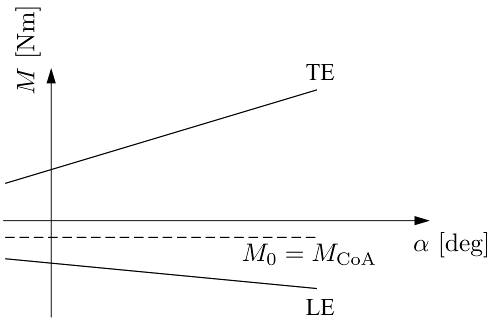

Figure 2.30: Aerodynamic moment plotted over reference points at the LE and TE with the resulting concept of the aerodynamic center.

Therefore, two reference points, the leading edge and the trailing edge, are selected and the moment curve is plotted against the angle of attack for these points in Fig. 2.30. It is assumed that the curves are straight lines [3] and a clockwise moment is defined as positive [3], indicating a nose down moment. At the two reference points, a positive moment acts around the trailing edge for a positively cambered airfoil and a negative moment acts around the leading edge with the corresponding curve as shown in Fig. 2.30. Due to the change in gradient between the leading and trailing edge, a point with a zero gradient can be found on the airfoil. The moment at this point is therefore independent of the angle of attack [3]. This point is called the center of aerodynamics (CoA) and is usually located near the quarter-chord point [3]. A small example can be used to show that this angle-of-attack-independent moment M_{CoA} applies to reference points at any position for zero-lift: Considering a diagram as in Fig. 2.29 for a zero-lift situation, meaning both vectors have the same length, any reference point of the airfoil can be chosen, while the location of the reference point has no influence on the moment. This consideration means that for zero-lift, the angle-of-attack-independent moment M_{CoA} is equal to the moment anywhere on the airfoil, including the CoG and therefore $M_{\text{CoA}} = M_{0,\text{CoG}} = M_0$ [3]. Note that if in the following the moment M is given without further indices, this notation refers to the CoG. For positive cambered airfoils, this so-called zero-lift moment is usually negative $M_0 < 0$ [99]. This relationship has been discussed more extensively in the preceding section, as it is crucial for the analysis of the longitudinal stability of an airfoil (Section 2.4.2) and, consequently, the stability of an entire aircraft (Section 2.4.3).

2.4.2 Static longitudinal stability of an airfoil

In order to examine the static longitudinal stability of airfoils, the absolute angle of attack α_a [3] is first defined, where $\alpha_\mathrm{a} = 0$ at $C_l = 0$[‖]. This notation improves the readability of the following diagrams. The concept of the aerodynamic center is applied with the zero-moment M_0 and the lift placed in this point [3]. For the static stability, it is important that an equilibrium state between lift and moment around the CoG can exist in the first place, i.e. $M = 0$, and that the system returns to equilibrium if it is perturbed [3]. The dynamic stability with an examination over time is not analyzed here. In the following, the dimensionless coefficient is used for the moment, which is defined for a wing with a reference length s_ref as [3]:

$$C_M = \frac{M}{U_\infty^2 \cdot S_\mathrm{ref} \cdot 0.5 \cdot \rho_\infty \cdot s_\mathrm{ref}}. \tag{2.14}$$

There are four possible situations with regard to the static stability properties, firstly whether the CoG is in front of or behind the CoA and secondly whether the zero-moment is greater or less than zero. In Section 2.4.1, it was described that $M_0 < 0$ usually applies to positively cambered airfoils, but there are also airfoils, such as reflexed airfoils, for which $M_0 > 0$ can apply [88]. The four combinations regarding CoG position and $C_{m,0}$ are shown in Fig. 2.31(a)-(d).

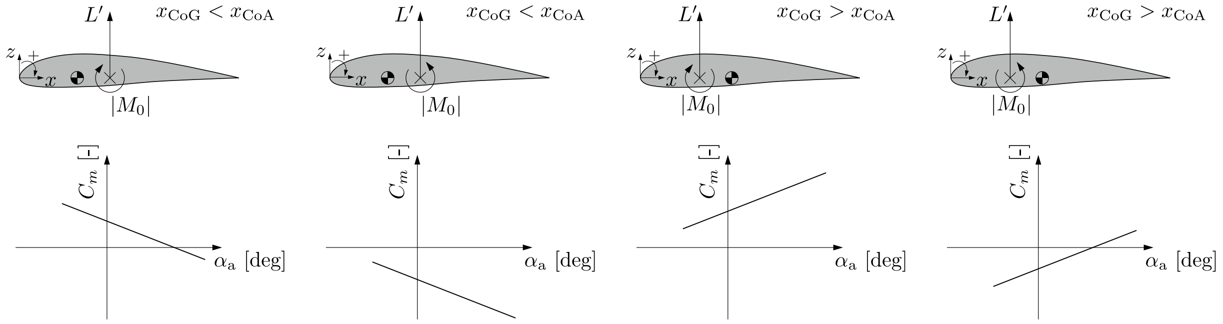

(a) $C_{m,0} > 0$, $C_{m\alpha} < 0$

(b) $C_{m,0} < 0$, $C_{m\alpha} < 0$

(c) $C_{m,0} > 0$, $C_{m\alpha} > 0$

(d) $C_{m,0} < 0$, $C_{m\alpha} > 0$

Figure 2.31: Combinations of $C_{m\alpha}$ and $C_{m,0}$ on an airfoil with regard to longitudinal stability.

The only statically stable combination results for a positive $C_{m,0}$ and a position of the CoG in front of the CoA in Fig. 2.31(a). The curve has an intersection point with the x-axis, in other words there is a $C_m = 0$. Furthermore, if the equilibrium is perturbed, for example by a head on gust, the increased lift acts with a nose down moment around the CoG and thus provides stabilization. This behavior is represented by the negative slope of the curve $\partial C_m / \partial \alpha = C_{m\alpha} < 0$ [3].

However, if a negative $C_{m\alpha}$ is combined with a negative $C_{m,0}$, as in Fig. 2.31(b), there is no state of equilibrium in the entire lift-generating range of α_a, likewise with the combination of $C_{m\alpha} > 0$ and $C_{m,0} > 0$, as in Fig. 2.31(c). In the case of a negative $C_{m,0}$ and a positive $C_{m\alpha}$,

---

[‖] Note that an uppercase subscript denotes a coefficient associated with a three-dimensional body, whereas a lowercase subscript refers to the coefficient of an airfoil section.

as in Fig. 2.31(d), an equilibrium state exists in the lift-generating range of α_a, but this state is unstable. In the event of a perturbation, a self-reinforcing pitching moment occurs [3].

2.4.3 Trim with horizontal tail plane

As shown in Section 2.4.2, the only statically stable state of an airfoil is obtained for $C_{m,0} > 0$ and $C_{m\alpha} < 0$. Several factors lead to a need of using an additional control surface, the horizontal tail plane. Firstly, as described above, a cambered airfoil usually yields $C_{m,0} < 0$ [3, 88], and if the wing is combined with the body (WB), the influence of the body usually adds a negative increment to the $C_{M,0}$ [3]. Furthermore, the static stable system shown in Fig. 2.31(a) is valid for one center of gravity position and one α_a [3]. If the CoG shifts during the flight, e.g. due to the decreasing fuel mass, or if the pilot intends to change the speed, the equilibrium would be disturbed [3]. Equation (2.15) gives the speed required for unaccelerated straight flight [3] with $L = W$ according to Eq. (2.1).

$$U_\mathrm{trim} = \sqrt{\frac{2\,W}{\rho_\infty\, S_\mathrm{ref}\, C_{L,\mathrm{trim}}}} \tag{2.15}$$

If the pilot, for example, chooses to fly at a lower speed, the C_L must increase to maintain the lift required for a straight flight. However, this increase in C_L results in an increase in α_a and, referring to Fig. 2.31(a), leads to a negative moment, and eventually to the aircraft no longer being trimmed [3].

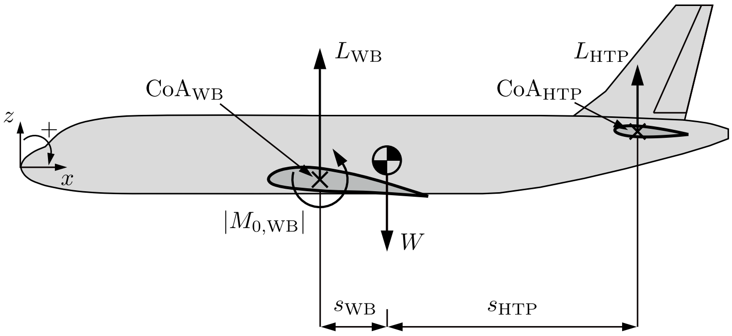

Figure 2.32: Simplified illustration of the moment budget on an aircraft, shown with the CoG behind the CoA of the wing and body combination, adapted from [99].

According to Anderson [3], some simplifications can be applied, starting with the combination of wing and body (WB), followed by the integration of the HTP. The small-angle approximation applies to the angle of attack, the drag is estimated to be significantly lower than the lift, and lever arms in the vertical z-direction are considered as negligible. It is also emphasized that the wing and fuselage components do not allow for isolated influences, due to mutual interactions, but instead have to be considered in a wing-body combination [3]. For the HTP, the same assumptions are valid, in addition, the moment around the HTP is estimated to be negligible [3]. With these assumptions, the following equation is obtained for the moment balance around the CoG, which has to be equal to zero for a trimmed condition:

$$0 \overset{!}{=} C_{M,\mathrm{CoG}} = C_{M,0_{\mathrm{WB}}} + C_{L_{\mathrm{WB}}} \cdot \frac{s_{\mathrm{WB}}}{c_{\mathrm{Wing}}} - C_{L,\mathrm{HTP}} \cdot V_{\mathrm{HTP}}. \tag{2.16}$$

The volume coefficient V_{HTP} as defined in Eq. (2.17) is used to take into account the different reference surfaces of the wing and the HTP, as well as the wing chord c_{Wing} and the HTP lever arm s_{HTP} [3], as depicted in Fig. 2.32.

$$V_{\mathrm{HTP}} = \frac{s_{\mathrm{HTP}} \cdot S_{\mathrm{ref,HTP}}}{c_{\mathrm{Wing}} \cdot S_{\mathrm{ref,Wing}}} \tag{2.17}$$

Alternatively, the lift for the calculation of the $C_{L,\mathrm{HTP}}$ could also be referred to the reference surface of the wing, but this reference would lead to inconsistent lift coefficient definitions. The important aspect is to ensure that the use of the applied reference values is consistent for the nondimensionalization. Now, there are two cases to be distinguished, according to which the CoG can be in front of or behind the CoA of the wing body combination, resulting in a downward or upward force required by the HTP. BURNS [20] clarifies that it is a common misconception that an HTP exclusively generates a downward force, even tough this is usually the case. Figure 2.32 shows the case for the CoG behind the CoA. Regarding the definition of a positive moment direction, note that $M_{0,\mathrm{WB}}$ is plotted as the absolute value in the effective direction.

Initially, it can be assumed that the HTP is not under load in the design case [99], but since, as described above, this assumption only applies to a single flight condition, the HTP usually has to be deflected in order ensure a trimmed condition resulting in and upward or downward force.

The influence of the HTP on the trim is shown in a diagram analogous to Fig. 2.31(a). Figure 2.33(a) shows that an increase in the HTP deflection, i_{HTP}, affects the moment balance with a parallel shifted curve [3]. For the sake of clarity, Fig. 2.32 can be considered to illustrate that

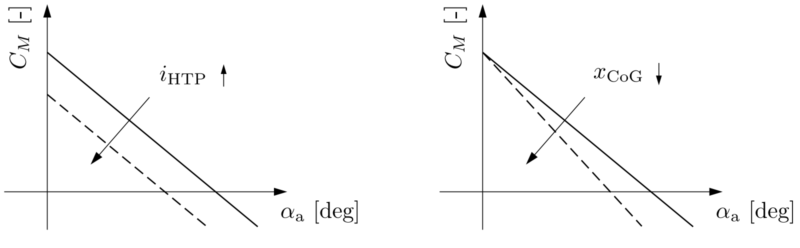

(a) Change in HTP angle.

(b) Change in CoG position.

Figure 2.33: Progression and options for influencing the moment coefficient over α_{a}, adapted from [3].

effect: with a constant α_a, a higher HTP deflection induces a negative moment in the system, as shown in Fig. 2.33(a).

Another method of trimming should be mentioned here for the sake of completeness, namely by changing the center of gravity [3]. Using this method, considering an unchanged aircraft geometry, fuel is pumped between so-called trim tanks depending on the flight condition. The corresponding effect on the moment diagram is shown in Fig. 2.33(b). Instead of the parallel shift due to the influence of the HTP, there is a change in the gradient [3]. It should be noted that the zero moment is the same because, as described in Section 2.4.1, the moment is independent of the reference point at zero lift.

The neutral point is another commonly used tool, where all influences of the aircraft, i.e., wing, fuselage, and HTP are summarized in this single point [3]. For a statically stable condition, the neutral point must be located behind the CoG, with the distance between the CoG and the neutral point defining the static margin, which is also used for controllability investigations [3].

Summary This section shows the fundamental relationships for the moment balance on the airfoil and the longitudinal stability on the aircraft. These foundations are required in the course of this thesis for the implementation of a trim method in the preliminary aircraft design in Section 3.4.4.

2.5 Concept of variable camber technology

A controlled adjustment of the wing camber allows for a wing shape optimization during cruise flight, depending on the current mission point including the prevailing conditions, contributing to an increase in the aircraft's efficiency [115]. This technology is referred to as variable camber.

Given the ecologic and economic considerations stated in the motivation in Chapter 1, an efficient aircraft design in terms of fuel consumption is important, as the commercial success of an aircraft depends on it [39]. However, product strategies usually aim to create a transport aircraft family based on a common wing and by adapting the fuselage [39]. This policy of high fleet commonality can reduce development, manufacturing, and maintenance costs. However, the wing designer must choose a suitable wing for the most stretched version and find the best compromise between design and off-design conditions [39]. In addition, the missions that a particular aircraft type has to fulfill within its operational lifetime often vary, depending on the place of departure and destination and on the operating airline [115, 119].

Fixed wing geometries are designed as a compromise geometry to allow operation over a spectrum of flight conditions; however, performance within each condition often deviates from the best achievable level [8, 39, 115]. Furthermore, a fixed wing represents a compromise between aerodynamic and structural optimization over the entire operational range [91]. In this context, the wing of a passenger aircraft is optimized for the highest efficiency, but leaves little margin for a variation of lift and payload [119]. Thus, aircraft often operate under off-design conditions [39, 119]. Variable camber offers the possibility for operational flexibility and aerodynamic optimization according to the given operating conditions [16, 39].

In the following, the working principles of VC are described. In Section 2.5.1, the application of VC in the course of a mission will be explained, followed by a more detailed discussion of the lift distribution and the induced drag. While this thesis refers to VC as an implementation on conventional high-lift devices, Section 2.5.2 concludes with an overview of various technical implementations.

2.5.1 Principles and mechanics of variable camber systems

To discuss specific effects of VC deployment, this section begins by demonstrating these effects over the course of a mission. This thesis focuses on the optimization by means of aerodynamic drag reduction for each operation point and therefore primarily refers to the lift-to-drag ratio L/D.

The high-lift control surfaces enabled for VC application influence the spanwise lift distribution. The so-called induced drag is an important component of the total drag and will be discussed in detail. The relationships identified herein are relevant for interpreting the results of variable camber application in Section 4.2.

Variable camber application in terms of a flight mission

In order to explain the influence of VC, the course of a flight mission is presented first. If an unaccelerated level flight is assumed, Eq. (2.1) with $L = W$ can be applied. In cruise flight, the weight and thus the required lift decrease steadily due to fuel consumption.

This relation is illustrated by the lift coefficient curve in the segments with constant flight altitude, shown in Fig. 2.34. As a consequence, the aircraft cannot operate at a constant, optimized $C_{L,\mathrm{opt}}$. This deviation from the design point is illustrated in Fig. 2.35, in which a characteristic polar plot of the lift-to-drag ratio L/D against the lift coefficient C_L is shown.

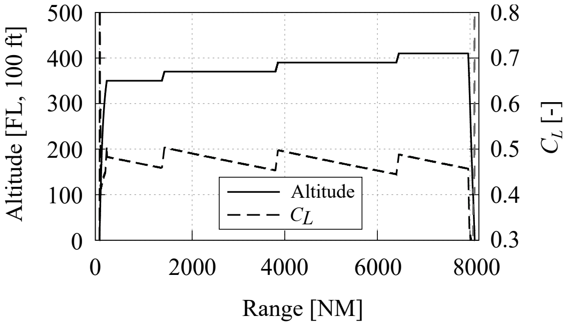

Figure 2.34: Exemplary mission profile with step climbs and the corresponding C_L.

According to Eq. (2.1), when the aircraft's weight decreases due to fuel consumption while maintaining constant speed, there are several options to keep a constant lift coefficient C_L at its optimum value. One option is to reduce the density ρ, which can be achieved by a continuous climb [77]. Since distinct flight altitudes are specified by air traffic control for most aircraft, a mission profile with several step climbs to specific flight levels is used to compensate for leaving the optimal C_L point. An exemplary mission profile with associated lift coefficient is shown in Fig. 2.34. The effects of a step climb and the weight reduction due to fuel consumption with respect to the L/D are shown in Fig. 2.35. Although the L/D may be maintained in a range around the optimum, the limited number of possible step climbs causes the aircraft to operate outside the optimum operating point for the majority of the mission. With these constraints, the VC application becomes relevant, since it modifies the wing geometry by adjusting the deflection angle of control surfaces and thus optimizes the wing for the current mission point.

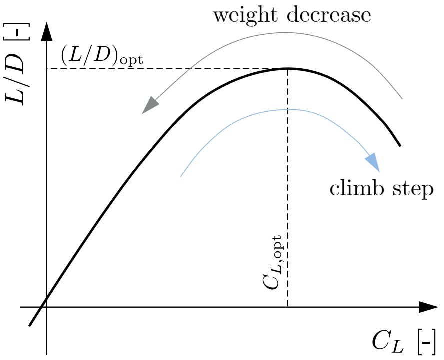

Figure 2.35: Impact of weight decrease due to fuel combustion and of step climbs on the L/D curve, adapted from [85].

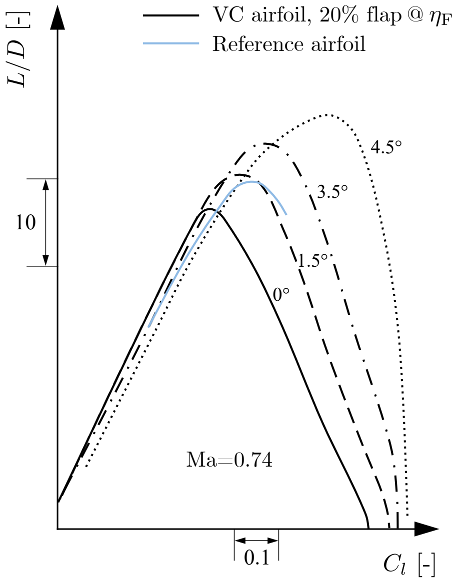

Figure 2.36: Airfoil level: L/D ratio of different flap settings, compared to the fixed camber airfoil, adapted from [119].

Szodruch and Hilbig [119] initially present the influence of increased camber using the case of airfoils as an example. Figure 2.36 shows that the optimum C_l, as well as the maximum achievable L/D, increases for higher camber due to a deflected trailing edge. At the same time, lower camber values exhibit a slightly more favorable L/D in the lower C_l range. However, these correlations are only valid in a limited range. An excessively high flap angle can cause early flow separation, leading to no gain in maximum L/D. For a discussion on flow separation, refer to Section 2.1.1. Similarly, an increased flow acceleration due to the flap deflection in transonic flow conditions can significantly increase the onset of the shock, and thus the so-called wave drag, to such an extent that no L/D gain is achieved [115]: At the critical Mach number, the local flow on the airfoil surface reaches sonic conditions, initiating the formation of shock waves and causing a sudden, substantial increase in drag [5]. As these shocks intensify, the wave drag continues to rise in the transonic regime [93]. This effect is considered further in Section 4.2.

The characteristics of the L/D curve are comparable when transferred to the overall flight level. Figures 2.37 show distinct polars for certain flap settings [119]. In general, these can be caused by a uniform or a differential deflection of the flaps.

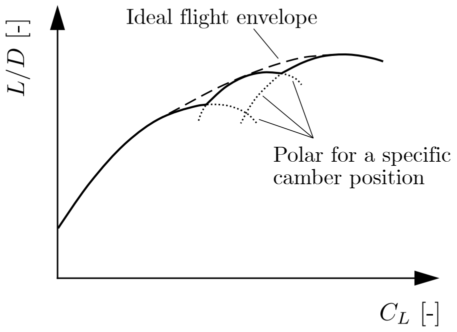

Figure 2.37: Aircraft level: Impact of VC settings during cruise on L/D, adapted from [119].

The envelope is shown as well, which would ideally be achieved by VC settings. Using the approach that this envelope from the possible flap settings represents one new merged VC polar, it is worth noting that the optimal C_L increases with higher camber, similar to the airfoil level. Furthermore, for the investigation at mission level, it is still the case that the aircraft does not fly in the optimum of the new merged VC polar; however, the VC application allows the aircraft to use the optimum flap setting and thus individual wing geometries for the current operating point during operation. This flexibility is not provided by a fixed wing setting.

Spanwise lift distribution and induced drag

Extending the flaps influences, among other things, the spanwise lift distribution. This lift distribution is directly related to the so-called induced drag. The induced drag is of great importance in the VC application, as discussed in more detail in Section 4.2. In order to provide the theoretical basics, an abbreviated form of the derivation of the induced drag is given below. For the detailed derivation, refer to [5]. The case of an elliptical lift distribution is discussed in particular, since, for a fixed wingspan, this distribution minimizes induced drag [17]. Another highly recommended source, especially in terms of discussing and understanding induced drag, can be found in [72].

Note that a precise subdivision of drag is not feasible in reality [72], but under certain assumptions, drag components can be subdivided. This division allows for a more convenient analysis of the effects in aircraft design. In this work, a subdivision based on [93] is adopted, according to which, in addition to the induced drag component, a wave drag component is incorporated, as well as a viscous component including friction and form drag. The wave drag has a significant impact on potential flap settings, as its effects are discussed in more detail in Section 4.2.

Fundamentals regarding the induced drag Prior to the specific application on the wing, the theoretical principles for a vortex filament and its abstraction to a semi-infinite vortex filament are given. These are based on the assumption of an inviscid, incompressible flow [5].

The differential of the velocity vector at an arbitrary point P, induced by the vortex filament as shown in Fig. 2.38, is described by the Biot-Savart law [5]:

$$\mathbf{dV} = \frac{\Gamma}{4\pi}\frac{\mathbf{dl} \times \mathbf{r}}{|\mathbf{r}|^3}. \tag{2.18}$$

This equation considers the circulation in addition to the geometric properties as factors influencing the velocity differential. Regarding the definition of the circulation, refer to Section 2.1.1.

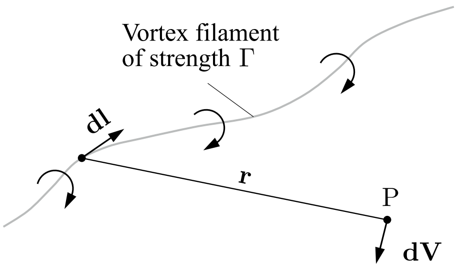

Figure 2.38: Vortex filament and illustration of the Biot-Savart law [5].

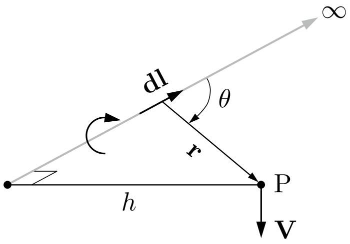

Figure 2.39: Abstraction to a straight, semi-infinite vortex filament [5].

In the following discussion, semi-infinite straight vortex filaments are used, as shown in Fig. 2.39. For this case, the differential from Eq. (2.18), integrated over the vortex filament length, can be solved. The individual steps are given in the appendix in Eqs. (A.1) and (A.2). The solution as stated in Eq. (2.19)[**] is sufficient at this point:

$$U = \frac{\Gamma}{4\pi h}. \tag{2.19}$$

Before the application to a wing is given, the statements of Helmholtz's vortex theorems, which apply to incompressible and inviscid flows, are required [104].

1. A fluid particle that is not already rotating will not start to rotate. The rotation of a particle remains constant over time, as long as no external forces act on it.
2. The particles that are part of a vortex line at a given time will continue to be part of the same vortex line as they move.
3. The vorticity flux, i.e. the product of the cross-section and rotational speed of a vortex tube, is constant along the entire vortex tube and does not change its value when the vortex tube moves. Vortex tubes must therefore either be self-contained or end at the boundaries of the flow field (which can be ±∞ [5]).

Application to the wing With these fundamentals, a wing is abstracted. As shown in Section 2.1.1, the deflection of the streamlines in the case of aerodynamic lift can be represented by the circulation.

In a first step, the lift-generating wing is replaced by one vortex line, the so-called bound vortex. According to the aforementioned theorems, this vortex needs to have a constant circulation and cannot end in the fluid. Therefore, two semi-infinite boundary free vortices are added to satisfy Helmholtz's third vortex theorem. The abstraction to a horseshoe vortex system as introduced by Prandtl is shown in Fig. 2.40 [5].

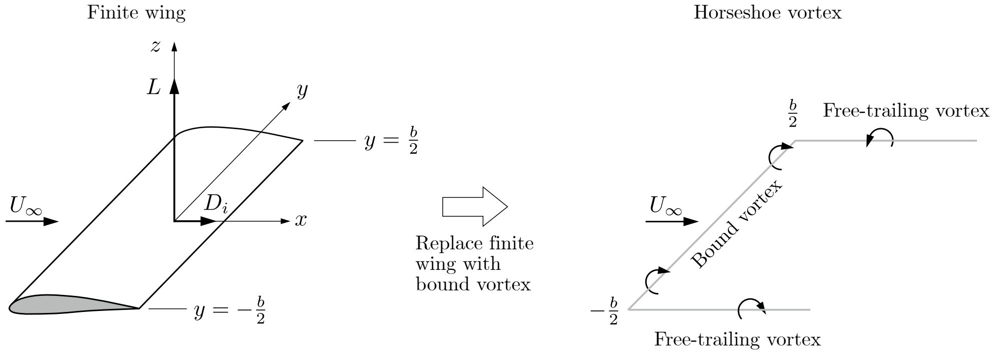

Figure 2.40: Replacement of the finite wing with a bound vortex, adapted from [5].

[**] Note that $\mathbf{V}$ denotes vector velocities, while U denotes scalar velocities.

However, this representation has shortcomings: on the one hand, Eq. (2.19) for both free vortices would result in an infinitely high induced velocity at the wing tips at ±b/2 [5]. Secondly, keeping in mind that the Kutta-Joukowski theorem in Eq. (2.9) is linking the circulation and lift, a realistic wing would most likely not have a constant lift distribution and thus does not have a constant circulation. Note that the lift distribution is not to be confused with the lift coefficient distribution [132].

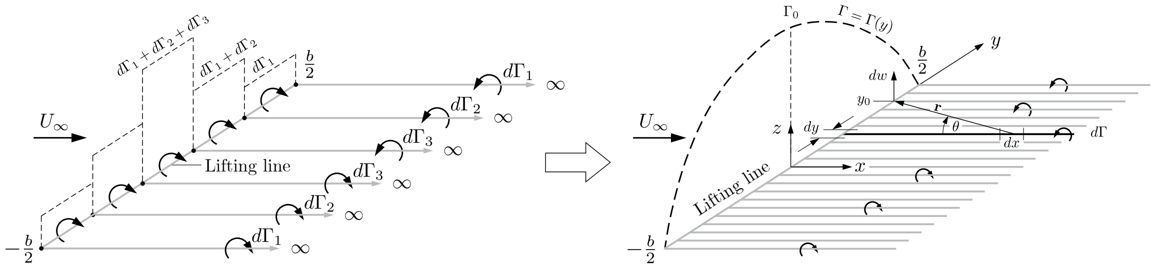

Figure 2.41: Superposition of a finite (left) and infinite (right) number of horseshoe vortices along the lifting line, adapted from [5].

Prandtl proposed a solution to this problem by representing the wing not by one, but by a multitude of horseshoe vortex systems [5]. The respective bound vortices have an infinitesimal step size and are located on a common axis. This approach is called Prandtl's lifting line theory [5].

Equation (2.19) is extended to the present vortex system in an infinitesimal form, replacing the general V with the vertical component w [5]:

$$dw = -\frac{(d\Gamma/dy)\,dy}{4\pi(y_0 - y)}. \tag{2.20}$$

Integrated over the entire wingspan, Eq. (2.20) yields an expression for the induced vertical velocity component w at any point y_0 on the line of bound vortices [5]. As shown in Fig. 2.41, the upward direction is defined as positive.

$$w(y_0) = -\frac{1}{4\pi}\int_{-b/2}^{b/2} \frac{(d\Gamma/dy)\,dy}{y_0 - y} \tag{2.21}$$

The quintessence of the findings is consequently that the lift of the wing is inevitably linked to a vortex system that generates a velocity component $w(y_0)$ directed vertically downwards on the wing itself. This induced velocity is related to the circulation distribution over the entire wing. This knowledge is essential for the evaluation in Section 4.2. In the following paragraph, the consequence of the induced velocity is interpreted as the so-called induced drag.

Interpretation of the induced velocity as induced drag In order to make the findings more practicable, it is desirable to convert the induced velocity $w(y_0)$ into a drag component.

For this purpose, the common representation on an airfoil as in Fig. 2.42 is used, even if this representation implies some considerable misunderstandings that need to be clarified:

- The induced drag occurs exclusively on lift-generating wings, not on two-dimensional airfoils.
- The representation gives the impression that $w(y_0)$ is constant for all airfoil sections of the wing, but Eq. (2.21) states that $w(y_0)$ is a function of the spanwise position y_0.
- Similar depictions are commonly used to describe lift and different forms of drag, and how they combine to form the resulting aerodynamic force. However, other types of drag do not induce the velocity component $w(y_0)$.
- The velocity component $w(y_0)$ is often referred to as downwash, which is intentionally omitted in this thesis. From the author's point of view, the term downwash rather refers to the deflected flow, which, with its mass, results in the momentum that corresponds to the lift, see Section 2.1.1. However, this case also applies to the two-dimensional case, and is therefore incompatible with the three-dimensional case of the induced drag.

Apart from the mentioned drawbacks, the diagram shows quite well in what way the induced drag caused by an induced vertically downward velocity component $w(y_0)$ can be visualized. A conceptual representation can be made of the wing moving in its own vortices. It is significant to note that this representation refers to the integration of all free vortices according to Eq. (2.21). With this visualization, it can further be shown that the angle between the flow velocity U_∞ and the induced velocity component $w(y_0)$ results can be expressed as an induced angle of attack α_i. This expression is stated in Eq. (2.22a) and the simplification, assuming small angles, is stated in Eq. (2.22b) [5]. The geometrical angle of attack of the wing α is thus reduced by the induced angle α_i to an effective angle of attack α_{eff} [5].

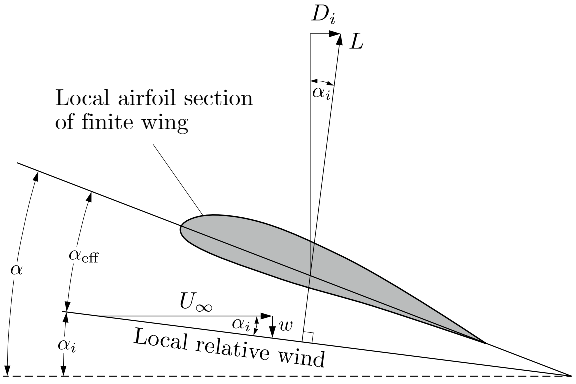

Figure 2.42: Airfoil section at an arbitrary point y_0 to illustrate the induced angle of attack α_i, adapted from [5].

$$\alpha_i(y_0) = \arctan\left(\frac{-w(y_0)}{U_\infty}\right) \tag{2.22a}$$

$$\alpha_i(y_0) = \frac{-w(y_0)}{U_\infty} \tag{2.22b}$$

Determining the induced drag D_i shown in Fig. 2.42 from the angular proportion yields Eq. (2.23).

$$D_i = \int_{-b/2}^{b/2} L'(y)\,\alpha_i(y)\,dy \tag{2.23}$$

Both the sectional lift $L'(y)$ and $\alpha_i(y)$ need to be integrated over the wing span. The sectional lift $L'(y)$ can be further calculated using the Kutta-Joukowski theorem from Eq. (2.9), resulting in the Eq. (2.24) for the induced drag [5].

$$D_i = \rho_\infty U_\infty \int_{-b/2}^{b/2} \Gamma(y)\,\alpha_i(y)\,dy \tag{2.24}$$

Although this equation shows the physical relationships of the induced drag, it still requires knowledge of the spanwise distribution of $\Gamma(y)$ and $\alpha_i(y)$. A convenient solution can be achieved for the specific case of an elliptical lift distribution, which is discussed in the following paragraph.

The case of an elliptical lift distribution The elliptical lift distribution allows Eq. (2.24) to be solved in a particularly convenient way. Even if this elliptical lift distribution may seem like an artificially constructed special case, it can be used to derive simple relationships that are particularly advantageous for the preliminary aircraft design.

In order to solve Eq. (2.24) for the elliptical lift distribution, an expression for both $\Gamma(y)$ and $\alpha_i(y)$ is required. According to Eq. (2.9), an elliptical lift distribution also means an elliptical circulation distribution. Thus, $\Gamma(y)$ is defined by the shape of the ellipse, as stated in Eq. (2.25).

$$\Gamma(y)_{\text{ellipt}} = \Gamma_0\sqrt{1-\left(\frac{2y}{b}\right)^2} \tag{2.25}$$

Furthermore, Anderson [5] shows how $\alpha_i(y)$ from Eq. (2.22b) can be simplified to the following term using Eq. (2.25).

$$\alpha_{i,\text{ellipt}} = \frac{\Gamma_0}{2bU_\infty} \tag{2.26}$$

Note that $\alpha_{i,\text{ellipt}}$ in Eq. (2.26) is, in contrast to the general form $\alpha_i(y_0)$ in Eq. (2.22a), constant over the wingspan, a characteristic that is unique to the elliptical lift distribution. Inserting the identified terms for the variables into Eq. (2.24), results in:

$$D_{i,\text{ellipt}} = \rho_\infty U_\infty \int_{-b/2}^{b/2} \underbrace{\Gamma_0 \sqrt{1 - \left(\frac{2y}{b}\right)^2}}_{\Gamma(y)} \cdot \underbrace{\frac{\Gamma_0}{2bU_\infty}}_{\alpha_i(y)} \, dy. \tag{2.27}$$

By solving the integral and defining the geometric wing aspect ratio $\Lambda = b^2/S$, the final result for the induced drag coefficient of an elliptical lift distribution is obtained [5].

$$C_{D,i,\text{ellipt}} = \frac{C_L^2}{\pi \Lambda} \tag{2.28}$$

As Anderson [5] shows in detail, these findings can also be transferred to general lift distributions by dividing by only one additional factor, the so-called Oswald factor e. It describes the ellipticity of the lift distribution and range from 0 to 1 [5]. Although this factor also needs to be determined for each wing, it simplifies the representation of the induced drag compared to Eq. (2.24).

Short discussion of the induced drag With these derived findings in Eq. (2.28), some basic statements can be made about induced drag. First of all, lift on a wing always comes at the cost of drag, even under the stated assumptions of inviscid, incompressible flow [5]. Furthermore, this drag coefficient component is reduced by an increased aspect ratio Λ of the wing [5]. A particular characteristic of the induced drag is that its magnitude decreases with increasing speed [72]. And finally, for a given wingspan, the induced drag increases if the shape of the lift distribution shifts away from an elliptical shape [5].

Besides the source used in the derivation above [5], McLean [72] offers a particularly recommendable source for the interpretation. Two common misunderstandings are highlighted here, as they lead for example to questionable designs for wingtip devices [72]. The first is referred to as the *induction myth* and describes the assumption that the rolled-up vortex behind the wing is the cause of the induced drag [72]. The cause and effect are reversed, as the rolled-up vortex is rather the manifestation of the flow pattern of lift-generating wings [72]. One reason for this misunderstanding may be the naming, as in electromagnetism the term induction is defined as a reciprocal mechanism, which is not the case for fluid mechanics [72]. The second is the *compactness myth*, which refers to the idea that the wake vortex of an aircraft originates from the wingtip and can therefore be counteracted compactly at this location [72]. However, as discussed in detail in the section above, the flow pattern over the entire wing is relevant.

2.5.2 Approaches to different variable camber realizations

Several technical approaches exist to implement variable camber technology. A concise overview is provided in [115] and is summarized below, and Barbarino et al. [8] offer a more comprehensive review of the topic.

Numerous studies have been conducted on the subject of the shape variable wing, with different approaches being specified. One approach mainly investigates a flexible, continuous trailing-edge, often called morphing, although this term does not clearly differentiate from other realizations. Numerical studies of the flow and structure have been performed on the Common Research Model (CRM) [19, 68], calculating a potential fuel saving of about 1 %. Experimentally, the applicability of the morphing concept was shown on a Gulfstream G3 aircraft by Kota et al. [56, 57], achieving a range increase of up to 15 % on the one hand, but showing limitations especially in the high-lift application on the other hand. A specific variant of this technology is the Variable Camber Continuous Trailing Edge Flap (VCCTEF), where the continuous trailing-edge is equipped with special flaps that move around multiple pivot points [78]. The objective is to adapt aerodynamics to changing flight situations by means of the variable wing shape, mainly through aeroelastic effects. This approach is being examined thoroughly by a NASA research group [35, 55, 61, 62, 78–80, 122, 126]. An interesting result was obtained by Ting et al. [122] regarding an aircraft based on the NASA generic transport model, showing that the outboard flap segmentation has a more significant influence on drag reduction than the segmentation of the inboard flaps. This finding for the study case can be attributed to the wave drag reduction, as the optimization results demonstrated that increasing the number of outboard flap sections leads to a more substantial decrease in wave drag, which dominates the overall drag reduction in the shown case. The study further illustrates that this effect is due to the redistribution of aerodynamic load, shifting lift inboard and reducing the intensity of outboard shocks.

Another approach investigates shape variation in flight with conventional leading and/or trailing-edge flaps, hereinafter referred to as variable camber (VC). In this context, for example, high-lift flaps are detached from their unilateral task and become multifunctional movables [91]. Utilizing already established flaps also offers the advantage of keeping development and certification costs low compared to new systems [39].

Further studies utilizing experimental and CFD data followed [43, 65, 74, 85, 89, 119], which found potential for reduction of drag and fuel and increased range. As the jet fuel saving potential is dependent on the individual aircraft type, the study results range from 1-3 % with a drag reduction in most of the flight phases [16], to 4 % [15] respectively 3 - 6 % [39] for a redesigned wing with VC as a requirement. In addition, it is pointed out that a flap deflection affects the pitching moment [39], which is in particular the motivation for the methodology for longitudinal trimming in MICADO discussed in Section 3.4.4. The link between flap deflection and a possible increase in wave drag is also discussed [39], which is examined in this thesis in the application Section 4.2.

Reckzeh [91] shows that this technology is already feasible on existing large-capacity passenger aircraft with Adaptive Dropped Hinge Flaps for gapless VC trailing-edge utilization, see also Section 2.1.3. Active Differential Gearboxes [67, 129] allow for a differential flap setting of trailing-edge devices on a single torque shaft in the standard system. It is noteworthy that as early as 1990, Greff [39] already discusses the application of differential gears. Recksiek [90] provides additional considerations on corresponding actuator architectures, whereas Lampl et al. [60] provides a comparison of different architectures as well as considerations on failure cases.

Summary With the discussed information in this chapter regarding the basic idea of a variable camber application, its theoretical foundations with the induced drag in particular, as well as the insights into technical solutions, the implemented preliminary design methodology is discussed in Section 3.4.3 and the methodology for the evaluation is elaborated in Section 4.2.

3 Aircraft design methodologies

This chapter covers the methodologies relevant to this thesis in the preliminary aircraft design with regard to trailing edge modifications. The objective is to provide methodologies for each step in the design process. The methods are designed to be modular, allowing for individual components to be reused in future works.

Section 3.1 deals with the device configuration of high-lift airfoils. As discussed in the fundamentals in Section 2.1.2, the high-lift design always needs to be carried out with regard to the entire airfoil, including the leading edge. In order to predict the aerodynamic trailing edge flap loads as part of the preliminary aircraft design, Section 3.2 presents a neural network-based modeling approach. Subsequently, the thesis deals with the required control surface actuator design and presents a component-wise modeling in Section 3.3 for three different power-by-wire actuators. The final Section 3.4 describes MICADO, the preliminary aircraft design software used in this thesis, with focus on the process for implementing variable camber. For this thesis in particular, a methodology for longitudinal trim is developed, which is explained separately. All methodologies discussed in this thesis——except for the status quo of the MICADO modules described in the Sections 3.4.1 - 3.4.3——were developed during the course of this thesis.

A brief comment on the terms *methods* and *methodologies* should be made. Methods refer to specific techniques or procedures used in tasks, like a formula for calculating loads in aircraft design. Methodologies refer to the overall framework or strategy that guides the selection and application of these methods in a broader context, such as the structured approach to aircraft component design. [6]

3.1 High-lift airfoil configuration methodology

This section provides three methodologies for the preliminary configuration setup that can be applied to any given airfoil. In particular, the high-lift devices slats and ADHF, including spoiler and flap, are investigated; however, other devices may be included by modifying the process shown. Note that the master's thesis of SCHOTTMÜLLER [105], supervised by the author, also deals with this topic. First, this section describes the logic behind the positioning of the devices and the flow simulations. Subsequently, Section 3.1.1 establishes a flowchart of the process chain for high-lift airfoil configuration setup. In Section 3.1.2, three specific methodologies are derived, which provide a variation in computational time and accuracy.

Spatial positioning of the high-lift devices

For the following design of the high-lift devices, a well-defined standard for the geometry is required. Therefore, a comparison of different possibilities is given below.

The high-lift device positions, as exemplary shown in Fig. 2.14, may be defined spatially in different ways from which three options are discussed. All three options eventually reproduce the same geometry, but yield advantages and disadvantages in the setup. The first option states gaps and overlaps, which are the aerodynamically relevant parameters, as described in Section 2.1.3. The following two options rely on Cartesian coordinates. The second option measures the displacement of the leading edge of the slat or flap from its respective retracted position. The third option measures the distance from the slat's trailing edge to the airfoil's leading edge and the flap's leading edge to the airfoil's trailing edge [132]. This option, illustrated and introduced by Woodward et al. [135], is straightforward since it does not require additional steps to set the desired position of the elements. For instance, setting a specific gap value according to option one involves complex calculations or iterative processes for positioning the high-lift elements. The alternative Cartesian method, introduced as the second method, is similar but has drawbacks in further optimizing the spoiler, as its angle also shifts the trailing edge. Using a fixed coordinate system means the flap position must always be defined relative to the spoiler angle. However, positioning the coordinate system at the trailing edge allows for a consistent and comparable flap position across studies, as it moves with the spoiler. For aerodynamic evaluation, positions are still converted into gap and overlap parameters.

Based on a consideration of the advantages and disadvantages, particularly with regard to automating the geometry displacement in a predefined investigation matrix for a parameter study, the third option is selected, as shown in Fig. 3.1. An airfoil normalized to a unit length is shown, meaning that one step in the grid represents 1 % of the chord length.

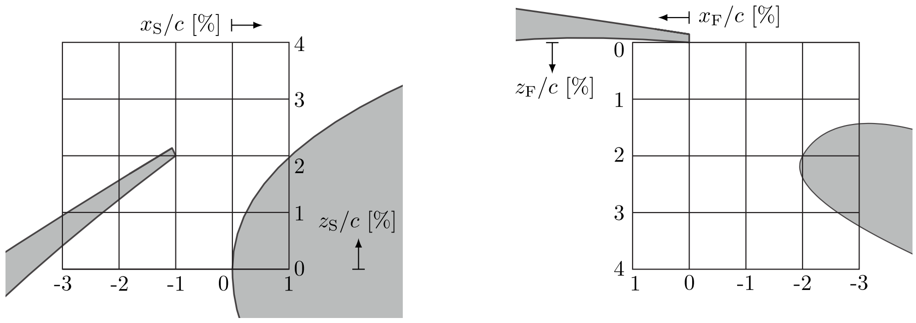

Figure 3.1: Cartesian displacement matrix, originating from the respective upstream element, adapted from [131].

Angle of attack polar calculation

For the following analyses, angle of attack polars are calculated with the CFD program ANSYS Fluent [7] for each geometry combination to be examined, with computational meshes created using CENTAUR [23]. According to SCHINDLER ET AL. [102], the SST k-ω turbulence model provides accurate, albeit conservative, correlations with wind tunnel experiments for high-lift configurations. The flow is assumed to be fully turbulent, modeled at a turbulent intensity of 1 %. The pressure and the flow velocity utilize the coupled method. The pressure gradient is determined using the least squares cell based method, while discretizations employ a second order upwind or second order approach. Detailed settings and configurations are available in the appendix in the Tables B.2 and B.3.

For the meshing strategy, an unstructured mesh with y^+ values less than 1 is adopted; for further information refer to Fig. B.5 in the appendix. Appendix B.2 provides additional notes on CFD, containing detailed information about y^+. To ensure the reliability of simulation results, a mesh independence study is performed, analyzing the parameters C_l, C_d, C_p, and velocity profiles on the airfoil surface at the slat, the flap, and the spoiler. The study concluded that beyond 140 000 cells, no significant changes in these parameters were observed. To adopt a conservative approach, 150 000 cells are therefore used for mesh generation. [105]

3.1.1 Flowchart steps for high-lift airfoil design

In this section, a comprehensive explanation of the developed optimization process for high-lift elements consisting of slats and ADHF on airfoils is provided, including a detailed case study of the iterative approach. Broad ranges for parameter variation are considered to analyze trends and understand the influence of various parameters. This process is depicted in the flowchart presented in Fig. 3.3. For further details on the ADHF system, refer to Section 2.1.3. The optimization includes the deflection angles of all elements, as well as the gaps and overlaps of both the slat and the flap. From the analyses conducted in this section, three methodologies are developed later in Section 3.1.2.

The high-lift elements are first optimized for their position in the landing phase configuration, defining the hinge points of the ADHF, and then for the takeoff phase. This sequential optimization approach, adopted from WILD [132], is based on the rationale that the landing position involves the largest deflection. Both the landing and the takeoff configuration are optimized regarding individually introduced target functions. The parameters for the optimization include the deflection angles of slat, spoiler, and flap, as well as the spatial positioning of the slat and the flap. Within the landing and takeoff phase, the individual control surfaces are adjusted using an iterative approach. Thus, this approach does not cover all possible parameter combinations as this would lead to an unacceptable number of simulations.

The individual steps are discussed below and the evaluation is shown using a selected case study airfoil[*], shown in Fig. 3.2. It is assumed that the airfoil is optimized for cruise flight, with high-lift devices subsequently integrated into the airfoil, as described in Section 2.1.

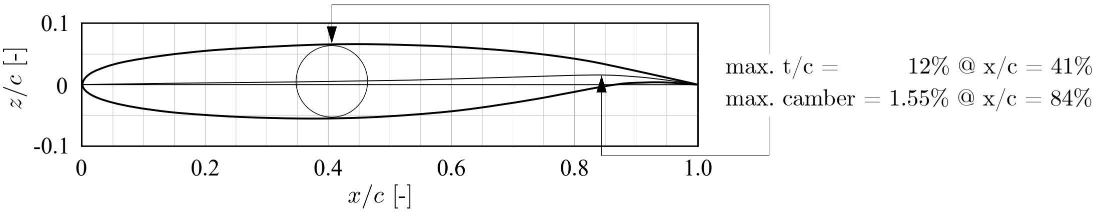

Figure 3.2: Case study airfoil for high-lift configuration optimization methodologies.

I. Setup steps: Preliminary investigations and geometry definition

A preliminary investigation is initially carried out on the airfoil with a droop nose, see Fig. A.3 in the appendix, and flap but without a spoiler. The aim is to spatially position the flap for a given angle as favorably as possible prior to the main optimization process in order to reduce the number of ensuing CFD simulations. For this preliminary investigation, the fixed droop nose is used to provide a necessary leading edge system without the requirement to consider the gap effects at the leading edge. Note that the results of this setup step only serve as an initial value. In subsequent investigations, the influence of the spoiler is taken into account as well. With the support of the spoiler, significantly larger flap deflections can be achieved [117]. Without a spoiler, the flap angles are limited. Therefore, a fixed angle of $\eta_\mathrm{F} = 30\,\mathrm{deg}$ is used for the preliminary investigation, aligning with [101] where the range is estimated to be between 30 deg and 40 deg.

Following the flowchart in Fig. 3.3, a further setup step involves specifying the geometric sections for the slat, the spoiler, and the flap. The procedure below for sectioning high-lift elements is based on [58] and is expanded to include custom definitions as well as slats and spoilers. Only a few points are defined in order to describe the entire contour, for a detailed description, refer to [105]. In essence, the respective shape of the control surfaces slat, spoiler, and flap are defined by Bézier curves and specified points as shown in Fig. B.4 in the appendix. While the slat and spoiler chord lengths remain unchanged in this approach, the flap chord may be optimized in a later step, but is initially set to 25 % of the clean airfoil chord.

II. Optimization of the landing configuration

The main optimization process begins with the landing configuration, which provides the starting point for the takeoff configuration by subsequently establishing the flap kinematics. As takeoff and landing configuration differ significantly, both cases are considered separately. The landing

---

[*] Note that this airfoil corresponds to the F15-12 airfoil of the CeRAS CSR-01 aircraft. The airfoil data are available on the CeRAS website. Further information can be found in [95].

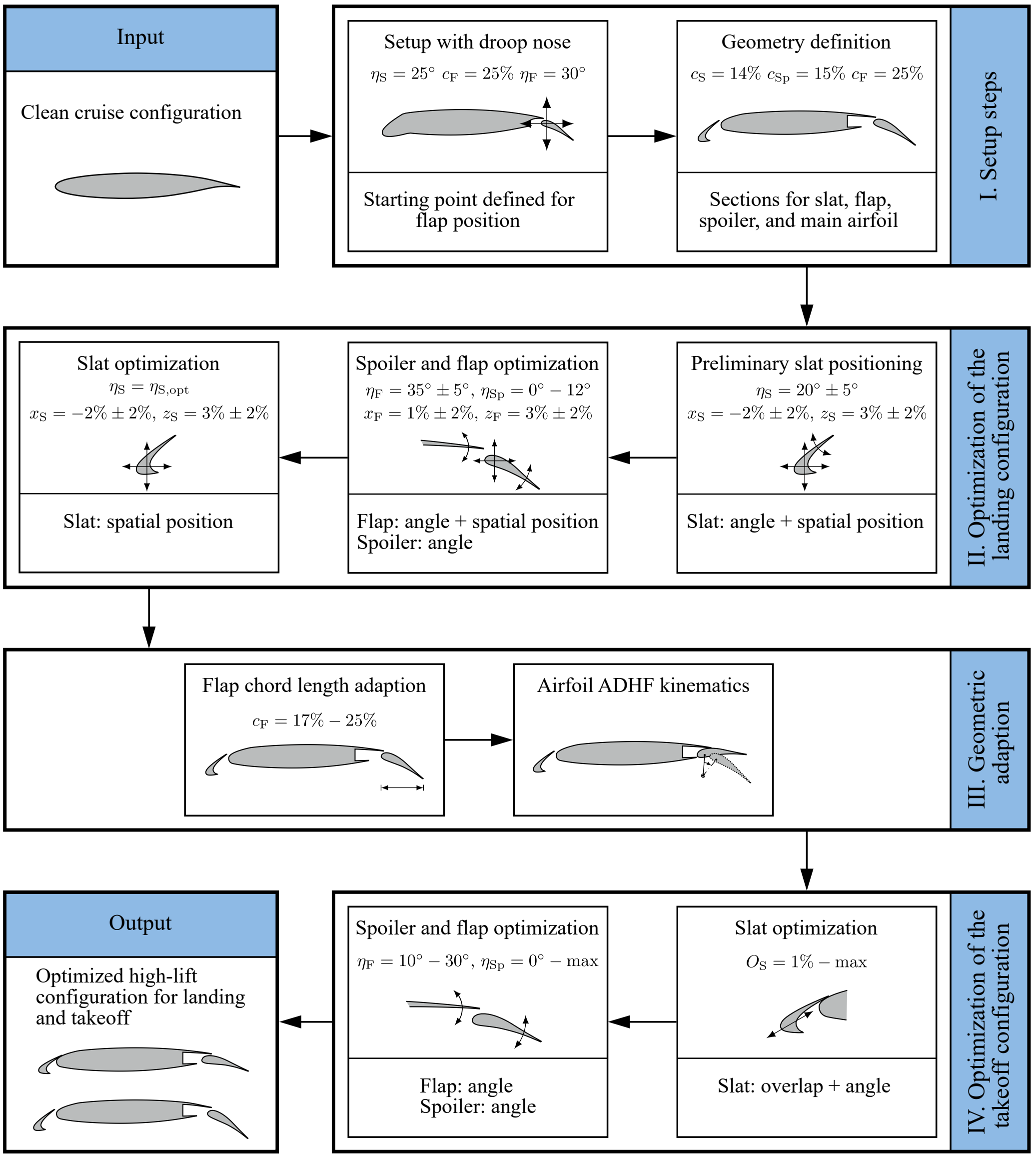

Figure 3.3: Flowchart for the introduced methodology for high-lift airfoil configuration setup in preliminary aircraft design, modified from [105]. Note: specific chord lengths in relation to clean chord c.

configuration is examined first, as this exhibits the highest flap angles [132]. In this case, the optimization procedure in accordance with [66], extended by the spoiler, is applied.

Preliminary slat positioning (landing) Initially, the slat is analyzed for three angles, $\eta_S = 15\,\text{deg}$, $20\,\text{deg}$, and $25\,\text{deg}$, with the flap setting as derived from the setup investigations. For each slat angle, a spatial position optimization is carried out. This preliminary examination of the slat is intended to identify the positioning for the highest possible angle of attack. As described in Section 2.1, the task of the slat is not directly to maximize the lift coefficient, but to enable the highest possible angle of attack.

The in-depth analysis for the preliminary slat positioning in the landing configuration of the case study airfoil from Fig. 3.2 is given in the Appendix B.1.1. In summary, the optimum position for the different slat angles at $\alpha = 16\,\text{deg}$ is initially determined, as shown in Fig. B.2. The results discussed in the appendix are based on the theoretical foundations of high-lift systems outlined in Section 2.1. Subsequently, angle of attack polars are calculated based on these determined positions. It is particularly relevant to identify the η_S that enables the highest angle of attack range, i.e. $\eta_\text{S} = 25\,\text{deg}$ in the shown case study.

As Fig. B.2(c) indicates, the optimum range for positioning the slat at $\eta_\text{S} = 25\,\text{deg}$ is relatively narrow. In order to demonstrate the effect of deviations from the optimum a brief investigation is conducted in the following.

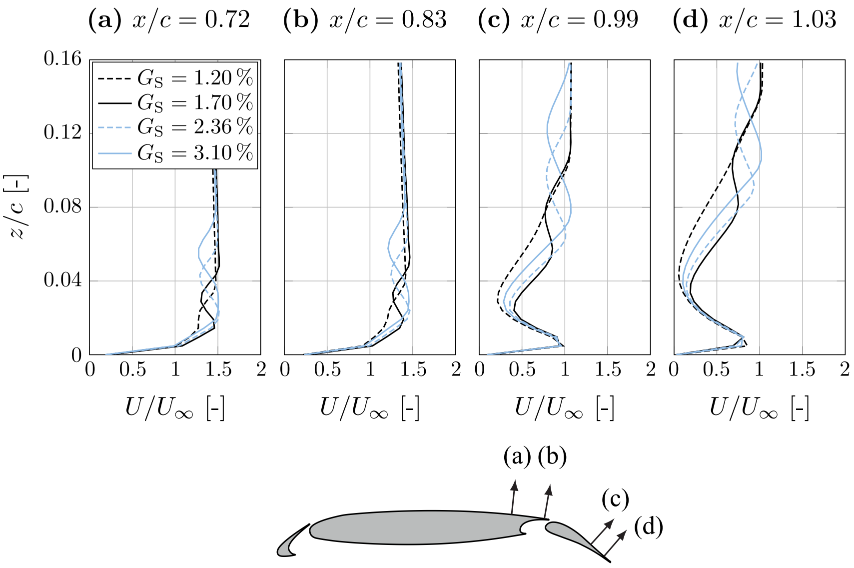

Figure 3.4: Velocity profiles for different slat gaps at a constant overlap $O_\text{S} = -1\,\%$ with $\eta_\text{S} = 25\,\text{deg}$ and $\alpha = 16\,\text{deg}$, modified from [105].

For this investigation, the identified optimal gap of $G = 1.7\,\%$, see Fig. B.2(d), is preset and subsequently increased and decreased. Figure 3.4 shows four distinct positions on the upper side of the airfoil at an angle of attack of $\alpha = 16\,\text{deg}$. Position b), located at the tip of the spoiler, indicates that for smaller slat gaps, such as $G = 1.2\,\%$, the mixing of the boundary layer and the wake leads to significantly thickened velocity profiles This thickening is evident from the lack of a clear separation between the boundary layer and the wake, as detailed in Fig. 2.11, resulting in a risk of flow separation. Conversely, for larger gaps, it can be seen that the wake of the slat and the boundary layer of the airfoil are still clearly separated, i.e. the gap is unnecessarily large, referring to the high-lift effects detailed in Section 2.1.2. In summary, the preliminary slat positioning for the landing configuration identified a slat angle of $\eta_\text{S} = 25\,\text{deg}$ at an positioning of $[x/c,\, z/c] = (-1\%,\, 2\%)$, resulting in a gap of $G_\text{S} = 1.7\%$ and an overlap of $O_\text{S} = 1\%$.

Spoiler and flap optimization (landing) A two-step process is used to determine the design of the trailing edge with spoiler and flap. In the first step, the spoiler angle is defined and subsequently, in the second step, the positioning of the flap is evaluated by means of a target function.

To determine the spoiler angle in the first step, a parameter combination of the three angles is used: the spoiler angle, the flap angle, and the angle of attack. The ranges of the angles are listed in Table 3.1. In the first step, the spatial positioning of the flap in relation to the spoiler remains as preset in the setup analysis. The combinations are evaluated in Fig. 3.5 for $\alpha = 16\,\text{deg}$. Note that the depicted angle of attack range is wider and the step size is smaller than the values listed in Table 3.1 in order to provide more detailed information, especially for high flap angles. The flap angles are plotted on the x-axis and the family of curves represents the different spoiler settings. Relevant for the choice of spoiler angle is, in addition to achieving a high lift coefficient, that stalling does not occur. Thus, taking into account all angles of attack, the spoiler angle of $\eta_{\text{Sp}} = 6\,\text{deg}$ is selected for this study case.

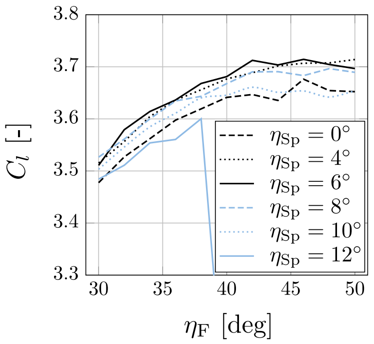

Figure 3.5: Impact of the spoiler angle on the performance of the flap at $\alpha = 16\,\text{deg}$, modified from [105].

Table 3.1: Parameter range for spoiler angle study.

Parameter	Unit	Values
Spoiler	[deg]	$0 - 12,\ \Delta = 2$
Flap	[deg]	$30 - 40,\ \Delta = 5$
Angle of attack	[deg]	8, 16

After determining the spoiler angle, the second step addresses the positioning of the flap. Since a high-lift configuration does not only have to perform for one particular combination of slat, spoiler, flap and angle of attack, but rather has to perform in other scenarios as well, a target function is introduced to take this demand into account. Based on [133], high lift coefficients are required for slow landing speeds as well as an attached flow in the entire flight regime. Note that noise emissions are not addressed in this method. Therefore, the target function $\mathbf{F}(x)$ regarding the landing configuration is established and used in this thesis:

$$\mathbf{F}(x) = 0.5 \cdot C_l|_{\alpha=0\,\text{deg}} + 0.5 \cdot C_l|_{\alpha=16\,\text{deg}} \rightarrow \text{max.} \tag{3.1}$$

Thus, the target function $\mathbf{F}(x)$ assigns equal weights to the lift coefficients at angles of attack of $0\,\text{deg}$ and $16\,\text{deg}$. However, because the lift coefficient at $\alpha = 16\,\text{deg}$ is significantly higher, it has a greater influence on the maximization of $\mathbf{F}(x)$. In the following, the flap angle is examined for 30 deg, 35 deg,and 40 deg; for each setting, the spatial positioning is determined using the Cartesian grid. The contour plots in Fig. 3.6 represent the target function from Eq. (3.1); note that both $\alpha = 0$ deg and $\alpha = 16$ deg are included. The red dot indicates the specific CFD simulation employing a particular x_F-z_F combination on the Cartesian grid where the optimal value are obtained. Furthermore, the conversion of the Cartesian positioning of the flap at 35 deg into the gap is provided.

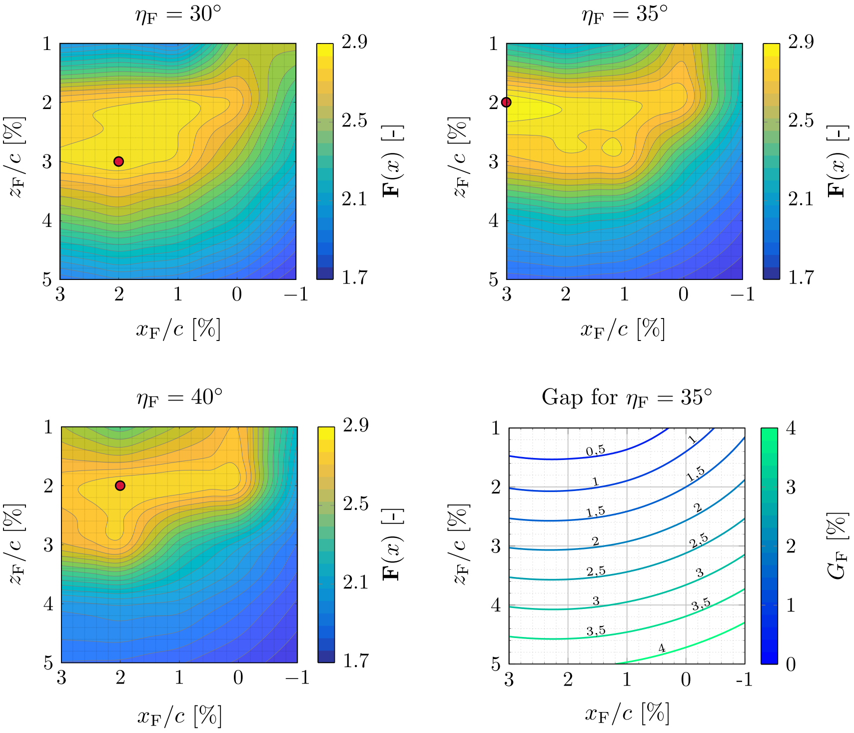

Figure 3.6: Evaluation of the target function $\mathbf{F}(x)$ for flap optimization at different flap deflection angles, including a transformation of the Cartesian coordinates to a gap value for $\eta_F = 35$ deg, adapted from [105].

A slight tendency towards smaller gaps for increasing flap angles is observed, but in general there are no major deviations from the optimum positioning for the different flap angles. Table 3.2 shows the values of the maximum achieved values of the target function $\mathbf{F}(x)$ together with the associated gaps and overlaps. This shows that the highest value of the target function is achieved for the flap angle of $\eta_F = 35$ deg.

Table 3.2: Overlap and gap settings of the respective flap angles for a maximized $\mathbf{F}(x)$ value.

η_F [deg]	G_F [%]	O_F [%]	$\mathbf{F}(x)_{\max}$ [-]
30	1.74	2.15	2.857
35	0.98	3.20	2.920
40	1.12	2.25	2.827

Figure 3.7 shows the angle of attack polar of the different flap angles. Thereby it is apparent that the flap angle of 40 deg is the lowest evaluated in terms of $\mathbf{F}(x)$, since flow separation occurs in the low angle of attack range. This characteristic is due to the thickened boundary layer

and wake at higher angles of attack that can lead to a dampening effect and thus an attached flow. However, this context is also dependent on the Reynolds number and was discussed in Section 2.1.2.

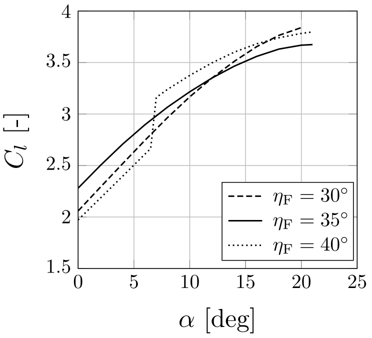

Figure 3.7: Angle of attack polars at different flap deflection angles with optimized positioning in each case, modified from [105].

In the following, the specified flap angle of $\eta_F = 35$ deg is discussed in more detail. Figure 3.8 shows the evaluations of the two angles of attack $\alpha = 0$ deg and $\alpha = 16$ deg used in $\mathbf{F}(x)$ for the spatial positioning of the flap. As this demonstrates, it is important to evaluate the relevant angles of attack in combination in the target function, as there are significant differences for optimal flap positioning. In the case study shown, a considerably larger overlap is required for low angles of attack, to achieve an attached flow.

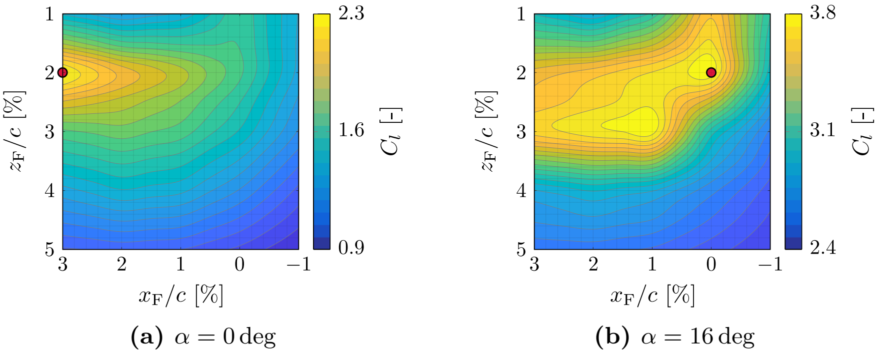

(a) $\alpha = 0$ deg **(b)** $\alpha = 16$ deg

Figure 3.8: Evaluation of the lift coefficient for the optimized flap at $\eta_F = 35$ deg, adapted from [105].

At higher angles of attack, the damping effect is stronger and allows a different spatial flap positioning. This gives the target function the crucial task of identifying a trade-off between the included cases. As Fig. 3.8 shows, there is only a narrow range for the optimum position for $\alpha = 0$ deg in the case study, but a larger range for $\alpha = 16$ deg. This evaluation confirms the increased risk of the flow separation at lower angles of attack. This relationship is also made obvious in Fig. 3.9, which shows that the positioning optimized for $\alpha = 16$ deg is only able to perform well for very high angles of attack but drops sharply between 13 deg and 14 deg. With the target function $\mathbf{F}(x)$, the solid curve is identified as optimal. This positioning corresponds to a gap of $G_F = 0.98\%$ with an overlap of $O_F = 3.2\%$. Based on the target function $\mathbf{F}(x)$, this positioning achieves the best results and the flow on the flap is attached over the entire angle of attack range.

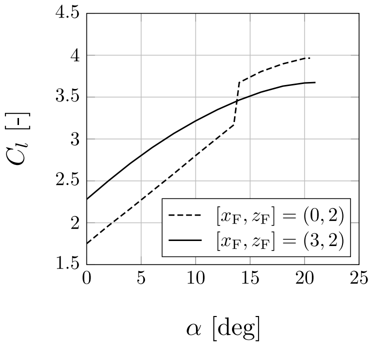

Figure 3.9: Angle of attack polars for $\eta_\mathrm{F} = 35\,\mathrm{deg}$ with the flap positionings optimized for $\alpha = 0\,\mathrm{deg}$ (straight line) and $\alpha = 16\,\mathrm{deg}$ (dashed line) from Fig. 3.8, modified from [105].

Slat optimization (landing) The final step for the landing configuration is the optimization of the slat, as shown in the flowchart in Fig. 3.3. This procedure ensures that any changes after the first slat positioning due to the lowering of the spoiler or the repositioning of the flap are also taken into account. The slat angle η_S remains as determined in the first step, based on the assumption that the setup steps have established a realistic flap configuration, allowing the slat angle to be set accordingly. This approach follows an iterative design methodology. Although iterating this process multiple times would enhance accuracy, it would significantly increase computational time. The results are shown in Fig. 3.10 with the established contour plot for the target function $\mathbf{F}(x)$. In this case study, the position of the optimum remains unchanged, thus completing the optimization of the landing configuration. The transformed Cartesian coordinates at $[x_\mathrm{S}/c,\, z_\mathrm{S}/c] = (-1\%,\, 2\%)$ result in a gap of $G_\mathrm{S} = 1.7\,\%$ and an overlap of $O_\mathrm{S} = -1\,\%$.

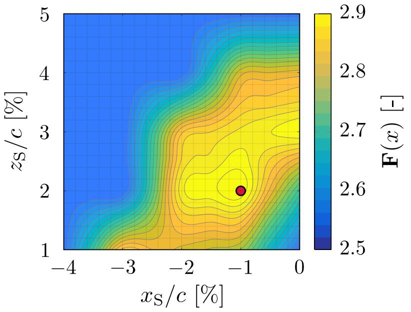

Figure 3.10: Second slat optimization: Evaluation of the slat positioning with regard to the target function $\mathbf{F}(x)$ at $\eta_\mathrm{S} = 25\,\mathrm{deg}$, adapted from [105].

III. Geometric adaption

After optimizing the high-lift elements for the landing configuration, two steps follow before the takeoff configuration is optimized. First, the flap chord length is adapted, followed by the definition of the hinge point for the ADHF kinematics.

Flap chord length The initially assumed flap chord length of 25 % represents a conservative estimate for an ADHF [117]. In order to avoid designing an unjustifiably large flap chord and thus impose unnecessary demands on the structure and integration, an investigation is carried out to determine the chord length that is actually required. For this purpose, first of all the required maximum lift of the aircraft is needed, which needs to be estimated at this stage of the preliminary design. In order to convert the value of the aircraft to an airfoil, the conversion according to [124] may be used, for example. The specified parameters—the spoiler angle, as well as the gap and overlap for flap and slat respectively—are kept fixed, only the flap chord is gradually varied. The aim is to achieve the required lift coefficient, including a safety margin [132].

Airfoil ADHF kinematics Based on [132], the landing configuration described above is optimized before the takeoff configuration. The determined flap position, together with the retracted position of the flap, defines two points of the kinematics. For this study, a simple dropped hinge kinematics is assumed, in which the flap rotates around a hinge located under the airfoil. A particular characteristic of this kinematics is that the position of the hinge is explicitly defined by the two positions. Due to the fixed kinematics, it is not possible to optimize the takeoff configuration with the same method as for the landing configuration. The flap movement follows the predefined circular path. The gap is adjusted by moving of the spoiler [91]. The overlap, however, cannot be set independently for the takeoff configuration and inevitably results from the combination of the flap and spoiler angles. Due to this reduction in parameters, the number of simulations for the takeoff configuration is decreased.

IV. Optimization of the takeoff configuration

The takeoff configuration is optimized subsequently, as shown in the flowchart in Fig. 3.3, first at the leading edge and then at the trailing edge. The specifications defined for the landing configuration are taken into account. Since high climb rates are required for takeoff, a low drag is important in addition to a high lift. This is expressed by the target function $\mathbf{H}(x)$ in Eq. (3.2), derived from [133].

$$\mathbf{H}(x) = \left.\frac{C_l^3}{C_d^2}\right|_{\alpha=10\,\mathrm{deg}} \rightarrow \max \tag{3.2}$$

Note that the target function for the takeoff configuration $\mathbf{H}(x)$ uses an angle of attack of $\alpha = 10\,\mathrm{deg}$. While WILD [133] originally uses angles of 8 deg and 11.91 deg, the rounded average of 10 deg is selected to reduce computational time [105].

Slat optimization (takeoff) To provide a low drag for the takeoff, the gap between the slat and the main airfoil is sealed in the takeoff configuration, based on [117]. Furthermore, the angle of the slat is set to be tangential to the main airfoil. This eliminates the gap as design parameter of the slat in the takeoff configuration. Furthermore, the slat angle and the overlap are directly linked to each other, as shown in Fig. 3.11 for the case study.

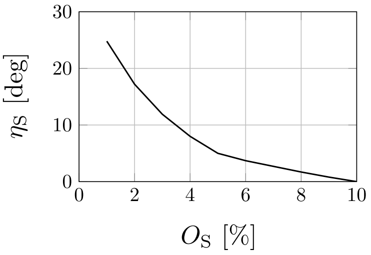

Figure 3.11: Geometric dependence of η_S in the takeoff configuration with respect to O_S, modified from [105].

For the following study, the overlap is used as the only parameter for variation, analyzed at values between 1 % and 10 % in steps of 1 % whereby, as shown in Fig. 3.11, 1 % overlap corresponds to a slat angle of 25 deg. An overlap of 10 %, on the other hand, corresponds to a fully retracted slat. As stated above, the mutual interactions of leading and trailing edge devices are crucial and the flap is usually less extended in the takeoff position than in the landing configuration. However, according to the procedure shown in Fig. 3.3, the flap has not yet been repositioned for takeoff. In order to compensate for this, a temporary flap angle of $\eta_F = 20\,\mathrm{deg}$ is assumed in accordance to [101].

In Fig. 3.12, the influence of slat overlap, O_S, on aerodynamic performance, expressed as C_l^3/C_d^2, is evaluated. The left plot presents the aerodynamic performance for a fixed angle of attack of $\alpha = 10\,\mathrm{deg}$, corresponding to $\mathbf{H}(x)$ according to Eq. (3.2). $\mathbf{H}(x)$ is plotted against the overlap O_S. As the overlap increases from 0 % to 10 %, the performance decreases significantly. The right plot focuses on three specific overlap values: 1 %, 5 %, and 10 %. For these overlaps, the aerodynamic performance C_l^3/C_d^2 is analyzed across a range of angles of attack. The curves show that the performance varies with α, peaking at different values depending on the overlap. The arrows connect the two plots, indicating that the value of $\mathbf{H}(x)$ at $\alpha = 10\,\mathrm{deg}$ in the left plot can be identified in the right plot for each respective overlap value. The evaluation in Fig. 3.12 indicates that the highest values of the target function $\mathbf{H}(x)$ are achieved for the case study with small overlaps.

The shift in the curves and their respective maxima is shown, demonstrating that the selection of the angle of attack in the target function can be decisive. The corresponding pressure curves

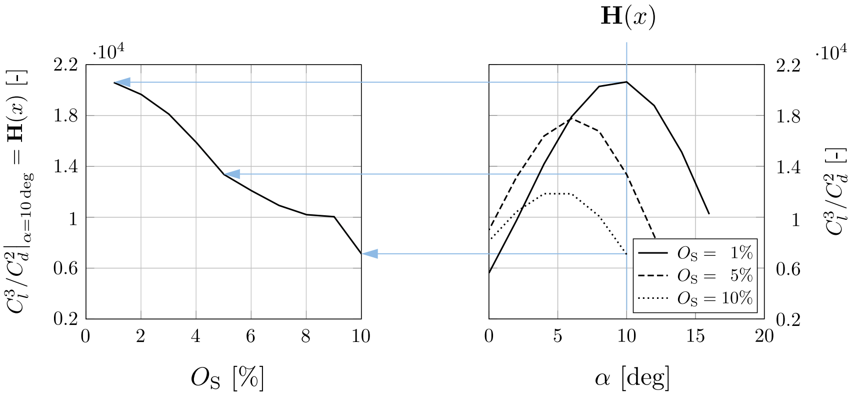

Figure 3.12: Evaluation for C_l^3/C_d^2. Left: with regard to the overlap at $\alpha = 10\,\text{deg}$, thus corresponding to the target function $\mathbf{H}(x)$, see Eq. (3.2). Right: with regard to a range of α, modified from [105].

over the airfoil are given in Fig. 3.13 for $\alpha = 10\,\text{deg}$ and give an insight on the characteristics shown in Fig. 3.12. While the flow is attached over the whole airfoil in all three examples, the overlap of 1 %, resulting in the highest deflection angle of the slat, reduces the suction peak the most, enabling the highest angles of attack. This effect gradually diminishes with decreasing slat angles, corresponding to increasing overlaps, until the slat is completely retracted at an overlap of 10 %.

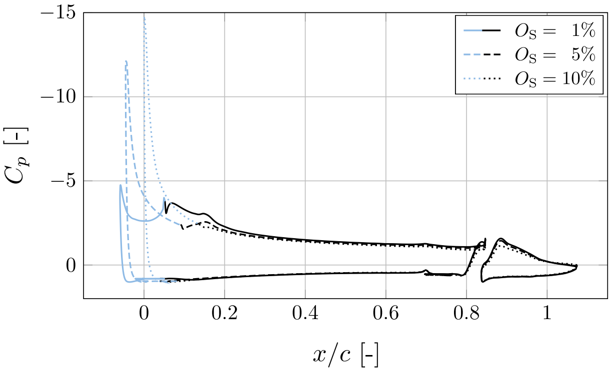

Figure 3.13: Pressure distributions for different overlaps at $\alpha = 10\,\text{deg}$, the pressure over the slat is depicted in blue, modified from [105].

Spoiler and flap optimization (takeoff) Due to the previously defined flap kinematics and the fixed hinge point, the flap movement is restricted to a circular path. According to [101], the optimum flap angle for a high L/D is in the range of $\eta_\text{F} = 10\,\text{deg}$ to $20\,\text{deg}$. To explore the potential for further optimization beyond this range, the following study examines flap angles from $\eta_\text{F} = 10\,\text{deg}$ to $30\,\text{deg}$. The gap is set by adjusting the spoiler. The overlap cannot be set independently, but results from the angles of the spoiler and the flap. Figure 3.14 shows on the left side the plots for different spoiler angles of the case study with η_F on the x-axis and $\mathbf{H}(x)$ on the y-axis. The spoiler angle of $\eta_\text{Sp} = 6\,\text{deg}$ is excluded from further considerations due to its poor performance. For the other spoiler angles, the combination with the corresponding flap angle for maximum $\mathbf{H}(x)$ is identified. For each combination, an angle of attack polar is calculated, as shown in Fig. 3.14 on the right side. Since the combination of $\eta_{\mathrm{Sp}} = 2\,\mathrm{deg}$ and $\eta_{\mathrm{F}} = 20\,\mathrm{deg}$ exhibits no considerable downsides such as flow separation for lower angles of attack, this combination is chosen in the case study.

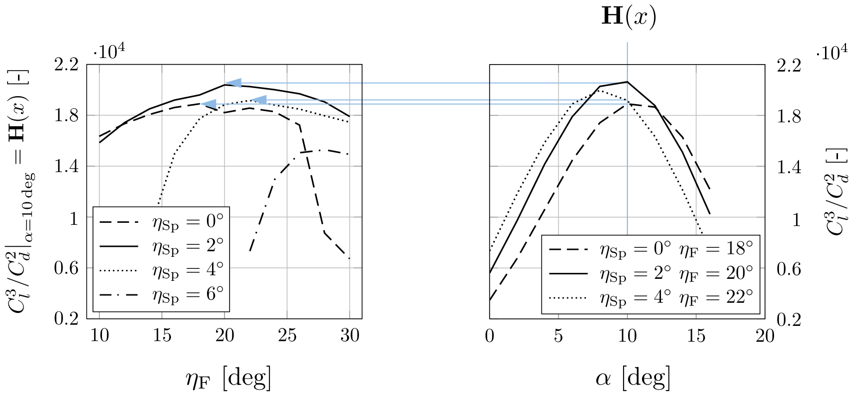

Figure 3.14: Trailing edge optimization. Left: target function $\mathbf{H}(x)$ over η_{F} for different η_{Sp} at $\alpha = 10°$. Right: C_l^3/C_d^2 evaluation for specific η_{F}-η_{Sp} combinations, modified from [105].

Based on these evaluations, the optimum for takeoff positioning is identified. Thus, all parameters in the focus of optimization for the case study airfoil from Fig. 3.2, are determined, the results of the case study are given in Table 3.3.

Table 3.3: Geometry parameters of the optimized case study.

Configuration	η_S [deg]	G_{S} [%]	O_{S} [%]	η_{Sp} [deg]	η_{F} [deg]	G_{F} [%]	O_{F} [%]
Landing	25	1.70	−1.00	6	35	0.98	3.20
Takeoff	25	-	1.00	2	20	0.95	5.97

This step concluded the process as shown in Fig. 3.3, where the optimization process is displayed in full for the case study. Using this process, three methodologies with different accuracy and computational requirements are derived in the following chapter.

3.1.2 Establishment and analysis of three methodologies of varying fidelity

In the Section 3.1.1, a detailed evaluation demonstrated the iterative approach to optimize the high-lift elements configuration on airfoils. Building upon this foundation, visualized in the flowchart in Fig. 3.3, this section derives three methodologies. These methodologies allow for a case-dependent selection of the appropriate level of accuracy and computational effort.

A) The first methodology closely aligns with the process presented in Section 3.1.1 and depicted in Fig. 3.3, with adjustments made to the bounds of parameter variation. This methodology requires the highest computational resources but provides the best accuracy. It is employed to create a database of optimized high-lift configurations for the airfoils in Fig. B.1, which serves as the foundation for developing design guidelines.

B) The second methodology combines the design guidelines established by the first methodology with parameter variations by conducting CFD simulations. This approach reduces the parameter space and, consequently, the computational resources required. By applying these guidelines and performing targeted simulations, it achieves a balance between accuracy and efficiency.

C) In the third and final methodology, the high-lift elements are determined solely based on the design guidelines without further computational optimization. This methodology is particularly suitable for integration into an iterative preliminary aircraft design process, where computational resources are limited. A CFD simulation may be conducted to obtain the data of the designed geometry for landing, or respectively, takeoff.

It should be mentioned once again that a full parameter study of all theoretically possible angles and positionings of the high-lift elements would require an unfeasible high computational effort for the preliminary design. With the three following methodologies, a case-dependent selection may be made regarding the appropriate level of accuracy and computing time.

A) Optimized High Resolution Parameter Space Methodology

As mentioned above, this methodology covers the largest parameter space and therefore provides the highest degree of accuracy. However, as stated in Section 3.1.1, not every possibility for angle and spatial positioning of the high-lift elements can be simulated in a full parametric study. A brief consideration is given for this purpose: a parameter resolution accuracy for the flap angle of 0 deg to 45 deg in 5 deg steps is assumed, which results in 10 different settings. The same number of settings is assumed for the flap and spoiler. The positioning of the slat and the flap is done on a 5x5 grid, the flap chord is varied in 4 steps. This approach even neglects a variation of the slat chord, the spoiler chord and possible finer grid resolutions. Nevertheless, the total number of simulations required for the landing configuration alone amounts for a full parametric approach to $10^3 \cdot (5x5)^2 \cdot 4 = 2\,500\,000$. Even if the parameter limits are narrowed down and thus the simulations are reduced, this does not result in a feasible number. In order to demonstrate this, the slat, flap, and spoiler angle steps are reduced to 4 instead of 10, as the range can be estimated reasonably well from empirical data. However, this would still result in an overall number of 160 000 simulations. These numbers provide the motivation for the process shown in Section 3.1.1 with the stated assumptions and incremental positioning, instead of a full parameter approach.

While in Section 3.1.1 some parameter spaces, such as the spoiler angle, cover a rather large range for demonstration purposes, this range is restricted for the final methodology. Table 3.4 outlines the parameter optimization process for methodology A), with the process reading from left to right. Each column represents a step in the optimization workflow. This table for methodology A) closely follows the flowchart presented in Fig. 3.3, but includes specific spaces for parameter variation. The initial steps lead to the defined landing configuration, and the process then continues to define the takeoff configuration. The blue boxes indicate that the enclosed parameters are optimized within the defined parameter ranges. A blue arrow means that the optimized values from the immediately preceding step are used, while a black arrow shows that values from an earlier step are carried forward. Note that the spatial positioning as described at the beginning of the chapter is usually kept in Cartesian coordinates for reasons of straightforward variation. In some cases, however, a gap or overlap is specified, indicated by a black frame; as described above, they correspond implicitly to Cartesian coordinates. The spatial resolution for positioning is 0.5 %, a brief study in this respect is given below.

Table 3.4: Parameter optimization process: methodology A).

Parameter		Unit	Process step number 1	2	3	4		5	6	
Slat	η_S	[deg]	15 – 25	→	→	→	Landing conf. defined	$f(O_S, G_S, \text{tang})$	→	Takeoff conf. defined
	x_S	[%]	-0.5 – 2.5	→	-0.5 – 2.5	→		$f(O_S, G_S = 0)$	→	
	z_S	[%]	1.0 – 3.0	→	1.0 – 3.0	→		$O_S[1-10]$	→	
	c_S	[%]	14	→	→	→		→	→	
Spoiler	η_{Sp}	[deg]	0	6 – 12	→	→		→	0 – 6	
	c_{Sp}	[%]	15	→	→	→		→	→	
Flap	η_F	[deg]	30	30 – 40	→	→		20	10 – 30	
	x_F	[%]	$f(O_F, G_F)$	-0.5 – 2.0	→	→		$f(\eta_F, \text{kinematic})$	$f(\eta_F, \text{kinematic})$	
	z_F	[%]	$f(1, 1.65)$	1.0 – 3.0	→	→				
	c_F	[%]	25	→	→	17 – 25		→	→	
Target function			$\mathbf{F}(x)$					$\mathbf{H}(x)$		

Parameter optimizing

Implicit geometry definition

→ Previous value

→ Optimized value

This procedure is used to optimize the configurations of nine airfoils, selected for their different characteristics and geometries, as depicted in Fig. B.1 in the appendix and detailed in Table B.1. Figure 3.15 shows the resulting L/D polars for the individually optimized landing and takeoff configuration. These data are used to derive guidelines for the following methodologies in order to further narrow down the parameter space.

B) Reduced Parameter Methodology

The *Reduced Parameter Methodology* involves a number of simplifications as design guidelines derived from methodology A). On the one hand, the application of the design guidelines result in restricted parameter spaces. On the other hand, gap or overlap are partially prespecified, which is in contrast to the Cartesian specification of the spatial positioning. However, as explained above, gap and overlap are the aerodynamically relevant parameters and can thus be effectively incorporated into design guidelines; therefore, they are primarily used in this methodology.

Table 3.5 shows the individual steps in the same format as for the first methodology. The first step for the landing configuration is to optimize the leading edge device. For this purpose, an overlap of $O_S = -1.0\,\%$ is set for the slat; as defined in Fig. 2.14, the slat is accordingly in front of the main airfoil. The slat is then shifted vertically for the angles 25 deg and 30 deg. With the

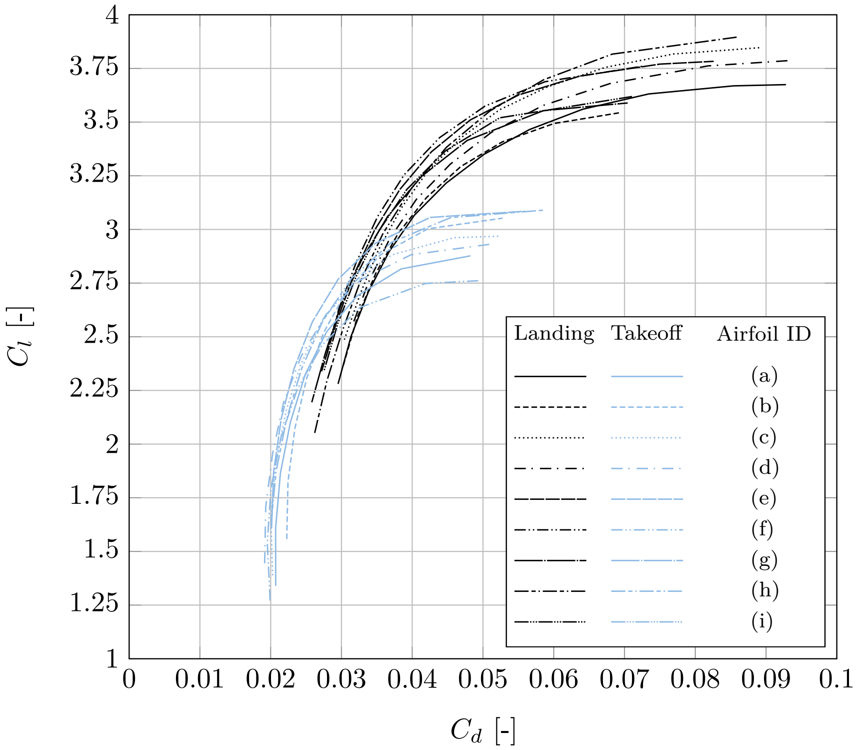

Figure 3.15: Polars in landing and takeoff configuration of selected airfoils for high-lift geometries optimized with methodology A), modified from [105].

optimum position determined, the second step for the landing configuration is carried out with the trailing edge device as the subject to optimization. The spoiler angle is varied over a range of 6 deg − 12 deg. The overlap is optimized for flap angles of 35 deg and 40 deg and a gap of $G_{\mathrm{F}} = 1.65\,\%$. With the optimization completed, the landing configuration and thus the trailing edge kinematics are finalized. The final step consists of optimizing the takeoff configuration. At the leading edge, the condition of a gapless configuration and a tangential contact of the slat with the main airfoil is set. Together with a varied slat angle of 20 deg, 25 deg, and 30 deg, this tangential contact condition determines the overlap. Regarding the trailing edge, the spoiler deflection angle is set to between 3 deg and 5 deg, the flap deflection angle is set to 20 deg. The gap and overlap are not free parameters, but are determined by the above settings and the already defined hinge point.

The optimization is completed by this step according to this abbreviated method. The results are discussed below together with all three methodologies.

C) Data-Driven Prediction Methodology

This approach is particularly suitable in cases where no capacity is available for multiple CFD simulations or where preliminary considerations need to be made in the shortest possible time. One potential application is the iterative preliminary overall aircraft design. For this so-called *Data-Driven Prediction Methodology*, the geometric data of the high-lift elements are deter-

Table 3.5: Parameter optimization process: methodology B).

Parameter		Unit	Process step number 1	2		3	
Slat	η_S	[deg]	25 – 30	→	Landing conf. defined	20 – 30	Takeoff conf. defined
	x_S	[%]	$f(O_\mathrm{S}=\text{-}1.0)$	→		$f(\text{tang}, \eta_S$ $\ldots G_\mathrm{S}=0)$	
	z_S	[%]	1.0 – 3.0	→			
	c_S	[%]	14	→		→	
Spoiler	η_Sp	[deg]	0	6 – 12		2 – 6	
	c_Sp	[%]	15	→		→	
Flap	η_F	[deg]	30	35 – 40		20	
	x_F	[%]	$f(O_\mathrm{F},G_\mathrm{F})$	$f(O_\mathrm{F},G_\mathrm{F})$		$f(\eta_\mathrm{F},\text{kinematic})$	
	z_F	[%]	$f(1, 1.65)$	$f(\text{-}0.5-2,\ 1.3-1.7)$			
	c_F	[%]	25	→		→	
Target function			$\mathbf{F}(x)$			$\mathbf{H}(x)$	

mined on the basis of derived design guidelines from methodology A). This methodology does not require a CFD simulation. Accordingly, no optimization is provided in Table 3.6 for this methodology. However, CFD simulations can be carried out to determine the aerodynamic data of the airfoils in the landing and takeoff configuration.

The previous studies conducted with the *Optimized High Resolution Parameter Space Methodology* in Table 3.4 indicated that a range for slat and flap angles and gaps can be estimated for landing and takeoff configuration. This indication is already applied for the *Reduced Parameter Methodology* in Table 3.5. The spoiler, however, is subject to greater variation; in particular, a dependency on the airfoil's thickness ratio t/c is identified. In this methodology, an approach is adopted wherein the spoiler angle for the landing configuration is determined using a regression curve. For this purpose, at a constant flap angle of $\eta_\mathrm{F} = 35\,\mathrm{deg}$ and the optimal flap positioning for each airfoil as determined with methodology A), the maximum spoiler angle $\eta_\mathrm{Sp,max}$ at which flow separation occurs at the spoiler is investigated. This maximum spoiler angle is plotted against the airfoil thickness t/c in Fig. 3.16 for the nine airfoils from Fig. B.1. Note that the physical relationships, as illustrated in Sections 2.1.2 and 3.1.1, are significantly more complex, but for this methodology, estimates need to be derived.

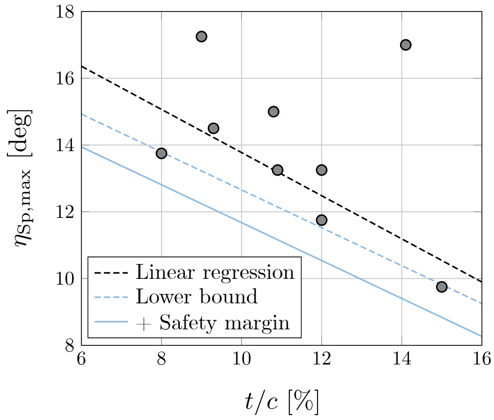

Figure 3.16: Representation of the curve for empirical determination of the maximum spoiler angle, adapted from [105].

A lower boundary curve is determined from these results in order to provide a conservative estimate. In addition, a safety margin Δ_{Sp} is maintained via a parallel shift, assuming that the flow might separate for higher spoiler angles, resulting in Eq. (3.3) for an assumption of the spoiler angle in the landing configuration.

$$\eta_{\mathrm{Sp}} = -56.8\,\mathrm{deg} \cdot t/c + 18.372\,\mathrm{deg} - \Delta_{\mathrm{Sp}} \tag{3.3}$$

In the following, $\Delta_{\mathrm{Sp}} = 1\,\mathrm{deg}$ is assumed, corresponding to the curve plotted in Fig. 3.16. The spatial positioning of the elements results from the preset gap or overlap. All specifications are given in Table 3.6.

Table 3.6: Parameter settings: methodology C).

			Process step number			
Parameter		Unit	1		2	
Slat	η_{S}	[deg]	25	Landing conf. defined	$f(O_{\mathrm{S}},\, G_{\mathrm{S}},\, \mathrm{tang})$ $O_{\mathrm{S}} = 1,\, G_{\mathrm{S}} = 0$	Takeoff conf. defined
	x_{S}	[%]	$f(O_{\mathrm{S}}, G_{\mathrm{S}})$ $f(\text{-}1.5, 2.2)$			
	z_{S}	[%]				
	c_{S}	[%]	14		→	
Spoiler	η_{Sp}	[deg]	$f(t/c)$		$f(G_{\mathrm{F}})$	
	c_{Sp}	[%]	15		→	
Flap	η_{F}	[deg]	35		20	
	x_{F}	[%]	$f(O_{\mathrm{F}}, G_{\mathrm{F}})$ $f(0.15, 1.65)$		$f(O_{\mathrm{F}},\, G_{\mathrm{F}},\, \eta_{\mathrm{F}},\, \mathrm{kinematic})$ $G_{\mathrm{F}} = 1.35$	
	z_{F}	[%]				
	c_{F}	[%]	25		→	

Methodology comparison and evaluation

In the following, the three methodologies introduced will be compared by means of three exemplary airfoils with differences in thickness and camber. The examined airfoils are (b), (g), and (h) from Fig. B.1 in the appendix. All three methodologies are applied to each airfoil. For evaluation, the determined geometries parameters are compared in the Tables 3.7 - 3.9. The respective chord lengths are maintained at the default in all methodologies. Note that the angles for the slat in the start configuration are specified with one decimal place; in the application, the values would be rounded, but in this case they are intended to make it clear that the slat angle is determined implicitly from other geometry specifications during takeoff. For reasons of readability, only the methodology abbreviations A) - C) are referred to below.

Table 3.7: Application of methodologies A) - C) to reference airfoil (g).

			Airfoil configuration methodology					
			Landing			Takeoff		
Parameter		Unit	A)	B)	C)	A)	B)	C)
	η_{S}	[deg]	25	25	25	25.1	25.1	25.1
Slat	G_{S}	[%]	2.13	2.05	2.20	0.0	0.0	0.0
	O_{S}	[%]	-1.5	-1.0	-1.5	1.0	1.0	1.0
Spoiler	η_{Sp}	[deg]	12.0	12.0	12.3	5.0	4.5	4.2
	η_{F}	[deg]	35	35	35	21	20	20
Flap	G_{F}	[%]	1.61	1.30	1.65	1.20	2.75	1.35
	O_{F}	[%]	0.15	0.65	0.15	1.19	3.26	4.54

Table 3.8: Application of methodologies A) - C) to reference airfoil (b).

			Airfoil configuration methodology					
			Landing			Takeoff		
Parameter		Unit	A)	B)	C)	A)	B)	C)
	η_{S}	[deg]	25	25	25	29.7	29.7	29.7
Slat	G_{S}	[%]	2.20	2.06	2.20	0.0	0.0	0.0
	O_{S}	[%]	-1.5	-1.0	-1.5	1.0	1.0	1.0
Spoiler	η_{Sp}	[deg]	9.0	9.0	8.9	3.0	2.5	0.4
	η_{F}	[deg]	35	35	35	23	20	20
Flap	G_{F}	[%]	1.33	1.30	1.65	1.59	1.40	1.35
	O_{F}	[%]	3.42	3.42	0.15	5.66	6.20	4.59

Table 3.9: Application of methodologies A) - C) to reference airfoil (h).

			Airfoil configuration methodology					
			Landing			Takeoff		
Parameter		Unit	A)	B)	C)	A)	B)	C)
	η_{S}	[deg]	25	25	25	29.8	29.8	29.8
Slat	G_{S}	[%]	2.26	1.85	2.20	0.0	0.0	0.0
	O_{S}	[%]	-1.5	-1.0	-1.5	1.0	1.0	1.0
Spoiler	η_{Sp}	[deg]	12.0	12.0	9.4	8.0	5.5	0.5
	η_{F}	[deg]	35	35	35	28	20	20
Flap	G_{F}	[%]	1.69	1.30	1.65	1.55	0.93	1.35
	O_{F}	[%]	1.23	1.23	0.15	3.85	4.77	4.47

Landing configuration Despite the lower resolution of the two methodologies B) and C), the leading edge geometry for the landing configuration of all three airfoils is consistently close to that of the high-resolution methodology A). The trailing edge is also mostly well covered by the methodologies of lower accuracy; in particular, a continuous tendency has been observed for the flap angles. However, a difference arises regarding the spoiler angle using methodology C) on airfoil (h). For this airfoil, the spoiler can be deflected by up to 12 deg according to the analysis with the more sophisticated methodologies A) and B). According to the estimation in Eq. (3.3), however, with a $t/c = 14.12\,\%$, only an angle of $\eta_{\mathrm{Sp}} = 9.4\,\mathrm{deg}$ is applied. In addition, the overlap of 0.15 % with the data-driven methodology C) is significantly lower than with the CFD-based methodologies A) and B), which both identify $O_{\mathrm{S}} = 1.23\,\%$.

Takeoff configuration The leading edge of the takeoff configuration is specified similarly for all methodologies. This is due to the closed gap and the tangential transition between the slat and the main airfoil, both requirements already pre-defining a large part of the geometry. Consequently, the overlap and the slat angle are directly interdependent. Since an overlap of 1 % is identified in all methodologies, respectively is specified in methodology C), the resulting slat angles of the methodologies are thus identical.

The most significant differences between the three methodologies arise at the trailing edge of the takeoff configuration. In this case, even minor variations in the trailing edge definition of the landing configuration lead to a series of resulting effects. As described in Section 3.1.1, the flap positioning in the landing configuration defines the hinge point, meaning that the flap can not be moved independently for the takeoff. While the movement is always a rotation around the hinge point, the gap can still be readjusted by the spoiler angle. The spoiler angles therefore deviate from each other. Noteworthy is methodology C), which results in small spoiler angles for the high thickness airfoils (b) and (h) in the starting configuration.

Cascade of effects Particularly considerable are the results on the symmetrical airfoil (g) using methodology B), as this demonstrates the cascade of effects of design decisions. In this case, the slat positioning is slightly different for the landing configuration compared to methodology A). This results from the specifications for the overlap in Table 3.5, see also the related discussion above. As a consequence, a smaller gap and a larger overlap are identified at the trailing edge for methodology B) compared to methodology A). The deviating flap hinge point leads to more pronounced differences for gap and overlap at the trailing edge in the takeoff configuration. Accordingly, this is the optimum that can be achieved under the constraints of the methodology B). Since, as mentioned above, one cause lies in the pre-specification of the overlap at the leading edge for the landing configuration in Table 3.5, the question arises whether methodology B) with such a pre-specification is sufficient at all, or whether the parameter space must be extended. In order to make a statement on this, methodology B) is compared with the higher resolution methodology A) on the basis of the aerodynamic results. Figure 3.17 shows the evaluation of the polars over the landing and takeoff configuration. The variables plotted on the y-axis correspond to those used in the target functions that guide the optimization methodologies for each case. For the landing configuration, according to Eq. (3.1), the decisive parameter is the lift coefficient, averaged over angles of attack of 0 deg and 16 deg. In the takeoff configuration, as per Eq. (3.2), drag is also considered, and the value of $\mathbf{H}(x)$ at an angle of attack of 10 deg is indicated in the bottom plots.

Methodology evaluation By comparing the aerodynamic results of the two methodologies A) and B) for all three airfoils, (b), (g), and (h), only marginal deviations can be observed for the respective specified landing configuration in Fig. 3.17. This indicates that, despite the reduced

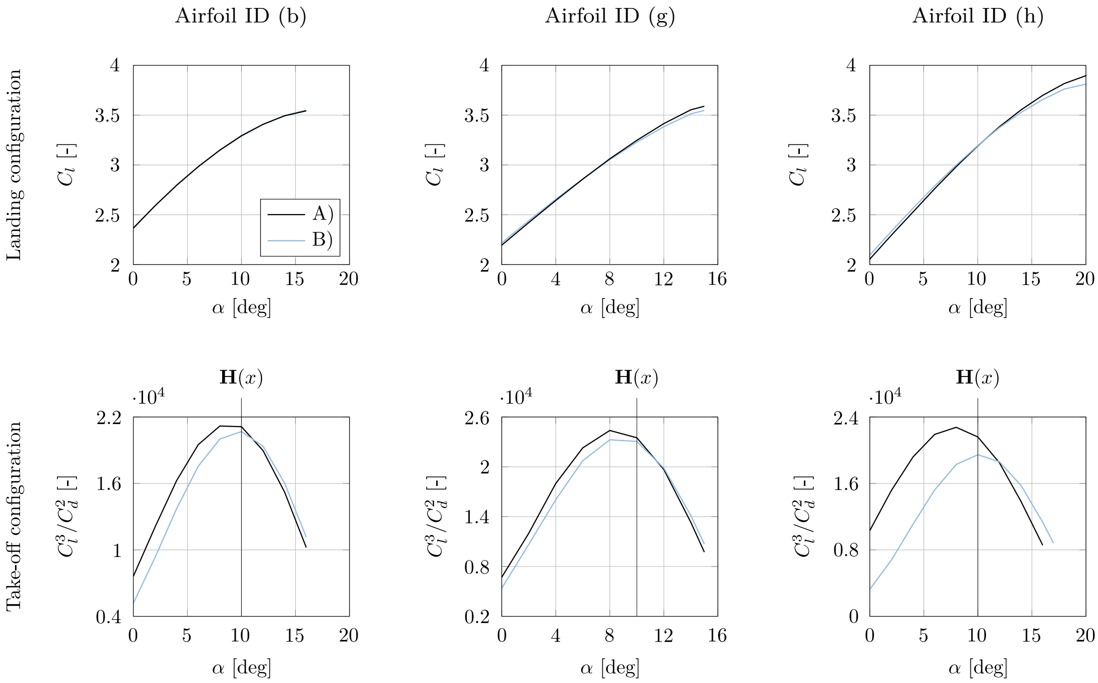

Figure 3.17: Comparing methodologies A) and B) with regard to the landing (top) and takeoff (bottom) configuration, modified from [105].

parameter space, methodology B) still has sufficient freedom to set an nearly optimal landing configuration.

A slightly different pattern emerges for the takeoff configuration. While the symmetrical airfoil (g) yields aerodynamic results for methodology B) that are close to methodology A) despite the geometric differences discussed above, the deviations for the airfoils (b) and (h) are more pronounced. In both cases it is noticeable that due to the more elaborate flap arrangement for takeoff in methodology A), the flap is deflected further than the fixed $\eta_\mathrm{F} = 20\,\mathrm{deg}$ in methodology B).

Thus, a final classification of the methodologies leads to the conclusion that methodology B) is reasonable for most cases, since the only gradually increased accuracy in methodology A) requires a considerable increase in the simulations. Methodology C) may be used to make an initial estimate but is not recommended for higher accuracy requirements because it relies solely on empirical data. Even though a broad range of airfoils was selected in Fig. B.1, optimizations based on CFD calculations—as in methodologies A) or B)—may be necessary for new airfoils.

The slat and flap settings as specified in the Tables 3.7 - 3.9 are very high compared to the settings of actual aircraft [101]. Therefore, it should be mentioned again that the geometries optimized in this thesis are airfoils and are not directly applicable to the aircraft. This is discussed in more detail in the following paragraph. Furthermore, in the detailed overall aircraft design, more parameters are involved than are included in the target functions $\mathbf{F}(x)$ and $\mathbf{H}(x)$.

Application classification and accuracy requirements

Following the above analysis of the methodologies, a few concluding words are to be given as a recommendation for application. At first, the logic behind the optimization of airfoils and the application to a wing will be discussed, as well as the spatial simulation resolution used for the above methodologies.

High-lift airfoil and wing design The typical development process for a high-lift configuration starts with the optimization of airfoils and then progresses to the wing [132]. This approach saves time and computational resources [132]. Nevertheless, the effects of cross flows on a wing have to be considered in high-lift design [132]. Therefore, it is important to carefully select these sections already for 2D investigations [132]. This careful selection allows for partial replication of flow conditions on a wing in the early design stage.

The choice of an appropriate airfoil section is based on a criterion such as the maximum wing loading. The wing loading does not refer to the lift distribution, but to the highest lift coefficient occurring along the span, where flow separation is likely to initiate first. According to Wild [132], this point is typically located at 55 % to 65 % of the wing span, although it varies depending on factors like wing planform or twist. Particular attention must be paid to the sweep and taper of the wing, as the flow reacts to a change in camber. Therefore, a geometric transformation perpendicular to the camber lines can be used for a first coarse approach; for further information and the mathematical description of the so-called local sweep transformation (LST) of the sections, refer to [132].

Spatial grid resolution Finally, a brief examination of the spatial resolution of the grid as shown in Fig. 3.1 is provided. A fine resolution requires a very high computational effort, as every possible geometric combination is simulated by means of CFD calculations. It is therefore important to consider the degree of resolution in advance.

For this purpose, the exemplary airfoil (h) is examined and evaluated in different spatial step sizes for the positioning of the high-lift elements. The step sizes for the investigation are $\Delta = 1\,\%$, 0.5 %, and 0.25 %. The graphical evaluation is shown in Fig. 3.18, where the contour maps the target function from Eq. (3.1). Note that the contour plots represent different ranges for $\mathbf{F}(x)$, which is necessary because otherwise no distinct boundaries would be recognizable in the spatial subsections that get progressively smaller from left to right. The examination of the first accuracy step size $\Delta = 1\,\%$ with its identified maximum is shown on the left. A sub-range is resolved more finely with the second accuracy level, $\Delta = 0.5\,\%$, based on the maximum of the target function identified by this first accuracy step size. The middle figure shows both the maximum identified in the first (red dot) and the second (blue dot) accuracy step. Again, a sub-range is resolved more precisely around this maximum with the third and finest accuracy level of $\Delta = 0.25\,\%$. The right-hand figure thus shows all three points of the identified maxima that are identified with the different spatial accuracy levels.

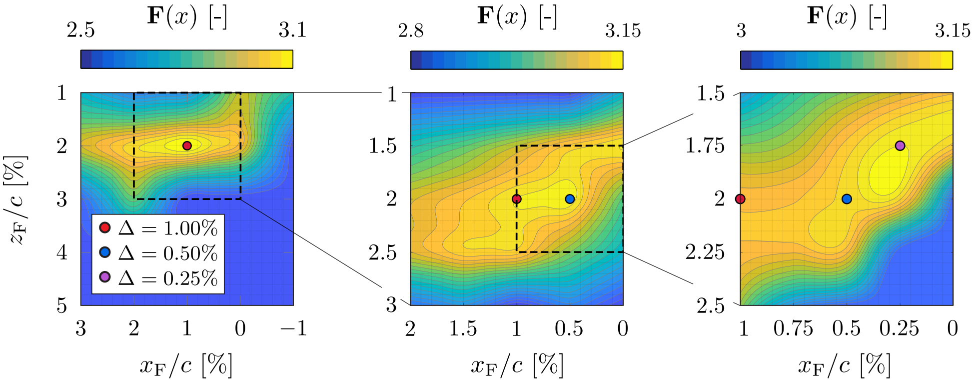

Figure 3.18: Investigation of spatial grid resolution with regard to $\mathbf{F}(x)$, adapted from [105].

The relevant parameters are listed in Table 3.10. The gap remains reasonably consistent, whereas the overlap of the identified optimum decreases with higher accuracy levels. Nevertheless, the performance of all accuracy levels remains almost unchanged. For example, an accuracy of $\Delta = 0.25\,\%$ achieves an improvement of $|\xi_{\mathbf{F}(x)}| = 0.6\,\%$ compared to the accuracy of $\Delta = 1\,\%$. This indicates that an accuracy of $\Delta = 1\,\%$ is sufficient for most performance analyses.

Table 3.10: Evaluation of the spatial grid resolution study with $\eta_F = 35\,\text{deg}$ and $\eta_{Sp} = 10\,\text{deg}$.

	G_F[%]	O_F[%]	$\mathbf{F}(x)$ [-]	$\xi_{\mathbf{F}(x)}$[%]
$\Delta = 1.00\%$	1.28	1.14	3.121	−0.6
$\Delta = 0.50\%$	1.39	0.64	3.130	−0.3
$\Delta = 0.25\%$	1.24	0.39	3.139	−−

Furthermore, a large area can be examined quickly at the accuracy level of $\Delta = 1\,\%$. The increased accuracy of $\Delta = 0.5\,\%$ is recommended if the approximate target area is known well in advance. The optimum can thus be determined more precisely with comparable effort. Furthermore, a combination of accuracies can be used for an initial localization, which is then refined. The third accuracy level offers only a small gain in accuracy with a significantly increased number of simulations and therefore should be considered for a final calculation, if at all.

Summary This section presents a process for optimizing high-lift geometries on airfoils, and derives and analyzes three methodologies based on the results. It is demonstrated that, despite a reduction in the parameter space, very good results can be achieved for optimization in terms of defined target functions for landing and takeoff.

3.2 Flap load modeling using artificial neural networks

This section addresses the data acquisition of input and target variables for the modeling of flap loads, the architecture of the applied artificial neural network, and the evaluation of the results. The motivation for the chosen approach as discussed in Section 2.2 is briefly summarized: In order to design the kinematics and actuation for the high-lift system, sophisticated data regarding the aerodynamic loads on the flaps are required. In addition to the demand for accuracy, preliminary aircraft design also requires a low computing time and an application that is generalizable as far as possible. The application in the present case is intended to cover a large range of aircraft, combined with the application in high-lift, as well as variable camber. These applications pose specific challenges for the calculation of the aerodynamic data, for example in high-lift, the interaction of the boundary layer and the wake as well as the flow in the gaps are of great importance, as described in Section 2.1.2. The VC application, which is applied in this work in the transonic flow regime, however, requires the ability to simulate the shock. These requirements exclude lower order flow simulations and demand RANS simulations. However, RANS simulations are too computationally intensive for the iterative preliminary design. This in turn provides the motivation to carry out the computationally intensive 3D CFD simulations, which results are referenced below as target variables, only a single time in an upstream process step.

The objective, as shown in Fig. 3.19, is to create a model that uses input parameters that can be determined with less effort, e.g., 2D CFD simulations of selected airfoil sections of the investigated wings. In addition, relevant geometric variables and flow parameters are included. In addition to the parameters used in the aircraft design process, target values are incorporated into the model development. In this case, 3D CFD results serve as the benchmark for the model. The computational effort of the 3D CFD simulations is thus drawn ahead of the iterative process. A database is created from the complete set of the data, which serves as the foundation for the regression used in the model. The resulting model provides accurate load data with minimal computational effort in the iterative preliminary design. An artificial neural network is selected for modeling as this allows for a fast regression.

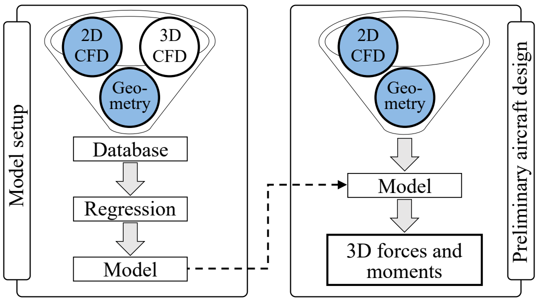

Figure 3.19: Schematic illustration of the modeling approach [113].

In Section 3.2.1, a description of the three reference aircraft used in this study is followed by a discussion of the acquisition of the required data. The process for creating the neural networks and optimize its architecture is then discussed in Section 3.2.2. This is concluded by analyzing the results in terms of their accuracy. The approach presented below and developed for this thesis was also addressed by the author in a journal article [113].

3.2.1 Flap load data acquisition

This section introduces the reference aircraft that provide the foundation for the flap load modeling. Selected geometry parameters of these aircraft serve as input parameters for training the neural network, as shown in Fig. 3.19. Further input parameters are provided by 2D CFD analyses. The 3D CFD simulations provide the flap loads representing the target values for the modeling.

Input values: Aircraft reference - geometry and flight conditions

As described in [113], the input values consist of data and parameters that are already known in the preliminary aircraft design or may be calculated with reasonable effort. The specific inputs vary by application; for instance, in variable camber scenarios, positions of all flaps are considered for differential flap setting. A complete list of the selected input values for high-lift and variable camber can be found in Table B.4 in the appendix. Table 3.11 contains parameters for each reference aircraft, not all of which are used as input values, but rather to clarify the aircraft class. For example, maximum takeoff mass (MTOM) and design range are not used in the model, while flap angles are used directly as input values. Other data such as flight altitude and mean aerodynamic chord (MAC) are used implicitly, e.g., the flight altitude defines the atmospheric conditions for the 2D CFD simulations. The resulting two-dimensional flap force and moment data are used directly as input values in the artificial neural network. [113]
The choice of reference aircraft is based on their design category. Thus, with MTOM between 77 t and 270 t, a wide range of aircraft sizes is represented. In addition, the medium range aircraft is included in the modeling as a high aspect ratio wing representative. All aircraft [94, 115, 134] have been designed with the MICADO software. [113]

Input values: 2D CFD airfoil simulations

A key challenge in the setup of the model is balancing computational efficiency with the precision needed for predicting three-dimensional flap forces and moments. While a flap load model based solely on a geometric model would be advantageous in terms of time demand in the iterative preliminary aircraft design, aerodynamic calculations are crucial to capture the flow phenomena. In order to avoid the extensive 3D CFD simulations for the input values, this work adopts 2D CFD simulations of airfoil sections, incorporating their results into the flap force modeling. Specifically, aerodynamic forces on the airfoil flaps are analyzed using the RANS solver Ansys Fluent with the k-ω SST turbulence model. Details on the CFD simulations are given in the

Table 3.11: Parameters of the different aircraft references for high-lift (HL) and variable camber (VC), as stated in [113].

Parameter		Reference aircraft					
		Short range [93]		Medium range [134]		Long range [115]	
Application		HL	VC	HL	VC	HL	VC
Re	[-]	$19.7 \cdot 10^6$	$25.3 \cdot 10^6$	$25.2 \cdot 10^6$	$34.2 \cdot 10^6$	$42.2 \cdot 10^6$	$42.4 \cdot 10^6$
Mach	[-]	0.2	0.78	0.2	0.83	0.2	0.85
Angle of attack α	[deg]	6, 7, 8, 9, 10, 11	0, 1, 2	6, 7, 8, 9, 10, 11	0, 1, 2	6, 7, 8, 9, 10, 11	0, 1, 2
Flight level	[-]	Sea level	350	Sea level	350	Sea level	420
Flap deflections	[deg]	12, 20, 26, 37.5	-1, 0, 1, 2, 3	12, 20, 26, 37.5	-1, 0, 1, 2, 3	12, 20, 26, 37.5	-1, 0, 1, 2, 3
Wing span	[m]	34.04		52.00		64.75	
MAC	[m]	4.17		5.28		8.84	
MTOM	[kg]	77 000		137 000		270 000	
Design range	[NM]	2 500		4 600		8 100	
Aspect ratio	[-]	9.47		12.28		9.48	
Area, wing	[m^2]	122.38		220.16		442.26	
Area, flaps (in + out)	[m^2]	4.43 + 5.72		7.11 + 10.82		11.03 + 11.58	

appendix, along with a breakdown on the applied settings in Table B.5. Mesh independence studies and $y^+ < 1$ checks are performed. [113]

In anticipation of Section 3.4, it should be mentioned at this point, that in the design methodology in MICADO, airfoils are distributed across the span in line-of-flight (LoF) orientation. This airfoil orientation provides the basis for constructing the wing geometry and evaluating the aerodynamic performance. Despite changes in wing geometry like sweep and taper, the line-of-flight airfoil geometry remains unchanged. Transforming airfoils with sweep angles might map three-dimensional flow effects more effectively [132], but transformed airfoils alter their shape with each modification in wing geometry due to changing sweep angles. [113]

Given the time consuming airfoil simulations using hybrid meshing and RANS, conducting new airfoil simulations for every design iteration is not feasible. However, conducting simulations for selected airfoils before the iterative design process certainly is feasible. As described above, the line-of-flight airfoils are not changed after an initial selection, thus their simulation data are suitable as input values. This trade-off between using flight path-oriented airfoils and transformed wing sections arises from the need for high-fidelity 2D CFD calculations. As stated above, aerodynamic simulations with less computational time requirement and of lower accuracy fail to capture important flow phenomena. Should more rapid methods be available in the future that can sufficiently accurately model the flow on airfoils without RANS, the use of transformed wing section airfoils is conceivable. [113]

Figure 3.20 shows an exemplary evaluation of the simulations for the variable camber case with a differential flap setting of 0 deg inboard and 1 deg outboard. For more information about VC flap settings, refer to Section 2.5. The inflow has an angle of $\alpha = 2$ deg at the short range configuration. In this case, the outboard flap is investigated, thus in the 2D simulation, the line-of-flight sections inboard and outboard of this flap are considered. The 2D simulation results enter the modeling as input value. Noticeably, the shock on the upper side of the airfoil of the 2D simulations is slightly more pronounced in comparison to a section from the 3D simulation shown above. In addition to this discrepancy, the 2D values are remarkably similar with respect to the pressure distribution over the slice of the 3D simulation. An analogous, exemplary case for the high-lift application is shown in the appendix in Fig. B.6. [113]

Target values: 3D CFD wing simulations

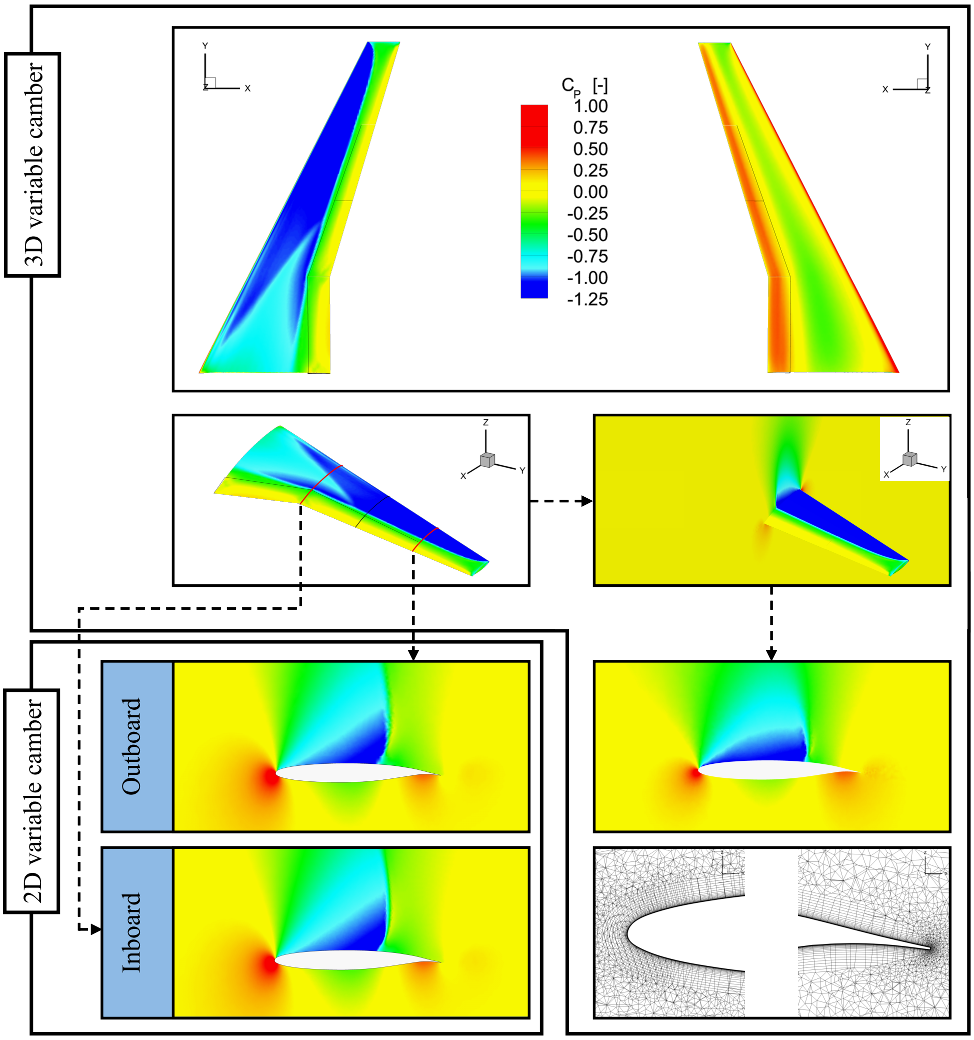

Figure 3.20: Exemplary pressure coefficient plot (fuselage blanked). Case: Short range reference with VC at $\alpha = 2\,\text{deg}$ and flap angles of 0 deg inboard and 1 deg outboard, as stated in [113].

The target values for the presented model are the aerodynamic forces F_z and F_x on the wetted area of the flap, as well as the moment M_y, measured at half the flap span. In order to obtain these target values, high-fidelity 3D CFD simulations are conducted for high-lift and variable camber application. The geometries for the short range, medium range, and long range reference are investigated for the VC settings and the high-lift settings as shown in Table 3.11 respectively at the stated Mach and Reynolds numbers. Further information are summarized in Tables 3.11 and B.5 [113]. Again, the k-ω SST turbulence model is applied and a $y^+ < 1$ is kept. Data from flight tests or wind tunnel experiments are rarely available for high Mach numbers, but especially for high Reynolds numbers, which poses a challenge for the validation of the present simulations. Published data from the *2nd AIAA CFD High Lift Prediction Workshop* [100] provide the foundation for the validation of the applied solver settings for the high-lift case. For more information on the mesh setup and validation, refer to [113].

3.2.2 Neural network architecture setup

This section deals with the development of the architecture setup process for the neural networks. For each of the three target variables F_z, F_x, and M_y, a separate neural network is set up for the high-lift case or the VC case, respectively. In the following, the exemplary architecture setup process of the F_z variable of the high-lift case is illustrated. The CFD simulation results and geometry data are processed according to the criteria in Section 2.2.2 and divided into training and test data sets.

A brief repetition of the explanation regarding the boxplots, as shown in Fig. 2.24, in particular the simultaneous visualization of training and test data is provided: In both cases, the relative deviations between the predicted and simulated target values are shown. Ideally, both plots show values as low as possible and at the same time be at approximately the same level. To counteract overfitting and thus de-generalization, the root mean square error of the test data set is used instead of the training data set for the selection of the neural network architecture. [113]

For the architecture setup process of the neural networks, the first step consists of an analysis of the number of repetitions with different initializations required for a consistent result. This is followed by an examination of the architecture with regard to hidden layers and neurons. Finally, the four activation functions from Section 2.2.1 are analyzed. Note that, similar to the process in Section 3.1, the sequential procedure is necessary since a full parametric study would require an unfeasible large amount of computing time. Accordingly, an architecture that already provides an acceptable prediction accuracy is needed to provide a reasonable starting point. For this purpose, a setup of two hidden layers, with 8 and 4 neurons, is used, the activation function is set to ELU and 200 repetitions are applied.

Initialization repetition study

The predictive performance of a neural network varies with its initialization, as detailed in Section 2.2.2, despite identical threshold settings. This case study, regarding the high-lift case with respect to the target value F_z, analyzes whether the results are consistent beyond a certain number of iterations. Again, a compromise between accuracy, i.e. repetitions, and computing time is attempted for this thesis. A small number of repetitions reduces the computing time, but does not provide a consistent creation process for neural networks. An arbitrarily high number of repetitions increase the computational cost exorbitantly. Strictly speaking, the number of repetitions may vary with each network architecture and choice of input and target values, but since the cases in this thesis are rather similar, the determined number of repetitions is applied to all studies. [113]

The study examines the numbers of repetitions 1, 3, 5, 10, 20, 40, 70, 120, 200, and 1 000. For instance, a repetition number of 200 means that the network is generated 200 times and the case with the lowest root mean square error regarding the test data set is selected. To assess the setup consistency, each repetition number setup is generated 30 times, analyzing the largest deviation represented by the upper whisker, excluding outliers. This consistency check is necessary, since a repetition number of, e.g., 3 could set up by chance a good neural network in one run, but fail to do so in a second run.

Figure 3.21 illustrates the maximum deviations of the upper whiskers across the introduced numbers of repetitions for the network initialization. It is important to clarify that the figure does not represent the predictive accuracy of the generated networks, but rather focuses solely on the worst-case scenario, represented by the upper whiskers of the deviations. In other words, in Fig. 3.21 there is a median of the upper whiskers, an upper whisker of the upper whiskers, quantiles of the whiskers, and so forth. The results regarding the test data set in Fig. 3.21 indicate, that repetition numbers below 20 still yield high upper whiskers, meaning a low consistency. Above 20 repetitions, the median upper whisker remains stable and the upper whisker tends towards a value just below 5 %. Above 40 repetitions, only marginal changes occur and a significant increase in the number of repetitions is required for improvement. Optimally, the dispersion of the upper whisker should become very small in order to speak of independence from the initializations. However, as can be seen in Fig. 3.21, even with 1 000 repetitions, the upper whiskers are still scattered in a range between about 1 % and 3 %. As the computational cost becomes very high, a trade-off is required. Consequently, a repetition number of 200 is selected for the following broader studies, while the neural network generation for the in-depth analysis is set up with a repetition number of 1 000. [113]

Neural network architecture - Hidden layer and neurons

The architecture of the neural network, especially the number of hidden layers and the distribution of neurons within them, significantly impacts the feed-forward method. In the following, different neuron distributions are tested with 200 repetitions, with a more detailed analysis on the selected configurations using 1 000 repetitions. The neural network architectures under investigation are listed in Table 3.12 and the plot analysis is shown in Fig. 3.22. The case study refers to the high-lift for the target value F_z using the ELU activation function. Starting from the baseline assumption of two hidden layers with 8 and 4 neurons, 7 variations (B-H) are im-

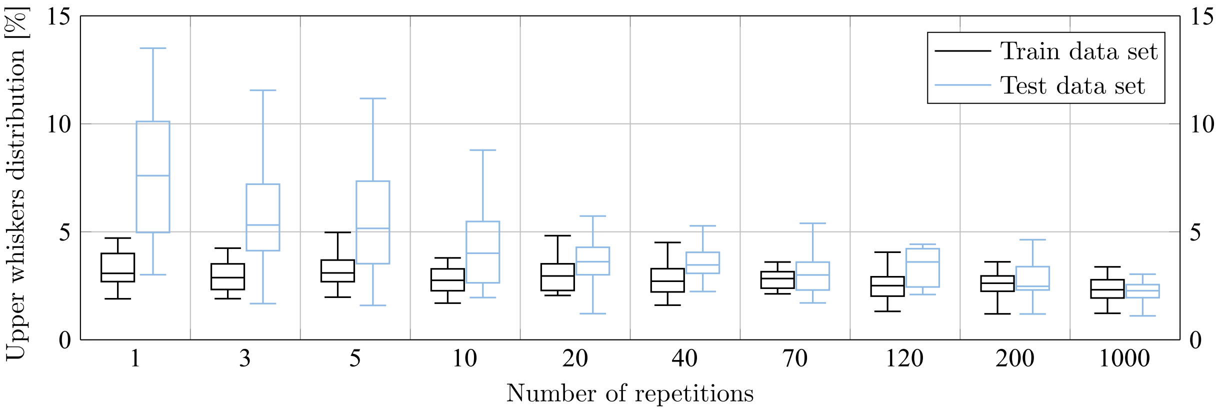

Figure 3.21: Maximum deviations of the upper whiskers of a fixed neural network structure depending on the number of repetitions for initialization, as stated in [113].

plemented within these layers. Subsequently, another hidden layer is added and variations I-L are created based on the obtained results.

Figure 3.22 indicates that for this case, architectures with two hidden layers are advantageous compared to architectures with three hidden layers in terms of predictive performance. Note that, as explained above, the distributions of the test data shown in blue are of particular interest. For the two-layer networks, a small number of neurons in the second layer leads to improved predictions. On this basis, the median of the upper quartile, and the upper whisker of the test data set are used to select the variants with the IDs B, D, F, and H, marked in bold letters in Fig. 3.22, for further investigation with 1000 iterations. [113]

Table 3.12: Architecture variants at the case example: F_z at high-lift, as stated in [113].

Variation ID	A	B	C	D	E	F	G	H	I	J	K	L
Layers	2	2	2	2	2	2	2	2	3	3	3	3
Neurons	8|4	8|2	8|1	12|4	12|12	12|2	4|4	20|2	8|8|2	8|2|2	12|8|4	20|15|10

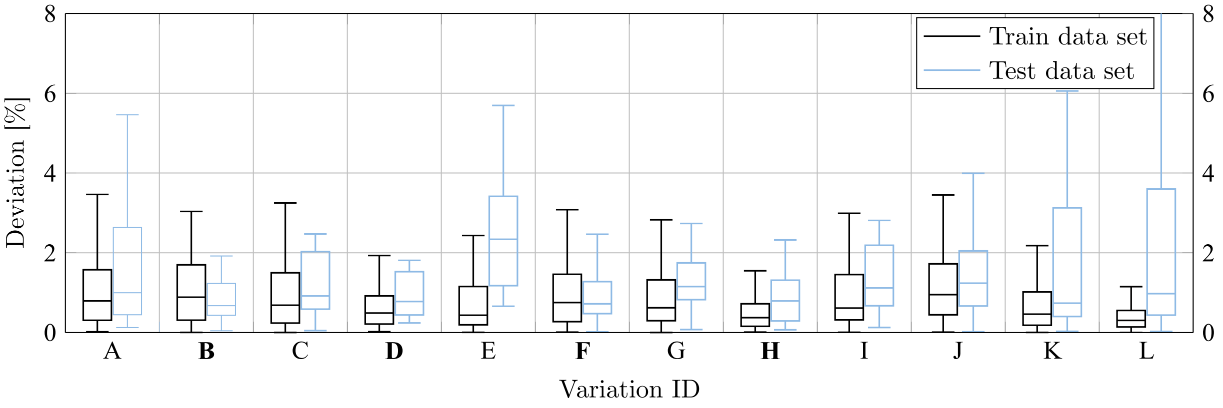

Figure 3.22: Deviations for the architecture variants with 200 repetitions at the case example: F_z at high-lift, as stated in [113].

The four architectures selected for the detailed analysis differ only marginally after 1 000 repetitions, highlighting the adequacy of using 200 repetitions for broader studies. The detailed analysis is shown in Fig. 3.23 in an analogous manner to the preliminary analysis in Fig. 3.22. All four variants display a deviation of less than 1 % in the median from both the test and the training data set. Versions D and H are slightly advantageous as the upper whiskers are below 2 % deviation. Since the network generation for variant D, with two hidden layers of 12 and 4 neurons, requires slightly less computing time, it is selected for the following investigations. [113]

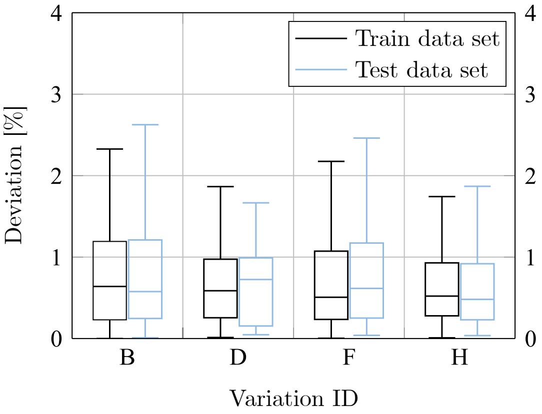

Figure 3.23: Deviations for selected architecture variants with 1 000 repetitions at the case example: F_z at high-lift [113].

Neural network architecture - Activation function

An analysis is conducted to identify the most suitable activation function for the specified neural network architecture with two hidden layers of 12 and 4 neurons. Note that the previous optimization steps were performed for an ELU activation function, therefore it holds an advantage. However, the network architecture in the feed-forward design is relatively simple, thus no excessive specialization excludes certain activation functions. The effectiveness of different activation functions varies with the set threshold.

Therefore, for the following study, the threshold is reduced individually to the lowest possible value for each activation function to ensure network convergence. As described in Section 2.2.2, selecting a network based on the predictions for the test data set helps preventing the selection of an overfitted mesh. Using this approach, the meshes for the ELU and softplus activation functions were generated with a threshold of 0.01, ReLU at 0.05, and the sigmoid function at 0.001. [113]

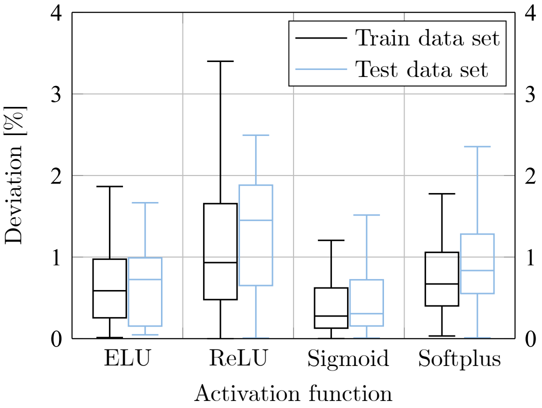

Figure 3.24: Deviations for the architecture variants with 1 000 repetitions for selected activation functions at the case example: F_z at high-lift [113].

Figure 3.24 shows the graphical evaluation of the deviations of the predictions with the four activation functions. Notably, ELU and sigmoid functions demonstrate high prediction accuracy, each with an upper whisker of less than 2 % in relative deviation. Among the four models, the ReLU performs the worst. Notably, when considering the upper whiskers, the training set is represented more poorly than the test set. Convergence problems often occurred during ReLU network generation, indicating inactivated neurons as described in Section 2.2.1. With respect to the median, the sigmoid function yields slightly better values and thus emerges as the selected activation function. [113]

3.2.3 Data analysis and interpretation of model results

Using the network parameter selection procedure described above, this section presents the results of the models for the three target values for the high-lift and variable camber cases, as analyzed by the author in [113].

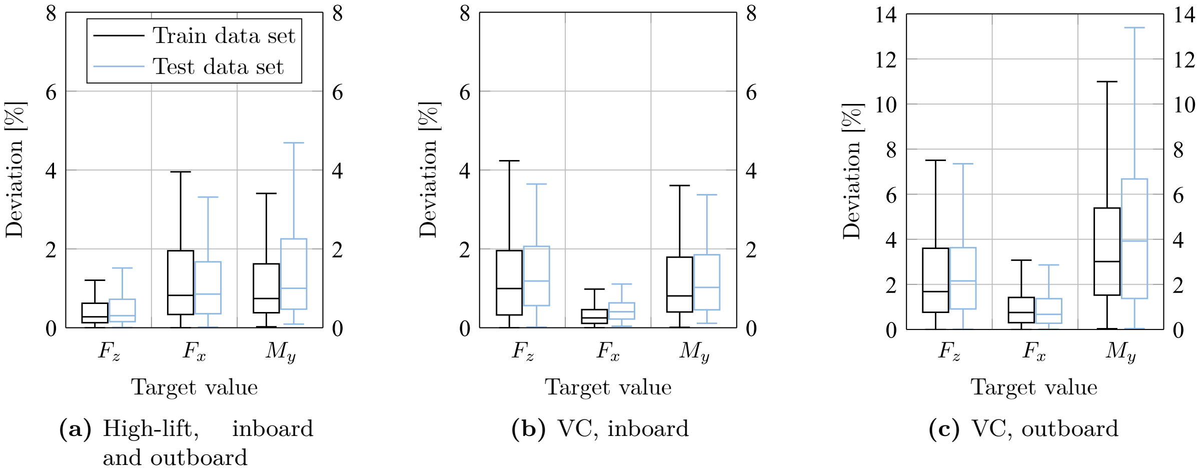

(a) High-lift, inboard and outboard **(b)** VC, inboard **(c)** VC, outboard

Figure 3.25: Model prediction accuracy evaluation, as stated in [113].

The results for high-lift, as shown in Fig. 3.25(a), show a small relative deviation, especially for the force F_z. The force F_x and the moment M_y are predicted slightly less accurately. First, the reference value is higher for F_z, which makes the relative error in the case of F_x larger for the same absolute deviation. The drag, which is mostly corresponding with F_x, is considered to be more difficult to capture by simulations than the lift. This uncertainty is already included in the CFD data, thus it is not a direct reason for a more difficult prediction with neural networks. For the neural network, this is a plain data problem, with no physical correlations. However, as a consequence of the more difficult drag prediction using CFD, the neural network may get more scattered target values, which it has to predict, which in turn affects the prediction accuracy. The moment on the other hand is sensitive to the point of force onset. The median of all three target values is less than 2 % relative deviation. In the case of variable camber, another characteristic is added. Comparing the pressure distributions in Figs. 3.20 and B.6, there is a distinct difference between the VC and the high-lift wing. While the VC wing shows a significant pressure difference from the inboard to the outboard wing, this difference is much less pronounced in the high-lift case. Besides the influence of the fuselage, whose geometry is not displayed in the figures, it is mainly the differential flap setting in VC that causes this phenomenon, while the high-lift settings are uniformly deflected. For example, in Fig. 3.20 the inboard area is not deflected, but the outboard area is deflected by 1 deg. Accordingly, the pressure distribution over the wing changes mainly in the outboard area. This leads to the situation that a modeling over all training cases would have to cope with the balancing between the inboard and outboard flap and corresponding dependencies would have to be included in the regression. Although this is possible, significantly more accurate predictions can be made by creating separate models for the inboard and outboard regions.

The corresponding evaluations are shown in Figs. 3.25(b) and 3.25(c). All six targets for the variable camber case can be predicted with a median deviation of less than 4 %, and for the inboard case, the median deviation is less than 2 %. Regarding the prediction accuracy F_z and F_x, the situation is reversed for variable camber compared to high-lift. The values for F_z are more widely scattered due to the many different differential flap deflections, which reduce the accuracy compared to the F_x force. The moment M_y, particularly for the outboard case, shows higher deviations. As explained above for the high-lift case, the moment is highly sensitive to changes in both the forces and their points of onset. Scattered data points make it more challenging to achieve high prediction accuracy. This effect is further intensified by disturbances such as shocks in the present variable camber case. [113]

Summary The demonstrated procedure allows for the reliable setup of a neural network in the frame of similar problems. The artificial neural networks created and analyzed with this method provide accurate predictions of the flap load with little computing time. In the case of significantly varying phenomena occurring with new aircraft, for example with a forward swept wing, the existing neural networks can be extended. In the context of this thesis, a tool is thus provided to predict the flap load data of the optimized flaps in Section 3.1 and to allow for the design of actuators in Section 3.3, assuming known kinematics.

3.3 Power-by-wire flight control actuation methodology

The design of an actuator device in aerospace applications involves a complex set of constraints, including individual installation modalities, and customer-specific requirements. Each component must meet standards for quality, durability, and maintainability and is therefore designed in specialist departments. However, the effect of different actuator concepts such as the installation of electromechanical and electrohydrostatic actuators on the overall aircraft level is of interest for a high-lift or variable camber actuation. Knowledge of realistic actuator masses at early design stages is of importance, due to the mass growth factor [45] in the integrated design process and the resulting design optimizations or limitations for new aircraft configurations. To be capable of calculating with the often varying actuator requirements in the early design stage, a fast and precise preliminary design of actuators is necessary, which is in contrast to the mentioned detailed design processes. In preliminary design processes—refer to Section 3.4 for more details on MICADO—computing time for individual components must be kept to a minimum to ensure the entire aircraft's systems are evaluated within a reasonable time frame. The methodology for the preliminary design of power-by-wire actuators that was developed in the course of this thesis, was also addressed by the author in a journal article [116].

3.3.1 Approach to a component-based actuator modeling

The presented methodology designs the respective actuator modularly, allowing for the exchange of individual component modules, if desired. The design requirements are transferred component-wise as well, beginning with the demanded mechanical output of the entire actuator. These output requirements cover both a linear actuation movement, including maximum extension, force and speed, and a rotary actuation movement, including torque and speed. For integration into the early stages of overall aircraft design, where detailed design parameters are not yet defined, only the aforementioned mechanical output requirements are necessary for the presented sizing methodology. This offers the significant advantage of not having to rely on a database of previously built actuators. Various optional settings for components, like the number of pole pairs in the motor and several efficiency factors, allow for a user-specific customization if desired; otherwise, standard values are applied. [116]

The methodology differentiates between maximum values of force and speed (identified by the index max) and their values at maximum power (identified by the index $P_{\max}$). As maximum speed and force do not necessarily occur together, selecting values at the maximum power point provides a more accurate design, although the respective maximum values are still needed for the individual component sizing. The calculations follow physical relationships where possible, but since, as described above, actuators are often specialized solutions, some correlations have to be fitted via product-related datasets. The results of the calculations are individual component masses, and thus the total mass of the actuator, as well as the electrical input power requirement and the overall volume. [116]

Linear electromechanical actuator

In the following, the developed methodology will be demonstrated using the example of the linear electromechanical actuator, as shown in Fig. 2.26. Using this example, the component-wise relationships and processes are discussed. The complete statement and explanation of all equations can be found in the source mentioned above [116] as this would exceed the scope of this thesis. The flowchart in Fig. 3.26 illustrates all the components required for the LEMA and their respective interdependencies. Note that the methodology presented passes the chain of cause and effect backwards through the components. In the physical application, electrical

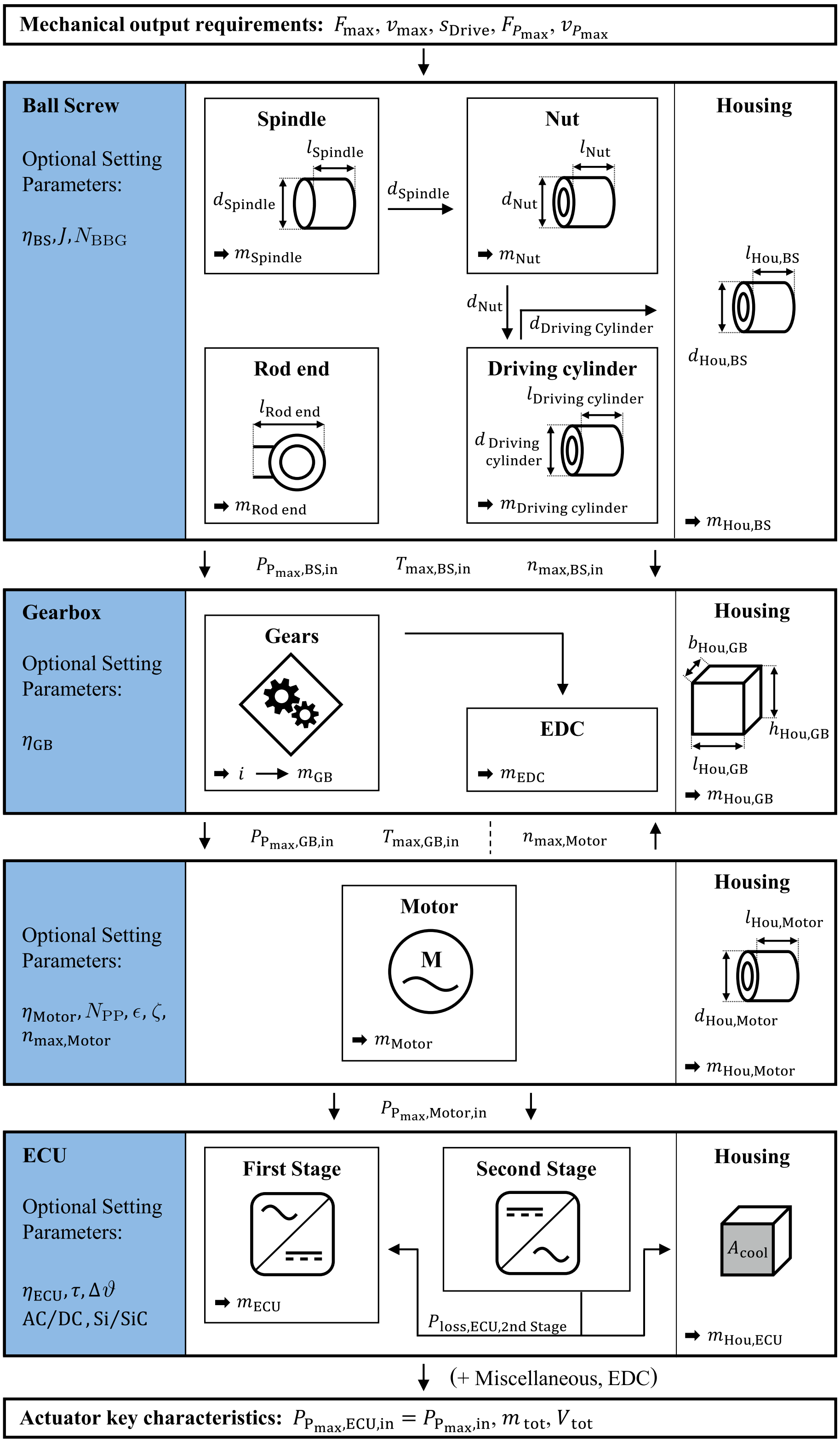

Figure 3.26: Flowchart of linear electromechanical actuator design, as stated in [116].

power and signals would be supplied to the power electronics, and the generated rotation of the motor moves—via the gearbox—the ball screw. For the methodology, the output motion and power requirement is specified and thus calculated backwards to the electrical power input.

Ball screw: The mechanical outputs demanded from the actuator are initially incorporated into the ball screw. The left column lists the optional setting parameters for possible design customization. For the example of the ball screw, this covers the efficiency η_{BS}, the ball screw pitch J and the number of ball-bearing gears N_{BBG}. The pitch ranges typically between 6 and 10 mm. If within the realm of construction feasibility, 6 mm should be targeted [116]. This pitch reduces the torque to be transmitted. Torque is more sensitive to the subsequent component sizing than the simultaneously increasing rotational speed. The demanded loads size the spindle, which in turn imposes requirements on the nut. The driving cylinder, in turn, has to accommodate the sized nut accordingly, ensure the travel path, and be designed for the load to be transferred. In addition, a rod end is installed for attachment and load bearing. Figure 3.27 provides a sketch of the ball screw in order to visualize the composition of the aforementioned components.

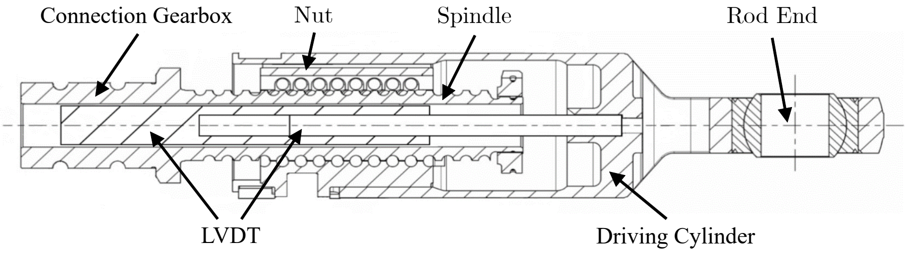

Figure 3.27: Parts of the ball screw (LEMA) [116].

Gearbox: The ball screw drive translates between the linear output movement and a rotary movement. Accordingly, torque and speed requirements are passed on to the gearbox by the ball screw, as well as the maximum power point mentioned above. For the gearbox, a special characteristic applies: the motor connected downstream in the design chain determines the maximum input speed $n_{\mathrm{max,Motor}}$. This speed is defined in advance depending on the motor type and can be modified as an optional setting parameter if desired. The transmission ratio is determined from these requirements imposed on the gearbox and should range between 10 and 15 [116]. If these limits are exceeded due to the no-load speed specifications, adjusting the motor to accommodate the maximum speed is recommended. A ratio that is too low can cause high torque demands on the motor, resulting in a larger motor design. Conversely, a ratio that is too high results in a heavier gear.

Motor: As mentioned above, the maximum speed is specified for the motor, which is usually in the range between 4 000 and 7 000 rpm for EMAs. Other factors are the number of pole pairs N_{PP}, a motor type-dependent scaling of the maximum power ϵ, and a peak load factor ζ.

To calculate the motor mass, the relationship developed in [123] and used by [25] is adopted. According to the methodology, the torque requirement of the gearbox has a particularly scaling effect on the overall actuator mass.

Electric control unit: The electronic control unit transforms the electrical power input into the requirements of the motor and additional components. This conversion involves three steps: the rectification of the input current, smoothing, and the frequency modulation to meet the required specifications. The calculation process is divided into two stages. The first stage, which rectifies and smooths the voltage, is only applicable for an AC input. The second part, which includes the control boards responsible for modulation, does not depend on the input voltage type.

Thus, the main components shown in the flowchart in Fig. 3.26 are designed with the detailed set of equations in [116]. In addition, the optional extension and damping control unit may be added. The mass of components that are not directly assigned to one of the components is estimated and added.

Rotary electromechanical actuator

For the following power-by-wire actuators, the procedure is discussed in abbreviated form, as individual components such as the ECU are modeled using an approach analogous to the LEMA. For the electromechanical actuator in rotary design, the corresponding flowchart is shown in Fig. 3.28.

Gearbox: The primary difference to the LEMA involves the gearbox, as in the actuator concept of the REMA, the mechanical output movement is directly connected to the rotational movement of the gearbox via an output lever, as shown in Fig. 2.27. Similar to the LEMA, the maximum torque and speed values are determined to identify the optimal power point. The gearbox converts the speed of the motor to the rotational speed required by the control surface, demanding high transmission ratios of up to 900 [116]. These ratios are typically achieved by using Wolfrom or planetary gear systems. The planetary gear option usually employs four planets. A selection of up to four gear stages is proposed for both the planetary gearbox or the Wolfrom gearbox. The number of gear stages is formulated as a function of the diameter of the entire REMA installation space, which in turn is dimensioned by the required cooling surface of the power electronics.

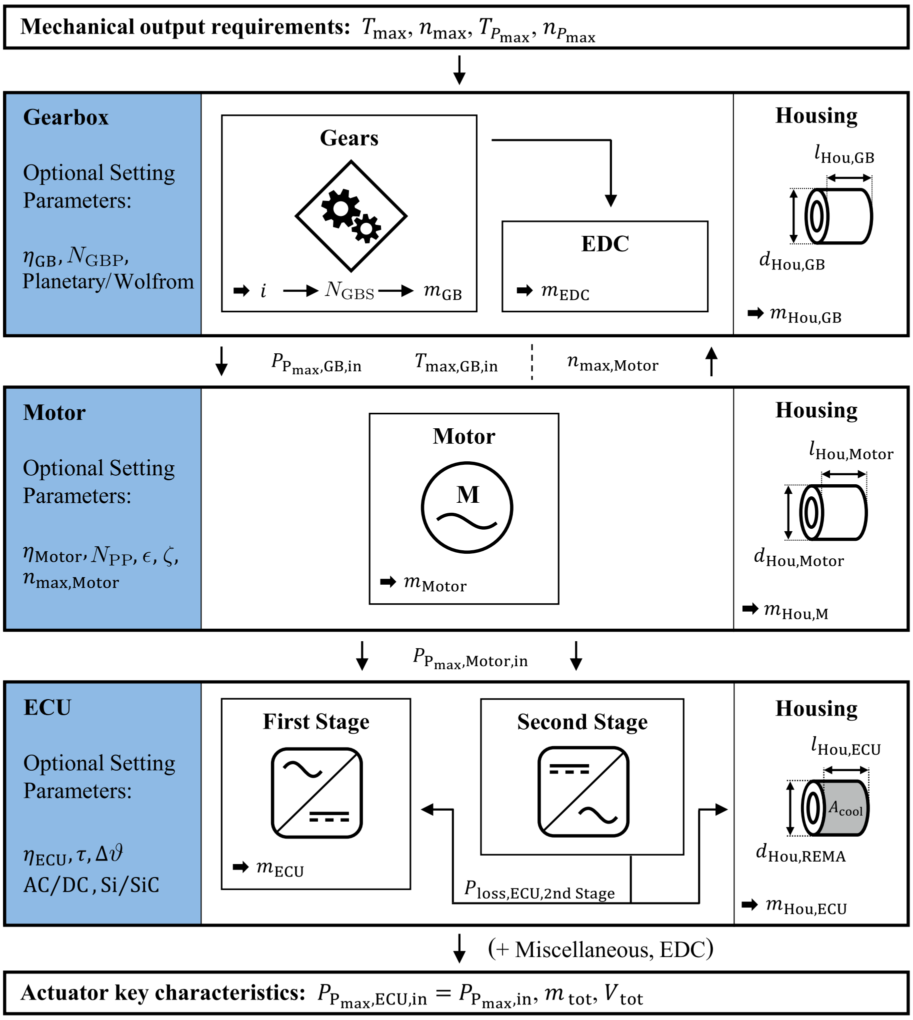

Figure 3.28: Flowchart of rotary electromechanical actuator design [116].

Electrohydrostatic actuator

Only the power electronics for the EHA are modeled in the same way as shown for the electrical actuators presented above. The motor is designed in a different way due to the interaction with the required pump. The flowchart is shown in Fig. 3.29, corresponding to the EHA shown in Fig. 2.28.

Ram: The ram refers to an assembly of components that transforms the pressure difference generated by the pump into linear motion, as illustrated in Fig. 3.30. This assembly includes the moving piston rod with its attached rod end, the sealing, the linear variable differential transformer (LVDT) for measuring the movement, and the rod end fixed to the cylinder. Additionally, the figure shows two cylinders—cylinder (1) enclosing the piston and cylinder (2) enclosing the piston rod. The maximum force determines the diameter of the piston rod, whereas the diameter of the piston depends on the surface subject to pressure. The total length of the component is dependent of the required maximum stroke and the width of the piston. With the designed

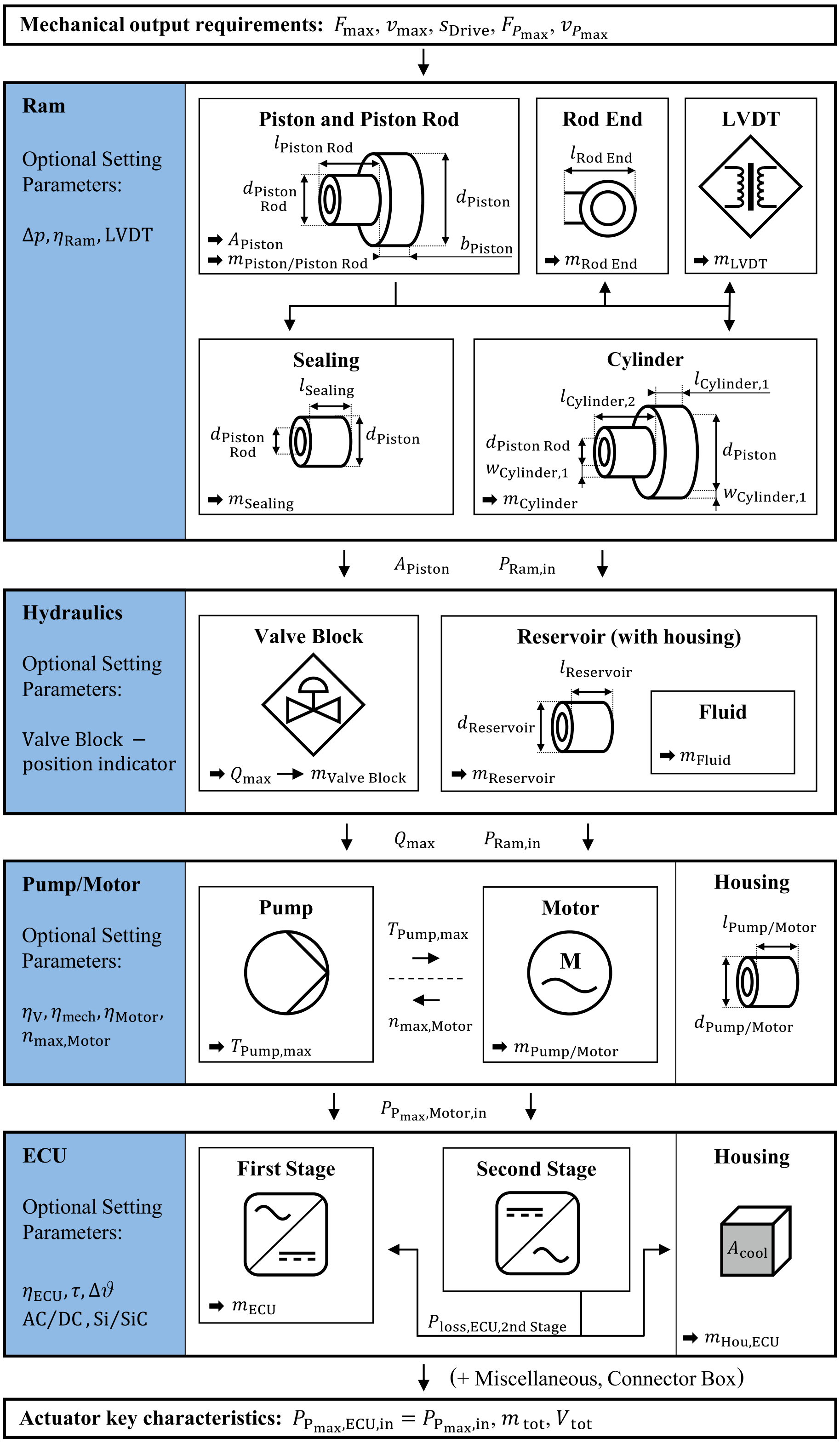

Figure 3.29: Flowchart of linear electrohydrostatic actuator design [116].

piston and piston rod as the central component of the ram, the other components are then designed and adapted to match the geometrical dimensions and applied forces. In addition, the volume flow is dimensioned using the maximum travel speed and the piston area.

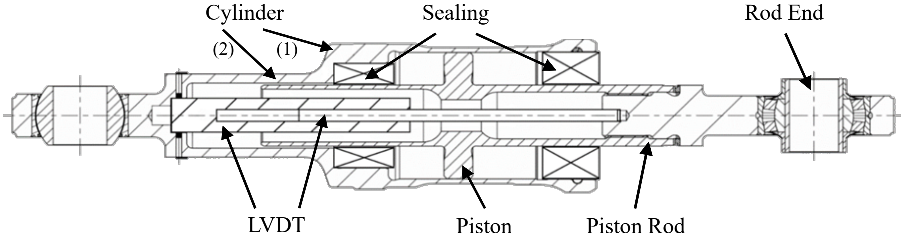

Figure 3.30: Ram of a primary flight control actuator (EHA) [116].

Hydraulics: With regard to the hydraulics, the central component is the valve block. The valve block connects the ram with the pump and the reservoir. The dimensioning parameter is the maximum volume flow. The valve block consists of the block component, the mode selector valve, a solenoid, and a differential pressure transducer.

Pump and motor: The pump provides the required pressure to operate the ram and is directly powered by the motor without any intermediate gearbox. An axial piston pump with fixed displacement is commonly used for EHAs. Like the motor mass of an EMA, the EHA motor mass largely depends on the torque.

3.3.2 Validation and sensitivity studies

The methodology introduced here is evaluated against actual flight control actuator data and a calculation method cited from existing literature [25]. In the first step, individual components of both EMAs and EHAs are investigated. In the second step, the overall mass of 11 different actuators is examined. Unless otherwise stated, the data used are derived from product-related data supplied by Liebherr-Aerospace Lindenberg GmbH in the referenced article [116].

Component validation

In this section, the calculations of the components for both EMAs and EHAs are evaluated as shown in [116]. This demonstrates that the presented methodology achieves a high level of accuracy at component level. This eliminates the possibility of matching results at overall actuator level due to randomly compensating errors at component level. Consequently, the approach of exchanging the modeling of individual components, if desired, is valid.

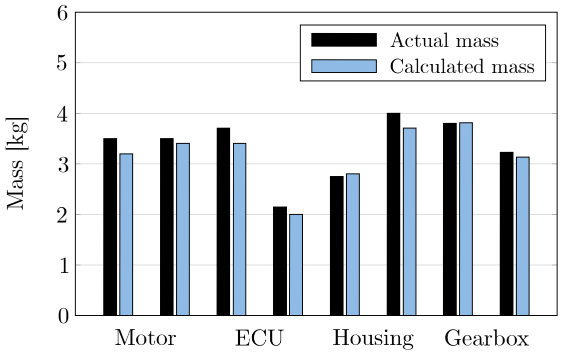

Figure 3.31: Validation of the EMA component calculations [116].

In terms of the EMA, the comparison of calculated component weights against product-specific data is displayed in Fig. 3.31. The mass of the motor, the ECU, the housing, and the gearbox of one rotary and one linear EMA, for which detailed data were available, are shown together. The calculation methods presented above closely align with the considered actuators and show only small deviations for all components. With mass differences of 0.30 and 0.15 kg, the ECU is estimated to be slightly too light, which is also due to the fact that, depending on the application, the power electronics is subject to rapid development. The gearbox weights for both linear and rotary designs show accurate estimations in the comparison.

In the case of EHAs, two central components are evaluated in detail. The ram is evaluated in terms of mass and length, and the valve block is evaluated in terms of mass. The three resulting evaluations show in detail how the presented methodology performs with respect to the most important and EHA-specific components based on available datasets.

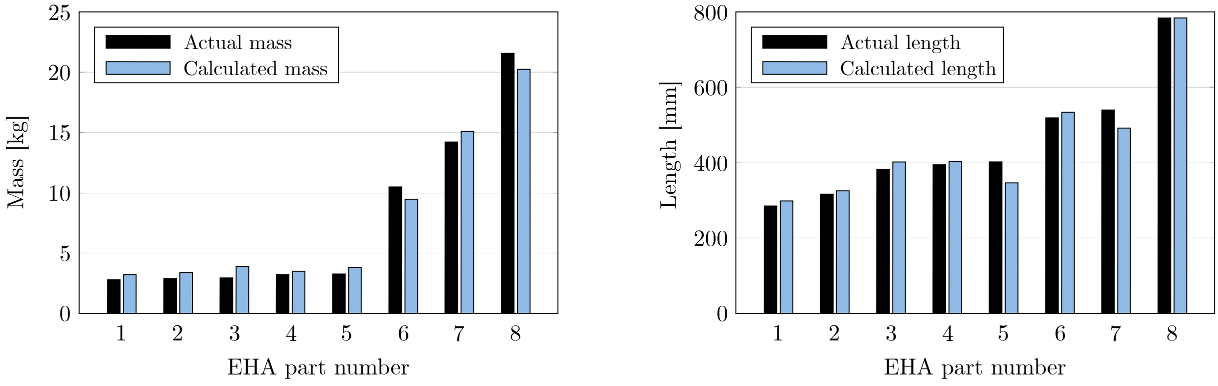

(a) Ram mass

(b) Ram length

Figure 3.32: Validation of the EHA ram component calculations [116].

The calculated mass and length of the EHA ram are compared with actual flight control actuator data, as shown in Fig. 3.32. The predictions in terms of mass, see Fig. 3.32(a), generally match the actual component weights across a broad spectrum, ranging from 3 kg to 20 kg. Regarding the length, as depicted in Fig. 3.32(b), covering 290 mm to 790 mm and defined as the distance between the rod ends' bearing centers in the retracted position, the predicted values align well with the actual values. Note that manufacturer documents are rarely made publicly available, which leads to a limited set of data to be exploited.

The available data for the valve block mass range between 4 and 12 kg and are consistently well represented by the methodology. The result is plotted in Fig. 3.33, covering a large design space, especially considering that the valve block is designed and optimized differently, depending on installation space and targeted costs.

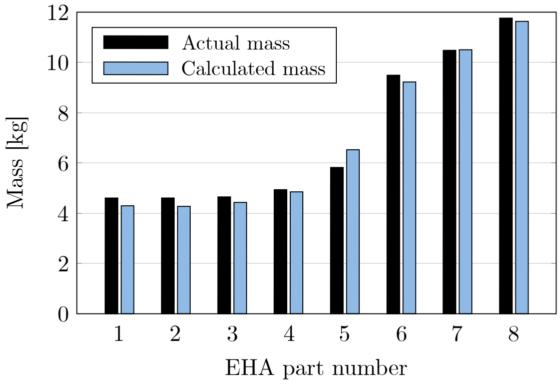

Figure 3.33: Validation of the EHA valve block component mass calculations [116].

Overall actuator mass validation

In a second step, in order to assess the accuracy provided by the methodology, the overall mass is evaluated for all three actuator types. Furthermore, an existing approach from the literature [25] is compared. The evaluation of actuator total mass involves comparing calculated values with actual data, using both proprietary data [116] and publicly available sources [70, 109]. The actuators are identified by a reference number and the results are shown in Fig. 3.34 and Table 3.13.

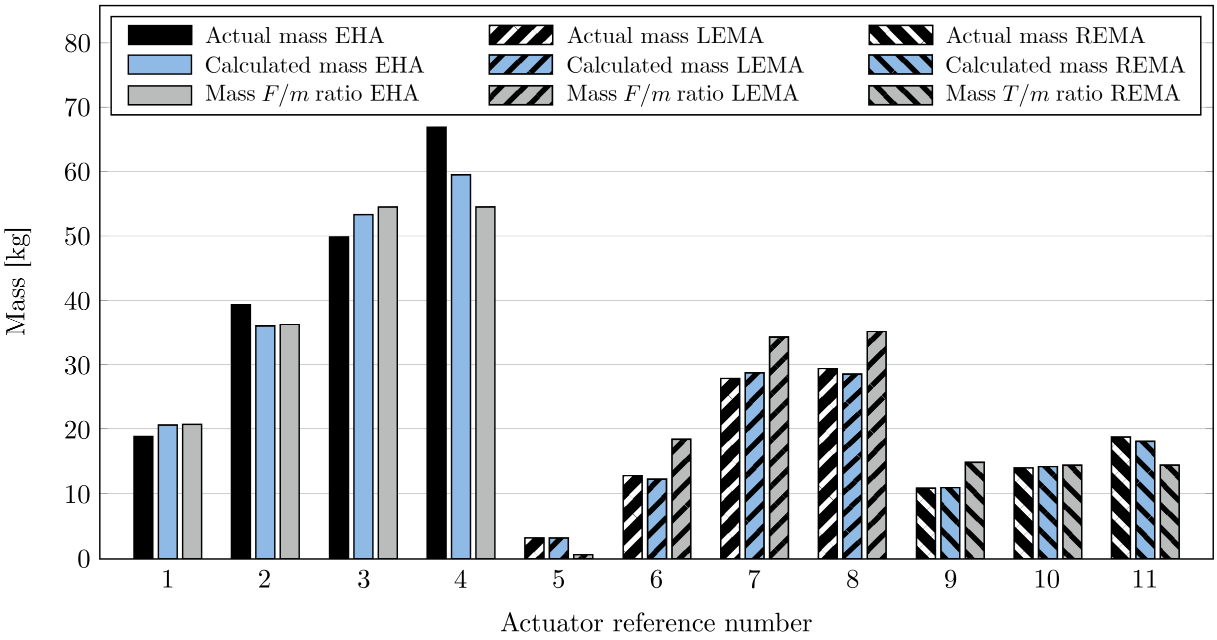

Figure 3.34: Overall actuator mass results comparing the actual mass with the introduced methodology and with a force-to-mass, resp. torque-to-mass approach [116].

Regarding the evaluation for the EMAs, the results as obtained by the presented sizing calculations are compared to actual actuators in the mass range of 3.2 kg to 29.5 kg. The calculations show a highly accurate match. The deviations for EMAs, both linear and rotary, are below 5 %. The EHAs, which range from 19.0 kg to 66.9 kg, exhibit a slightly greater variance from real values but remain within an acceptable margin for the preliminary aircraft design phase. During the prolonged presence of EHAs, technology leaps have occurred, all of which must be accommodated by the equations in [116]. The most notable discrepancy, reaching 12.4 %, occurs for the EHA with the reference number 4, primarily due to the unique design of its valve block. Its design is tailored to enable operation within a electric backup hydraulic actuator and demands the incorporation of a greater quantity of components.

Table 3.13: Results of the total actuator masses, as stated in [116].

Actuator type	Reference number	Actual mass [kg]	Calculated mass [kg]	Absolute deviation [kg]	Relative deviation [%]
EHA	1 (EGIDE [70])	19.0	20.8	1.8	9.5
	2	39.4	35.6	-3.8	-9.6
	3	49.9	52.9	3.0	6.0
	4	66.9	58.6	-8.3	-12.4
LEMA	5 (HP Smart [109])	3.2	3.2	0.0	0.0
	6	12.9	12.3	-0.6	-4.7
	7	28.0	28.6	0.6	2.1
	8 (C141 [70])	29.5	28.5	-1.0	-3.4
REMA	9	11.0	11.1	0.1	0.9
	10	14.2	14.4	0.2	1.4
	11	18.9	18.2	-0.7	-3.7

Furthermore, the presented methodology is contrasted with an existing methodology from the literature [25], the results are shown in Fig. 3.34 as well. This approach with a focus on state-of-the-art investigations, states fixed force-to-mass (F/m) ratios for linear EMAs and EHAs derived from the sources [26, 128]. The ratio involves the overall actuator mass without detailing individual components. Rotary actuators with the reference numbers 9 – 11 from Table 3.13 are not covered by a force-to-mass ratio; therefore, in order to investigate the feasibility of a torque-to-mass (T/m) ratio, the available data were used to determine such a factor and apply it to the rotary actuators.

As shown in Fig. 3.34, the approach of using fixed ratios provide acceptable results, given the very small calculation time. However, they overlook critical factors like stroke and output speed. For instance, despite having the same output force, actuator 4 is about 16 kg heavier than actuator 3 due to a higher stroke. Regarding the four LEMAs, the presented methodology provide more accurate results than a force-to-mass ratio. For the example of the actuator with the reference number 8, the force-to-mass ratio predicts the actuator mass with an error of 6.5 kg, while the method presented here deviates by 1.0 kg. Even more drastic, for the actuator with the reference number 5, a mass near zero is predicted using just the one fixed ratio to calculate the mass.

Summary A component-wise design methodology for the preliminary aircraft design stage regarding three types of power-by-wire actuators is presented and evaluated. On the basis of mechanical output parameters, physical constraints, and correlations are used to size the actuators at the component level in terms of power, mass, and volume. The investigation at the overall actuator level, as well as at the component level, shows that a very good agreement is achieved between the predicted data with this methodology and the actual data of the flight control actuators.

3.4 Preliminary overall aircraft design environment MICADO

Civil aircraft design is a multi-stage iterative process involving increasing levels of detail as the development progresses. There is a lot of profound literature available that provides models for application, typically based on existing aircraft, and often includes a classification of terms for the different design phases. Particularly noteworthy here are the contributions of HOWE [45], RAYMER [88], ROSKAM AND LAN [98], and TORENBEEK [124].

The initial stage, which is called *conceptual* design, is where the fundamental aircraft characteristics are shaped. It starts with establishing requirements based on customer needs or market predictions, leading to various aircraft configuration proposals [88]. In this stage, compromises between disciplines, such as aerodynamics, structures, and systems, are essential to balance competing demands and converge on the best possible design [45]. For the individual disciplines, this means that they have to deviate from their ideal solutions, meaning the best possible solution without any boundary conditions, and find the optimal solution, meaning the best possible solution under the given boundary conditions.

The second, *preliminary* design stage focuses on refining the chosen concept. It includes a comprehensive examination and optimization of the design, assessing technological maturity to ensure the concept is feasible within the projected time frame [88]. This phase consolidates the design, preparing it for the detailed development stage.

Finally, the *detailed* design stage is where the actual aircraft components are designed. The workforce is significantly increased and the experts in the specialist departments work on the detailed elaboration of the components to be finalized and passed to manufacturing [88].

Across these stages, the design evolves from broad concepts to specific, detailed plans, ready for production. Each phase contributes to a gradual increase in detail, ensuring the aircraft meets both the performance criteria and market expectations.

In this thesis, the preliminary aircraft design software MICADO [94] of the Institute of Aerospace Systems of the RWTH Aachen University is used for method application and aircraft design evaluation[†]. Note that the Institute's internal software MICADO was branched off to create UNICADO in 2020, which is further developed in a consortium of six German universities. However, MICADO contains specialized tools with higher accuracy, for example in the field of aerodynamics. In the acronym, the C denotes *Conceptual*, although MICADO can also be used as a platform for more sophisticated analysis of individual systems or components at the preliminary design level. MICADO is therefore situated between the conceptual design stage and the preliminary design stage described above.

3.4.1 Design logic in MICADO

The fundamental idea of MICADO consists of breaking down each discipline into individual tools, which can be executed independently of each other. A central exchange file represents all of the aircraft's data, from which each tool can obtain the required input and write its own output [107]. This modular structure allows individual tools to be exchanged, for example, if more sophisticated tools are available or if other implementations are being tested, e.g., for validation purposes.

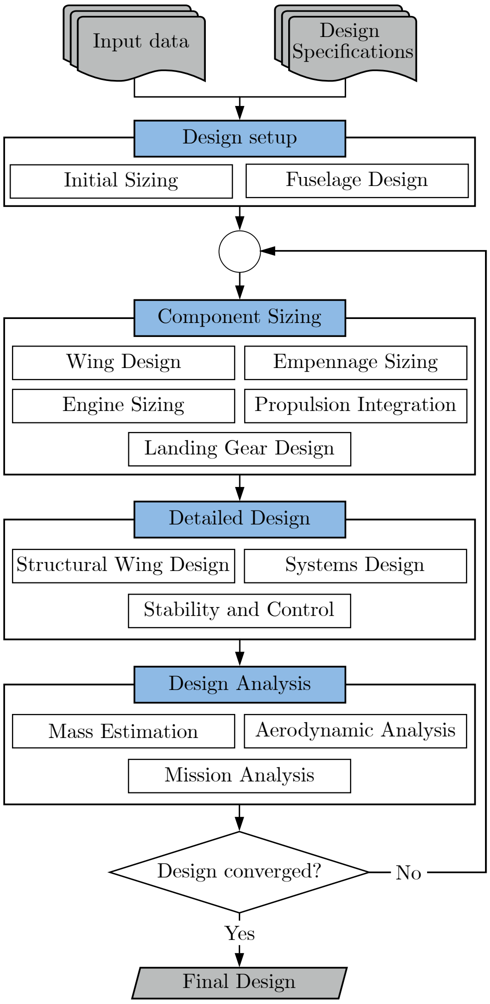

Figure 3.35: MICADO design process, adapted from [107].

MICADO can be operated in several modes. The first is the so-called clean sheet design of a completely new aircraft based on top-level aircraft requirements and specifications [107]. These include range, payload, cruise speed, runway length, etc. As shown in the flowchart in Fig. 3.35, these requirements are first processed in the initial design, converting them into technical performance requirements such as engine thrust, wing area. For more information refer to [88]. Furthermore, the fuselage is dimensioned. These information are now available to all other tools via the aircraft exchange file or its attached data. Thus, the iterative process is initiated, in which a superordinate tool, the so-called convergence loop, controls all other tools [107]. In this iterative process, all further design tools are executed in a previously defined sequence and, after the last tool in the chain is executed, aircraft parameters such as maximum takeoff mass (MTOM) and

---

[†] The tool status corresponds to April 2023.

center of gravity, are compared with the last iteration step [107]. If the convergence criteria are met, the aircraft design is considered to be converged. The created design is evaluated and reports are written using a series of downstream tools.

Besides the clean sheet design mode, known aircraft data can be specified in advance, for example if a model of an existing aircraft is desired [107]. Typically, the initial sizing and the fuselage design are omitted in this case. Depending on the design tools, individual settings may be specified to avoid the recalculation of the specified values. Given the complexity of aircraft systems, MICADO's generalized semi-empirical methods might not precisely match every unique system implementation, leading to differences in key parameters like the MTOM or the operating empty mass (OME). However, MICADO offers a calibration mode that allows the MTOM to be influenced by calibrating the aerodynamic or engine efficiency [107]. Similarly, the OME can be influenced by calibrating the fuselage weight.

The modes of application previously mentioned focus on running the full MICADO design loop. The last mode discussed here refers to studies on a converged aircraft without making any changes in its design. With the so-called study loop it is possible in particular to simulate a mission for an aircraft that deviates from the design mission in order to assess its off-design performance. This takes place in an encapsulated loop, which only takes into account tools for the mission and system performance requirements, but does not re-dimension any components.

3.4.2 Discussion of selected tools

Four tools in particular are of great importance for this work and their functionality is discussed in more detail below. These tools involve the aerodynamic analysis, the wing mass estimation, the system design, and the mission analysis. Note that for a consistent overall design, all applied tools should be balanced in terms of their complexity, accuracy, and impact [93].

In simplified terms, four factors of impact are decisive for an aircraft in straight and level flight: lift, drag, weight, and thrust. The first two factors, lift and drag, are determined aerodynamically, therefore a higher level of complexity and computing time is appropriate. The corresponding aerodynamic analysis takes place in the tool `calculatePolar`. The total weight is calculated by summing the weights of individual components. Heavier components have a greater influence and are therefore especially important, justifying a higher computational effort. Using the `wingMassEstimation` tool, the wing structure is determined on the basis of the aerostructural coupling. The `systemsDesign` tool determines both system masses and their power requirement, which affects the thrust generation of the engine. The thrust generation itself is determined by using the data sets calculated with the aircraft propulsion design tool GasTurb [38] in order to provide a full thermodynamic gas-turbine cycle analysis [115]. Since this thesis uses prespecified engines and does not address the engine design methodology itself, it is recommended to refer to Risse [93] for further details. The mission analysis, in the eponymous tool `missionAnalysis`, does not directly design any of the mentioned parameters, but influences them through the evaluation of the aircraft.

`calculatePolar`

This tool computes the polars of the aircraft for different flight conditions, such as cruise, high-lift, or intermediate preset Mach numbers. The polar curves can be calculated using two distinct approaches. In both approaches, the combination of the wing and the HTP is first simulated under different free stream conditions for a range of angles of attack using the multi-lifting-line code `LIFTING_LINE` [44]. The results provide information on the lift and the induced drag [93], by considering the wing in its clean configuration. Note that the high-lift coefficients are determined semi-empirically [45, 88], since the iterative preliminary design does not allow the time consuming detailed calculations as in Section 3.1.

For the first approach, the drag components except for the induced drag are modeled using semi-empirical equations [45, 88, 124]. In the second approach, which was developed by RISSE [93] and extended by SCHÜLTKE AND STUMPF [108], a much more computational intensive method is applied to simulate the viscous and wave drag components at airfoil level. The simulation results are stored in a database, which is why this method is referred to hereinafter as the airfoil database approach. This approach takes into account that in addition to overall parameters like cruise speed and wing span, the specific aerodynamic data of airfoils are crucial for enhancing wing performance and reducing drag [115]. The airfoil database method allows to obtain the impact of airfoil geometry on the overall wing drag already in an early stage of preliminary aircraft design [115]. These correlations are important for this thesis, especially with regard to the application for variable camber, therefore the airfoil database method is applied and is discussed in the following. High-resolution 3D CFD analyses are inappropriate at this stage of aircraft design due to the difficulties of automation and the high computational processing time. Therefore, the airfoil database method described here is used with 2D CFD simulations on the airfoil and transfers the information to the wing.

In a step preceding the iterative design loop, the name-giving database is created. For this purpose, sections of the wing are transformed using the local sweep transformation [132]. In a very abbreviated form, this attempts to reproduce the thickness and curvature distribution of the tapered and swept wing on a two-dimensional wing section [132]. These transformed airfoils are now simulated over a predefined free stream range using the 2D CFD Euler/boundary layer flow solver MSES [28], and the results are saved in the database [93].

The process used in the iterative design process is discussed with reference to Fig. 3.36, derived from [93]; the following section refers to the individual depictions (A) - (I).

The geometry of the aircraft (A) serves as input for `calculatePolar`. For this aircraft, the aerodynamic polars need to be calculated (C), in this example using the C_L/C_D polar. The

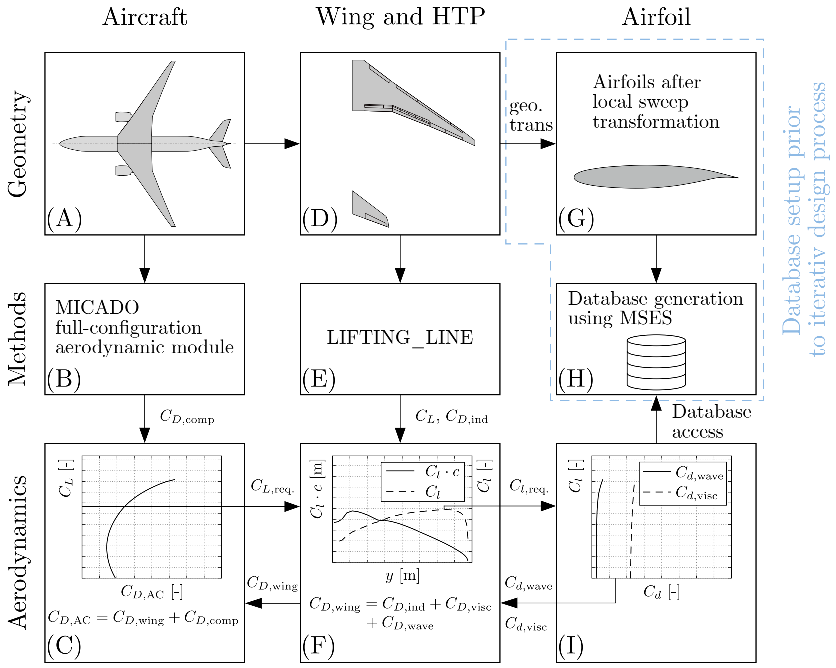

Figure 3.36: Interdependencies at aircraft, wing, and airfoil level within `calculatePolar` with activated airfoil database method, modified from [93].

C_L is covered at a prespecified angle of attack range and at a defined step size. A query is made for each C_L to the combination of the wing and HTP, which are considered to be the only lift-generating components. The geometry extracted from the overall aircraft for the wing and HTP (D) is simulated in LIFTING_LINE for a clean wing configuration over an angle of attack range (E). For the C_L query from (C), the lift distribution over the wing is then obtained (F) using the simulation results from (E). Note that the lift coefficient integrated over the wing does not necessarily correspond to the aircraft C_L, depending on whether the HTP generates lift or downforce. At the two-dimensional spanwise sections of the lift distribution of the wing (F), the two-dimensional lift coefficients C_l are queried to the database values (I). At each section polar, the values for the viscous drag and the wave drag are interpolated from the database (H), taking into account the previously performed geometric transformation for the 2D wing section geometries (G).

These values for the airfoil sections are now computed for the wing (F), together with the induced drag from LIFTING_LINE (E), to obtain a total wing drag. The drag calculation for the HTP is carried out on a semi-empirical basis. The thus-known drag value for the combination of wing and HTP is then returned to the overall aircraft polar for the queried C_L (C). Using semi-empirical methods to determine the remaining drag component of the aircraft (B), the total aircraft drag coefficient $C_{D,\mathrm{AC}}$ is calculated for the queried C_L. This process is repeated for all queried aircraft lift coefficients (C).

`wingMassEstimation`

In the conceptual and preliminary design phase, a sophisticated estimation of the wing mass is required to show the influence of geometric changes to the wings on the overall aircraft design [29]. In regard of this thesis, an accurate wing mass estimation is particularly important to represent variations in wing twist, but also to make statements in the case of variable camber integration.

The development process regarding the wing mass calculation in MICADO is described in [29]. Previously, a rigid wing flight shape was specified and the mass was estimated using semi-empirical methods [94]. Subsequently, it is described how the tool `wingMassEstimation` now extends MICADO with a more sophisticated methodology from the literature. The methodology is based on a flexible, aero-elastic wing, which also takes into account the so-called jig shape, i.e. the wing shape without aerodynamic loads. An accordingly dimensioned wing box is designed for the wing using FEM calculations, taking into account various load cases. The basic procedure, as shown in Fig. B.7 in the appendix, distinguishes between two possible processes, depending on whether the jig shape or the flight shape is known a priori. [29]

The flow chart in Fig. B.7 is briefly summarized here for both cases. First of all, note that both cases have in common that the underlying aero-structural coupling is based on a jig shape input [29, 46]. This jig shape is subjected to selected load cases under said aero-structural coupling in an inner convergence loop [29, 46]. As a result, the required wing box structure is obtained. Based on the now dimensioned wing box, a 1-g load case under cruising conditions is simulated, resulting in the flight shape. However, if a flight shape is specified as input, an initial jig shape is estimated and subsequently updated via an outer iteration loop until the calculated flight shape matches the prespecified flight shape [29]. As a further function, `wingMassEstimation` allows the examination of predesigned wing boxes under different flight conditions, for example with regard to their change in shape.

Three selected studies are conducted to investigate the influence of the more sophisticated method for the wing mass estimation. First, it is shown that for a reference aircraft, the change in wing shape within the limits of cruise flight due to varying lift coefficients during the mission does not have any relevant impact at this design stage. It is further shown that the influence of the wing shape change due to the deflection of flaps for a VC application is also negligible with regard to the mission fuel. However, the impact becomes evident when the same wing planform is simulated with different geometric twists. The resulting different load distributions over the wing lead to considerable changes in the required wing box dimensions and thus the aircraft mass. [29]

`systemsDesign`

A system modeling approach for MICADO is described by Lammering [59], which is derived from the classical ATA chapters, but due to its modularity provides enough space for the adoption of future innovative architectures, which cannot be classified into single chapters [115]. Each system is assigned a mass, a power demand in the respective mission segments, and a center of gravity [115].

Since this thesis focuses on the trailing edge flaps, the following addresses the underlying actuation system design in particular. As described in Chapter 2, the actuator system design for the approach chosen here requires a chain of methods. This includes the design of the high-lift surfaces, the acquisition of the load data, as well as their force and speed requirements via the kinematics for the actuator, and finally the actuator design itself. For this purpose, a process is integrated in `systemsDesign` that allows the actuator requirements to be acquired both in the high-lift case and in a VC application. When the design request is made within `systemsDesign`, the required parameters such as flow conditions and angle displacement of the flaps are transferred to the process chain.

The deployment of both the high-lift system and VC is modeled using hinge kinematics for a lowerable spoiler, broken down into 100 discrete steps to capture the process with high fidelity [115]. The aerodynamic loads, the component weight forces, and the dimensions of the kinematics determine the actuator load [115]. With the required load parameters, the actuators are designed either in centralized architecture, as described in Section 2.3, or as power-by-wire actuators, as described in Section 3.3.

`missionAnalysis`

The mission analysis uses a previously computed aircraft, either in the design loop as shown in Fig. 3.35, or in the study loop, based on an already converged aircraft. A detailed mission profile is simulated for this aircraft with specific parameters such as payload, range and cruise Mach number. The mission is divided into incremental steps for each of which the equations of motion are solved. Both the previously calculated mass and the trimmed aerodynamic polars, as described in Section 3.4.4, are taken into account [115]. Since the polars also contains the information about the flap deflection angle of each wing segment and the HTP angle, the respective angular positions in each mission step are obtained. The power requirements of the engines and systems are taken into account and the respective fuel consumption is calculated [93, 115]. The mission fuel is of particular importance as an evaluation parameter in the analyses in Section 4.2. In addition to a specified initial cruise altitude and step climbs, off-design studies and an optimization of the mission profile with regard to the specified flight range may be considered [93, 115].

`convergenceLoop`

The results of the individual design tools need to converge, as shown in Fig. 3.35, in order to enable a consistent aircraft design. The execution of the tools in a predefined sequence, the specification of the convergence criteria, and the monitoring of the convergence progress take place in the so-called `convergenceLoop` [93]. In addition to executing and monitoring the convergence, the `convergenceLoop` provides the functionality to calibrate aircraft designs to specified MTOM and OME values [107]. While the OME is calibrated to the desired value using a mass factor for the fuselage, two options are available regarding the MTOM. This allows the aerodynamic efficiency as well as the engine efficiency to be used for calibration. In this thesis, the approach to calibrate the engine is applied and the so-called fuel flow factor is used, which artificially increases or decreases the fuel consumption of the engine.

Additionally, the existing convergence loop includes a trimming approach. An angle of incidence for the horizontal tail plane is identified to trim the aircraft at the design point. However, this angle remains fixed throughout the entire mission, leading to untrimmed flight conditions outside the design range. This approach is inadequate for the applications considered in this thesis; therefore, a new methodology is introduced in Section 3.4.4.

3.4.3 Variable camber integration within MICADO

The integration of the functionalities of a VC application, as described in Section 2.5, in MICADO is extended in this thesis on the basis of the procedure discussed in [84]. Note that MICADO's design logic, as discussed in Section 3.4.1, assumes a single wing geometry that can be optimized within the tool. However, as described in Section 2.5.1, in the case of VC applications, the numerous possible flap settings effectively result in multiple wing geometries, not just one. This extends beyond the typical design scope of MICADO. A fundamental premise for the VC application applied in this thesis assumes that VC is applied to an existing aircraft without requiring it to be redesigned. The related concept of retrofit design is discussed in more detail in Section 4.2.

It is therefore important for the integration logic in MICADO that, as shown in the flowchart in Fig. 3.37, the VC application is based on a converged aircraft. Furthermore, relevant airfoil stations are selected and these geometries are stored in two ways for all permitted flap settings. In the first way, airfoils are stored in their line-of-flight orientation in order to analyze flap loads and the subsequent investigation of the actuators. The actuator investigation with the methodologies as described in Section 3.2 is used to analyze, whether a system redesign is required by the VC application. In this regard, reference is made to the results from [115], according to which the actuators are dimensioned by the high-lift application. The second way to store airfoil sections regards the local sweep transformation of airfoil sections, which are created to determine the wing and aircraft polars using the airfoil database approach as discussed in Section 3.4.2.

In order to incorporate flap deflections into `LIFTING_LINE`, either so-called mini-segments can be inserted in order to maintain a continuous trailing edge [53, 114], or the trailing edge exhibits discontinuities [29, 115], as applied in this thesis. In order to confirm the accuracy of the `LIFTING_LINE` calculations regarding a VC deployment, reference is made to analyses in the literature. Especially [52, 53] compare the `LIFTING_LINE` results to higher order CFD calculations; in [53] for the spanwise lift distribution and in [52] for overall aircraft polars.

The polars are calculated for every flap permutation to cover the whole range of possible VC settings. But in order to keep the computational costs for a large number of flaps within reasonable limits, a restriction of the angles of two adjacent flaps can be specified. After calculating all polars, the optimum flap setting per C_L increment is determined, resulting in an envelope polar, as depicted in Fig. 3.38. This procedure can be understood analogously to the procedures shown in the literature [119], as in Fig. 2.37. Details on the implementation can be found in [84], as the introduced polar merger allows for the criterion for the optimal flap setting to be defined. In this thesis, the optimum flap setting is defined to the minimum total drag, which leads to an optimization of the L/D.

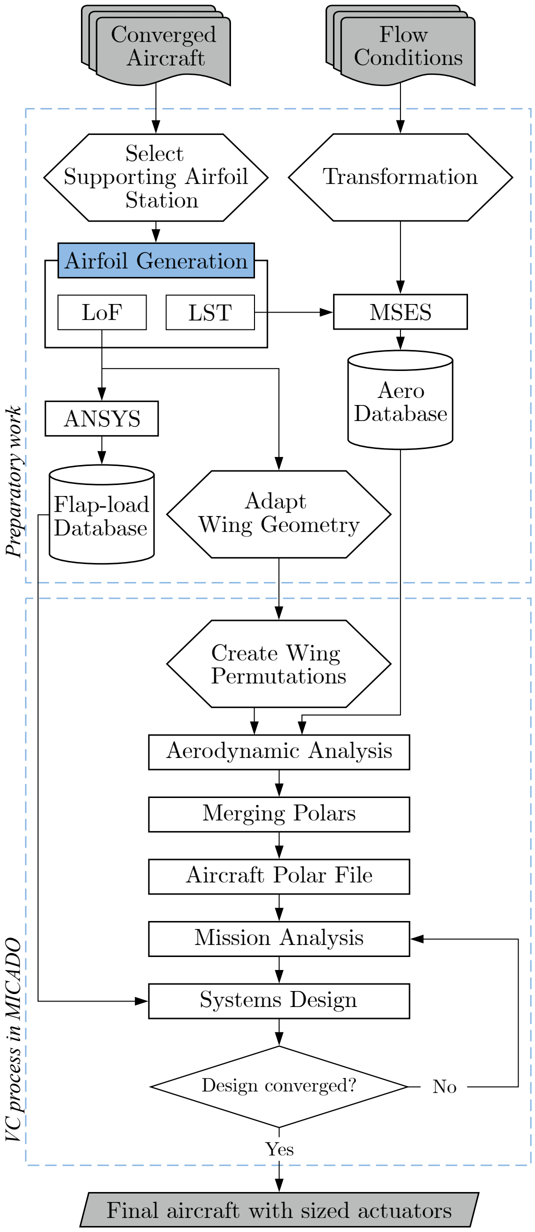

Figure 3.37: VC with DFS process chain within MICADO, with optional system design, adapted from [115].

Note that the high computational time requirement during the airfoil database generation and its use in the aerodynamic calculation of the polars is a limiting factor in the investigations. However, the influence of the geometry change due to VC on the wave drag, as also shown in Section 4.2, is of significant importance and therefore requires the application of the airfoil database.

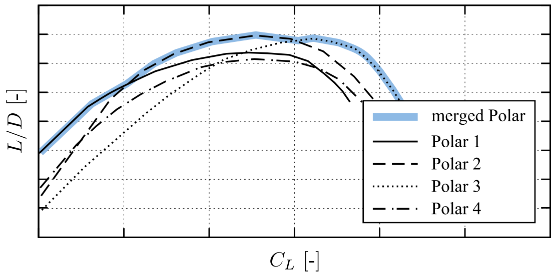

Figure 3.38: Schematic of the polar merging process [115].

3.4.4 Longitudinal trim integration within MICADO

In this section a novel methodology for a sophisticated longitudinal trim consideration is presented along with its implementation in MICADO. A meaningful preliminary aircraft design analysis requires a trimmed flight condition, especially when investigating VC applications, as discussed in Section 2.5. In the following, the novel methodology is explained, including various adjustable levels of detail as well as an explanation for the specific need for a distinct methodology. The limitations of the previous trimming method are briefly described in Section 3.4.2, resulting in the need for this novel methodology. The subsequent case study evaluates the novel methodology, compares it with the previous methodology, and provides application recommendations. Note that the master's thesis of Weber [130], supervised by the author, also addresses this topic.

Methodology using a grid interpolation scheme

To clarifying the challenge of considering a trimmed flight condition—meaning $C_M \overset{!}{=} 0$—in the preliminary aircraft design, reference is made to the procedure described in Section 3.4.2. The calculation of a demanded C_L value is carried out for the lift surfaces, combining the wing and the HTP at one fixed angle, considering the aerodynamic influence of other components empirically in the `calculatePolar` tool. The mass is determined in a separate tool. However, as the resulting center of gravity needs to be known for the moment balance for the trim, an iterative and therefore more time-consuming procedure is required. As detailed in Section 2.4, each point of the C_L polar curve needs to be trimmed by a different HTP angle, meaning that this procedure would additionally be required for each C_L step on the polar curve. Finally, if a change in the center of gravity during the mission is taken into account, the iterative trimming process would have to be performed for every possible mission step. This highlights that it is not feasible to determine the trimmed condition in this manner, as the computational effort would be excessive. In addition, the use of the airfoil database method for polar calculation already requires a very high computational effort, even for only a few HTP settings. However, neglecting a continuously trimmed flight condition would make any statements drawn from the calculations meaningless.

To address this problem, the methodology presented here uses an interpolation procedure. The starting point is the design condition for the aircraft. The design condition in this case refers to the $C_{L,\mathrm{Design}}$ and the set x_{CoG} in that design case. Consequently, the i_{HTP} is identified to provide a trimmed design condition.

In the following, two variables, i.e. i_{HTP} and x_{CoG}, are the available parameters for trimming regarding off-design cases. Figure 2.33 shows the respective influence on the trim. An interpolation grid is established for these two variables on the basis of the design case. This interpolation grid is shown in Fig. 3.39, with the respective effects on the moment curve indicated schematically by the $C_M - \alpha_{\mathbf{a}}$ curve. For the purpose of readability, the interpolation between i_{HTP} values with a fixed x_{CoG} in the design point is discussed first and subsequently, the influence of a variable center of gravity is addressed.

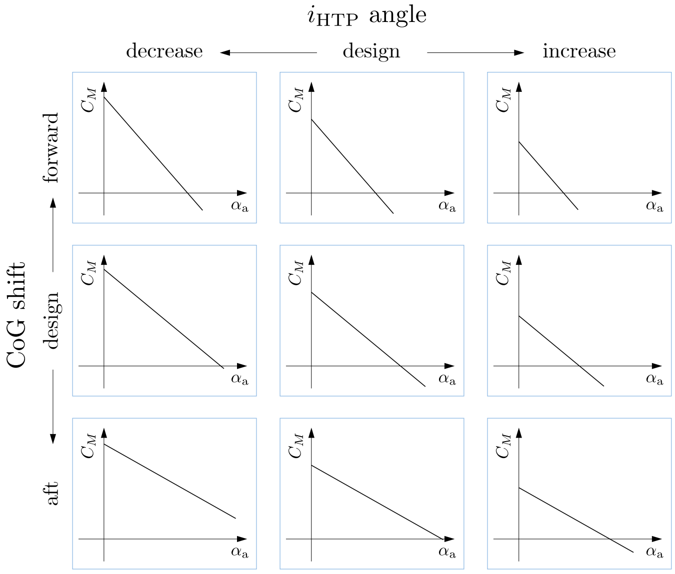

Figure 3.39: Schematic interpolation grid for longitudinal trimming over the HTP angle i_{HTP} and the center of gravity x_{CoG}.

Interpolation via the HTP angle Assuming that the center of gravity remains fixed in the design point, the polars are solely trimmed by the i_{HTP}, corresponding to the horizontal grid points in Fig. 3.39. As described in Section 3.4.2, the polars are determined for several flight conditions, i.e. different Mach numbers and flap configurations. All these polars need to be trimmed, but since the process is analogous, only exemplary polars are shown in the following.

As explained above, it is not feasible to perform new calculations for each flight condition occurring during the mission analysis, therefore the polars need to be determined prior to the mission analysis. The presented procedure of the interpolation grid allows to calculate all flight conditions requested with only a few grid points. The specific selection of grid points is discussed below, but first it is necessary to show that interpolation is permissible in the first place.

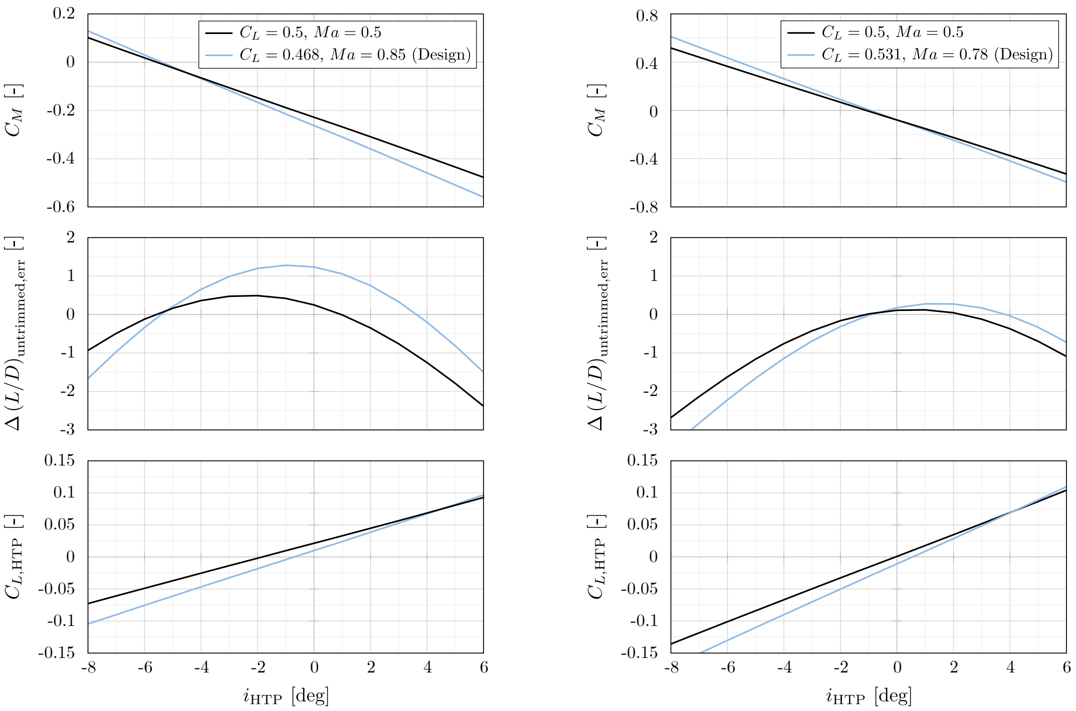

(a) Long range reference

(b) Short range reference

Figure 3.40: Check for interpolation capability via i_{HTP}, shown for two aircraft references and two flight conditions; top: Moment coefficient C_M, center: L/D deviation, bottom: HTP loading $C_{L,\text{HTP}}$.

For this purpose, Fig. 3.40 shows the curve of the moment coefficients, as well as the deviation of the L/D from the trimmed state, and the aerodynamic load on the HTP. This evaluation is carried out for both the long range reference (a) and the short range reference (b), as introduced in Table 3.11. Note that the curves shown in Fig. 3.40 represent only for the point at $C_M = 0$ a trimmed and therefore operable value. However, the purpose of this diagram is to demonstrate that the trimmed state can be interpolated from untrimmed grid points.

First, the moment coefficient C_M curve shown in Fig. 3.40(a) at the top is discussed. Two curves are shown, one for the C_L and Mach number combination of the design condition, the other for an exemplary alternative flight condition with $C_L = 0.5$ and $Ma = 0.5$. For both flight conditions shown, the strictly linear progression of the moment coefficient over the HTP angle is evident.

The curve shown in the middle representing the deviation of the calculated $(L/D)_{\text{calc}}$ from the $(L/D)_{\text{trim,design}}$ in the trimmed state for different i_{HTP} is more complex to analyze. This deviation is defined as

$$\Delta\,(L/D)_{\text{untrimmed,err}} = (L/D)_{\text{calc}} - (L/D)_{\text{trim,design}}\,. \tag{3.4}$$

Note that the definition of the $\Delta\,(L/D)_{\text{untrimmed,err}}$ deviation from the trimmed state is intended to underline that these i_{HTP} values do not lead to airworthy flight configurations for which the L/D could be achieved. Rather, every point on the curve except for $i_{\text{HTP}|C_M=0}$ is not trimmed, regardless of whether the L/D ratio might be favorable. In essence, this parameter provides a statement about the aerodynamic efficiency, therefore it is relevant to ensure that it can also be interpolated from untrimmed grid points to a trimmed state. Two points are of particular importance here, firstly the trimmed state itself indicating the design condition, which for the blue curve, lies at $i_{\text{HTP}} = -5.4\,\text{deg}$. Secondly, the curves reveal a maximum with regard to the L/D, which corresponds to the case of an unloaded HTP. In Fig. 3.40(a), bottom figure, this point of an unloaded HTP for the design condition (blue) lies at $i_{\text{HTP}} = -0.6\,\text{deg}$. To put it briefly, although the aircraft exhibits here the highest efficiency, expressed in L/D, it is not trimmed and would not be able to maintain the steady state of flight.

It is noticeable that in Fig. 3.40(b) for the short range, the trimmed state ($i_{\text{HTP}} = -0.9\,\text{deg}$) is significantly closer to the point of unloaded HTP ($i_{\text{HTP}} = 0.5\,\text{deg}$) for the design condition, depicted in blue. Consequently, the maximum of the L/D curve is considerably closer to the trimmed state. A further consideration and calibration option for this relationship follows below.

However, the curves of the $\Delta\,(L/D)_{\text{untrimmed,err}}$ ratios indicate that, in contrast to C_M and $C_{L,\text{HTP}}$, linear interpolation cannot be arbitrarily applied. Therefore, an analysis of different interpolation grid point configurations is provided below.

Interpolation via the center of gravity position Following the discussion of interpolation via the HTP angle, this section deals with interpolation in the case of a center of gravity shift during the flight, corresponding to the vertical interpolation grid in Fig. 3.39. In order to provide the aerodynamic data of the polars over the entire CoG range to the mission analysis, the process discussed above is repeated for two additional CoG positions in addition to the design CoG. These center of gravity positions are calculated in the mass estimation tool and represent the foremost and the rearmost possible center of gravity. Therefore, all the three center of gravity grid points yield a set of aerodynamic data, which are trimmed for their respective x_{CoG}. The aerodynamic data for the actual center of gravity positions that occur during the mission are interpolated from these data. In contrast to the interpolation via i_{HTP}, which is carried out within the `calculatePolar` tool and returns trimmed polar curves, the interpolation considering the center of gravity shift needs to be conducted in `missionAnalysis` for each single mission step. This leads to a significant increase in the required computing power. These two interpolation processes, via i_{HTP} and x_{CoG}, thus establish the designated interpolation grid, in the basic case with the nine grid points shown in Fig. 3.39.

Calibration with respect to an unloaded HTP in the design case As shown in particular in the middle image in Fig. 3.40(a), a heavily loaded HTP reduces the efficiency of the aircraft. Refer to Section 2.4.3 for the theoretical background. This circumstance needs to be taken into account in the aircraft design, but it might be the case that the methods do not adequately capture the moment coefficient. Furthermore, in some circumstances only unsuitable airfoils may be available, which result in a sufficient L/D but not a satisfactory moment balance. In these cases, the option to calibrate the zero moment $C_{M,0}$ is available. For the evaluation given above, this option was not applied.

Case studies and refinement strategy

Two aspects need to be addressed regarding the introduced methodology: Firstly, a recommendation for the choice of the interpolation grid is to be made. Secondly, to provide the foundation for this recommendation, an evaluation is needed regarding the impact of this methodology on the results of the preliminary aircraft design. This evaluation particularly compares the new methodology with the previous approach of identifying a fixed HTP angle throughout the entire flight envelope, determined from the design flight condition, as calculated within the `convergenceLoop`, see Section 3.4.2.

In order to provide conclusions on these aspects, refinement parameters of the methodology are varied for both the short range and the long range reference. First, a study of the i_{HTP} grid resolution is carried out, followed by an investigation of the impact of a x_{CoG} shift. All results for the different setting parameter combinations are derived from separate, converged aircraft designs with identical MTOM and OME constraints. Refer to Section 3.4.2 for information about the calibration process.

Grid study for i_{HTP} In order to evaluate the necessary grid resolution concerning the horizontal tail plane angle i_{HTP}, test cases were conducted across various levels of refinement. The information on the grid resolution of the test cases is given in Table 3.14, with the grid spacing relative to i_{HTP} under design conditions. The range for i_{HTP} is set to ±6 deg, which was identified as the maximum variation including safety factors under off-design conditions in preliminary studies.

Table 3.14: Grid refinement test cases for i_{HTP}.

Case	# i_{HTP} grid points	Grid spacing rel. to $i_{\text{HTP,design}}$ [deg]
Fixed HTP	1	0.0
Ultra Fine (ref.)	11	-6.0; -4.0; -2.0; -1.0; -0.5; 0.0; +0.5; +1.0; +2.0; +4.0; +6.0
Fine	7	-6.0; -4.0; -2.0; 0.0; +2.0; +4.0; +6.0
Medium A	5	-6.0; -2.0; 0.0; +2.0; +6.0
Medium B	5	-6.0; -0.5; 0.0; +0.5; +6.0
Coarse	3	-6.0; 0.0; +6.0

The "Fixed HTP" scenario is based on the aircraft being trimmed once under design conditions. This fixed HTP angle is maintained for all aerodynamic calculations. It is worth repeating that with a fixed HTP, the aircraft is untrimmed in any off-design condition. The "Ultra Fine" case, in contrast, offers the highest tested grid resolution with 11 points, with additional refinement close to the design point. In the following, this case serves as a benchmark reference for all other cases, as it provides the most accurate results due to its extensive coverage. The "Fine" case includes 7 grid points, whereas the medium cases, labeled "Medium A" and "Medium B", both incorporate 5 grid points. "Medium A" distributes these points more uniformly. In contrast, "Medium B" concentrates them near the design point for higher precision in this critical area, where the aircraft operated most of the mission span. Lastly, the "Coarse" grid case utilizes the most basic setup with just 3 grid points, one at the design condition and two at the boundary values of ±6 deg.

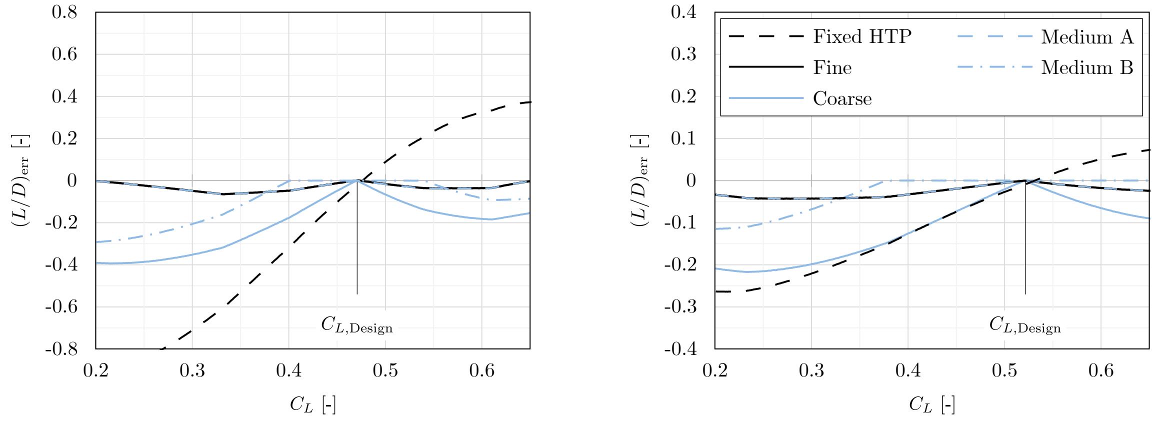

(a) Long range reference

(b) Short range reference

Figure 3.41: Effects of different grid resolutions for i_{HTP} with respect to the error in L/D.

To investigate the impact of the different i_{HTP} grid resolutions, the respective errors in L/D is analyzed with respect to the "Ultra Fine" reference over a C_L range. The curves of the errors, $(L/D)_{\text{err}}$, are shown in Fig. 3.41 for the long range and the short range reference aircraft at their respective cruise Mach number. It is important to emphasize again that, in the shown investigations, differences in $(L/D)_{\text{err}}$ do not represent an increase or decrease in the aircraft efficiency, but an error caused by an inaccurate trim consideration of the specific grid refinements.

The evaluation, starting with the case of the fixed HTP, shows that this case is precise only for the $C_{L,\text{Design}}$. This result is expected, since due to the fixed HTP, only the design condition is trimmed. However, this case also shows that the error in the L/D is negative for $C_L < C_{L,\text{Design}}$, but positive for $C_L > C_{L,\text{Design}}$. This circumstance results in the fact that solely analyzing the fuel consumption at the mission level would be inadequate since these errors would likely negate each other. The reason for this is that, as shown in Fig. 2.35, a C_L range is usually used on both sides of $C_{L,\text{Design}}$ during the course of the mission. The magnitude of the error differs depending on the configuration, e.g. for the long range reference an error in the L/D of -0.415 occurs at a of $\Delta C_L = -0.1$ to $C_{L,\text{Design}}$, while for the short range reference the error is only -0.093. Note that even if parameters such as mission fuel appear to be quite precise due to errors in the calculations negating each other, the calculation remains unreliable and therefore inadequate.

The "Fine" grid resolution yields low errors for both reference aircraft across the entire C_L range. Thus, the absolute error $|(L/D)_{\text{err}}|$ for the long range reference is consistently below 0.07 within the analyzed C_L range and below 0.05 for the short range reference.

It is worth highlighting that the "Medium A" case achieves the same good results with two less grid points than "Fine". This can be explained by the fact that in the C_L range under consideration, only the interpolation points -2.0, 0.0 and +2.0 are used. With the same number of grid points in case "Medium B", the small but in the flight mission particularly relevant C_L band near $C_{L,\text{Design}}$ is particularly accurate, but the accuracy outside of this band decreases slightly.

Finally, "Coarse" is the case that offers the fewest interpolation points with only three grid points. Due to the range in i_{HTP} of ±6 deg to be covered as required for this study, the three points are far apart to each other. For the short range reference, this is reflected in only slight gains in accuracy compared to the fixed HTP. However, a trend can also be observed, which is more apparent for the long range reference, showing that the $(L/D)_{\text{err}}$ does not continue to increase with greater C_L distance.

In order to draw a conclusion for an application recommendation from the findings, the required additional computing power has to be taken into account. An initial estimate for the `calculatePolar` tool suggests that a multiplication of the i_{HTP} grid points results in an equally high multiplication of the computing effort, as a full polar calculation is performed for each grid point. Depending on the method chosen for the calculation, this has a corresponding influence on the overall time of the aircraft design process. For example, with activated airfoil database method, `calculatePolar` is decisive for the overall run time. In relation to the expected accuracy gains described above, the "Ultra Fine" and "Fine" cases require significantly more computing time than justifiable. An application of the medium cases is more likely to be considered, as long as the computing time is not a strictly limiting factor. If the airfoil database method is activated, however, the "Coarse" case is recommended as a trade-off between computing time and accuracy. The case with ±6 deg as stated in Table 3.14 is set as default in the configuration files, but can be adapted as required. It is advisable to set the limits more narrowly in order to capture the relevant C_L range more accurately. However, this depends heavily on the reference aircraft.

Usually, the ±6 deg range does not cause any issues with the polar calculations, however, if the airfoil database method is activated, the following situation may occur in which the grid point limits need to be selected manually: should, due to the strongly deflected HTP angles of the interpolation grid points, the wing be exposed to higher loads than the airfoil database method is able to provide aerodynamic data for, no values will be interpolated for this C_L range and the polar curve becomes short. If these values are required during the flight mission, the design process is aborted. In such cases, an individual selection of the two grid points is necessary.

Consideration of x_{CoG} Finally, a brief evaluation is given regarding the option of considering the shift of the aircraft's center of gravity during the mission due to fuel consumption. In contrast to the interpolation analysis of i_{HTP} discussed above, this analysis has to be carried out at mission level, as the shift of the center of gravity only occurs during the mission. For this purpose, both the long range reference with 8 100 NM and the short range reference with 2 500 NM are assigned a fixed mission profile with corresponding step climbs. Further details on the missions are discussed in Section 4.1. The diagrams over the mission range for both reference aircraft are provided in Fig. 3.42, which provides the basis for analyzing the difference when taking the center of gravity shift into account. In order to solely analyze the impact of considering x_{CoG} shifts, the i_{HTP} interpolation grid "Fine" and, thus, the one with the highest accuracy is used.

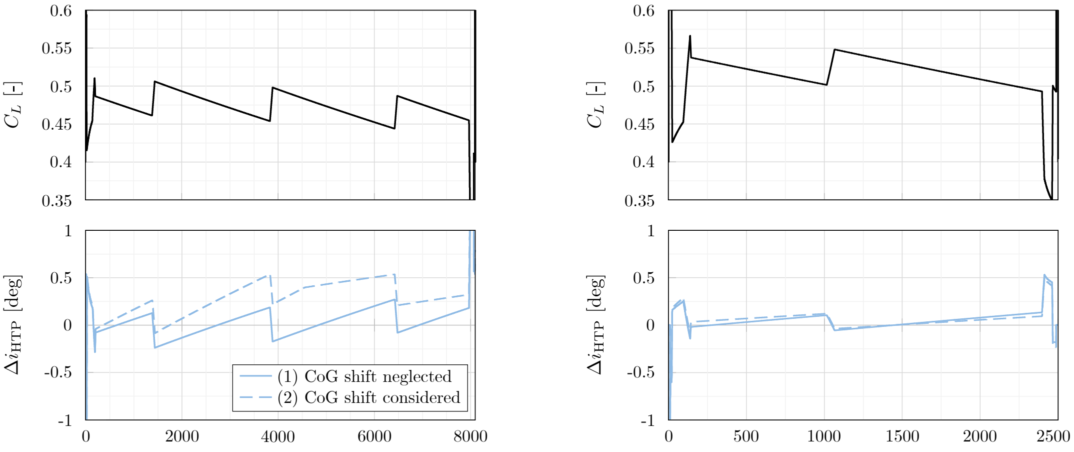

(a) Long range reference

(b) Short range reference

Figure 3.42: Impact of considering the CoG shift over the mission for two aircraft references; top: lift coefficient C_L, bottom: HTP angle deviation with and without CoG shift consideration.

For both reference aircraft, the C_L curve over the range is shown at the top. Since the difference between considering and neglecting the CoG shift is insignificant, only one curve is plotted. The bottom curve shows Δi_{HTP}, which is the deviation of the HTP deflection compared to the design conditions. To reference the cases more easily, the case with a fixed CoG is labeled (1) and the case with a shifting CoG is labeled (2).

Beginning with the short range reference in Fig. 3.42(b), the HTP angle follows a sawtooth pattern over the course of the mission for both cases (1) and (2) around the $i_{\text{HTP,Design}}$. This sawtooth pattern of the i_{HTP} trend is directly linked to the corresponding C_L profile over the mission segments, as seen in the C_L trend in Fig. 3.42(b). The impact of the different considerations (1) and (2) of x_{CoG} becomes evident in the varying slopes of the curves in the i_{HTP} trend. These different slopes arise due to the circumstance that the fixed center of gravity (1) calculated for the design case using semi-empirical methods is located between the start and end point of the shifting center of gravity. While this location is intuitive, it is not a necessity. Regarding the maximum deviation of i_{HTP} between cases (1) and (2), the differences are negligible. These negligible differences are caused by the small center-of-gravity shift in case (2) over the entire mission, amounting to only 0.17 % in relation to the aircraft length.

The situation is different for the long range aircraft, with a center of gravity shift of 0.57 % relative to the aircraft length. This larger shift of the CoG explains one aspect of the larger deviation in i_{HTP} between cases (1) and (2), reaching a maximum of 0.45 deg, shown in Fig. 3.42(a). The general sawtooth pattern of the i_{HTP} trend originates again from the sawtooth pattern in the C_L requirement shown in the above plot. In case (2), the center of gravity shifts further backwards from this position, hence the i_{HTP} in (2) does not move around $i_{\text{HTP,Design}}$. Another aspect is noticeable in the progression of Fig. 3.42(a): case (2) exhibits a slight kink in the progression at around 4 600 NM. This curve is caused by the tank configuration of the long range aircraft with a significantly larger center tank, whereas this is hardly significant for the short range aircraft.

This gain in accuracy needs to be considered against the increased calculation time. For instance, three times as many polars are calculated, in addition to the increased computing time within `missionAnalysis`. While the effects of the CoG shift consideration on conventional aircraft are relatively small, it is essential to take this into account for configurations with a tank in the rear or another configuration with a high CoG shift.

Summary In this section, the logic of the aircraft preliminary design software MICADO and selected tools are discussed. The way in which variable camber is integrated into the preliminary design process is shown. The focus in this section is on the methodology developed for longitudinal trim, as well as its evaluation and analysis, as the longitudinal trim is particularly important for the VC application.

4 Application and analysis of variable camber technology

This chapter addresses the application of the theoretical foundations and methodologies to the overall aircraft level. The implementation of variable camber at the trailing edge of the wing using segmented control surfaces is the key aspect.

Retrofit design definition In this thesis, the VC system is applied as a so-called retrofit. This approach means that the aircraft is not redesigned using the full MICADO process from Fig. 3.35, but the retrofit system is introduced to an existing aircraft and only the necessary system masses are added. However, by adding the systems mass or necessary structural mass from the retrofit application, the TOM must not exceed the MTOM, as the naming maximum takeoff mass also implies. Other systems, e.g. the landing gear, are designed for this MTOM and are not redesigned in this retrofit approach. All additional masses of the retrofit application need to be compensated for by less fuel or payload in order to avoid exceeding the MTOM. Less fuel does not necessarily lead to a reduction in range, as the retrofit system in this case increases the efficiency and therefore reduces fuel consumption. The reasoning of this retrofit approach is to investigate the potential that can be realized with existing aircraft. Entirely new aircraft redesigns for individual technologies are a less likely scenario due to the high associated costs.

The methodologies presented in Sections 3.1 - 3.3 focus on the design of high-lift systems, including the configuration, the flap loads, and the actuation. As described earlier, the concept behind this thesis is to provide the designer with reliable methods for establishing the high-lift system and thus a profound basis for the reference aircraft. Following this concept, in Section 4.2, the VC technology is subsequently retrofitted to existing high-lift systems, for which the design methodologies have been provided.

As stated in [115], the dimensioning case for the actuation system is the high-lift case, therefore the actuators do not need to be re-dimensioned in the retrofit approach for the VC application. Other systems, for instance those enabling the differential flap setting in a conventional actuator architecture, need to be added as a retrofit system.

For the application of VC to segmented trailing edge control surfaces, the analysis reference is first introduced in Section 4.1. This includes the aircraft references and the benchmark missions. In Section 4.2, the analysis is then carried out at the overall aircraft level. As the amount of potential VC application variants is extremely high due to the numerous segmentations and their respective flap setting permutations, an evaluation methodology is also introduced for a transparent analysis approach of selected VC variants. The application and methodology for analyzing a segmented variable camber system that was developed in the course of this thesis, was also addressed by the author in a journal article [115].

4.1 Reference aircraft setup and benchmark mission definition

This section defines the aircraft references and benchmark missions required for the following evaluation of the variable camber application on segmented trailing edge flaps. In Section 4.1.1, a total of three reference aircraft is introduced, including one long range and one short range reference based on the CeRAS framework, and one additional long range reference with an optimized wing twist distribution. In Section 4.1.2, for both the short range and the long range, two missions are introduced. These missions represent cruise profiles with advantageous steps, close to design conditions, as well as off-design missions.

4.1.1 Reference aircraft design

Two initial aircraft designs are employed, a long range reference (LR) and a short range reference (SR). Both the long range reference and the short range reference are derived from aircraft references within the framework of CeRAS[*]. These designs correspond to the aircraft references introduced in Section 3.2; however, in the following a larger flap angle range is enabled for the VC application. An additional reference is defined based on the given long range reference. This additional reference optimizes the wing regarding aero-structural interactions by means of an adapted twist distribution prior to the VC application. Thus, this pre-optimized long range reference aircraft provides a classification in the analysis of how the fuel savings potential of VC changes if other optimization measures are implemented simultaneously.

Long range reference

The long range reference, to which the VC application is subsequently to be applied as a retrofit system, is generated in MICADO on the basis of specifications and requirements, with the design process as described in Section 3.4. An excerpt of the specifications and requirements is given in Table 4.1. The wing planform and the fuselage are prespecified, a more detailed wing geometry description is given in Table 4.2.

---

[*] The CeRAS (Central Reference Aircraft Data System) project of the ILR is a publicly accessible database with data sets on various aircraft configurations. A short range reference is available, a long range reference will be published in the near future. Further information can be found in [95].

Table 4.1: Excerpt of the long range aircraft requirements.

Parameter	Unit	Value
PAX	[-]	325
Range	[NM]	8 100
Ref. wing area	[m^2]	443
Cruise Mach	[-]	0.85
Wing span	[m]	64.8

The resulting converged aircraft design serves as the starting point for the upcoming analysis and is referred to below as the baseline reference (LR-BSL-ref). With the above-mentioned approach that the aircraft fuel consumption may also be optimized in other ways than VC, the aero-structural optimization of the wing twist distribution is introduced based on the same requirements in Table 4.1. This second long range reference is referred to below as LR-ASO-ref. Again, the fuselage and wing geometry, except for the twist, is prespecified. With both the LR-BSL-ref and LR-ASO-ref, evaluations are enabled regarding the fuel saving potential for the baseline in three different ways: first, the straightforward VC application to the baseline aircraft, second, the wing twist optimization without a VC application, and third, the combined application of VC and the wing twist optimization.

Baseline reference (LR-BSL-ref) With this reference, an existing aircraft model is included in the analysis for the VC application without performing further optimization steps in order to provide a comparison case. The overall preliminary aircraft design performed in MICADO, according to Section 3.4.1, results in an MTOM of 270 t; this and further key aircraft parameters are given in Table 4.3. The calculations are conducted using the specification as stated in Table 4.1, as well as, the configuration values set in Table C.1 in the appendix. A discussion, which also includes details of the wing geometry, is presented below in comparison with the LR-ASO-ref. A schematic view model is shown in Fig. 4.3.

Aero-structural optimization reference (LR-ASO-ref) As stated above, the long rang baseline reference and its VC retrofit are contrasted with another approach to performance optimization that also enhances the lift distribution. This is done in particular with an adjustment of the twist distribution over the wing. This approach is also described by the author in [115]. The upcoming VC application is a retrofit design, with the definition given in the beginning of Chapter 4. However, changing the twist distribution alters the load distribution on the wing, which leads to a change in wing mass; this is a more fundamental modification that requires an entire redesign of the aircraft. The implications between the load distribution and the wing mass are calculated within the tool for the wing mass estimation, as described in Section 3.4.2, as well as [29]. The conducted adjustment mainly balances the opposing effects of the aerodynamic drag and the structural wing mass. As described in Section 2.5.1, the induced drag is minimized for an elliptical lift distribution [5], placing the center of lift further outboard, while an inboard lift center reduces the root bending moment, thus decreasing the wing's structural mass [91].

In addition to these opposing effects, effects such as the wave drag are also significant. The target parameter of the optimization is the minimization of the mission fuel during the design mission, as the quantitative influence of the above-mentioned variables hereby becomes evident. By executing the overall MICADO process for each twist distribution under investigation, the LR-ASO-ref aircraft is established for the identified optimum. The specifications as in Table 4.1 and the configurations as stated in Table C.1 apply. A direct comparison to the LR-BSL-ref follows below.

Comparison: LR-BSL-ref to LR-ASO-ref In order to compare the two long range references, the differences in the twist distribution are highlighted first. Note that the other wing parameters are given in Table 4.2 and are prespecified identically for both long range references as described above. Figure 4.1 details the spanwise twist distributions for both long range references separately. The inboard twist of the LR-ASO-ref is significantly reduced by the adjustment, which leads to the results given in Table 4.3 on the overall aircraft level.

Table 4.2: Geometric values of the wing for the LR-BSL-ref and LR-ASO-ref in flight shape [115].

Parameter	Symbol	Unit	Values				
Ref. Airfoil[†]			L1	L2	L3	L3	L3
Spanwise position	y	[m]	2.9	10.5	20.3	29.5	32.4
Chord length	c	[m]	13.5	7.9	4.9	2.3	1.5
LE sweep angle	φ_{LE}	[deg]	0.0	37.3	35.0	35.0	37.0
TE sweep angle	φ_{TE}	[deg]	0.0	1.8	21.4	22.8	24.8
Dihedral	ν	[deg]	0.0	9.4	8.3	13.0	17.0
Thickness ratio	t/c	[-]	13.1	11.0	9.4	9.4	9.4

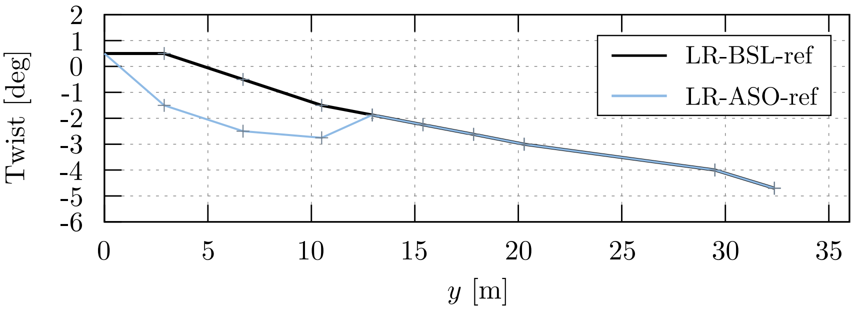

Figure 4.1: Twist distribution for both LR-BSL-ref and LR-ASO-ref.

The mission profile regarding the individual flight levels are depicted in Fig. C.1. Note that this design mission is shown in the appendix, since it is not considered for later comparisons including VC. Instead, benchmark missions are defined in Section 4.1.2. The reason for the introduction of a separate benchmark mission from the design mission is discussed in that section as well.

Figure 4.2(a) provides the lift distribution for both references and gives a good indication of how the fuel savings potential arise. Note that the comparison is conducted for the $C_{L,\mathrm{opt}}$ of the

---

[†] The stated reference airfoils are `L1: NASA SC(2)-0614`, `L2: NASA SC(2)-0712` and `L3: NASA SC(2)-0710`, which were adjusted in thickness according to Table 4.2.

Table 4.3: Key parameter of both the LR-BSL-ref and the LR-ASO-ref.

Parameter	Unit	LR-BSL-ref	LR-ASO-ref
MTOM	[kg]	270 135	267 692
OME	[kg]	140 136	141 176
Wing mass	[kg]	30 395	31 708
Design mission fuel	[kg]	99 370	95 886
$(L/D)_{\text{opt}}$	[-]	20.18	20.85
$C_{L,\text{opt}}$	[-]	0.504	0.494
$C_{D,\text{total}\,@\,C_{L,\text{opt}}}$	[-]	0.0250	0.0237
$C_{D,\text{ind}\,@\,C_{L,\text{opt}}}$	[-]	0.0096	0.0088
$C_{D,\text{visc}\,@\,C_{L,\text{opt}}}$	[-]	0.0143	0.0141
$C_{D,\text{wave}\,@\,C_{L,\text{opt}}}$	[-]	0.0011	0.0008

LR-BSL-ref, however, as stated in Table 4.3, the difference to the optimum of LR-ASO-ref is marginal. The LR-ASO-ref identifies a lift distribution to be optimal that de-twist in the inner wing region, as shown in Fig. 4.1. Thereby, the angle of attack increases, in order to provide the same overall lift. A consequence is that despite the same outboard twist distributions, see Fig. 4.1, the outboard lift distributions differ, see Fig. 4.2(a). However, the increased outboard lift of the LR-ASO-ref is limited by the sensitivity to a strong increase in wave drag of the outboard airfoils [115]. This basically makes a statement about VC applications before VC has even been analyzed: the airfoils are a limiting factor in VC, i.e., disadvantageous characteristics with positive or negative deflection reduce the potential considerably. Although in the case of VC, only the flap is deflected and not the entire airfoil as in the case of a change to the twist, the correlation persists.

Fig. 4.2(b) presents the drag components of the wing in comparison for both the LR-BSL-ref and the LR-ASO-ref. The majority of the drag reduction achieved on the wing results from the lowered induced drag caused by the differences in the load distribution, see Fig. 4.2(a). The changes in the viscous and wave drag components, however, remain significantly lower.

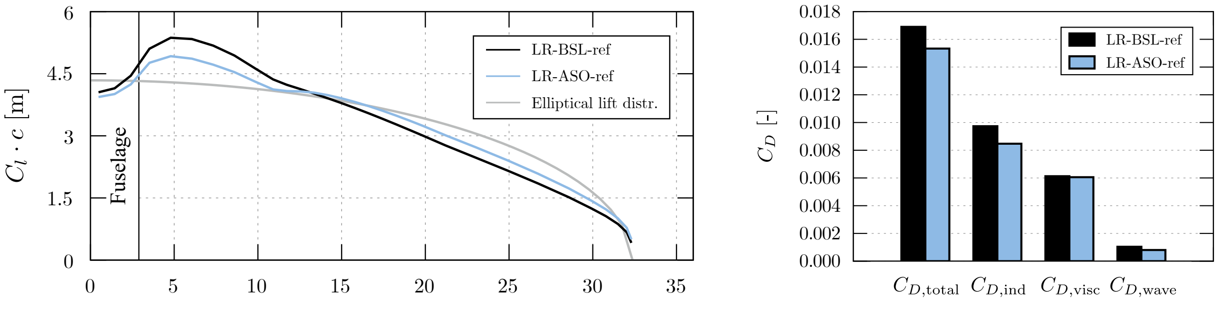

(a) Spanwise lift distribution

(b) Drag components of the wing

Figure 4.2: Comparison of the lift distributions and drag components of the LR-BSL-ref and LR-ASO-ref at $C_{L,\text{opt,BSL,Ref}}$ and $Ma = 0.85$ [115].

A visualization of the LR-BSL-ref aircraft is given in Fig. 4.3 on the left side. Due to the same pre-defined wing planform, this visualization is very close to the LR-ASO-ref, which is why it is not shown separately. In addition, the airfoil sections of the wing are marked in blue, which are necessary to enabled the VC with DFS application in Section 4.2.

The identified optimum incorporated in LR-ASO-ref, which achieves on the aerodynamic side an increase of 3.3 % in L/D compared to LR-BSL-ref, has to compensate for a 4.3 % increase in wing structure mass. In the overall aircraft design, this leads to a 0.9 % reduction in MTOM relative to the LR-BSL-ref while maintaining the same top-level aircraft requirements and specifications from Table 4.1. It is worth repeating that the resulting change in structural mass of the wing leads to the necessity of performing a redesign at the overall aircraft level. The elliptical lift distribution, as shown in Fig. 4.2(a), is optimal from an aerodynamic point of view for a given wing span. However, this aerodynamic optimum does not necessarily represent the overall optimum at the aircraft level, since the outward shift in lift necessitates additional reinforcement of the wing structure, leading to a considerable increase in the aircraft mass and, therefore, mission fuel [115].

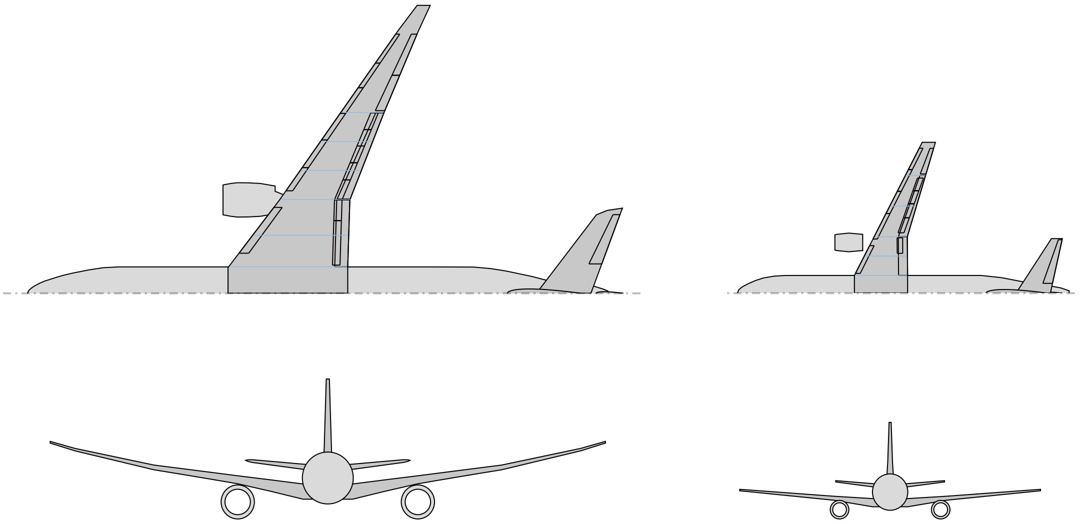

Figure 4.3: Schematic views of the LR-BSL-ref (left) and the SR-BSL-ref (right) with marked (blue) airfoil sections for VC.

Short range reference

In addition to the two long range reference aircraft introduced above, this study incorporates a short range reference to provide an independent baseline. The short range aircraft is developed using the same MICADO design process based on the CeRAS CSR-02 reference aircraft. The design process is conducted adhering to specifications outlined in Table 4.4 and tool configuration settings from Table C.1. Detailed wing parameters are given in Table 4.5. The reference airfoil is the DLR F15 [108], which is adjusted in thickness at the distinct spanwise sections according to Table 4.2. The design mission profile is given in Fig. C.2. This reference is significantly lighter, with a maximum takeoff mass of 77 tons, compared to the approximately 270 tons of the long range references. Figure 4.3 illustrates the short range aircraft configuration. The key aircraft parameter are stated in Table 4.6.

Table 4.4: Excerpt of the short range aircraft requirements.

Parameter	Unit	Value
PAX	[-]	150
Range	[NM]	2 500
S_{ref}	[m^2]	123
Cruise Mach	[-]	0.78
b	[m]	34.1

Table 4.5: Geometric values of the wing for the SR-BSL-ref.

Parameter	Symbol	Unit	Values			
Ref. Airfoil			S1	S2	S3	S3
Spanwise position	y	[m]	2.0	6.4	13.3	17.0
Chord length	c	[m]	6.0	3.8	2.3	1.5
LE sweep angle	φ_{LE}	[deg]	0.0	27.0	27.0	27.0
TE sweep angle	φ_{TE}	[deg]	0.0	-0.6	16.6	16.6
Dihedral	ν	[deg]	0.0	5.0	5.0	5.0
Thickness ratio	t/c	[-]	15.0	12.0	11.3	11.0

4.1.2 Benchmark mission definition

Two distinct approaches can be considered for evaluating the influence of variable camber. One approach involves analyzing the impact of VC on predefined mission profiles, while the other allows the aircraft to operate on individual mission profiles. Both methods have their merits. Tailoring individual mission profiles will closely align with an aircraft's optimal performance characteristics. However, using predefined mission profiles offers a more straightforward comparison of effects across different VC scenarios. With these considerations in mind, and to get the best of both approaches for a comprehensive evaluation, two benchmark missions have been established for both the long range and the short range aircraft references, respectively.

Benchmark Mission I is close to the design mission and incorporates predefined step climbs, ensuring that the aircraft operates under realistic and advantageous conditions. However, tailoring these step climbs specifically to match one particular aircraft's design lift coefficient would distort the results in favor of that particular aircraft, thus compromising fairness in evaluation. With this in mind, the long range Benchmark Mission I exhibits two step climbs at 33 % and 66 % of the mission range, as shown in Fig. 4.4(a) in the top plot. Analogously, the short range Benchmark Mission I exhibits one fixed step climb at 50 % of the range.

Benchmark Mission II deviates more significantly from the design point. This setup showcases how the VC technology can enhance aircraft performance across a broader range of operating conditions. For this case, the long range and the short range Benchmark Mission II initiate the cruise flight at one fixed altitude and keep that altitude for the whole cruise segment. The respective flight profiles are given in the bottom plots of Fig. 4.4.

Table 4.6: Key parameter of the SR-BSL-ref.

Parameter	Unit	SR-BSL-ref
MTOM	[kg]	77 012
OME	[kg]	42 109
Wing mass	[kg]	7 590
Design mission fuel	[kg]	17 989
$(L/D)_{\mathrm{opt}}$	[-]	17.00
$C_{L,\mathrm{opt}}$	[-]	0.542
$C_{D,\mathrm{total}\,@\,C_{L,\mathrm{opt}}}$	[-]	0.0319
$C_{D,\mathrm{ind}\,@\,C_{L,\mathrm{opt}}}$	[-]	0.0109
$C_{D,\mathrm{visc}\,@\,C_{L,\mathrm{opt}}}$	[-]	0.0200
$C_{D,\mathrm{wave}\,@\,C_{L,\mathrm{opt}}}$	[-]	0.0010

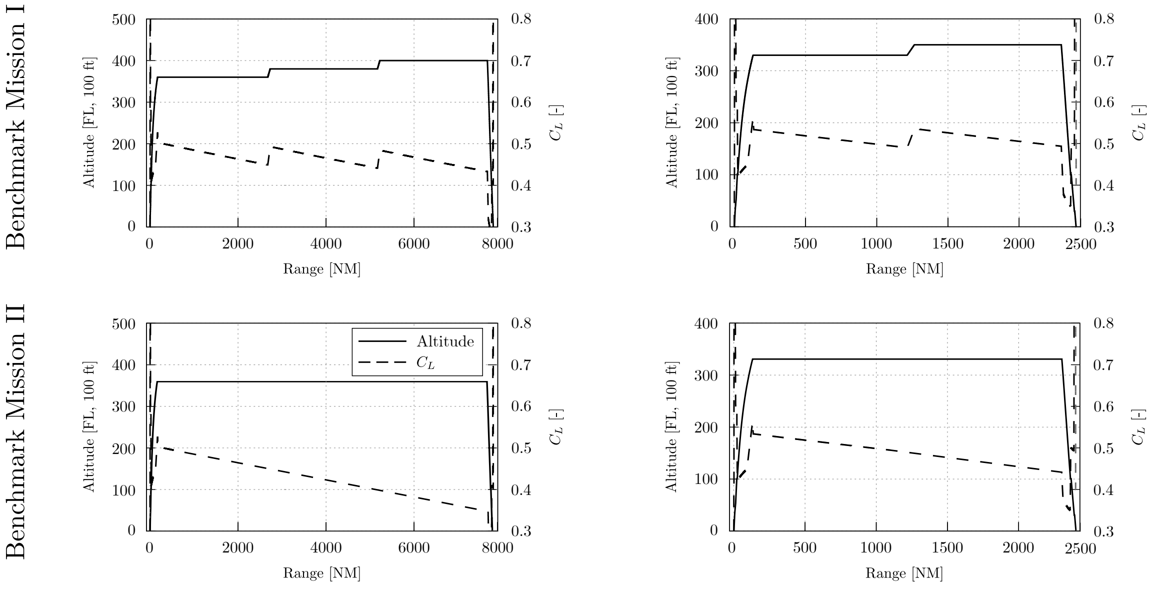

(a) Long range reference **(b)** Short range reference

Figure 4.4: Profiles of Benchmark Mission I and II for the long range operation (7800 NM) and the short range operation (2400 NM).

Summary This section introduced three reference aircraft: two long range and one short range reference. The first long range aircraft serves as the initial reference model, while the second long range aircraft is optimized regarding the lift distribution via the twist distribution over the wing. This optimized reference reveals the effects of pre-optimizing the initial aircraft for VC application, focusing on twist distribution due to its impact on spanwise load distribution, similar to VC. However, this twist adjustment results in changes of the wing mass as a *redesign*, in contrast to the VC application, which is considered a *retrofit* design.

Benchmark missions are introduced in order to assess the performance of the upcoming VC application. The advantages of pre-defined mission profiles for analysis are discussed. Benchmark Mission I is aligned closely with an optimal operational scenario, while Benchmark Mission II provides an off-design scenario, giving insights to the aircraft's performance under suboptimal conditions.

4.2 Analysis of variable camber application on segmented trailing edge devices

In order to provide a structured and concise procedure for the investigation of the three reference aircraft, their high number of retrofit designs of all possible VC segmentations and the additional redesign of the wing by a VC application, a flowchart is given in Fig. 4.5. This is an extension of the procedure introduced by the author in [115].

The first step defined in the flowchart sets up the references, as shown in Section 4.1.1. This is followed by the VC retrofit process methodology described in Section 4.2.1. Since the number of possible trailing edge segmentations results in a large number of VC aircraft variants, a corresponding decision process is introduced in Section 4.2.2 in order to determine which VC variants are to be considered further. Subsequently, Section 4.2.3 evaluates the selected VC variants and the identified fuel saving potential. An in-depth analysis is conducted, including an additional mission range, an evaluation of the interaction of flap deflections, horizontal tail plane settings, and angle of attack, as well as a case study for deactivated VC at the inboard and outboard flaps. For this in-depth analysis in Section 4.2.4, the LR-ASO-ref is selected for the case studies. Finally, Section 4.2.5 presents an examination that assumes a redesign of the wing and its structural mass instead of the introduced retrofit design for VC. The aim is to classify the impact of the assumption of a retrofit application.

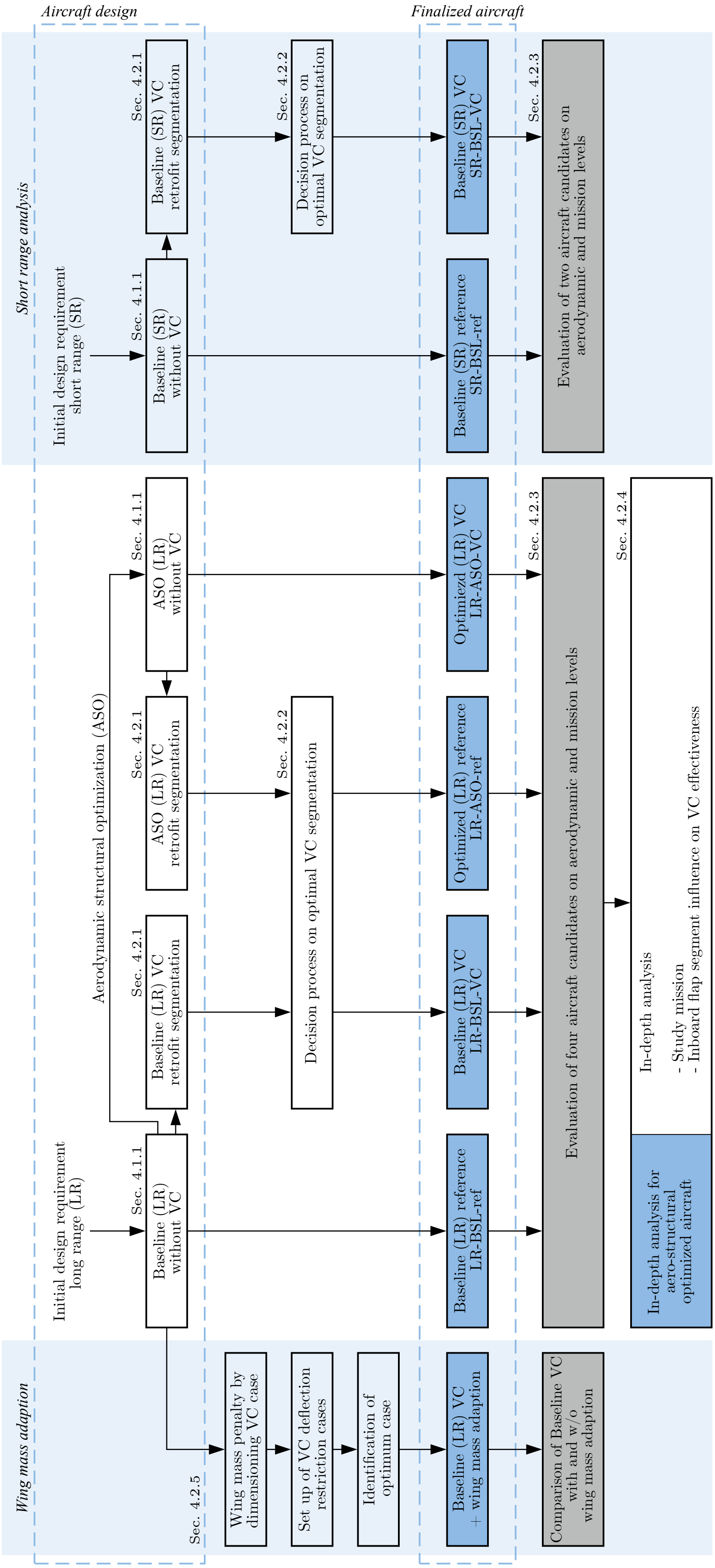

Figure 4.5: VC evaluation methodology flowchart.

4.2.1 VC retrofit process methodology

This section explains the methodology of setting up a VC retrofit [84] and outlines the enhancement for a segmented trailing-edge flap [115]. Regarding the two long range references, the analyses include six different segmentations of the inboard and outboard flap, as listed in Table 4.7. In the case of the short range reference aircraft, four different segmentation variants are identified. This is due to the outer flap being divided into a maximum of two segments instead of four, reflecting the aircraft's shorter wingspan.

Table 4.7: Investigated trailing-edge device configurations.

	Applicable to		TED	No. of flap
ID	Long range	Short range	configuration	permutations
A	yes	yes	1inb-1outb	34
B	yes	yes	1inb-2outb	150
C	yes	yes	2inb-1outb	150
D	yes	yes	2inb-2outb	668
E	yes	no	1inb-4outb	2 986
F	yes	no	2inb-4outb	13 362

The wings are built up from several airfoils which are arranged along the span, as indicated in Fig. 4.3. The VC functionality is therefore ensured by six airfoils for the supporting stations on the wing from $y = 2.9$ to $20.3\,\mathrm{m}$ for the long range aircraft, respectively by five supporting stations from $y = 2.0$ to $13.3\,\mathrm{m}$ for the short range aircraft. The introduction of segmented VC flaps is enabled by adding wing sections to the reference geometry. These airfoils include flap deployment angles ranging from -3 deg to +4 deg in steps of 1 deg. To meet the requirement of directly inserting the VC airfoils into the wing geometry, the respective flaps of each airfoil are deflected by the desired angle up and down and fulfill the following functional requirements:

- Spanwise interpolation of airfoils between given basic airfoils
- Flap deployment around a hinge point with spoiler droop as with the ADHF system, see Section 3.1
- Transformation of the airfoil geometry according to the local sweep theory after WILD [132] to account for quasi-3D aerodynamic properties of the wing, using 2D simulations of the airfoils performed with the 2D flow solver MSES [28]

The hinge point is defined by the high-lift requirements, as described in Section 3.1, meaning the motion path for VC deflections is predetermined. To ensure consistency with the aerodynamic tools used, the airfoil sectioning shown in Fig. 4.3 is applied to all VC variants, even if, for example, VC variant A would require fewer sections. However, in the applied design process, a uniform paneling is ensured, preventing a dependence of the results on the panel resolution. It is worth repeating that this preliminary aircraft design process is optimized for the evaluation of one aircraft with a fixed wing geometry at a time, as described in Section 3.4.3. The application of differential flap settings enables the independent operation of the segmented trailing edge devices. Therefore, numerous aircraft with all possible permutations of the flap deployment angle are generated for the six different wing configurations. To reduce the number of aircraft to be analyzed, a condition is introduced that restricts the deployment angle difference of two adjacent flaps to $\pm 2\,\mathrm{deg}$. The resulting number of flap deployment permutations and, hence, the number of aircraft for the different wing segmentations are given in Table 4.7. The number of permutations, particularly with variant F, demonstrates that an excessively high number of segmentations leads to so many permutations that, in terms of computational time, realistically executable calculations become a limiting factor. The assembly of the permutations to the associated aircraft using the VC application with DFS is described in detail in Section 3.4.3. As a brief summary, it can be stated that the L/D polars of all possible permutations are merged to an optimal envelope, together with the information about the deployment of each flap at every C_L step. This merged polar represents the aerodynamic performance in cruise flight for the aircraft with activated VC with DFS.

The varying systems and fairing masses by actuating different numbers of segmented independent flaps are taken into account in the retrofit approach. This avoids privileging an overdistribution of arbitrarily high flap segmentations regarding the increasing systems and fairing mass. Considering that the modifications are retrofitted, the wing mass is not changed, assuming that the flap settings are retracted in dimensioning conditions and that VC is exclusively used in regular cruise flight. A discussion of this assumption is given in Section 4.2.5.

4.2.2 Decision process on optimal VC segmentation

This section introduces the decision-making process used to select which VC variants will be further evaluated. Initially, the fuel saving potentials at Benchmark Mission I is considered to make a preliminary selection. Subsequently, the L/D polars of the remaining variants are analyzed to identify advantageous characteristics in the off-design areas. This evaluation balances the benefits of higher segmentation with regard to potentially better off-design characteristics against the associated increase in system mass. Note that a more detailed evaluation, including the flap angles and HTP settings, is given in Section 4.2.3. The process is detailed for the two long range references, see also [115], and then briefly applied to the short range reference as well.

Long range references

The VC variants A-F, as listed in Table 4.7, are investigated for the LR-BSL-VC and the LR-ASO-VC, respectively. The respective L/D polars are evaluated in their optimum and the off-design range. Additionally, for an overall aircraft consideration, the mission fuel consumptionfor each variant is evaluated, taking into account, e.g., the changes in system mass components. In the following, the respective references LR-BSL-ref and LR-ASO-ref are compared to their VC variants.

The results regarding the $(L/D)_{\text{opt}}$ and the mission fuel are summarized in the Tables 4.8 and 4.9, for the LR-BSL and the LR-ASO, respectively. Additionally, in order to provide a more readable visualization of the numerous values, the $(L/D)_{\text{opt}}$ for all variants is plotted in Fig. 4.6. Considering the $(L/D)_{\text{opt}}$, it is evident for the LR-BSL as well as for the LR-ASO that the VC variants A, i.e., aircraft with one inboard and one outboard flap without further segmentation already lead to considerable increases in L/D, when compared to their respective reference aircraft. This result for the long range aircraft means that a considerable part of the potential can be gained without further segmentation, just by enabling VC with DFS. For a quantitative evaluation at the overall aircraft level, the mission fuel consumption on Benchmark Mission I of all VC variants and the respective references, for the LR-BSL and the LR-ASO, respectively, is considered.

Table 4.8: Benchmark Mission I: Data of each LR-BSL-VC variant at range of 7 800 NM.

Parameter	Unit	LR-BSL-ref	A	B	C	D	E	F
TOM	[kg]	266 025	261 018	260 635	260 954	260 726	260 761	260 852
Mission fuel	[kg]	95 260	90 213	89 766	90 087	89 795	89 776	89 804
Delta Mission fuel	[%]	-	-5.3	-5.8	-5.4	-5.7	-5.8	-5.7
$C_{L,\text{opt}}$	[-]	0.504	0.473	0.477	0.483	0.477	0.478	0.478
$(L/D)_{\text{opt}}$	[-]	20.18	20.94	21.04	21.00	21.04	21.05	21.05

Table 4.9: Benchmark Mission I: Data of each LR-ASO-VC variant at range of 7 800 NM.

Parameter	Unit	LR-ASO-ref	A	B	C	D	E	F
TOM	[kg]	263 697	261 247	261 126	261 045	261 120	261 295	261 277
Mission fuel	[kg]	91 891	89 401	89 216	89 136	89 147	89 269	89 188
Delta Mission fuel	[%]	-	-2.7	-2.9	-3.0	-3.0	-2.9	-2.9
$C_{L,\text{opt}}$	[-]	0.494	0.476	0.469	0.475	0.475	0.469	0.473
$(L/D)_{\text{opt}}$	[-]	20.85	21.18	21.22	21.25	21.25	21.22	21.25

Taking the mission fuel consumption from Table 4.8 for the LR-BSL into account, the VC variant A already provides a fuel savings potential of 5.3 % compared to the reference. Furthermore, it can be seen that the LR-BSL-VC variants with an outboard flap segmented at least once (B, D - F) can further reduce consumption, whereby variants B and E are the most advantageous with a saving of about 5.8 %. Common to all variants is that the fuel saving potentials are achieved in cruise.

Analogously, the LR-ASO-VC variant A provides a high proportion of the achievable savings potential, as shown in Table 4.9. Because of the previously optimized reference, the VC potential in mission fuel savings for variant A only amounts to 2.7 %. The highest calculated savings potential of 3.0 % is achieved with for variants C and D. For the decision process, a determination is required for both the LR-BSL candidates (B, E) and the ASO candidates (C, D) as to whether further segmentation of the outboard flap is advisable in each case. For reasons of system complexity, an unnecessarily high segmentation is to be avoided, however, in this thesis the

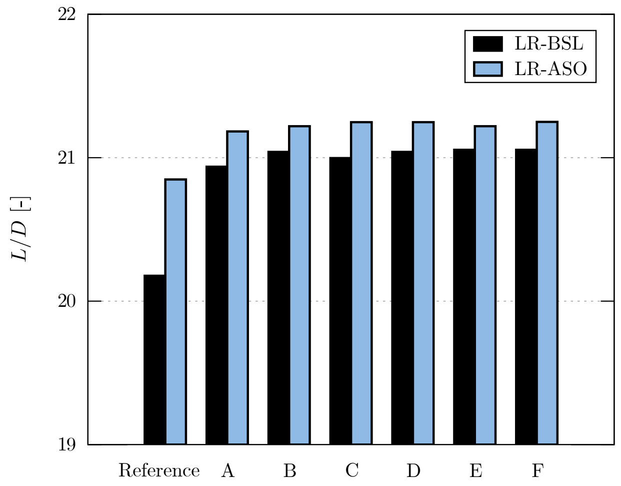

Figure 4.6: L/D maxima for both of the long range reference aircraft and their VC configurations A-F at $Ma = 0.85$ [115].

focus lies on optimal performance in the design point and for off-design operations. For both cases the off-design performance with the further segmentation is advantageous. To analyze the aerodynamic performance for design and off-design operations, the L/D polars for the reference and its VC variants are plotted over a range of lift coefficients, in Fig. 4.7(a) for the LR-BSL and in Fig. 4.7(b) for the LR-ASO[‡]. Note that in Fig. 4.7(b) for the outermost C_L range, the step-like discontinuities observed in the graph indicate that not all permutation simulations converged. The affected C_L values are not used for the investigated cruise flight regime.

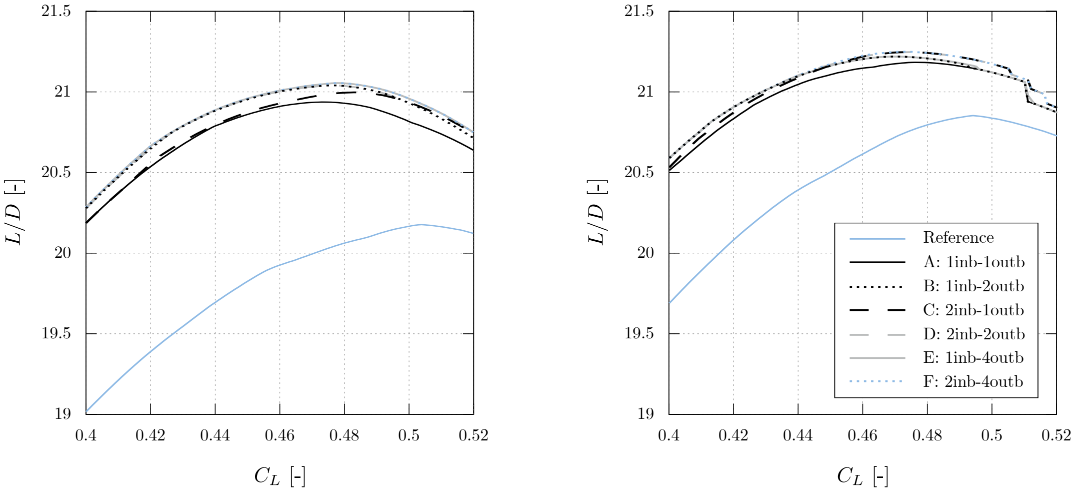

(a) LR-BSL **(b)** LR-ASO, [115]

Figure 4.7: L/D polars of the respective reference aircraft and their VC configurations A-F at $Ma = 0.85$.

Regarding the LR-ASO, it can be seen how variants C and D align for values above a C_L of 0.45, whereas below this C_L value, variant D yields a higher L/D. Although this is accompanied by a higher system mass, which offsets the savings potential, the advantage would be more pronounced

---

[‡] Note that these plots are not comparable to plots such as Fig. 2.36 or 2.37, which show an airfoil or aircraft with different VC flap settings. Figure 4.7 shows different segmentations, meaning different aircraft.

for off-design missions with even lower C_L. Consequently, the further discussed optima are the LR-ASO-VC variant D, with two inboard and two outboard flaps, and analogously the LR-BSL-VC variant E with one inboard and four outboard flaps.

Short range reference

This section briefly discusses the analogous process for the short range reference. As explained in Section 4.2.1, only VC Variants A-D are considered in the short range scenario referring to the naming in Table 4.7. The results for the aerodynamic parameters $C_{L,\text{opt}}$ and $(L/D)_{\text{opt}}$, as well as mission fuel results, are presented in Table 4.10. The results indicate that splitting the inboard flap is more significant from an aerodynamic perspective. It can be seen that $C_{L,\text{opt}}$ and $(L/D)_{\text{opt}}$ are identical for the same inboard split, i.e., variants A and B, as well as C and D. However, variations in mission fuel consumption do occur, albeit minor, because a higher flap segmentation in the retrofit design requires more actuation mass, see [115]. Taking these circumstances into account, variant C is selected for the short range aircraft for the following analyses.

Table 4.10: Benchmark Mission I: Data of each SR-BSL configuration at range of 2 400 NM.

Parameter	Unit	SR-BSL-ref	A	B	C	D
TOM	[kg]	76 413	76 345	76 405	76 384	76 444
Mission fuel	[kg]	17 389	17 282	17 292	17 270	17 280
Delta Mission fuel	[%]	-	-0.62	-0.56	-0.69	-0.63
$C_{L,\text{opt}}$	[-]	0.542	0.523	0.523	0.527	0.527
$(L/D)_{\text{opt}}$	[-]	17.00	17.09	17.09	17.12	17.12

4.2.3 Evaluation of finalized aircraft

Following the flowchart in Fig. 4.5, this section compares the three reference aircraft—LR-BSL-ref, LR-ASO-ref, and SR-BSL-ref—with their selected VC variants. For clarity, it is worth repeating that the reference aircraft represent the flap settings in retracted, i.e. clean, configuration. The VC variants, according to the segmentation layout in Table 4.7, are LR-BSL-VC variant E, LR-ASO-VC variant D, and SR-BSL-VC variant C. The evaluations are based on the Benchmark Missions I and II introduced in Section 4.1.2. The evaluation of the long range aircraft is carried out first, followed by the analogous procedure for the short range aircraft.

Long range references

Initially, the two long range aircraft are evaluated separately in order to analyze the effects of the VC application on the respective references, namely LR-BSL-ref and LR-ASO-ref, see also [115]. In detail, the impact of the previous aero-structural optimization of the LR-ASO-ref and the consequences on a VC application are discussed. Both mission profiles, along with the flap deflections of the VC aircraft, are shown in Fig. 4.8[§]. From this illustration it can be seen, following the introduced methodology, how the aircraft with VC application respond to changing flight conditions. A detailed discussion and analysis of this interaction is provided in Section 4.2.4. The quantitative evaluation at the overall aircraft level with respect to the mission fuel is conducted next. The corresponding data, combined with the respective savings potential, can be found in the Tables 4.11 and 4.12.

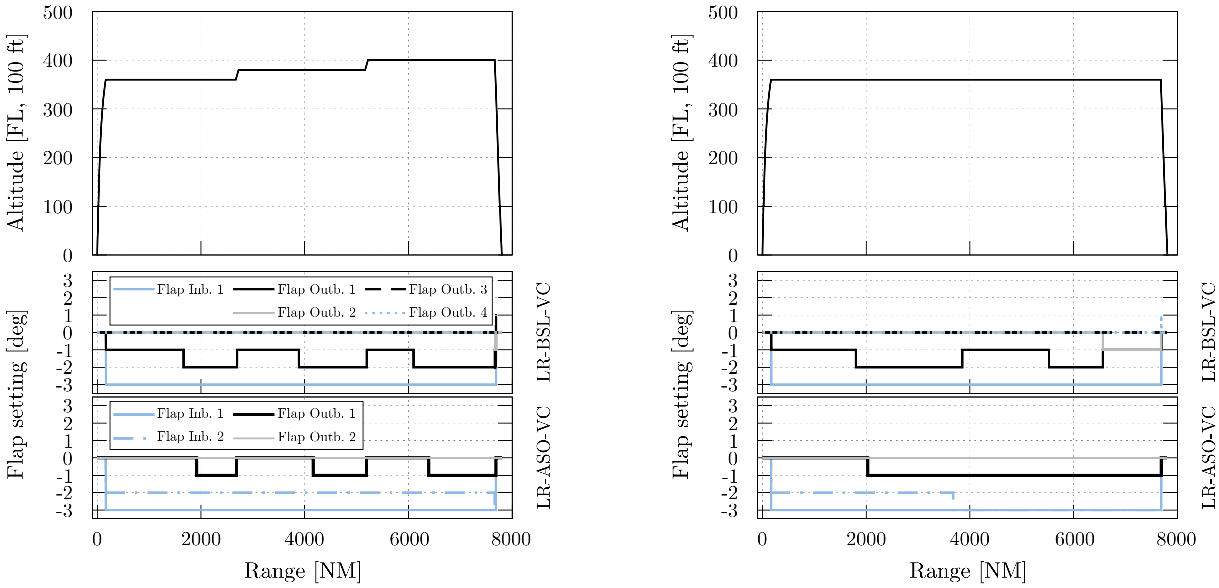

(a) Benchmark Mission I **(b)** Benchmark Mission II

Figure 4.8: Mission profile of both Benchmark Missions with the respective flap deployments; long range, adapted from [115].

Table 4.11: Benchmark Mission I: Mission fuel compared to LR-BSL-ref [115].

Parameter	LR-BSL		LR-ASO	
	Reference	VC - Var. E *(1inb-4outb)*	Reference	VC - Var. D *(2inb-2outb)*
TOM [kg]	266 025	260 761	263 697	261 120
Mission fuel [kg]	95 260	89 776	91 891	89 147
Delta in [%]:				
Mission fuel	-	−5.8	−3.5	−6.4

Table 4.12: Benchmark Mission II: Mission fuel compared to LR-BSL-ref [115].

Parameter	LR-BSL		LR-ASO	
	Reference	VC - Var. E *(1inb-4outb)*	Reference	VC - Var. D *(2inb-2outb)*
TOM [kg]	268 155	262 286	265 893	262 356
Mission fuel [kg]	97 390	91 301	94 086	90 384
Delta in [%]:				
Mission fuel	-	−6.3	−3.4	−7.2

[§] As the large number of individual flaps impairs readability, Tables C.2 and C.3 are provided in the appendix, which details the flap settings according to the specific C_L range for each aircraft.

Comparison: LR-BSL-ref to LR-BSL-VC In this section, the Baseline reference is evaluated against the Baseline VC configuration, in order to demonstrate the fundamental effects, which are applicable to all VC applications in this chapter. The principal aerodynamic mechanism is illustrated in Fig. 4.9(a), showing the two lift distributions for LR-BSL-ref and LR-BSL-VC, as well as the elliptical case, highlighted in grey. Note that the lift distributions are displayed at $C_{L,\mathrm{opt}}$ of the LR-BSL-ref, see Table 4.3, and that the name tag for the VC aircraft refers to the VC wing permutation (flaps from left to right) at this specific lift coefficient. The VC application notably shifts the lift distribution towards the elliptical case. It is important to note that this behavior is not imposed artificially, but results from computing all possible flap permutations and merging them into an optimal envelope, as discussed in Section 3.4.3. The approximation towards an elliptical lift distribution, similar to the LR-ASO-ref in Fig. 4.2(a), leads to a reduction in induced drag, as explained in Section 2.5.1. Figure 4.9(b) provides a breakdown of the wing drag components. While the viscous drag component is only marginally changed, the characteristic wave drag is reduced by 23.5 % for this example. Although this relative reduction in wave drag is high, its impact on the total drag is rather small due to the low absolute value of $C_{D,\mathrm{wave}}$. The significant majority of the absolute reduction in $C_{D,\mathrm{wing}}$ is due to the lowered induced drag. The lift distribution shown is achieved by decambering the inner flaps in combination with a higher angle of attack. An approximation of the lift distribution in the contrary path, i.e., a deflection of the outer flap and a lowering of the angle of attack, would significantly increase the wave drag due to the high local lift coefficients in the outer wing area [115]. Thus, considering the wave drag increase leads to the characteristic that the elliptical lift distribution is not further approximated, since the further potential reductions in induced drag are negated by a higher wave drag.

Figure 4.8 shows how the flap settings are changed during the mission for both Benchmark Missions. First of all, a continuous and pronounced inboard decambering can be observed, which leads to the load distribution in Fig. 4.9(a). This behavior is analogous to the characteristics of the long range reference aircraft with the optimized twist distribution, see Section 4.1.1. Over the course of the mission, the wing is decambered slightly further as C_L decreases, for example for Benchmark Mission I in Fig. 4.8(a) at a range of around 1 700 NM. At the step climb at around 2 600 NM, which is accompanied by an increase in C_L, the camber is increased accordingly. An exception occurs for LR-BSL at Benchmark Mission II. This is related to the trim and is analyzed in detail in [130]. The interaction of the flap setting with the angle of attack will be discussed in more detail in Section 4.2.4.

Taking into account the mentioned effects, an increase in $(L/D)_{\mathrm{opt}}$ of 4.3 % is achieved for the the VC aircraft compared to the Baseline reference, as shown in Fig. 4.6. At the overall aircraft level, the application of VC has a significant impact on both missions. Thus, a saving of 5.8 % is possible for the Benchmark Mission I, see Table 4.11, and when operating strongly in off-design, as is the case for the Benchmark Mission II without step climbs, fuel savings of as much as 6.3 % are calculated, see Table 4.12. The ability of VC systems to adapt to different flight conditions yields this even higher fuel savings potential in off-design conditions. The comparison is based

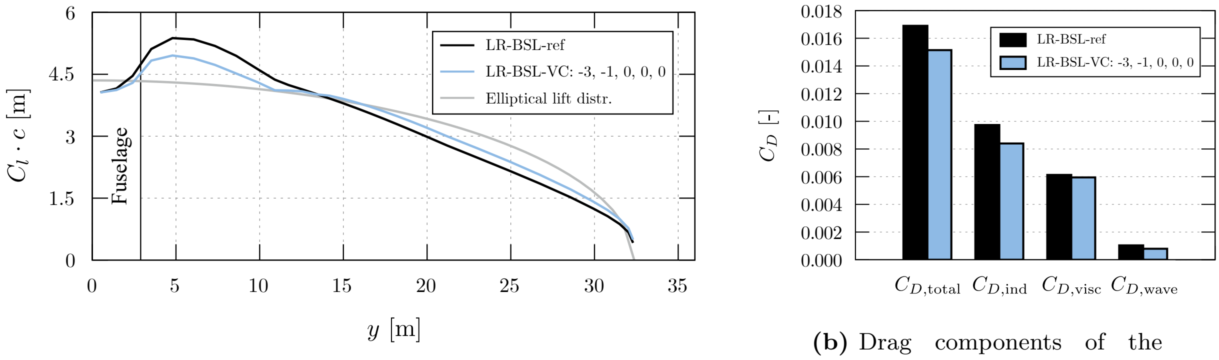

(a) Spanwise lift distribution

(b) Drag components of the wing

Figure 4.9: Comparison of lift distributions and drag components of the LR-BSL-ref and LR-BSL-VC Var E *(1inb-4outb)* at $C_{L,\text{opt,Baseline,Ref}}$ and $Ma = 0.85$ [115].

on the LR-BSL-ref, i.e., an aircraft that has not yet been optimized, thus the VC application has a larger operating margin. In the following section, the comparison is made using the aero-structural optimization without the use of VC.

Comparison: LR-ASO-ref to LR-ASO-VC The combined potential of an optimized reference and an additional application of VC is quantified in the following. The principle mode of action of the two individual techniques was discussed in the previous sections. Since Tables 4.11 and 4.12 give fuel savings relative to the LR-BSL-ref, the stated absolute values are used below.

Considering the Benchmark Mission I, the fuel consumption of the LR-ASO-ref can be reduced from 91 891 kg to 89 147 kg (-3.0 %) by means of a VC deployment. The potential is even more significant for the off-design Benchmark Mission II, with fuel consumption reduced from 94 086 kg to 90 384 kg (-3.9 %). The flap setting decreases the camber with decreasing C_L during the mission and the camber is increased with a conducted step climb, in accordance to the principles discussed in Section 2.5.1. The fuel savings show that a VC application has a significant potential even in the case of a reference that has been previously optimized with respect to the load distribution and aero-structural interactions. This is reflected in the load distribution and drag breakdowns that are given in Fig. 4.10. It needs to be discussed, why a VC application yields such fuel savings potentials, even with a reference aircraft that is already optimized by means of the twist distribution. The twist distribution alters the lift distribution, so it could be argued, that an additional VC application should only be advantageous in off-design conditions. The reason why a VC application is nevertheless advantageous is that due to the retrofit approach, the wing is not re-dimensioned for VC applications and therefore can optimize the load distribution for cruise flight without a structural mass penalty. According to this approach, VC is not employed in design load cases. [115]

Furthermore, the results in Tables 4.11 and 4.12 show the disadvantage of an optimization considering one specific flight design condition as in the case of the LR-ASO-ref without VC in off-design. Especially this strength of the VC application to optimize the wing to the flight conditions during the mission is not given, thus the savings potential for the LR-ASO-ref in the off-design mission is considerably lower than with the VC applications.

Overall, the combined application of the twist optimization including VC application yields the highest savings potentials. However, it should be emphasized that the VC retrofit application already yields a large portion of this potential for this given baseline reference. The continuous decambering of the wing raises the question, why the wing does not already have this characteristic in its clean configuration. This is explained by the fact that the retrofit approach as explained above assumes that VC does not generate any load cases that are dimensioning. This assumption is based on the reasoning that the VC control devices are retracted in-flight prior to dimensioning load case conditions. If these load cases are taken into account, the wing would become heavier, analogous to the LR-ASO-ref design in Section 4.1.1. A further investigation, which assumes the VC application as a dimensioning case of the wing structure, is given in Section 4.2.5.

Comparison: LR-BSL-VC to LR-ASO-VC Since all fundamental relationships have already been discussed and are analogous for this comparison, only a brief direct comparison of the two VC aircraft is provided here. As presented in the Tables 4.11 and 4.12, under flight conditions close to the design condition in Benchmark Mission I, the application of VC to the pre-optimized aircraft reference, LR-ASO-VC, results in a mission fuel consumption of 89 147 kg. In contrast, applying VC alone, without wing twist optimization, results in a fuel consumption of 89 776 kg (+0.7 %) for the LR-BSL-VC aircraft. A similar trend is observed in Benchmark Mission II under off-design conditions, where LR-ASO-VC requires 90 384 kg compared to 91 301 kg (+1.0 %) for LR-BSL-VC.

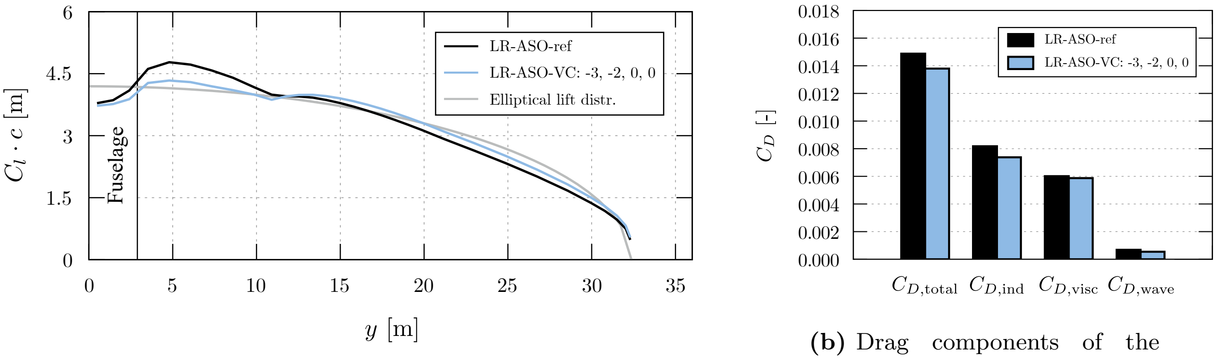

(a) Spanwise lift distribution

(b) Drag components of the wing

Figure 4.10: Comparison of the lift distributions and drag components of the LR-ASO-ref and LR-ASO-VC *(2inb-2outb)* at $C_{L,\text{opt,ASO,Ref}}$ and $Ma = 0.85$ [115].

Short range reference

The approach for the short range configuration is analogous and is therefore analyzed briefly, focusing on the results. Figure 4.11 shows the flap settings for the Benchmark Missions I and II.

Table C.4 in the appendix provides the flap settings depending on the C_L range for better readability. The effects of the VC deployment likewise cause a general decambering of the wing, albeit to a lesser extent than in the long range mission. As shown in Fig. C.3(a), VC helps to approach the elliptical lift distribution. However, compared to LR-BSL-ref, the SR-BSL-ref is already closer to the elliptical lift distribution without significantly increasing wave drag, partly because the short range operates at a lower cruise Mach number of 0.78. Consequently, as depicted in Fig. C.3(b), while induced drag is reduced, the extent of reduction is smaller than that observed for the long range aircraft. Overall, the application of VC results in calculated fuel savings of 0.7 % and 0.9 % for the respective Benchmark Missions, as stated in Table 4.13.

Table 4.13: Benchmark Mission I and II results for the short range configuration.

Parameter	Benchmark Mission I		Benchmark Mission II	
	Reference	VC - Var. C *(2inb-1outb)*	Reference	VC - Var. C *(2inb-1outb)*
TOM [kg]	76 413	76 384	76 545	76 484
Mission fuel [kg]	17 389	17 270	17 522	17 370
Delta in [%]:				
Mission fuel	-	−0.7	-	−0.9

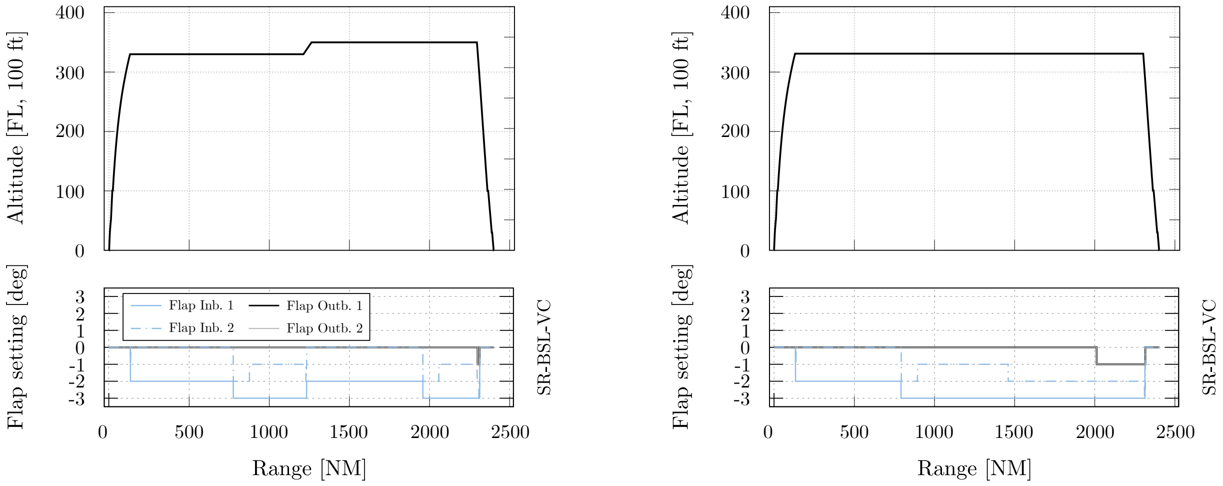

(a) Benchmark Mission I **(b)** Benchmark Mission II

Figure 4.11: Mission profile of both Benchmark Missions with the respective flap deployments; short range.

4.2.4 In-depth discussion of the optimal configuration

This section discusses individual phenomena in detail, using the LR-ASO-ref as the case study, see also [115]. A mission analysis is carried out first, whereby the interaction of angle of attack, VC settings, HTP settings, and the mission requirement are examined. This is followed by an investigation of the effects of disabling the inner and the outer flap segments, respectively.

In-depth analysis of a study mission

In order to perform a detailed mission analysis, the mission profile shown in Fig. 4.12 is considered. With a range of 4 000 NM, this corresponds, for instance, to a typical transatlantic flight. For classification purposes, the fuel consumption is shown in Table 4.14; the savings potential with VC application in relation to the LR-ASO-ref is 3.2 % and, thus, similar to the data shown in Section 4.2.3 for another mission. For the following considerations, the focus lies on the mutual interaction of the different changes of flap settings, angle of attack, and the HTP, in response to different flight conditions.

The mission progression, coupled with the current aircraft mass, results in a lift demand on the aircraft. Between the step climbs, while the altitude remains constant, the required C_L decreases due to the burned fuel. With the step climbs, the required C_L increases again due to the changed atmospheric conditions. Thus, the required C_L value is kept closer to the design point, and the aircraft operates more efficiently.

For a decreasing C_L requirement, for instance, at about 1 500 NM and 3 800 NM, it can be observed how the VC deflection decambers the wing. This results in a more efficient flight condition according to the previously calculated polars. Any change in flap settings is always accompanied by a change in angle of attack, since the C_L is supposed to have a steady progression over the mission segment. In the examples given, the angle of attack is slightly increased during the decamber accordingly. Conversely, with an increased C_L requirement, especially at step climbs, the wing is cambered accordingly. An additional form of interaction emerges from the trimming. For instance, at a distance of 2 050 NM shortly after the step climb, the adjustments in the VC setting result in an altered trim angle of the HTP. [115]

Note that all three parameters, i.e., angle of attack, flap setting, and HTP angle influence each other and that the respective optimum for each mission point for a trimmed condition is selected by the presented methodology.

Table 4.14: Study mission data evaluation at study range of 4 000 NM [115].

Parameter	LR-ASO-ref	LR-ASO-VC - Var. D *(2inb-2outb)*
TOM [kg]	219 236	217 877
Mission fuel [kg]	47 430	45 905
Delta [%]:		
Mission fuel	-	-3.2

Inboard flap segment influence on VC effectiveness

Since the importance of the inboard flaps for the reference aircraft has already been highlighted in the previous chapters, two case studies are presented below to demonstrate the consequences of deactivating the VC functionality inboard and outboard, respectively. The studies are con-

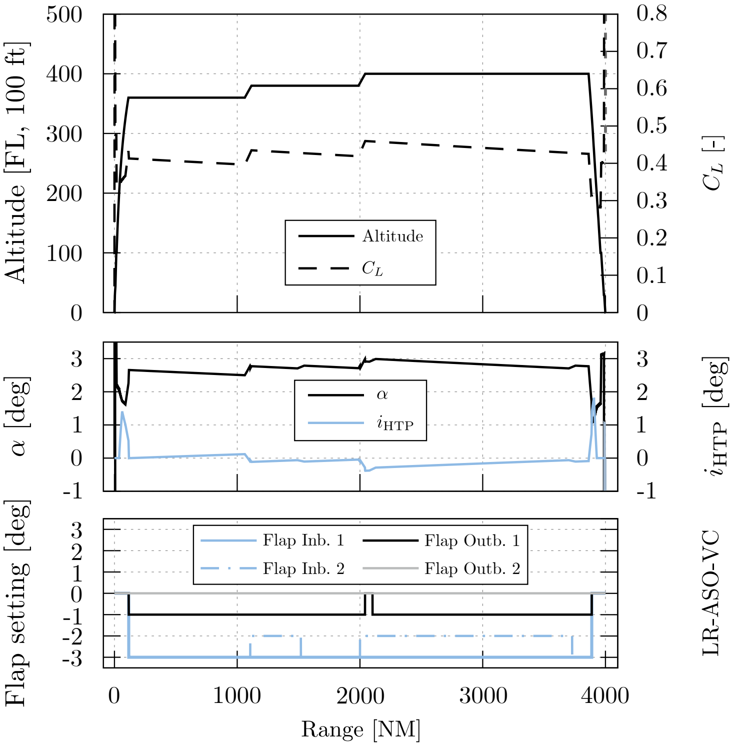

Figure 4.12: Study mission profile, including angle of attack, flap/stabilizer deflection for LR-ASO-VC *(2inb-2outb)* [115].

ducted based the Benchmark Mission II without step climbs as introduced in Section 4.1.2. Table 4.15 summarizes the results with reference to the fuel consumption for the fully activated VC application. Since the augmentation of the load distribution is mainly driven by the inboard flaps, there is a significant loss of efficiency with the inboard flaps' VC function disabled. The fuel consumption in comparison to the fully activated VC variant increases by 4.0 %, leaving only a small benefit compared to the LR-ASO-ref, with no VC at all. Accordingly, the opposite is the case for deactivated outboard VC flaps, a deactivation only leads to a slight increase in fuel consumption of 0.2 % compared to the fully activated variant.

Table 4.15: Benchmark Mission II data evaluation at a range of 7 800 NM with the inboard, respectively outboard flaps excluded from VC actuation, [115].

	LR-ASO-ref	LR-ASO-VC - Var. D *(2inb-2outb)*		
Parameter	clean	all active	w/o inboard VC	w/o outboard VC
TOM [kg]	265 893	262 356	266 014	262 537
Mission fuel [kg]	94 086	90 384	94 042	90 565
Delta to ref.:				
Mission fuel [%]	+4.1	-	+4.0	+0.2

In this case study, the use of the inboard flaps already provides a large part of the possible fuel savings potential. However, it is important to put this result into perspective, as this behavior is strongly dependent on the selected reference aircraft and the flight condition. Since in the aircraft reference presented in this thesis, the wing in the area of the outboard flaps is subject to high loads during cruise flight, a strong increase in the wave drag occurs correspondingly with positive deflections. But in order to influence the lift distribution towards an elliptical distribution with deactivated inboard flaps, the outboard flaps would have to be deflected. These two contradictory requirements drastically reduce the operating range of the outboard flaps. Accordingly, a different behavior would be expected for aircraft references with an airfoil and wing design that allows a greater margin regarding the wave drag increase over the entire flap range. Furthermore, the operating range could also be extended for the presented references, for example for lower Mach numbers, since the wave drag would be less critical. [115]

4.2.5 Wing mass adaption due to VC

So far, the VC has been applied under the assumption of a retrofit approach. As discussed at the beginning of Chapter 4, this approach means that the system is applied to an existing aircraft without redesigning it. However, additional masses required for the implementation, such as actuator mass in the case of VC, are added, see also [115]. This approach assumes that the dimensioning load cases of the wing, as considered in the wing mass determination, see Section 3.4.2, are not influenced by VC. It is assumed that the flaps are retracted in such load cases and only deployed during regular cruise flight. With regard to this assumption, a brief analysis is presented below. A graphical display is shown in the flowchart in Fig. 4.5 on the left side. As depicted, this study case uses the LR-BSL-VC, redesigns the wing structural mass. For a detailed procedure, refer to the master's thesis supervised by the author [130]; the essential points of the methodology and the results are shown below.

Due to the exceptionally high number of permutations as shown in Table 4.7, a thorough redesign of every possible flap permutation is not feasible. As it was observed in Fig. 4.8, the inboard flap deflection of the LR-BSL-VC consistently remains at -3 deg. Therefore, three gradations are created and considered for the wing mass design. Firstly, a maximum negative flap deflection inboard is applied, which results in an additional wing mass of 1 718 kg. For more information on the structural wing mass calculation, refer to Section 3.4.2 or [29]. Secondly, an inboard flap deflection not exceeding -2 deg shifts the load distribution less far outward, resulting in a less significant increase in root bending moment and necessitating an additional wing mass of 1 233 kg. Thirdly, a flap deflection limited to -1 deg results in a wing mass increase of 869 kg.

These three gradations are then evaluated on the Benchmark Missions I and II from Section 4.1.2. Despite the increased wing mass, a potential for fuel savings is found for all gradations. The greatest fuel savings potential, despite the largest increase in wing mass, occurs with the gradation allowing the full flap deflection of up to -3 deg. Thus, a savings potential of 5.0 % is calculated for the Benchmark Mission I; compared to 5.8 % with the unchanged wing structure mass for the retrofit approach in Table 4.11. This difference is due to considering the adverse effect of dimensioning the wing for loads under VC settings. For the Benchmark Mission II, in which VC can better exploit its advantages through the off-design operation, a fuel savings potential of 5.7 % is calculated in the case of a higher wing mass, compared to the 6.3 % in the retrofit approach, see Table 4.12. This case study incorporates only one aircraft but demonstrates that VC application can be worthwhile even when considering potential increases in wing structure mass by omitting the retrofit approach.

Summary Based on the previously introduced reference aircraft and benchmark missions, this section presents an approach for evaluating a VC with DFS application using segmented trailing edge flaps. The selected, and deemed as optimal, segmentations are analyzed regarding the underlying effects. A quantitative comparison of the aircraft is performed, both near the design condition and in off-design conditions. Finally, a study is conducted on the applicability of the retrofit approach.

4.3 Result discussion

This section summarizes and classifies the results of the VC with DFS application on segmented trailing edge flaps. Four key conclusions are drawn:

1. The application of VC with DFS within the preliminary aircraft design using MICADO consistently results in a reduction of mission fuel consumption. The benefits of VC outweigh the disadvantages introduced by additional retrofit masses, such as those required for actuator implementation. Even when redesigning the wing structural mass due to the influence of VC, a net benefit remains.

2. The underlying wing is decisive for the fuel saving potential. This is demonstrated by the introduction of the pre-optimized long range reference (LR-ASO-ref). This optimization is based on the twist distribution and thus affects the lift distribution - similar to the working principle of VC. This pre-optimization has a significant impact on the VC potential: while the baseline long range reference (LR-BSL-VC) achieves a fuel savings potential of 5.8 % on Benchmark Mission I, which operates near the design point, the VC application following prior aero-structural optimization (LR-ASO-VC) achieves only 3.0 %.

3. As described in Section 2.5, VC is particularly advantageous in off-design operations, enabling the wing geometry to respond more favorably to altered flight conditions. For the baseline long range aircraft, the fuel savings increase to 6.3 % when VC with DFS is used in the off-design Benchmark Mission II, compared to the 5.8 % in Benchmark Mission I. The LR-ASO-VC aircraft shows a similar trend, with a saving of 3.9 % in relation to LR-ASO-ref in Benchmark Mission II, compared to 3.0 % in Benchmark Mission I.

4. The segmentation of the trailing edge flap for an even more adaptable use of the VC with DFS application and more response options to different flight conditions helps to further reduce fuel consumption. However, the application of VC with DFS on two flaps already shows substantial fuel savings potential. It should be emphasized that the calculations in this thesis take place in the preliminary aircraft design with the discussed limitations and assumptions. Effects that might be associated with highly segmented flaps, such as noise, increased maintenance, or aerodynamic effects not captured by the solvers used here, are thus not considered.

For applications beyond the preliminary design phase, these effects must be taken into account, including compliance with certification regulations such as CS 25.345(c) for high-lift devices in en route conditions. Existing aircraft types that may operate climate-optimized trajectories in the future, instead of mission fuel-optimized trajectories as assumed in this thesis, may benefit in particular from the VC application. As stated above, aircraft with VC with DFS application are able to react to trajectories that are further away from the original design point of the aircraft. The importance of the underlying wing design is highlighted. While redesigning wings of existing aircraft is unlikely, VC applicability in new generations could be considered to ensure a broader range of effective VC deployment, for example to avoid the discussed characteristic where significantly increasing wave drag prevents positive outboard VC deflection.

5 Conclusions and Outlook

Within the scope of this thesis, methodologies for the optimization and design of control surfaces were developed. This provides the foundation for a segmentation of these control surfaces as part of a variable camber application in the overall aircraft design and the analysis of potential fuel savings. The motivation for this strategy is derived from the necessity to reduce the climate impact of aviation. The presented approach provides tools for the design of the relevant elements at system level as well as an analysis of the fuel saving potential of the thus enabled variable camber application at overall system level.

Summary In order to understand and classify the various subject areas covered in this thesis, Chapter 2 provides the necessary foundation, together with an overview of the state of the art. The mutually influencing effects in high-lift are discussed in detail. The topics of lift in general, flow separation, and calculation methods are also discussed, as they are relevant in this context. In the course of modeling flap loads, the fundamentals of the artificial neural networks are introduced. With regard to actuator technology, an overview is provided, in particular for the actuator technology on the high-lift control surfaces. This is followed by a discussion of existing preliminary design approaches for actuators. To provide the basis for the developed trimming methodology, the aerodynamic moment on an airfoil is first considered together with important coefficients. On this basis, longitudinal stability criteria are introduced, and subsequently transferred to an aircraft with a horizontal tail plane. Finally, the concept of the variable camber application is described with a brief outline of previous scientific considerations. Particular attention is paid to the comprehension of the induced drag.

In accordance with their application in preliminary aircraft design, the methodologies developed for this thesis are presented in Chapter 3. The focus is placed on the restrictions and requirements in said preliminary design stage, which on the one hand implies a scarcity of available data and computing time, but on the other hand, demands a high level of accuracy, as subsequent calculations require the results. First, the methodology regarding the optimization of high-lift airfoils is presented, with a discussion of the limitation of the optimization parameter space in order to keep the number of simulations feasible. Three different use cases of varying accuracy and corresponding computational effort are derived from the results. Thus, the user is provided with a suitable tool depending on the availability of computational resources. In order to predict the aerodynamic loads on the flap, the established data base is presented initially. This includes three different reference aircraft with detailed 3D CFD simulations for both the high-lift and the variable camber case. This is followed by the incremental methodical procedure for the architecture setup of the artificial neural network and an evaluation of the predictive accuracy. With regard to the actuators required to operate the flaps, the tendency towards local actuator packs is outlined and methodologies for three different power-by-wire actuators are shown. In each case, a modular, component-wise approach is used for the design, allowing for future adaptations. Finally, the aircraft design software MICADO is discussed in the contexts of the conceptual and the preliminary design stages. The most relevant tools are outlined and the implementation of variable camber is discussed. In addition, the integration of an extended longitudinal trimming methodology is presented, with an analysis of the adjustable accuracy levels. This also includes trimming with a shifting center of gravity over the mission and provides recommendations for future applications.

The investigation at overall aircraft level for the application of variable camber with segmented trailing edge flaps is carried out in Chapter 4. First, the reference aircraft are introduced; these aircraft include a long range reference, a derivative with pre-optimized twist distribution, and a short range reference. In addition, the benchmark missions for the following investigations are discussed. This is followed by an analysis of fuel savings potential by means of the variable camber application. Due to the numerous configurations possible with segmented trailing edge flaps, a systematic method is described for selecting appropriate candidates for detailed analysis. In addition to the assumption of a retrofit design, a brief comment is made on the case in which the variable camber design resizes the wing. Furthermore, a detailed aerodynamic analysis of the occurring effects is conducted.

Contextualization of the results The results of the methodologies at system component level as well as at overall aircraft level need to be considered in the context of the preliminary aircraft design. The requirements in this context are, in short, to achieve the most accurate results possible for a generalizable application with a scarcity of data and computing time. The key statements on the results of the individual sections of this thesis are summarized in the following.

High-lift configuration optimization: Three procedures of different accuracy and computing time intensity were derived, whereby the highest accuracy is only recommended for detailed investigations in high-lift. The medium accuracy requires considerably fewer simulations, and the deviations in the landing configuration are negligible in the context of the preliminary design. The methodologies only require an airfoil as input and can therefore be applied universally within the preliminary design. Gaps and overlaps may also be relevant beyond the scope of performance optimization, for example for noise calculations. Thus, an option is now given to determine these values at the preliminary design stage.

Flap load modeling: Using artificial neural networks, a median prediction accuracy of approximately 2 % is achieved regarding the forces, with most errors below 2 % or slightly exceeding it. The aerodynamic moment exhibits a maximum median prediction accuracy of 4 %. The modeling is based on three reference aircraft for the high lift case and the variable camber case.

Within these limits, the modeling is reasonably feasible, for strongly deviating aircraft, for example with a forward sweep, an extension based on the existing data and modeling foundation is recommended.

Power-by-wire actuator design: The modular structure of the methodology allows actuators to be reliably modeled using only actuating force or torque, speed and stroke as input variables. If an abbreviated form is desired, acceptable results are achievable by force-to-mass or torque-to-mass ratios for the preliminary design, although it is not possible to react to special characteristics in the design, e.g., variable actuating speeds. Power-by-wire actuators offer, for example, a higher degree of flexibility for future tasks, especially for an increasing application of multifunctional control surfaces. These future developments can thus be considered in the preliminary design based on validated results.

Longitudinal trimming: The introduced trimming method allows valid statements in the course of the preliminary design on longitudinal stability. A trade-off was carried out between a high degree of accuracy in the choice of interpolation points and the associated computing time, enabling a user choice to be made depending on the application. In the standard case, however, three interpolation points are sufficient. Considering a center of gravity shift is not recommended in the preliminary design for conventional aircraft, but would be relevant, for example, in the case of a liquid hydrogen tank configuration in the tail and thus a large lever arm.

Variable camber on segmented flaps: The results at overall aircraft level demonstrate that the fuel saving potential is highly dependent on the reference aircraft. For example, the calculated fuel savings potential for the long range reference without prior optimization amounts to 5.8 %, whereas with prior aero-structural optimization the savings potential is only 3.0 % on a regular long range mission. For short range, a regular mission showed a savings potential of only 0.7 %. A segmentation of the flaps has proven to be advantageous. These potentials must therefore be determined individually for each aircraft, moreover the operated missions are highly important. For future missions, which may require climate-optimized operations at different altitudes and thus outside the designed optimum, a significantly increased operational flexibility can be expected by means of variable camber. Within the preliminary aircraft design, high-fidelity flow solvers are not feasible due to their extensive computational demands. However, for these studies, the airfoil database method was selected to capture the critical wave drag component more accurately, offering an improvement over the semi-empirical default options.

Outlook Future applications could extend the findings demonstrated by the methods shown in this thesis to a broader range of reference aircraft. In particular, the application of variable camber to climate-optimized routes, once available, presents an interesting perspective. The studies and evaluations demonstrated that the effectiveness of variable camber heavily depends on the wing's airfoils. Therefore, an airfoil optimization for variable camber instead of the applied retrofit approach could greatly increase the operating flexibility. To study the numerous resulting parameters, a reduction of the computation time, especially when using the aero-database, is necessary. Another approach could involve creating a database from full-aircraft high fidelity CFD simulations for variable camber deflections and developing a calibration method based on semi-empirical data or incorporating the results in a variably fidelity approach.

Bibliography

[1] Airbus: Global Market Forecast, 2023.
URL: https://www.airbus.com/sites/g/files/jlcbta136/files/2023-06/GMF%202023-2042%20Presentation_0.pdf (accessed April 25, 2024)

[2] Aksu, G.; Güzeller, C. O.; Eser, M. T.: The Effect of the Normalization Method Used in Different Sample Sizes on the Success of Artificial Neural Network Model. International Journal of Assessment Tools in Education, Vol. 6, No. 2, pp. 170–192, 2019.
DOI: 10.21449/ijate.479404

[3] Anderson, J. D.: Introduction to flight, New York, NY: McGraw-Hill Education, 2016.
ISBN: 978-0-07-802767-3

[4] Anderson, J. D.: Computational fluid dynamics: The basics with applications. McGraw-Hill series in aeronautical and aerospace engineering, New York: McGraw-Hill, 1995.
ISBN: 0070016852

[5] Anderson, J. D.: Fundamentals of aerodynamics. McGraw-Hill series in aeronautical and aerospace engineering, Singapore: McGraw-Hill, 2011.
ISBN: 978-0-07-339810-5

[6] Andiappan, V.; Wan, Y. K.: Distinguishing approach, methodology, method, procedure and technique in process systems engineering. Clean Technologies and Environmental Policy, Vol. 22, No. 3, pp. 547–555, 2020.
DOI: 10.1007/s10098-020-01819-w

[7] ANSYS, Inc: ANSYS Fluent 2022 R1, 2022.
URL: https://www.ansys.com/products/fluids/ansys-fluent (accessed October 10, 2024)

[8] Barbarino, S.; Bilgen, O.; Ajaj, R. M.; Friswell, M. I.; Inman, D. J.: A Review of Morphing Aircraft. Journal of Intelligent Material Systems and Structures, Vol. 22, No. 9, pp. 823–877, 2011.
DOI: 10.1177/1045389X11414084

[9] Benson, C. M.; Ingram, J. M.; Battersby, P. N.; Mba, D.; Sethi, V.; Rolt, A. M.: An Analysis of Civil Aviation Industry Safety Needs for the Introduction of Liquid Hydrogen Propulsion Technology. In: Volume 3: Coal, Biomass, Hydrogen, and Alternative Fuels; Cycle Innovations; Electric Power; Industrial and Cogeneration; Organic Rankine Cycle Power Systems, 2019.
DOI: 10.1115/GT2019-90453

[10] Bergero, C.; Gosnell, G.; Gielen, D.; Kang, S.; Bazilian, M.; Davis, S. J.: Pathways to net-zero emissions from aviation. Nature Sustainability, Vol. 6, No. 4, pp. 404–414, 2023.
DOI: 10.1038/s41893-022-01046-9

[11] Betz, A.: Theory of the slotted wing (NACA-TN-100), 1992.
URL: https://ntrs.nasa.gov/citations/19930080889 (accessed April 12, 2024)

[12] Biedermann, O.; Geerling, G.: Power control units with secondary controlled hydraulic motors - a new concept for application in aircraft high lift systems. In: Recent Advances in Aerospace Hydraulics, 1998.
DOI: 10.15480/882.227

[13] Blakseth, S. S.; Rasheed, A.; Kvamsdal, T.; San, O.: Combining physics-based and data-driven techniques for reliable hybrid analysis and modeling using the corrective source term approach. Applied Soft Computing, Vol. 128, 2022.
DOI: 10.1016/j.asoc.2022.109533

[14] Blume, S.: Eine experimentelle Methodik zur aerodynamischen Optimierung von Mehrelement-Hochauftriebskonfigurationen. Technische Universität Berlin, Ph.D. thesis, 2008.
ISBN: 978-3-86664-509-7.

[15] Boeing Commercial Airplane Company: Assessment of variable camber for application to transport aircraft (NASA-CR-158930), 1980.
URL: https://ntrs.nasa.gov/citations/19810003508 (accessed February 27, 2024)

[16] Bolonkin, A.; Gilyard, G. B.: Estimated Benefits of Variable-Geometry Wing Camber Control for Transport Aircraft (NASA-TM-1999-206586), 1999.
URL: https://ntrs.nasa.gov/citations/19990090019 (accessed February 27, 2024)

[17] Bowers, A. H.; Murillo, O. J.; Jensen, R.; Eslinger, B.; Gelzer, C.: On Wings of the Minimum Induced Drag: Spanload Implications for Aircraft and Birds (NASA-TP-2016-219072), 2016.
URL: https://ntrs.nasa.gov/citations/20160003578 (accessed October 9, 2024)

[18] Budinger, M.; Liscouët, J.; Hospital, F.; Maré, J.-C.: Estimation models for the preliminary design of electromechanical actuators. Proceedings of the Institution of Mechanical Engineers, Part G: Journal of Aerospace Engineering, Vol. 226, No. 3, pp. 243–259, 2012.
DOI: 10.1177/0954410011408941

[19] Burdette, D. A.; Kenway, G. K.; Martins, J.: Aerostructural design optimization of a continuous morphing trailing edge aircraft for improved mission performance. In: AIAA Aviation, 2016.
DOI: 10.2514/6.2016-3209

[20] Burns, B. R. A.: Canards: design with care. FLIGHT International, Vol. 127, No. 3948, pp. 19–21, 1985.
ISSN: 0015-3710

[21] Butter, D. J.: Recent progress on development and understanding of high lift systems. In: Improvement of aerodynamic performance through boundary layer control and high lift systems - AGARD conference proceedings, No. 365, 1984.
ISBN: 92-835-0358-9

[22] Cabrera, E.; Sousa, J. M. M. de: Use of Sustainable Fuels in Aviation—A Review. Energies, Vol. 15, No. 7, p. 2440, 2022.
DOI: 10.3390/en15072440

[23] CentaurSoft: CENTAUR v15.0, 2021.
URL: https://home.centaursoft.com/ (accessed October 10, 2024)

[24] Chakraborty, I.: Subsystem architecture sizing and analysis for aircraft conceptual design. Georgia Institute of Technology, Ph.D. thesis, 2015.
URL: http://hdl.handle.net/1853/54427 (accessed January 30, 2024).

[25] Chakraborty, I.; Mavris, D. N.; Emeneth, M.; Schneegans, A.: A methodology for vehicle and mission level comparison of More Electric Aircraft subsystem solutions: Application to the flight control actuation system. Proceedings of the Institution of Mechanical Engineers, Part G: Journal of Aerospace Engineering, Vol. 229, No. 6, pp. 1088–1102, 2015.
DOI: 10.1177/0954410014544303

[26] Chakraborty, I.; Trawick, D. R.; Jackson, D.; Mavris, D.: Electric Control Surface Actuator Design Optimization and Allocation for the More Electric Aircraft. In: AIAA Aviation, 2013.
DOI: 10.2514/6.2013-4283

[27] Dietz, M.: Aerodynamik des Fliegens, Berlin, Heidelberg: Springer Berlin Heidelberg, 2024.
DOI: 10.1007/978-3-662-68234-0

[28] Drela, M.: A User's Guide to MSES 3.05: User Manual, MIT Department of Aeronautics and Astronautics, 2007.
URL: https://web.mit.edu/drela/Public/web/mses/mses.pdf (accessed May 6, 2024)

[29] Effing, T.; Stephan, R.; Stumpf, E.: Influence of a Detailed Mass Estimation for a Wing with known Flight Shape in Conceptual Overall Aircraft Design. In: Deutscher Luft- und Raumfahrtkongress, 2023.
DOI: 10.25967/610340

[30] European Union Aviation Safety Agency (EASA): Certification Specifications and Acceptable Means of Compliance for Large Aeroplanes (CS-25) - Amendment 28 - 2023/021/R, 2023.
URL: https://www.easa.europa.eu/en/downloads/139073/en (accessed January 9, 2024)

[31] Flightpath 2050: Europe's vision for aviation; maintaining global leadership and serving society's needs; report of the High-Level Group on Aviation Research. European Commission, Luxembourg, 2012.
ISBN: 9789279262296

[32] Foster, D. N.: Flow around Wing Sections with High-Lift Devices. Journal of Aircraft, Vol. 9, No. 3, pp. 205–210, 1972.
DOI: 10.2514/3.58958

[33] Fowler, H. D.: The Fowler Wing Flap. Aircraft Engineering and Aerospace Technology, Vol. 8, No. 9, pp. 247–249, 1936.
DOI: 10.1108/eb030092

[34] Franke, D. M.: Multidisciplinary Design of High-Lift Systems. Technische Universität Carolo-Wilhelmina zu Braunschweig, Ph.D. thesis, 2019.
URL: https://elib.dlr.de/129276/ (accessed January 8, 2024).

[35] Fujiwara, G. E.; Nguyen, N. T.; Livne, E.; Bragg, M. B.: Aerostructural Design Optimization of a Flexible Wing Aircraft with Continuous Morphing Trailing Edge. In: Multidisciplinary Analysis and Optimization, 2018.
DOI: 10.2514/6.2018-3571

[36] Gaillot, T.; Beauchet, S.; Lorne, D.; Krim, L.: The impact of fossil jet fuel emissions at altitude on climate change: A life cycle assessment study of a long-haul flight at different time horizons. Atmospheric Environment, Vol. 311, 2023.
DOI: 10.1016/j.atmosenv.2023.119983

[37] Garmendia, D. C.; Chakraborty, I.; Mavris, D. N.: Multidisciplinary Approach to Assessing Actuation Power of a Hybrid Wing–Body. Journal of Aircraft, Vol. 53, No. 4, pp. 900–913, 2016.
DOI: 10.2514/1.C033390

[38] GasTurb GmbH: GasTurb 14: Design and Off-Design Performance of Gas Turbines, 2023.
URL: https://gasturb.com/Downloads/Manuals/GasTurb14.pdf (accessed May 2, 2024)

[39] Greff, E.: The development and design integration of a variable camber wing for long/medium range aircraft. The Aeronautical Journal, Vol. 94, No. 939, pp. 301–312, 1990.
DOI: 10.1017/S0001924000023186

[40] Grewe, V.; Matthes, S.; Frömming, C.; Brinkop, S.; Jöckel, P.; Gierens, K.; Champougny, T.; Fuglestvedt, J.; Haslerud, A.; Irvine, E.; Shine, K.: Feasibility of climate-optimized air traffic routing for trans-Atlantic flights. Environmental Research Letters, Vol. 12, No. 3, p. 034003, 2017.
DOI: 10.1088/1748-9326/aa5ba0

[41] Günther, F.; Fritsch, S.: neuralnet: Training of Neural Networks. The R Journal, Vol. 2, No. 1, p. 30, 2010.
DOI: 10.32614/RJ-2010-006

[42] Held, I. M.; Soden, B. J.: Water Vapor Feedback and Global Warming. Annual Review of Energy and the Environment, Vol. 25, No. 1, pp. 441–475, 2000.
DOI: 10.1146/annurev.energy.25.1.441

[43] Hilbig, H.; Wagner, H.: Variable Wing Camber Control For Civil Transport Aircraft. In: 14th Congress of the International Council of the Aeronautical Sciences, 1984.
ISBN: 0-915928-89-2

[44] Horstmann, K.: Ein Mehrfach-Traglinienverfahren und seine Verwendung für Entwurf und Nachrechnung nichtplanarer Flügelanordnungen (DFVLR-FB 87-51). TU Braunschweig, Ph.D. thesis, 1988.
ISSN: 0171-1342.

[45] Howe, D.: Aircraft conceptual design synthesis, London: Professional Engineering Publishing, 2010.
DOI: 10.1002/9781118903094

[46] Hürlimann, F.: Mass Estimation of Transport Aircraft Wingbox Structures with a CAD/CAE-Based Multidisciplinary Process. ETH Zurich, Ph.D. thesis, 2010.
DOI: 10.3929/ethz-a-006361295.

[47] ICAO Annex 16 - Environmental Protection: Volume IV - Carbon Offsetting and Reduction Scheme for International Aviation (CORSIA). International Civil Aviation Organization, 2018.
URL: https://www.icao.int/environmental-protection/CORSIA/Pages/SARPs-Annex-16-Volume-IV.aspx (accessed February 6, 2024)

[48] Impact Assessment: Revision of the EU Emissions Trading System for aviation - SWD(2021) 603. European Commission, Brussels, 2021.
URL: https://eur-lex.europa.eu/legal-content/EN/TXT/PDF/?uri=CELEX:52021SC0603 (accessed February 16, 2022)

[49] Industry High-level Group: Aviation Benefits Report, 2019.
URL: https://www.icao.int/sustainability/Documents/AVIATION-BENEFITS-2019-web.pdf (accessed April 25, 2024)

[50] James, G.; Witten, D.; Hastie, T.; Tibshirani, R.: An introduction to statistical learning: With applications in R. Springer texts in statistics, New York et al.: Springer, 2013.
ISBN: 978-1-4614-7138-7

[51] Jandaurek, K.; Johst, M.: Analysis of Different Methods for Calculation of High-Lift System Loads in Test Means Applications. In: AIAA Scitech Forum, 2019.
DOI: 10.2514/6.2019-0938

[52] Jentys, M.; Effing, T.; Breitsamter, C.; Stumpf, E.: Multifidelity aerodynamic analyses of a hybrid laminar flow control and variable camber coupled wing. In: Aerospace Europe Conference - 10th EUCASS - 9th CEAS, 2023.
DOI: 10.13009/EUCASS2023-384

[53] Jentys, M.; Effing, T.; Breitsamter, C.; Stumpf, E.: Numerical analyses of a reference wing for combination of hybrid laminar flow control and variable camber. CEAS Aeronautical Journal, Vol. 13, No. 4, pp. 989–1002, 2022.
DOI: 10.1007/s13272-022-00598-y

[54] Joseph, V. R.: Optimal ratio for data splitting. Statistical Analysis and Data Mining: The ASA Data Science Journal, Vol. 15, No. 4, pp. 531–538, 2022.
DOI: 10.1002/sam.11583

[55] Kaul, U. K.; Nguyen, N. T.: Drag Optimization Study of Variable Camber Continuous Trailing Edge Flap (VCCTEF) Using OVERFLOW. In: AIAA Aviation, 2014.
DOI: 10.2514/6.2014-2444

[56] Kota, S.; Flick, P.; Collier, F.; Collier, F. S.: Flight Testing of the FlexFloil Adaptive Compliant Trailing Edge. In: 54th AIAA Aerospace Sciences Meeting 2016, 2016.
DOI: 10.2514/6.2016-0036

[57] Kota, S.; Osborn, R.; Ervin, G.; Maric, D.: Mission Adaptive Compliant Wing - Design, Fabrication and Flight Test: NATO S&T Meeting Proceedings RDP - RTO-MP-AVT-168, 2009.
URL: https://www.sto.nato.int/publications/STO%20Meeting%20Proceedings/RTO-MP-AVT-168/MP-AVT-168-18.pdf (accessed February 27, 2024)

[58] Kumar, P.; German, B. J.: Optimization of High-Lift Systems at Takeoff Conditions Subject to Kinematic Constraints. Journal of Aircraft, pp. 1–6, 2022.
DOI: 10.2514/1.C036493

[59] Lammering, T.: Integration of aircraft systems into conceptual design synthesis. RWTH Aachen University, Ph.D. thesis, 2014.
URL: https://publications.rwth-aachen.de/record/229107 (accessed January 31, 2024).

[60] Lampl, T.; Königsberger, R.; Hornung, M.: Design and Evaluation of Distributed Electric Drive Architectures for High-Lift Control Systems. In: Deutscher Luft- und Raumfahrtkongress, 2017.
URL: https://www.dglr.de/publikationen/2017/450110.pdf (accessed January 30, 2024)

[61] Lebofsky, S.; Ting, E.; Nguyen, N. T.: Aeroelastic Modeling and Drag Optimization of Aircraft Wing with Variable Camber Continuous Trailing Edge Flap. In: 32nd AIAA Applied Aerodynamics Conference, 2014.
DOI: 10.2514/6.2014-2443

[62] Lebofsky, S.; Ting, E.; Nguyen, N. T.: Multidisciplinary Drag Optimization of Reduced Stiffness Flexible Wing Aircraft With Variable Camber Continuous Trailing Edge Flap. In: 56th AIAA/ASCE/AHS/ASC Structures, Structural Dynamics, and Materials Conference, 2015.
DOI: 10.2514/6.2015-1408

[63] Lee, J. J.: Can we accelerate the improvement of energy efficiency in aircraft systems? Energy Conversion and Management, Vol. 51, No. 1, pp. 189–196, 2010.
DOI: 10.1016/j.enconman.2009.09.011

[64] Liebeck, R. H.; Smyth, D. N.: Study of Slat-Airfoil Combinations Using Computer Graphics. Journal of Aircraft, Vol. 10, No. 4, pp. 254–256, 1973.
DOI: 10.2514/3.60221

[65] Liu, Y.; Ouyang, S.; Zhao, X.: Drag Reduction Effect of a Variable Camber Wing of a Transport Aircraft Based on Trailing Edge Flap Deflection of Small Angles. In: The Proceedings of the 2018 Asia-Pacific International Symposium on Aerospace Technology, 2018.
DOI: 10.1007/978-981-13-3305-7_120

[66] Ljungström, B. L. G.: Experimental study of viscous flow on multiple element airfoils. In: Proceedings of the 9th Congress of the International Council of the Aeronautical Sciences, 1974.
URL: https://www.icas.org/ICAS_ARCHIVE/ICAS1974/Page%20369%20Ljungstr%C3%B6m.pdf (accessed January 17, 2024)

[67] Lulla, C.: Functional Flexibility of the A350XWB High Lift System. In: Deutscher Luft- und Raumfahrtkongress, 2011.
ISBN: 9783932182747

[68] Lyu, Z.; Martins, J. R. R. A.: Aerodynamic Shape Optimization of an Adaptive Morphing Trailing-Edge Wing. Journal of Aircraft, Vol. 52, No. 6, pp. 1951–1970, 2015.
DOI: 10.2514/1.C033116

[69] Maré, J.-C.: Aerospace Actuators 1: Needs, Reliability and Hydraulic Power Solutions. Systems and Industrial Engineering - Robotics Series, London and Hoboken, NJ: ISTE and Wiley, 2016.
DOI: 10.1002/9781119307662

[70] Maré, J.-C.: Aerospace Actuators 2: Signal-by-wire and power-by-wire. Systems and industrial engineering. Robotic series, Somerset: John Wiley & Sons Incorporated, 2017.
DOI: 10.1002/9781119332442

[71] Maré, J.-C.: Aerospace Actuators 3: European Commercial Aircraft and Tiltrotor Aircraft, Hoboken, NJ, USA: John Wiley & Sons, Inc, 2018.
DOI: 10.1002/9781119505433

[72] McLean, J. D.: Understanding aerodynamics: Arguing from the real physics. Aerospace series, Chichester: Wiley, 2013.
ISBN: 978-1-119-96751-4

[73] Miller, M.: The Multi-Objective Design of Flatback Wind Turbine Airfoils. Carleton University, Ph.D. thesis, 2016.
DOI: 10.13140/RG.2.2.20396.67201.

[74] Moens, F.: Augmented Aircraft Performance with the Use of Morphing Technology for a Turboprop Regional Aircraft Wing. Biomimetics, Vol. 4, No. 3, 2019.
DOI: 10.3390/biomimetics4030064

[75] Morgan Jr., H. L.; Ferris, J. C.; Mcghee, R. J.: A study of high-lift airfoils at high Reynolds numbers in the Langley low-turbulence pressure tunnel, 1987.
URL: https://ntrs.nasa.gov/citations/19900000686 (accessed April 12, 2024)

[76] Murru, N.; Rossini, R.: A Bayesian approach for initialization of weights in backpropagation neural net with application to character recognition. Neurocomputing, Vol. 193, pp. 92–105, 2016.
DOI: 10.1016/j.neucom.2016.01.063

[77] National Aeronautics and Space Administration (NASA): U.S. Standard Atmosphere (NASA-TM-X-74335), 1976.
URL: https://ntrs.nasa.gov/citations/19770009539 (accessed January 9, 2024)

[78] Nguyen, N. T.; Lebofsky, S.; Ting, E.; Kaul, U.; Chaparro, D.; Urnes, J.: Development of Variable Camber Continuous Trailing Edge Flap for Performance Adaptive Aeroelastic Wing. In: SAE Technical Paper Series, 2015.
DOI: 10.4271/2015-01-2565

[79] Nguyen, N. T.; Livne, E.; Precup, N.; Urnes, J. M.; Nelson, C.; Ting, E.; Lebofsky, S.: Experimental Investigation of a Flexible Wing with a Variable Camber Continuous Trailing Edge Flap Design. In: AIAA Aviation, 2014.
DOI: 10.2514/6.2014-2441

[80] Nguyen, N. T.; Precup, N.; Livne, E.; Urnes, J. M.; Dickey, E.; Nelson, C.; Chiew, J.; Rodriguez, D. L.; Ting, E.; Lebofsky, S.: Wind Tunnel Investigation of a Flexible Wing High-Lift Configuration with a Variable Camber Continuous Trailing Edge Flap Design. In: AIAA Aviation, 2015.
DOI: 10.2514/6.2015-2417

[81] Obert, E.; Slingerland, R.: Aerodynamic Design of Transport Aircraft, Amsterdam: IOS Press BV, 2009.
ISBN: 978-1-58603-970-7

[82] Pagani, C. C.; Souza, D. S.; Medeiros, M. A.: Experimental investigation on the effect of slat geometrical configurations on aerodynamic noise. Journal of Sound and Vibration, Vol. 394, pp. 256–279, 2017.
DOI: 10.1016/j.jsv.2017.01.013

[83] Parenteau, M.; Sermeus, K.; Laurendeau, E.: VLM Coupled with 2.5D RANS Sectional Data for High-Lift Design. In: 2018 AIAA Aerospace Sciences Meeting, 2018.
DOI: 10.2514/6.2018-1049

[84] Peter, F.: A methodology for variable camber assessment in conceptional aircraft design. RWTH Aachen University, Ph.D. thesis, 2025.
(Submitted).

[85] Peter, F.; Risse, K.; Schültke, F.; Stumpf, E.: Variable Camber Impact on Aircraft Mission Planning. In: 53rd AIAA Aerospace Sciences Meeting, 2015.
DOI: 10.2514/6.2015-1902

[86] Pope, S. B.: Turbulent flows, Cambridge: Cambridge Univ. Press, 2000.
ISBN: 978-0521598866

[87] Prandtl, L.: Über Flüssigkeitsbewegung bei sehr kleiner Reibung. Verhandlungen des III. Internationalen Mathematiker-Kongresses, Heidelberg, 1904.
URL: http://www.damtp.cam.ac.uk/user/tong/fluids/prandtl.pdf (accessed May 6, 2024)

[88] Raymer, D.: Aircraft Design: A Conceptual Approach, Sixth Edition, Washington, DC: American Institute of Aeronautics and Astronautics, Inc, 2018.
DOI: 10.2514/4.104909

[89] Rea, F.; Amoroso, F.; Pecora, R.; Moens, F.: Exploitation of a Multifunctional Twistable Wing Trailing-Edge for Performance Improvement of a Turboprop 90-Seats Regional Aircraft. Aerospace, Vol. 5, No. 4, p. 122, 2018.
DOI: 10.3390/aerospace5040122

[90] Recksiek, M.: Advanced high lift system architecture with distributed electrical flap actuation. In: Proceedings of the 2nd International Workshop on Aircraft System Technologies, 2009.
ISBN: 3-8322-8071-5

[91] Reckzeh, D.: Multifunctional wing moveables: Design of the A350XWB and the way to future concepts. In: 29th Congress of the International Council of the Aeronautical Sciences, 2014.
ISBN: 3-932182-80-4

[92] Reckzeh, D.: Aerodynamic design of the high-lift-wing for a Megaliner aircraft. Aerospace Science and Technology, Vol. 7, No. 2, pp. 107–119, 2003.
DOI: 10.1016/S1270-9638(02)00002-0

[93] Risse, K.: Preliminary Overall Aircraft Design with Hybrid Laminar Flow Control. RWTH Aachen University, Ph.D. thesis, 2016.
DOI: 10.18154/RWTH-2017-00974.

[94] Risse, K.; Anton, E.; Lammering, T.; Franz, K.; Hoernschemeyer, R.: An Integrated Environment for Preliminary Aircraft Design and Optimization. In: 53rd AIAA/ASME/ASCE/AHS/ASC Structures, Structural Dynamics and Materials Conference, 2012.
DOI: 10.2514/6.2012-1675

[95] Risse, K.; Schäfer, K.; Schültke, F.; Stumpf, E.: Central Reference Aircraft data System (CeRAS) for research community. CEAS Aeronautical Journal, Vol. 7, No. 1, pp. 121–133, 2016.
DOI: 10.1007/s13272-015-0177-9

[96] Ritchie, H.: What share of global CO2 emissions come from aviation? Our World in Data, 2024.
URL: https://ourworldindata.org/global-aviation-emissions (accessed April 25, 2024)

[97] Röben, T.: Hybrid Actuation in Primary Flight Control Systems - A Force-Fight Inhibiting System Architecture. RWTH Aachen University, Ph.D. thesis, 2018.
DOI: 10.18154/RWTH-2019-00621.

[98] Roskam, J.; Lan, C.-T. E.: Airplane aerodynamics and performance, Lawrence, Kan.: DARcorporation, 1997.
ISBN: 1-884885-44-6

[99] Rossow, C.-C.; Wolf, K.; Horst, P., eds.: Handbuch der Luftfahrzeugtechnik, München: Carl Hanser Verlag, 2014.
ISBN: 978-3-446-42341-1

[100] Rudnik, R.; Huber, K.; Melber-Wilkending, S.: EUROLIFT Test Case Description for the 2nd High Lift Prediction Workshop. In: 30th AIAA Applied Aerodynamics Conference, 2012.
DOI: 10.2514/6.2012-2924

[101] Rudolph, P. K. C.: High-lift systems on commercial subsonic airliners (NASA-CR-4746), 1996.
URL: https://ntrs.nasa.gov/citations/19960052267 (accessed January 9, 2024)

[102] Schindler, K.; Reckzeh, D.; Scholz, U.; Grimminger, A.: Aerodynamic Design of High-Lift Devices for Civil Transport Aircraft Using RANS CFD. In: 28th AIAA Applied Aerodynamics Conference, 2010.
DOI: 10.2514/6.2010-4946

[103] Schlichting, H.; Gersten, K.: Grenzschicht-Theorie, Berlin: Springer, 2006.
ISBN: 978-3-540-23004-5

[104] Schlichting, H.; Truckenbrodt, E.: Aerodynamik des Flugzeuges: Erster Band: Grundlagen aus der Strömungstechnik Aerodynamik des Tragflügels (Teil I), Berlin, Heidelberg: Springer Berlin Heidelberg, 2001.
DOI: 10.1007/978-3-642-56911-1

[105] Schottmüller, H.: Numerische Untersuchung zum Einfluss der Positionierung verschiedener Hochauftriebskonfigurationen am Flügelprofil. RWTH Aachen University, Master thesis (Supervisor: Stephan, R.), 2022.
URL: https://publications.rwth-aachen.de/record/958234 (accessed January 8, 2024).

[106] Schröder, W.: Fluidmechanik. Aachener Beiträge zur Strömungsmechanik, Wissenschaftsverlag Mainz in Aachen, 2010.
ISBN: 3-86130-371-X

[107] Schültke, F.; Aigner, B.; Effing, T.; Strathoff, P.; Stumpf, E.: MICADO: Overview of Recent Developments within the Conceptual Aircraft Design and Optimization Environment. In: Deutscher Luft- und Raumfahrtkongress, 2020.
DOI: 10.25967/530093

[108] Schültke, F.; Stumpf, E.: Implementation of an Airfoil Information Database for Usage in Conceptual Aircraft Wing Design Process. In: AIAA Scitech Forum, 2019.
DOI: 10.2514/6.2019-0814

[109] SENER group: HP-SMART EMA. Development of high power density electrical actuators, 2016.
URL: https://cordis.europa.eu/project/id/255819 (accessed March 27, 2024)

[110] Sharma, S.; Sharma, S.; Athaiya, A.: Activation functions in neural networks. International Journal of Engineering Applied Sciences and Technology, Vol. 04, No. 12, pp. 310–316, 2020.
DOI: 10.33564/IJEAST.2020.v04i12.054

[111] Smith, A. M. O.: High-Lift Aerodynamics. Journal of Aircraft, Vol. 12, No. 6, pp. 501–530, 1975.
DOI: 10.2514/3.59830

[112] Soori, M.; Arezoo, B.; Dastres, R.: Artificial intelligence, machine learning and deep learning in advanced robotics, a review. Cognitive Robotics, Vol. 3, pp. 54–70, 2023.
DOI: 10.1016/j.cogr.2023.04.001

[113] Stephan, R.; Heyen, C.; Stumpf, E.; Ruhland, J.; Breitsamter, C.: Neural-Network-Based Model for Trailing-Edge Flap Loads in Preliminary Aircraft Design. Journal of Aircraft, Vol. 61, No. 4, pp. 1131–1142, 2024.
DOI: 10.2514/1.C037632

[114] Stephan, R.; Schneiders, N.; Schültke, F.; Peter, F.; Stumpf, E.: Evaluation of a Distributed Variable-Camber Trailing-Edge Flap System at Preliminary Aircraft Design Stage. In: AIAA AVIATION 2022 Forum, 2022.
DOI: 10.2514/6.2022-3519

[115] Stephan, R.; Schneiders, N.; Weber, G.; Schültke, F.; Stumpf, E.; Peter, F.: Methodology for Evaluating a Distributed Variable-Camber Trailing-Edge System in Preliminary Aircraft Design. Journal of Aircraft, Vol. 61, No. 4, pp. 1057–1070, 2024.
DOI: 10.2514/1.C037145

[116] Stephan, R.; Stumpf, E.; Schottmüller, H.; Röben, T.; Dreyer, N.; Immler, T.: Methodology for Preliminary Flight Control Actuator Design. Journal of Aircraft, Vol. 60, No. 5, pp. 1538–1552, 2023.
DOI: 10.2514/1.C036717

[117] Strüber, H.: The aerodynamic design of the A350 XWB-900 high lift system. In: 29th Congress of the International Council of the Aeronautical Sciences, 2014.
ISBN: 3-932182-80-4

[118] Sustainable and Smart Mobility Strategy - putting European transport on track for the future. European Commission, Brussels, 2020.
URL: https://eur-lex.europa.eu/resource.html?uri=cellar:5e601657-3b06-11eb-b27b-01aa75ed71a1.0001.02/DOC_1&format=PDF (accessed September 9, 2024)

[119] Szodruch, J.; Hilbig, R.: Variable Wing Camber for Transport Aircraft. Progress in Aerospace Sciences, Vol. 25, No. 3, pp. 297–328, 1988.
DOI: 10.1016/0376-0421(88)90003-6

[120] Tetko, I. V.; Livingstone, D. J.; Luik, A. I.: Neural network studies. 1. Comparison of overfitting and overtraining. Journal of Chemical Information and Computer Sciences, Vol. 35, No. 5, pp. 826–833, 1995.
DOI: 10.1021/ci00027a006

[121] The European Green Deal. European Commission, Brussels, 2019.
URL: https://eur-lex.europa.eu/resource.html?uri=cellar:b828d165-1c22-11ea-8c1f-01aa75ed71a1.0002.02/DOC_1&format=PDF (accessed September 9, 2024)

[122] Ting, E.; Chaparro, D.; Nguyen, N. T.; Fujiwara, G. E. C.: Optimization of Variable-Camber Continuous Trailing-Edge Flap Configuration for Drag Reduction. Journal of Aircraft, Vol. 55, No. 6, pp. 2217–2239, 2018.
DOI: 10.2514/1.C034810

[123] Torabzadeh-Tari, M.: Dimensioning tools of MEA actuator systems, including modeling, analysis and technology comparison. KTH Electrical Engineering, Ph.D. thesis, 2008.
ISBN: 978-91-7415-157-2.

[124] Torenbeek, E.: Synthesis of Subsonic Airplane Design, Dordrecht: Kluwer Academic Publishers and Springer Netherlands, 1982.
DOI: 10.1007/978-94-017-3202-4

[125] Truckenbrodt, E.: Fluidmechanik: Band 2: Elementare Strömungsvorgänge dichteveränderlicher Fluide sowie Potential- und Grenzschichtströmungen, Berlin, Heidelberg: Springer, 2008.
DOI: 10.1007/978-3-540-79024-2

[126] Urnes, J.; Nguyen, N. T.: A Mission-Adaptive Variable Camber Flap Control System to Optimize High Lift and Cruise Lift-to-Drag Ratios of Future N+3 Transport Aircraft. In: Aerospace Sciences Meetings, 2013.
DOI: 10.2514/6.2013-214

[127] van Dam, C. P.: The aerodynamic design of multi-element high-lift systems for transport airplanes. Progress in Aerospace Sciences, Vol. 38, No. 2, pp. 101–144, 2002.
DOI: 10.1016/S0376-0421(02)00002-7

[128] van den Bossche, D.: The A380 Flight Control Electrohydrostatic Actuators, Achievements and Lessons Learnt. In: 25th International Congress of Aeronautical Sciences, 2006.
ISBN: 0-9533991-7-6

[129] Vechtel, D.; Hauber, B.; Looye, G.: Analysis of a multi-functional high-lift system driven by an active differential gear box. CEAS Aeronautical Journal, Vol. 5, No. 3, pp. 227–238, 2014.
DOI: 10.1007/s13272-014-0102-7

[130] Weber, G.: Untersuchung eines verteilten Hinterkantenklappensystems mit variabler Wölbung auf die Reiseflugeffizienz eines nachgerüsteten und getrimmten CS-25 Langstreckenflugzeugs im Flugzeugvorentwurf. RWTH Aachen University, Master thesis (Supervisor: Stephan, R.), 2023.
URL: https://publications.rwth-aachen.de/record/969888 (accessed January 4, 2024).

[131] Wentz Jr., W. H.: Wind Tunnel Tests of the GA (W)-2 Airfoil with 20% Aileron, 25% Slotted Flap, 30% Fowler Flap and 10% Slot-Lip Spoiler (NASA-CR-145139), 1976.
URL: https://ntrs.nasa.gov/citations/19790001850 (accessed March 1, 2024)

[132] Wild, J.: High-Lift Aerodynamics, Boca Raton: CRC Press, 2022.
DOI: 10.1201/9781003220459

[133] Wild, J.; Brezillon, J.; Amoignon, O.; Quest, J.; Moens, F.; Quagliarella, D.: Advanced High-Lift Design by Numerical Methods and Wind Tunnel Verification within the European Project EUROLIFT II. In: 25th AIAA Applied Aerodynamics Conference, 2007.
DOI: 10.2514/6.2007-4300

[134] Woehler, S.; Hartmann, J.; Prenzel, E.; Kwik, H.: Preliminary aircraft design for a midrange reference aircraft taking advanced technologies into account as part of the AVACON project for an entry into service in 2028. In: Deutscher Luft- und Raumfahrtkongress, 2018.
DOI: 10.25967/480224

[135] Woodward, D. S.; Hardy, B. C.; Ashill, P. R.: Some Types of Scale Effect in Low-Speed, High-Lift Flows. In: 16th Congress of International Council of the Aeronautical Sciences, 1988.
URL: https://www.icas.org/ICAS_ARCHIVE/ICAS1988/ICAS-88-4.9.3.pdf (accessed January 17, 2024)

[136] Ying, S. X.; Spaid, F. W.; McGinley, C. B.; Rumsey, C. L.: Investigation of Confluent Boundary Layers in High-Lift Flows. Journal of Aircraft, Vol. 36, No. 3, pp. 550–562, 1999.
DOI: 10.2514/2.2490

[137] Zaccai, D.; Bertels, F.; Vos, R.: Design methodology for trailing-edge high-lift mechanisms. CEAS Aeronautical Journal, Vol. 7, No. 4, pp. 521–534, 2016.
DOI: 10.1007/s13272-016-0202-7

A Supplementary information on fundamentals and state of the art

This appendix provides additional insights and data to complement Chapter 2. It offers extended theoretical derivations and schematics for a better understanding of the fundamental concepts introduced in the chapter.

A.1 Fundamentals

This section provides additional theoretical background, elaborating on key principles introduced in the main text. It includes derivations, schematics, and supplementary equations that support the understanding of foundational aerodynamic concepts.

A.1.1 Continuum flow and free-molecule flow

The differentiation between free molecular flow and continuum flow is made in Section 2.1.1 in the course of explaining the development of lift. Two corresponding images are provided in Fig. A.1 to illustrate the difference. For quantification, the Knudsen number Kn is introduced, which relates the mean free path of the molecules to a characteristic length scale. For a characteristic length of 10 m, Kn must remain below 0.01 for the fluid to be treated as a continuum [27].

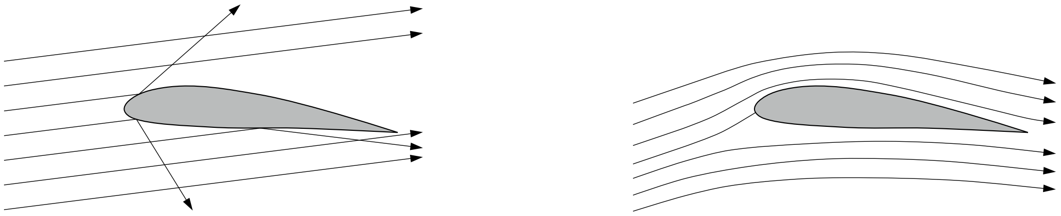

(a) Free molecular flow **(b)** Attached streamlines in continuum flow

Figure A.1: Schematic comparison of free molecular flow and continuum flow.

A.1.2 Derivation of the solution for the induced velocity for an infinite vortex filament

The induced drag is also discussed as part of the fundamentals and principles of variable camber. For this purpose, as shown in Figs. 2.38 and 2.39, the abstraction of an arbitrary vortex filament to a semi-infinite vortex filament is derived, with the corresponding velocity given in Eq. (2.19). The intermediate step over an infinite vortex filament is given below.

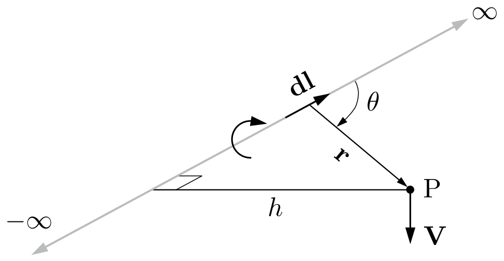

Figure A.2: Abstraction to a straight, infinite vortex filament, adapted from [5].

Integration of the Biot-Savart law, see Eq. (2.18), for an infinite, straight vortex filament [5], as depicted in Fig. A.2.

$$\mathbf{V} = \int_{-\infty}^{\infty} \frac{\Gamma}{4\pi} \frac{\mathbf{dl} \times \mathbf{r}}{|\mathbf{r}|^3} \tag{A.1}$$

Extraction of constant variables from the integral and integration by substitution with $r = \frac{h}{\sin(\theta)}$, $l = \frac{h}{\tan(\theta)}$, and $dl = -\frac{h}{\sin^2(\theta) d\theta}$ [5]:

$$U = -\frac{\Gamma}{4\pi h} \int_{\pi}^{0} \sin\theta \, d\theta = \frac{\Gamma}{2\pi h} \tag{A.2}$$

The velocity induced at a point P by an infinite, straight vortex filament, which lies at a perpendicular distance h from P, is thus calculated with Eq. (A.2). For a semi-infinite vortex filament, the result is obtained by dividing by two [5].

A.2 State of the art - leading edge devices

An overview of various trailing edge flap systems in the retracted and extended state is given in Section 2.1.3 in Fig. 2.15. As this thesis focuses on the trailing edge in the subsequent variable camber application, the analogous illustration for leading edge systems is provided here in the appendix.

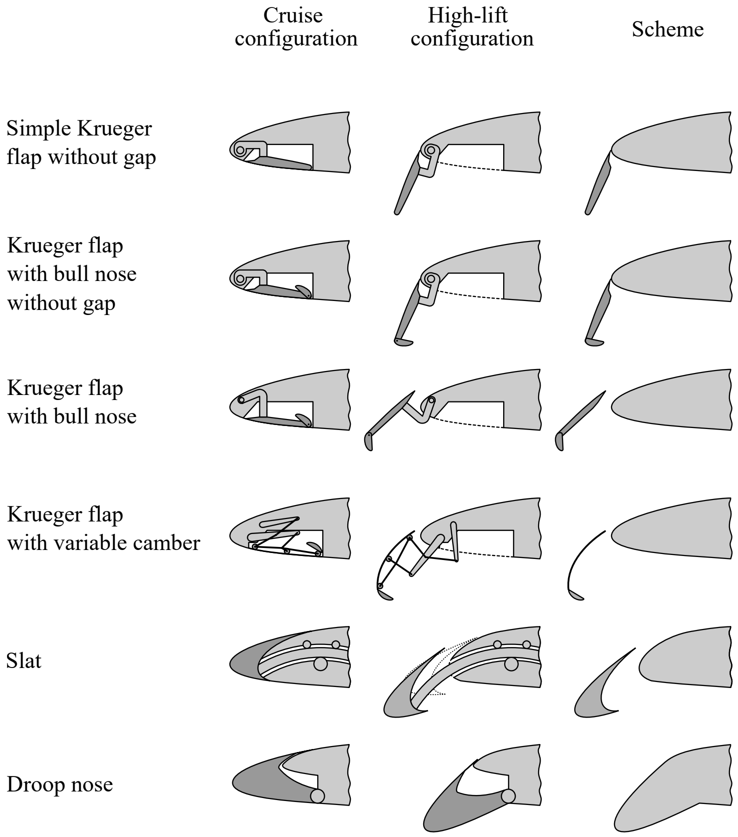

Figure A.3: Various leading edge devices in retracted and deployed settings [14].

B Supplementary information on aircraft design methodologies

This appendix provides additional details supporting the methodologies outlined in Chapter 3. It covers topics such as high-lift configuration optimization, computational approaches including CFD methods, neural network generation for aerodynamic predictions, and preliminary wing mass investigations using aircraft design tools.

B.1 High-lift airfoil configuration optimization

In the course of the high-lift airfoil optimization in Section 3.1.2, nine airfoils are fully optimized and serve as a foundation for deriving methodologies with partially or fully empirical approaches. These airfoils were selected due to their different airfoil characteristics and geometries, as depicted in Fig. B.1 and stated in Table B.1.

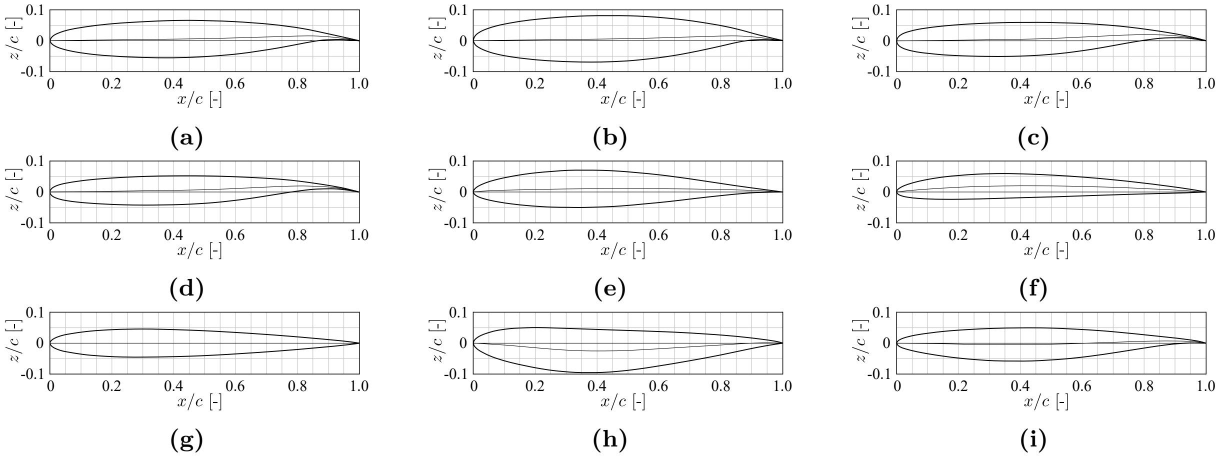

(a) (b) (c)

(d) (e) (f)

(g) (h) (i)

Figure B.1: Airfoils for the high-lift methodology.

Table B.1: Geometric airfoil parameter for high-lift configuration methodology, values in [%].

Airfoil ID	Note	max. t/c	$x/c\|_{\text{max. } t/c}$	max. camber	$x/c\|_{\text{max. camber}}$
(a)	Case study airfoil, Section 3.1.1	15.0	40.5	1.55	84.0
(b)	Methodology comparison, Section 3.1.2	12.0	41.0	1.55	84.0
(c)	-	10.9	36.3	2.0	81.5
(d)	-	9.3	36.8	2.0	81.3
(e)	-	12.0	35.0	1.1	53.0
(f)	-	8.0	30.0	2.0	40.6
(g)	Methodology comparison, Section 3.1.2	9.0	29.5	0	-
(h)	Methodology comparison, Section 3.1.2	14.1	33.6	-2.5	40.8
(i)	-	10.8	39.5	0.7	89.1

B.1.1 Analysis for the preliminary slat positioning of the landing configuration

In the following, the evaluation of the preliminary slat positioning in the course of the high-lift airfoil optimization is discussed using the selected case study from Section 3.1.1.

In the first step, the optimal positioning with regard to the lift coefficient C_L is determined for the slat angles η_S of 15 deg, 20 deg, and 25 deg at a constant angle of attack of $\alpha = 16$ deg. Unlike the approach in the literature [132], which incorporates the determination of the maximum angle of attack for each profile——a process that is time-consuming and must be conducted separately for each airfoil——a fixed angle of attack is selected to minimize effort. The angle of attack of 16 deg is chosen to ensure that nearly all airfoils can achieve it without flow separation while still operating close to their maximum angle of attack [105].

The graphical evaluation of the spatial grid with C_L as contour is shown in Fig. B.2. Note that the different spatial points are not operating states, but each point represents a distinct configuration. Therefore, broad areas of high C_L do not automatically indicate more efficient operation. In order to convert the spatial positioning, which is stated in the contour plots in x and y coordinates, into the more intuitive measurement of the gap, the line plot, given at the bottom right, specifies the resulting gap.

Note further that the slat is intended in particular to enable high angles of attack. Therefore, in a second step, with the positioning determined from Fig. B.2, an angle of attack polar is run for each η_S. These polars are shown in Fig. B.3.

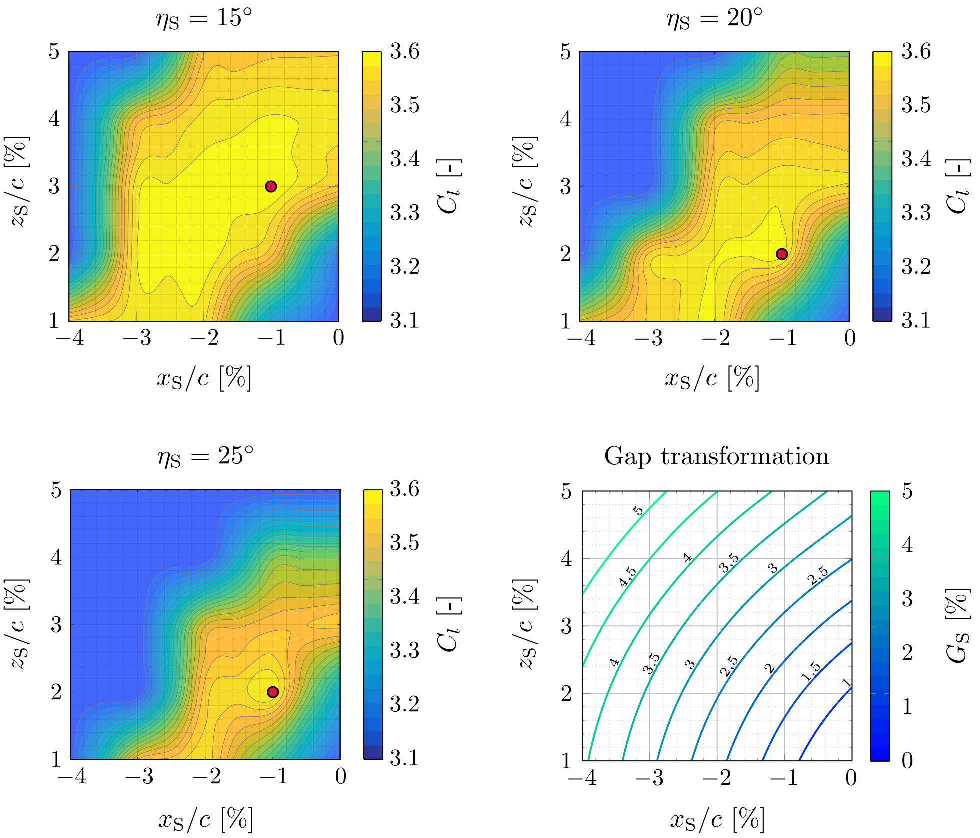

Figure B.2: Preliminary slat positioning optimization over a Cartesian grid for three different extension angles at $\alpha = 16\,\mathrm{deg}$.

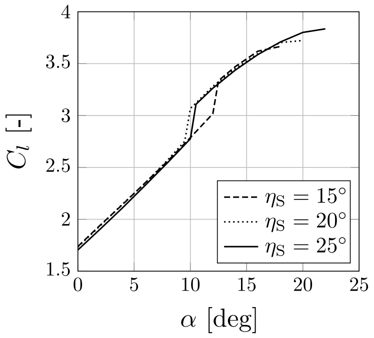

Figure B.3: Polars at different η_S with respective optimum positioning.

Regarding the polar curves, the lift coefficient for all slat angles is nearly identical across the entire range of angles of attack. The exception is the range from $\alpha = 9\,\mathrm{deg}$ to $13\,\mathrm{deg}$, caused by the flow around the flap. Below this range, the flow on the flap is separated. According to Section 2.1.2, the increased angle of attack leads to thickened boundary layers and wake flows, with the damping effect on the flap from approximately $\alpha = 10\,\mathrm{deg}$ is sufficient to prevent the flap from separating. The $2\,\mathrm{deg}$ delayed transition at $\eta_\mathrm{S} = 15\,\mathrm{deg}$ is caused by the larger gap, see the identified slat positions in Fig. B.2. Consequently, the wake of the slat at $\eta_\mathrm{S} = 15\,\mathrm{deg}$ provides the necessary damping is achieved only at $\alpha = 12\,\mathrm{deg}$. Ultimately, the slat angle of $\eta_\mathrm{S} = 25\,\mathrm{deg}$ is chosen, as in this case, angles of attack of up to $\alpha = 22\,\mathrm{deg}$ are feasible. The corresponding gap according to Fig. B.2 is $G_\mathrm{S} = 1.7\,\%$ with an overlap of $O_\mathrm{S} = -1\,\%$.

B.1.2 Airfoil sectioning illustration for high-lift configuration optimization

The method used in Section 3.1.1 for cutting out the control surfaces from an airfoil uses reference points for the Bézier curves. These points are shown in Fig. B.4 for the respective positions on the slat, spoiler, and flap. Further information can be found in [105].

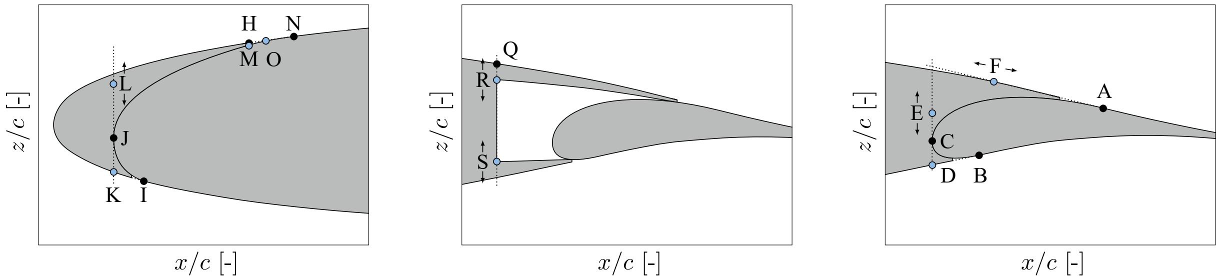

(a) Slat **(b)** Spoiler and coving **(c)** Flap

Figure B.4: Point distribution for sectioning the high-lift elements, adapted from [105].

B.2 Notes on computational fluid dynamics

In this thesis, CFD is used in several instances, a short summary of selected fundamentals is given below. Furthermore, tables with the respective applied parameter settings are provided. For more details, the reader is recommended to consult the works of Pope [86], Wild [132] and McLean [72].

In particular, this section refers to the Reynolds-averaged Navier-Stokes (RANS) equations, whereby the previously introduced Navier Stokes Eqs. (2.2)-(2.3c) are averaged over time to reduce the computational time. This averaging means that the fluctuation terms are eliminated and the mean values remain. These mean values are usually sufficient for engineering applications, although there are of course exceptions. [86]

However, specific terms remain where two fluctuation terms are multiplied, since these terms cannot be eliminated by time averaging. Since all the original Navier-Stokes equations would have to be solved in order to determine the remaining fluctuation terms, there would be no benefit in computing time. Therefore, these terms are modeled instead of simulated, which is an important distinction in this context. A number of different models exist for this purpose; the so-called k-ω model is primarily used in this thesis. [86]

Furthermore, a few aspects of meshing a geometry need to be discussed. With the exception of the 3D high-lift calculations for the flap loads, hybrid meshes are used in all cases, i.e. quads (2D) and prisms (3D) for the flow area near the wall. In the boundary layer, viscosity dominates the flow. Triangles (2D) or tetrahedra (3D) are used in the outer flow regime. In the following, the terms are used for the 2D case. In short, triangles (also referred to as unstructured) offer greater flexibility, especially for meshing complex geometries. However, with this unstructured approach, all connected node information has to be stored. In contrast, with quads, i.e. the structured approach, the connection of certain cells is predefined by the composition, which eliminates the need to store this information [4]. In addition, the structured approach is preferable in the boundary layer, as the orientation of the quads leads to the flow passing almost vertically over the cell boundaries, which results in a small angular error, or numerical error.

The required height of the prisms needs to be estimated, in order to match the boundary layer. This can of course be done iteratively with several simulation runs, but for an initial estimation, a turbulent flow on a flat plate yields a conservative approach. With Eq. (2.11), the height is known for this case. There is, however, another important parameter, which relates to the cell adjacent to the wall. For this purpose, a few other parameters, the friction coefficient $C_{f,x}$, the shear stress τ_w, and the friction velocity u_τ need to be introduced first, details of which can be found in [125].

$$\tau_w = \mu \left(\frac{\partial u}{\partial y} \right)_{y=0} = 0.5\, \rho\, U_{\text{ref}}^2\, C_{f,x} \quad \text{with} \quad C_{f,x} = \frac{0.074}{\sqrt[5]{Re}} \tag{B.1}$$

$$y^+ = \frac{y\, u_\tau\, \rho}{\mu} \quad \text{with} \quad u_\tau = \sqrt{\frac{\tau_w}{\rho}} \tag{B.2}$$

The dimensionless wall distance is called y^+, the significance of which becomes particularly apparent by considering the curve as shown in Fig. B.5. In this logarithmic representation, it becomes obvious that the progression near the wall is significant and that this directly results in requirements for the meshing. If, for example, the first cell at the wall exhibits a $y^+ = 100$, Fig. B.5 shows that all of the effects near the wall are neglected or has to be modeled. However, if this flow close to the wall shall be simulated, a $y^+ < 1$ is recommended [103].

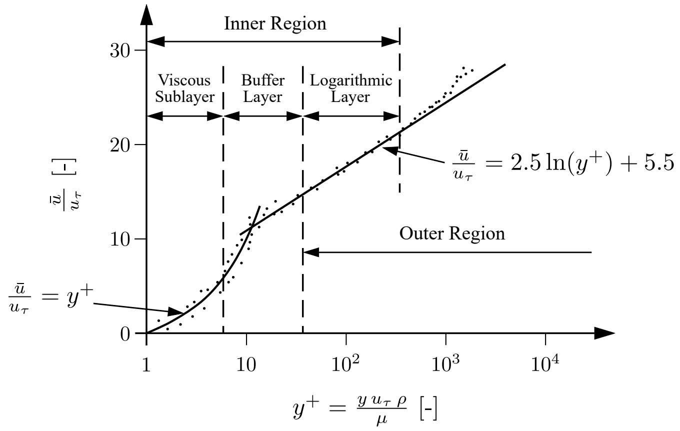

Figure B.5: Velocity profile in a turbulent boundary layer over the dimensionless wall distance y^+, adapted from [106].

This brief overview of RANS CFD is not comprehensive, but is merely intended to explain the most important context to the reader.

Parameter settings for CFD grid generation and solver setting

A large number of 2D CFD simulations were carried out as part of the high-lift airfoil optimization in Section 3.1. The corresponding settings are provided below to enable reproducibility. Table B.2 shows the settings applied for the CFD mesh generator Centaur. Table B.3 provides the settings used for the CFD solver Fluent.

Table B.2: Overview of the settings for Centaur in Section 3.1.

Surface	
Stretching ratio	1.5
Scaling factor	1
Maximum length scale (wall edges)	70
Minimum length scale (wall edges)	1.5
Factor for curvature clustering	20
Factor for proximity clustering	2
Factor for CAD clustering	2
Quads	
First layer thickness	0.001
Number of layers	37
Stretching ratio	1.2
Ramp angle (lateral thickness growth rate)	20
Chop layer	2e-05
Proportion of gaps to be filled by triangles	0.01
Variable stretching	
Stretching ratio up to layer 5	1
Stretching ratio up to layer 40	1.2
Triangles	
Stretching ratio	1.7
Interface length scales blending factor	0.8
Interface thickness ratio	2
Triangular quality	5
Maximum triangular length scale	1 000

Table B.3: Overview of the CFD simulation parameters for Ansys Fluent in Section 3.1.

Models	
Turbulence model	SST k-ω
Materials: Air	
Pressure	Ideal gas
Specific heat capacity	1.006.43 J/(kg K)
Thermal conductivity	0.0242 W/(m K)
Viscosity	Sutherland law
Molecular weight	28.966 g/mol
Boundary Conditions	
Farfield	velocity-inlet
	pressure-farfield
Velocity	70 m/s
Mach number	0.2
X-component	cos(α)
Y-component	sin(α)
Temperature	288.15 K
Turbulent intensity	1 %
Turbulent viscosity ratio	1

B.3 Neural network generation

The generation of artificial neural networks to determine the flap loads in Section 3.2 requires a number of input parameters. These are listed in Table B.4 with their respective range of values. Furthermore, a large number of CFD simulations have been carried out. For details, including validation, please refer to the author's publication [113], whereas the basic solver settings are given in Table B.5. An exemplary presentation of the results for high-lift case is given in Fig. B.6 analogous to the variable camber case in Fig. 3.20.

Table B.4: Input values for neural network generation, as stated in [113].

Application	Input values			
	Parameter		Range	
General				
	Geometry	Rel. flap spanwise position inboard and outboard	0.09 - 0.78	[-]
		Wingspan	34.04 - 64.75	[m]
		Wing aspect ratio	9.47 - 12.28	[-]
		Trailing edge sweep	-0.5 - 26.0	[deg]
Specific				
High-lift	Flow conditions	Angle of attack α	6 - 11	[deg]
	Geometry	Flap deflection	12 - 37.5	[deg]
		Flap area	4.43 - 11.58	[m^2]
	2D simulation	Flap force coefficient in x- and z-direction, inboard and outboard	0.00 - 0.42	[-]
Variable camber	Flow conditions	Angle of attack α	0 - 2	[deg]
	Geometry	Flap deflection, inboard and outboard	-1 - 3	[deg]
		Flap area, including segmented TEDs	2.83 - 11.58	[m^2]
	2D simulation	Flap force coefficient in x- and z-direction, inboard and outboard	0.00 - 0.20	[-]

Table B.5: Additional information on the CFD simulations at ISA+15, as stated in [113].

Parameter	High-lift		Variable camber	
	2D	3D	2D	3D
Solver	Ansys Fluent	Ansys Fluent	Ansys Fluent	TAU
Turbulence model	$k-\omega$ SST		$k-\omega$ SST	
Resulting datasets	136		696	

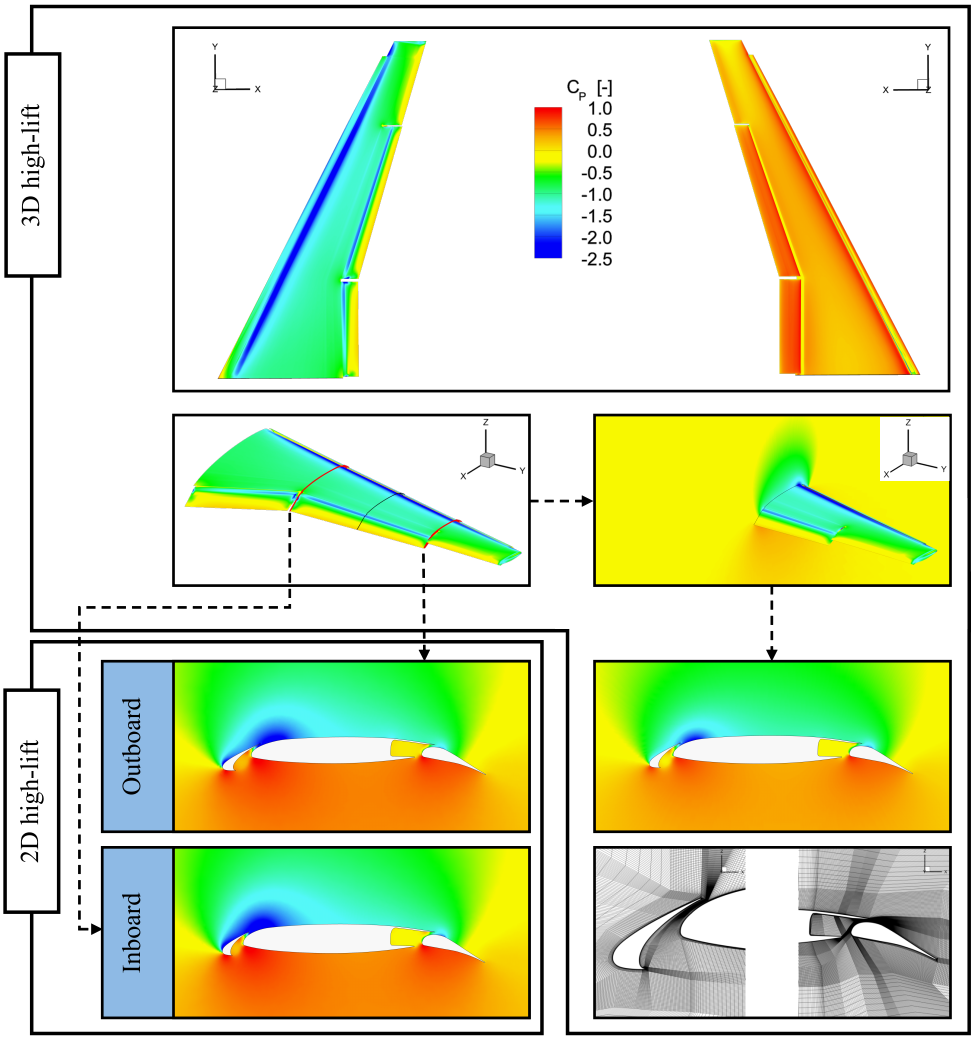

Figure B.6: Exemplary pressure coefficient plot (fuselage blanked). Case: Short-range reference, high-lift at $\alpha = 6°$ and flap angle of 20°, as stated in [113].

B.4 Flowchart of the MICADO tool wingMassEstimation

For the investigations at the overall aircraft level within MICADO, an improved methodology for the wing mass estimation as described in Section 3.4.2 is used in this thesis. Figure B.7 shows the complete flowchart from [29] for the sake of completeness. It is particularly relevant that, as illustrated, both a predefined flight shape or jig shape can be used.

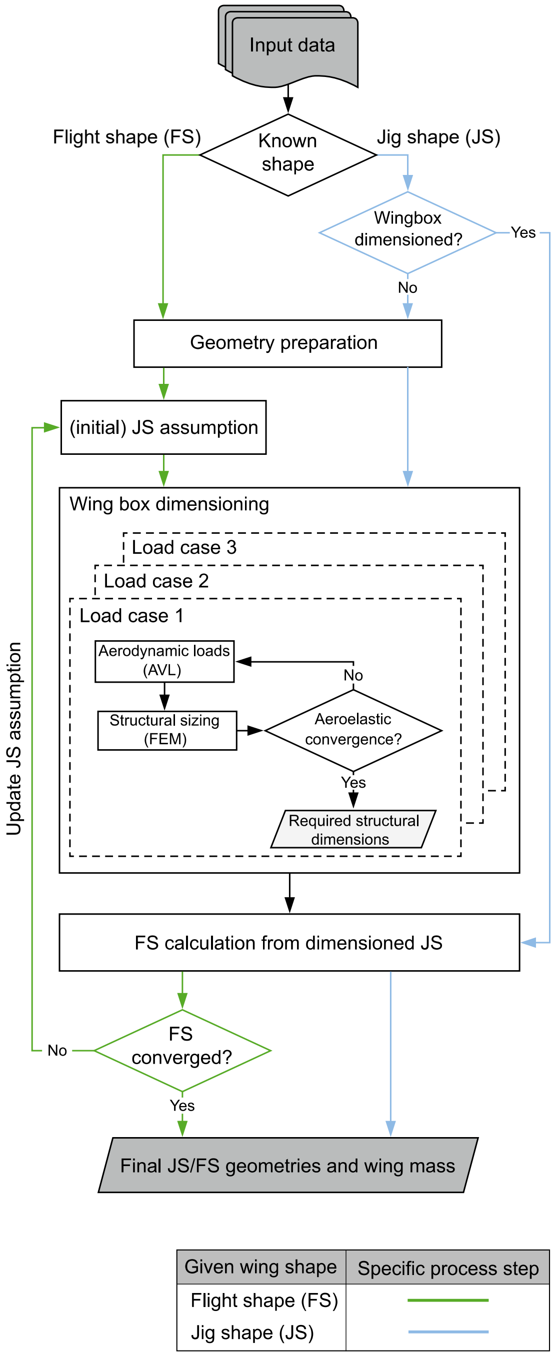

Figure B.7: Wing dimensioning process chain [29].

C Supplementary information on the application and analysis of variable camber technology

This appendix provides configuration settings applied in the MICADO design tool as well as additional information related to the application and analysis of variable camber technology, complementing the discussions in Chapter 4.

C.1 Applied MICADO configuration settings

A large number of configuration parameters may be specified for the iterative preliminary design within MICADO. Table C.1 provides the most important settings deviating from the default that were used to create the long and short distance reference. The default refers to the version of MICADO stated in Section 3.4.1.

C.2 Details on the analysis of variable camber application

The reference aircraft in Section 4.1.1 freely select their mission profile in terms of flight levels for the aircraft design, as stated in Table C.1. For the comparison of the different aircraft with VC application, however, fixed benchmark missions are used as described in Section 4.1.2. The design missions are no longer relevant for the evaluations, but rather have an informative character. Therefore, the design missions are shown in the appendix to avoid confusion. Both long range design missions are given in Fig. C.1

Table C.1: Configurations in MICADO for the long and short range references in Section 4.1.

Parameter	Long range	Short range
`calculatePolar`		
C_L step width for calculation	0.01	0.01
i_{HTP} manual grid points	-1.0; 5.0	-1.0; 3.0
Delta $C_{M,0}$	BSL: 0.22; ASO: 0.28	0.08
Airfoil database		
- Enabled?	yes	yes
- Flow transformation point	Fixed	Fixed
`engineSizing`		
Engine model	Trent 772-60	V2527-A5
Engine scaling	1.00	1.00
Engine fuel flow factor	0.76	0.97
`fuselageDesign`		
Fuselage mass factor	1.44	1.09
`wingMassEstimation`		
Technology factor	0.7	-
`createMissionXML`		
Auto select ICA	active	active
Auto select FL	active	active
`missionAnalysis`		
Fuel mass estimation	Breguet	Breguet

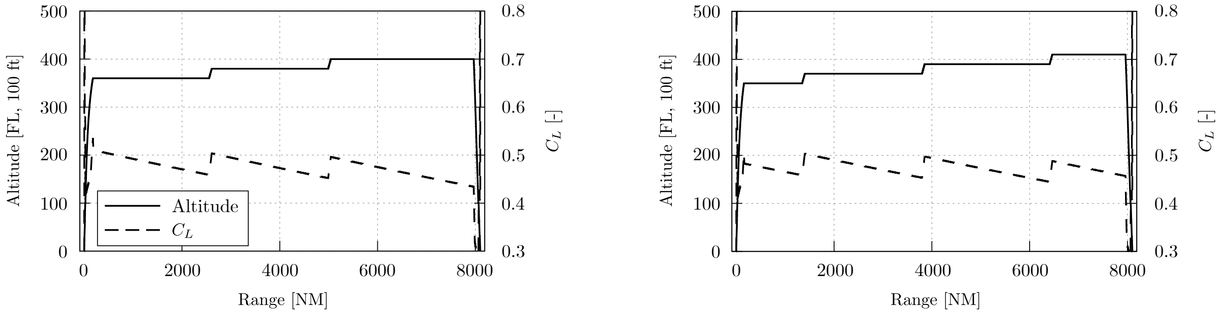

(a) LR-BSL-ref **(b)** LR-ASO-ref

Figure C.1: Long range reference aircraft design mission profiles.

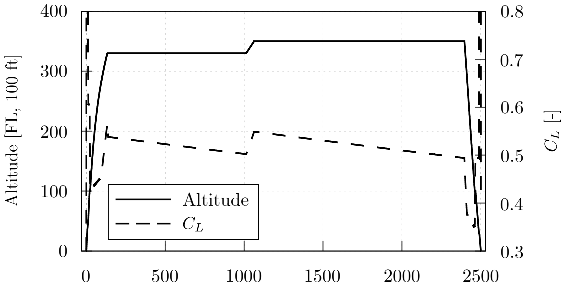

Figure C.2: Short range reference aircraft design mission profile.

Table C.2: Identified VC flap settings of the LR-BSL-VC variant E [130].

C_L range	Flap setting [deg]
0.52 - 0.46	-3, -1, 0, 0, 0
0.46 - 0.42	-3, -2, 0, 0, 0
0.42 - 0.38	-3, -1, 0, 0, 0
0.38 - 0.32	-3, -1, -1, 0, 0

Table C.3: Identified VC flap settings of the LR-ASO-VC variant D [130].

C_L range	Flap setting [deg]
0.52 - 0.46	-3, -2, 0, 0
0.46 - 0.43	-3, -2, -1, 0
0.43 - 0.36	-3, -3, -1, 0

Table C.4: Identified VC flap settings of the SR-BSL-VC variant C [130].

C_L range	Flap setting [deg]
0.55 - 0.54	-2, -1, 0
0.54 - 0.507	-2, 0, 0
0.507 - 0.504	-3, -2, 0
0.504 - 0.48	-3, -1, 0
0.48 - 0.46	-3, -2, 0
0.46 - 0.45	-3, -2, -1

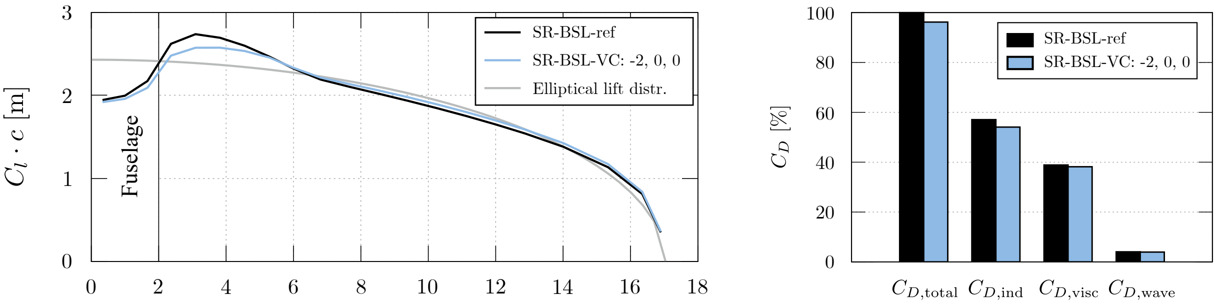

(a) Spanwise lift distribution

(b) Drag components of the wing

Figure C.3: Comparison of the lift distributions and drag components of the SR-BSL-ref and SR-BSL-VC *(2inb-1outb)* at $C_{L,\text{opt,SR-BSL-ref}}$ and $Ma = 0.78$.